Département de géomatique appliquée
Faculté des lettres et sciences humaines
Université de Sherbrooke

Modélisation de l'émission micro-onde hivernale en forêt boréale canadienne

Alexandre Roy

Thèse présentée pour l'obtention du grade de Philosophiae Doctor (Ph. D.) en télédétection,
Cheminement en physique de la télédétection

Janvier 2014

Directeur de recherche: Prof. Alain Royer

Membres du jury interne: Prof. Kalifa Goïta et Prof. Ramata Magagi

Membre du jury externe: Prof. Giovanni Macelloni

Résumé

La caractérisation du couvert nival en forêt boréale est un élément important pour la compréhension des régimes climatiques et hydrologiques. Depuis plusieurs années, l'utilisation des micro-ondes passives est étudiée pour l'estimation de l'équivalent en eau de la neige (SWE : *Snow Water Equivalent*) à partir de capteurs satellitaires. Les algorithmes empiriques traditionnels étant limités en forêt boréale, le couplage d'un modèle de transfert radiatif (MTR) micro-onde passive (qui prend en compte les contributions du sol, de la neige, de la végétation et de l'atmosphère) avec un modèle de neige pour l'inversion du SWE semble une avenue prometteuse. La thèse vise donc à coupler un MTR avec le schéma de surface du modèle climatique canadien (CLASS) dans une perspective d'application opérationnelle pour les estimations de SWE à partir de données satellitaires micro-onde à 10.7, 19 et 37 GHz. Dans ce contexte, certains aspects centraux du MTR, dont l'effet de la taille des grains ainsi que la contribution de la végétation sont développés et quantifiés. Le premier aspect étudié dans la thèse concerne l'adaptation du modèle d'émission micro-onde passive DMRT-ML (Dense media radiative transfer theory – multi layer) pour l'intégration d'une nouvelle métrique représentant la taille des grains (surface spécifique des grains de neige: SSA). L'étude basée sur des mesures radiométriques et de neige in situ, montre la pertinence de l'utilisation de la SSA dans DMRT-ML et permet d'analyser le sens physique de l'adaptation nécessaire pour amener le modèle à simuler les températures de brillance (T_B) de la neige avec une erreur quadratique moyenne minimale de l'ordre de 13 K. Dans un contexte du couplage entre le modèle de neige de CLASS et DMRT-ML, un modèle d'évolution de la SSA est ensuite implémenté dans CLASS. Les SSA simulées par le module développé sont validées avec des données in situ basées sur la réflectance de la neige dans l'infrarouge à courte longueur d'onde pour différents types d'environnement. Au niveau de la contribution de la végétation, le modèle γ-ω a été étudié à partir de différentes bases de données (satellite, avion et au sol) en forêt boréale dense. L'étude montre l'importance de la considération de la diffusion (ω) pour l'estimation de l'émission de la végétation, paramètre auparavant généralement négligé aux hautes fréquences. Ensuite, des relations entre les transmissivités et certains paramètres structuraux de la forêt, dont l'indice de surface foliaire (LAI), ont été établies pour des forêts boréales en été. Des valeurs d'albédo de diffusion (ω) ainsi que les paramètres définissant la réflectivité du sol (QH) en forêt boréale ont aussi été inversées. Finalement, les simulations de T_B issues du couplage du MTR (DMRT-ML, modèle γ-ω, et modèle

atmosphérique) avec CLASS (dont les SSA simulées) ont été comparées avec les données AMSR-E sur une série temporelle continue de sept ans. Les premières comparaisons montrent une différence entre les paramètres de végétation (γ-ω) d'été et d'hiver, ainsi qu'une importante contribution des croûtes de glace dans la neige au signal. Les simulations du modèle ajusté montrent une bonne correspondance avec les observations d'AMSR-E (de l'ordre de 3 à 7 K selon la fréquence et la polarisation). Des tests de sensibilité montrent par contre une faible sensibilité du MTR/CLASS au SWE pour des forêts denses et des couverts nivaux épais. Le MTR-CLASS développé pourrait permettre l'assimilation de températures de brillance satellitaires en forêt boréale dans des systèmes opérationnels pour l'amélioration de paramètres de surface, dont la neige, dans les modèles météorologiques et climatiques.

Mots-clés : Modèle de transfert radiatif (MTR), micro-ondes passives, CLASS, DMRT-ML, surface spécifique des grains de neige (SSA), modèle γ-ω, AMSR-E, température de brillance, équivalent en eau de la neige (SWE), forêt boréale.

Abstract

The characterization of the snow cover in boreal forests is an important element for the understanding of climate and hydrological regimes. For several years, the use of passive microwave to estimate the snow water equivalent (SWE) from satellite sensors has been studied. Because traditional empirical algorithms are limited in the boreal forest, the coupling of a radiative transfer model (RTM) (which takes into account the contributions of soil, snow, vegetation and atmosphere) with a snow model for the retrievals of SWE seems a promising avenue. The thesis aims to couple a RTM with the Canadian Land Surface Scheme (CLASS) from the perspective of operational application to retrieve SWE from passive microwave satellite data at 10.7, 19 and 37 GHz. In this context, some central aspects of the RTM, such as the effect of snow grain size and the contribution of vegetation, are developed and quantified. The first aspect studied in this thesis concerns the adaptation of snow emission model DMRT-ML (Dense media radiative transfer theory - multi layer) for the integration of a new metric representing the grain size (snow specific surface area: SSA). The study, based on radiometric and snow in situ measurements, shows the relevance of using SSA in DMRT-ML and analyzes the physical meaning of adaptation required to simulate the brightness temperature (T_B) of snow with a minimum root mean square error of about 13 K. Using CLASS and DMRT-ML, a model of the evolution of the SSA is then implemented in CLASS. Simulated SSA values are validated with in situ data based on the reflectance of snow in the short-wave infrared for different types of environments. With respect to the contribution of vegetation, the γ-ω model has been studied from different databases (satellite, airborne and ground-based) in dense coniferous forest. The study shows the importance of considering scattering (ω) to estimate the emission of vegetation, generally neglected at high frequencies. Then, the relationship between transmissivity and some structural forest parameters, including the leaf area index (LAI), were established for boreal forest in summer. Values of scattering albedo (ω) and the parameters defining the reflectivity of the ground (QH) in the boreal forest have also been inverted. Finally, simulations of T_B from the coupling of the RTM (DMRT-ML, γ-ω model and atmospheric model) with CLASS (including simulated SSA) were compared with AMSR-E satellite data over a continuous time serie of seven years. The first comparisons show a difference between the vegetation parameters (γ-ω) in summer and in winter, as well as an important contribution of ice crusts in the snow signal. The adjusted model simulations show a good correspondence with the AMSR -E observations (in the order of 3

to 7 K depending on the frequency and the polarization). Sensitivity tests, however, show a low sensitivity by the RTM/CLASS to SWE in dense forests and for deep snowpack. The RTM/CLASS developed could allow the assimilation of satellite brightness temperatures of the boreal forest in operational systems to improve surface parameters including snow in weather and climate models.

Keywords: Radiative Transfer Model (MTR), passive microwave, CLASS, DMRT -ML, specific surface snow grains (SSA), γ-ω model, AMSR -E brightness temperature, snow water equivalent (SWE), boreal forest.

Table des matières

Liste des figures

Liste des tableaux

Liste des acronymes

ASC : Passage d'orbite Ascendante

AMSR-E: Advanced Microwave Scanning Raiometer-EOS

AVHRR: Advanced Very High Resolution Radiometer

CG: Croûte de glace

CLASS: Canadian LAnd Surface Scheme

CLASS-SSA: Canadian LAnd Surface Scheme – Snow Specific Surface Area (Chap. 4)

CoReH2O: Cold Region Hydrology High-resolution Observatory

DBH: Diamètre d'un tronc d'arbre à hauteur de poitrine (*tree diameter-breast-height*)

DISORT: DIscrete Ordinate Radiative Transfer Method

DMRT-ML: Dense Media Radiative Transfer Theory – Multi Layer

DSC: Passage d'orbite Descendante

DUFISSS: Dual Frequency Intergrating Sphere for Snow SSA

ET: Equi-Temperature

FPS: Forest Structural Parameters

GHz: Gigahertz

HQ: Hydro-Québec

HUT n-layer: Helsinki University of Technology multi layer snow emission model

IPY: Année Polaire International (*International Polar Year*)

IRIS: InfraRed Integrated Sphere

LAI: Leaf Area Index

LCC: Land Cover Map of Canada 2005

LWC: Contenue en eau liquide de la neige (*Liquid water content*)

MCGC: Modèle Climatique Global Canadien

MDDEP: Ministère du Développement Durable, de l'Environnement et des Parcs du Québec

MEMLS: Microwave Emission Model of Layered Snowpacks

ML: Multi Layers

MODIS: Moderate Resolution Imaging Spectroradiometer

MOP : Micro-Ondes Passives

MPM: Millimiter-wave propagation model (modèle de trasnfert radiatif atmosphérique)

MRCC: Modèle Régional Canadien du Climat

MSEM: Microwave Snow Emission Model

MTR: Modèle de Transfert Radiatif

MTR/CLASS: Couplage du MTR et de CLASS

NARR: North American Regional Reanalysis

NCEP: National Centers of Environmental Predicion

NSIDC: National Snow and Ice Data Center

POSSSUM: Profiler Of Snow Specific Surface area Using SWIR reflectance Measurement

PR: Ratio de Polarisation

RMSE: Erreur quadratique moyenne (*Root Mean Square Error*)

SIEF: Système d'Information ÉcoForestier

SMAP: Soil Moiture Active Passive

SMOS: Soil Moisture and Ocean Salinity

SSA: Surface spécifique de la neige (*Snow Specific Surface Area*)

SMM/I: Special Sensor Microwave/Imager

SMMR: Scanning Multichannel Microwave Radiometer

SSC: Strong Soil Contribution

SV: Stem Volume

SWE: Équivalent en eau de la neige (*Snow Water Equivalent*)

SWIR: Infrarouge à ondes courtes (*Short-Wave InfraRed*)

T_B: Température de brillance (K) (*Brigthness Temperature*)

TG : Temperature Gradient

WSC: Weak Soil Contribution

Liste des symboles

D_{max}: diamètre maximal d'un grain de neige

e_{atm}: émissivité d'une couche atmosphérique

e_p: émissivité d'une surface pour un poalrisation (p) donnée

$e_{surface}$: émissivité d'une surface sous la canopée

f: volume fractionnel

k_a: coefficients d'absorption

k_e: coefficients d'extinction (DMRT-ML)

$k_{e\text{-}atm}$: coefficients d'extinction d'une couche atmosphérique (MPM)

k_s: coefficients de difusion

k: nombre d'onde (π/λ)

QH: modèle de réflectivité du sol (Wang et al. 1983)

Q_R: Paramètre représentant l'effet de dépolarisation d'une surface

H_R: Paramètre représentant l'effet de rugosité d'une surface

H: polarisation horizontal (pol-H au Chap. 3)

$r_{Fresnel:}$ réflectivité d'une surface lisse (coefficient de Fresnel)

r_p: réflectivité d'une surface pour un polarisation (p) donnée

r_V: réflectivité d'une surface en polarisation verticale

r_H : réflectivité d'une surface en polarisation horizontale

R_s: rayon d'une sphère (grain de neige dans DMRT-ML)

R_{opt}: rayon optique d'un grain de neige

R_{eff} : rayon effectif d'un grain de neige

$SSA_{initial}$: SSA d'une neige fraîche dans CLASS-SSA (73.0 m^2 kg^{-3})

t: Âge d'une couche de neige

$T_{Bforest}$: émission d'un pixel en forêt

$T_{Bsurface}$: émission de la surface sous la canopée atténuée par la végétation

T_{Bveg}: émission de la végétation

$T_{Bveg\text{-}r}$: émissions de la végétation réfléchie par la surface

$T_{Batm\downarrow}$: émission descendante (vers la surface) de l'atmosphère

$T_{Batm\uparrow}$: émission ascendante (vers le capteur satellitaire) de l'atmosphère

$T_{Batm\downarrow\text{-}r\text{-}s}$: émission de l'atmosphère réfléchie par la surface

$T_{Batm\downarrow\text{-}r\text{-}veg}$: émission de l'atmosphère réfléchie par la végétation

T_{Bup}: mesure in situ au dessus de la vegetation (figure 5.3 #1)

T_{Bdown}: mesure in situ vers le haut en dessous de la vegetation (figure 5.3 #2)

$T_{Bsurface\text{-}forest}$: mesure in situ de la surface sous de la vegetation (figure 5.3 #3)

$T_{B\downarrow\text{-}r}$: émission du signal descendant réfléchie par la surface ($T_{Batm\downarrow\text{-}r\text{-}s} + T_{Bveg\text{-}r}$)

$TG_{threshold}$: seuil où l'on considère un régime de gradiant de température dans CLASS-SSA

T_{snow}: température de la neige

$T_{surface}$: température de la surface

T_{veg}: température de la végétation

V: polarisation verticale (pol-V au Chap. 3)

z: hauteur de la couche atmosphérique (MPM)

ρ_{ice}: densité de la glace (917 kg m^{-3})

θ: l'angle par rapport au nadir

θ_{eff}: l'angle effectif pour calculer le $T_{\mathrm{B}atm\downarrow}$ intégré

σ: Rugosité du sol

ε: constante diélectrique ou permittivité

ε_{eff}: constante diélectrique effective

ε_{ff0}: constante diélectrique effective sans diffusion

ε_s: constante diélectrique de la glace

ε_b: constante diélectrique de l'air

ϕ: facteur de correction sur la taille de grains dans les MSEMs

γ: transmissivité de la végétation

ω: albédo de diffusion de la végétation

τ: épaisseur optique de la végétation

τ_s: paramètre d'adhésion (*stickiness factor*)

γ_{atm}: transmissivité atmosphérique

$\gamma_{atm\text{-}nad}$: transmissivité atmosphérique au nadir

λ: longueur d'onde

ΔSSA: Taux de décroissance de la SSA (CLASS-SSA)

Remerciements

Je tiens d'abord à remercier personnellement mon directeur, Alain Royer (Centre d'applications et de recherches en télédétection CARTEL, Université de Sherbrooke). Je suis sincèrement reconnaissant de la confiance dont il m'a fait preuve dans cette entreprise. J'ai grandement apprécié ses innombrables conseils, sa disponibilité ainsi que sa passion contagieuse pour la recherche.

Cette recherche a été financée principalement par le Conseil de recherche en sciences naturelles et génie du Canada (CRSNG). Il faut aussi souligner les contributions financières du fond québécois de la recherche sur la nature et les technologies (FQRNT), ainsi que du CARTEL.

Je remercie Ghislain Picard de m'avoir accueilli comme « visiteur scientifique » à Grenoble à l'été 2011 et de m'avoir permis de participer au développement du modèle DMRT-ML. Ce périple a aussi été financé par le Global Environmental Climate Change Center (GEC3) et la Commission permanente de coopération Franco-Québécoise (Gouvernement du Québec).

Je tiens à remercier tous les co-auteurs des différents articles publiés dans le cadre de cette thèse. Je remercie plus particulièrement Alexandre Langlois, Benoit Montpetit et Florent Dupont pour les nombreux échanges scientifiques et les aventures vécues sur le terrain. Un merci tout spécial à Catherine Brown qui a eu l'amabilité de corriger l'anglais des articles, ainsi qu'à Denis Roy qui a révisé la thèse. Le département de géomatique appliquée ainsi que le CARTEL m'ont aussi offert un milieu de travail stimulant. Je remercie ainsi mes collègues étudiants et les professeurs avec qui j'ai beaucoup apprécié les différents échanges autant professionnels que personnels.

Finalement, je dédie ce travail à Roxanne, Esteban, Mariko et Ophélie qui m'ont continuellement offert un soutien inconditionnel.

Chapitre 1: Introduction

La forêt boréale est le deuxième plus grand biome forestier du globe (Brandt, 2009). Ces régions ont un impact significatif sur la climatologie saisonnière et annuelle de la majeure partie de l'hémisphère nord (Wramneby et al., 2010; Snyder et al., 2004), ainsi que sur le cycle hydrologique (Bonan, 2008). Plus spécifiquement, la neige en forêt boréale a un impact important sur les dynamiques climatiques et hydrologiques. En effet, l'albédo de la neige étant initialement très élevé, une transformation de ses caractéristiques optiques (métamorphisme) ou un changement dans sa couverture spatiale induit des rétroactions climatiques importantes (Vavrus, 2007; Klingaman et al., 2008). En hydrologie, l'eau retenue sous forme solide pendant l'hiver avant d'entrer dans le processus de ruissellement engendre une modification importante des débits et des événements de crues (Roy et al., 2010a; Bergeron et al., 2013). La neige, isolant thermique efficace, agit aussi grandement sur les échanges thermiques entre l'atmosphère et la surface. Les caractéristiques du couvert nival ont ainsi un fort impact sur les températures du sol en hiver qui conditionnent les zones actives du pergélisol (Gouttevin et al., 2011) ainsi que les flux de gaz à effet de serre provenant du sol en forêt boréale (Ullah et al., 2009). La caractérisation du couvert nival (accumulation, albédo, équivalent en eau de la neige [Snow Water Equivalent: SWE], épaisseur, fonte) est donc un élément central pour simuler adéquatement les bilans énergétiques et hydriques dans les régions froides telles que les forêts boréales.

Au Québec, 80% de la puissance hydroélectrique se trouve au nord du 49^{e} parallèle, située dans la sous-région centrale du Québec (figure 1.1 : encadré vert), caractérisée par la présence de la forêt boréale et considérée comme une «région ressource» par Ouranos. Une grande incertitude persiste en ce qui a trait à l'effet des changements climatiques sur les précipitations de ces régions. Une augmentation des précipitations hivernales d'entre 4 et 32 % est appréhendée d'ici 2050 (Bourque et Simonet, 2008). Par ailleurs, certaines observations montrent l'évidence d'une intensification des débits dans le nord du Canada (Déry et al., 2009). Ces ressources en eau à gérer sont d'une grande importance sur le plan économique, environnemental et social. Les simulations du couvert nival, dont le SWE, qui constituent une mesure de mitigation face aux changements climatiques (Turcotte et al., 2004), deviennent ainsi un élément clé dans les systèmes de prévisions hydrologiques.

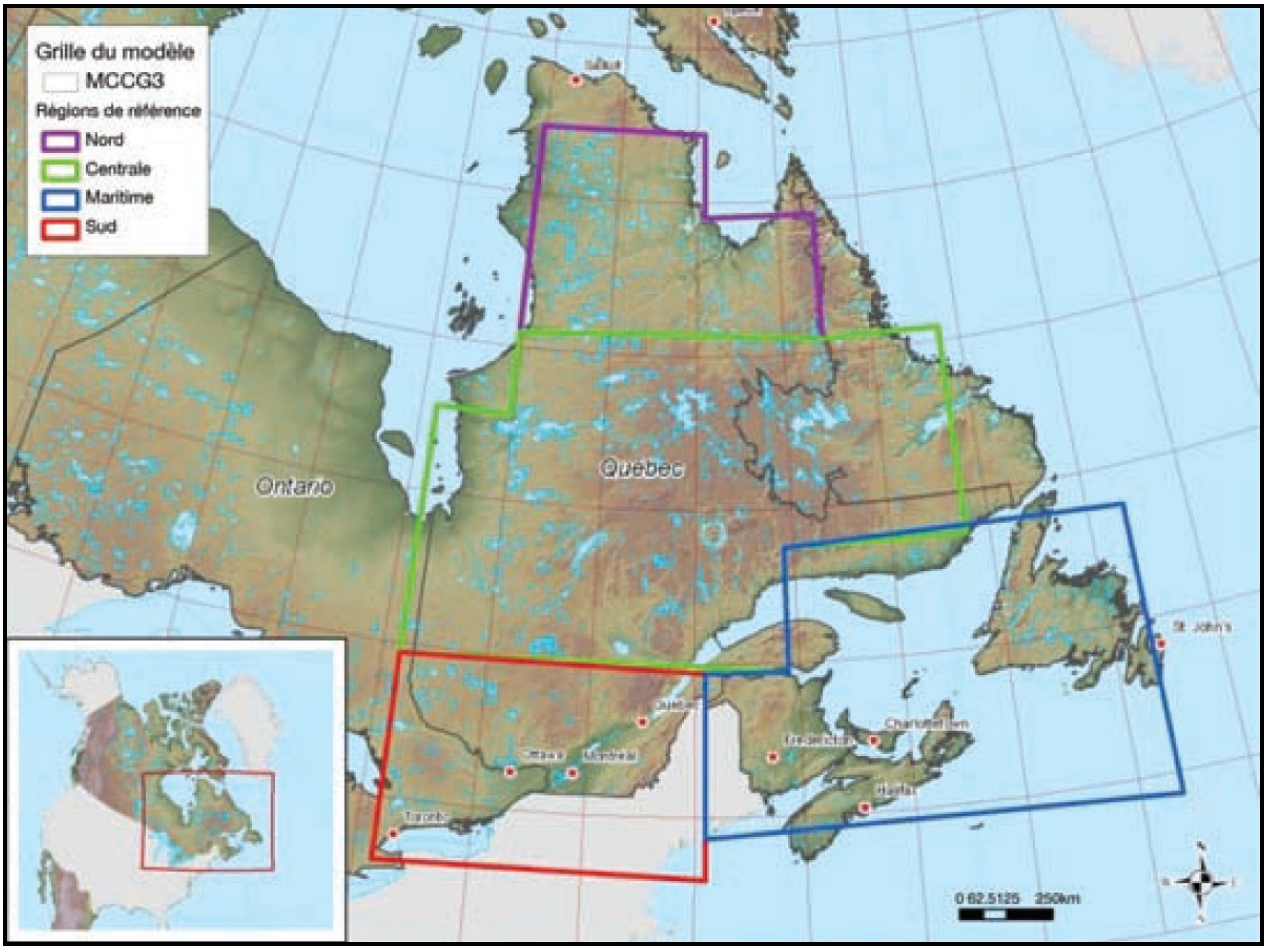

Figure 1.1: L'encadré vert représente la forêt boréale québécoise (région centrale). Tiré de Bourque et Simonet (2008).

Néanmoins, la plupart de ces régions se retrouvent dans des régions éloignées où la faible densité des réseaux de stations météorologiques ne permet pas de générer de l'information spatialement précise sur les attributs climatiques. De plus, les quelques stations météorologiques existantes sont toutes en milieu ouvert, et non représentatives de la situation en forêt (Trujillo et al., 2009). Des modèles de neige sont donc souvent utilisés afin d'estimer l'évolution du couvert nival sur une région donnée (Verseghy et al., 1991; Bélair et al., 2003; Turcotte et al., 2007) . Par contre, les erreurs dans les simulations des SWE issues de modèles de neiges peuvent provenir de différentes sources. Dans les modèles de climat et les modèles météorologiques, les erreurs dans les simulations des SWE sont souvent reliées aux imprécisions dans les données de précipitations (Doraz et Brown, 2008). En forêt boréale, il existe aussi une interaction complexe entre la neige et la végétation telle que les effets d'interception et de sublimation et l'effet d'ombre des arbres qui influencent grandement l'accumulation de neige au sol (Dutra et al., 2011; Ellis et al, 2010;

Wang et al., 2010). Ces processus restent difficiles à modéliser (Rutter et al., 2009; Musselman et al., 2008).

Les micro-ondes passives (MOP) sont un outil intéressant pour l'estimation du SWE à partir de capteurs satellitaires (Foster et al., 2011) pouvant possiblement pallier aux imprécisions des modèles. Ce type de données permet d'obtenir une information synoptique et en temps réel. La télédétection de la neige dans les MOP réside dans le fait que la neige, étant un diffuseur important pour certaines fréquences, atténue le signal reçu au capteur. L'émissivité d'une surface couverte de neige dépend ainsi de la fréquence et de la taille des grains de la neige (diffuseur). Par contre, différentes autres contributions (densité, croûte de glace, végétation, sol gelé/non gelé, humidité dans la neige et atmosphère) modifient les températures de brillance (T_B) mesurées par les capteurs satellitaires limitent grandement la précision des algorithmes traditionnels détectant le SWE du couvert nival, surtout dans la forêt boréale. La plupart de ces contributions restent mal comprises. L'utilisation de modèles de transfert radiatif (MTR), qui simulent les différentes contributions aux T_B mesurées, permet de séparer et mieux comprendre les éléments affectant le signal reçu par un capteur satellitaire. Un modèle de transfert radiatif en forêt doit donc comporter quatre éléments principaux (figure 1.2): un modèle d'émission micro-onde du sol, un modèle d'émission micro-onde de la neige (par la suite, ces deux modèles sont regroupés; *microwave snow emission model* : MSEM), un modèle de transfert radiatif de la végétation et un modèle de transfert radiatif atmosphérique.

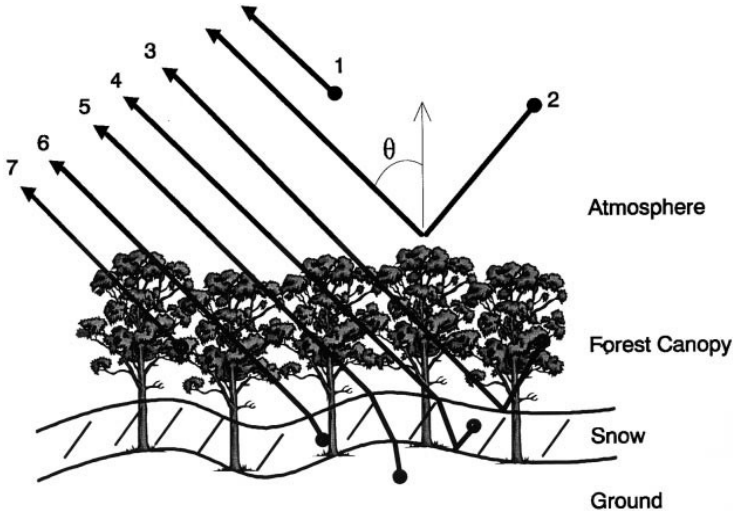

Figure 1.2: Contributions aux T_B reçues par un capteur satellitaire (tiré de Pulliainen & Hallikainen, 2001).

L'étude porte donc sur la modélisation de l'émission micro-onde hivernale en forêt boréale à l'aide d'un couplage d'un MTR dans le schéma Canadien de surface (Canadian Land Surface Scheme: CLASS). Pour arriver à modéliser le signal micro-onde passif, le travail s'attarde principalement sur l'effet de la taille des grains sur l'émissivité de la neige ainsi que l'effet de la contribution de la végétation sur le signal reçu par un capteur satellitaire. L'étude s'insère dans une perspective d'assimilation opérationnelle des T_B dans CLASS pour l'amélioration des estimations de SWE. À noter que dans la suite du travail, le couplage du MTR dans CLASS sera nommé MTR/CLASS. Dans ce chapitre, les principaux éléments de la problématique seront décrits plus en détail avant de présenter les objectifs et la méthode générale du travail.

1.1 Problématique

Cette section développe sur les deux principaux éléments de la problématique. D'abord, une présentation des erreurs issues des simulations du SWE dans CLASS motivant l'utilisation de la télédétection micro-onde est donnée. Ensuite, les principales difficultés pour l'utilisation des MOP pour l'estimation du SWE seront rapidement présentées.

1.1.1 Erreurs dans les simulations du SWE de CLASS

Cette étude se concentre sur le schéma de surface Canadien CLASS. CLASS, développé à Environnement Canada pour modéliser l'évolution des caractéristiques physiques de la surface terrestre, permet notamment de simuler l'évolution du couvert nival au Canada. Initialement, CLASS a été produit pour fonctionner au sein du Modèle climatique global canadien (MCGC). Les sorties du modèle climatique constituent ainsi normalement les données entrantes de CLASS qui calcule ensuite les paramètres de surface (évolution du couvert nival, albédo, flux radiatifs et turbulents, etc.) qui sont ensuite retournés au modèle atmosphérique. Le modèle CLASS est actuellement utilisé opérationnellement dans le MCGC (Scinocca et al., 2008) ainsi que le Modèle régional canadien du climat (MRCC : Music & Caya, 2007; Caya & Laprise, 1999).

Le modèle de neige inclus dans CLASS est à une couche (voir Brown et al., 2006). Le bilan énergétique du couvert nival dans CLASS prend en compte le rayonnement à courtes longueurs d'onde, le rayonnement à longues longueurs d'onde, l'albédo de la neige et sa densité, les flux de chaleurs sensibles et latentes ainsi que le flux de chaleur provenant du sol. Les variables d'état de la neige simulées par le modèle sont ainsi la température moyenne, la densité, la hauteur et la

quantité d'eau liquide (*Liquide water Content* : LWC). Le modèle calcule les bilans de masses et d'énergie. Ainsi, si la température de surface simulée est au-dessus du point de congélation, la température de surface est remise à zéro et l'énergie excédentaire induit de la fonte. La quantité d'eau liquide qui percole dans le couvert nival est déterminée à partir d'un bilan de chaleur. Si la température du couvert est sous le point congélation, l'eau liquide gèle et la chaleur est transmise au couvert. Le modèle inclut aussi une rétention d'eau dans le couvert. La fonte à l'interface neige-sol est aussi considérée lorsque la température y est supérieure à zéro. La densité et l'albédo de la neige sont modélisés en fonction du vieillissement de la neige avec des relations empiriques décroissantes exponentielles.

Même si lors du *Snow Model Intercomparison Project (SnowMIP)*, CLASS est ressorti comme l'un des meilleurs modèles de neige à une couche inclus dans la comparaison, il existe néanmoins une importante variabilité interannuelle dans la précision de l'estimation du SWE par le modèle CLASS (Brown et al., 2006). Étant donné qu'un modèle est une représentation simplifiée d'un système, une erreur inhérente à la simulation des différentes variables du système est présente. Les imprécisions dans l'estimation des différentes variables d'état dans CLASS (déficit énergétique ; température de la surface de la neige, de la neige et du sol ; albédo ; fonte ; hétérogénéité ; etc.) font en sorte qu'il existe une erreur dans le calcul du SWE reliée directement à la simplification du modèle conceptuel. Il faut aussi considérer que les données entrantes alimentant le modèle peuvent constituer une source de biais significative au modèle. Au niveau du calcul du SWE, les modèles de neige sont principalement sensibles aux précipitations. Doraz & Brown (2008) ont montré que le MRCC sous-estimait le SWE maximal au Québec principalement à cause de précipitations solides simulées trop faibles.

La figure 1.3 montre la comparaison des simulations des paramètres du couvert nival de MRCC4 (incluant CLASS) et des mesures in situ prises avec un carottier à travers le Québec. On voit que l'erreur quadratique moyenne (RMSE) de 73.4 mm sur le SWE est plus du double de l'erreur généralement accepté de 30 mm établie dans le projet CoreH2O (Rott et al., 2010). Langlois et al., (2013) montrent que le modèle est très sensible au calcul de l'albédo de la neige ainsi qu'à la phase des précipitations. Ces résultats démontrent ainsi un besoin important d'améliorer les calculs de SWE.

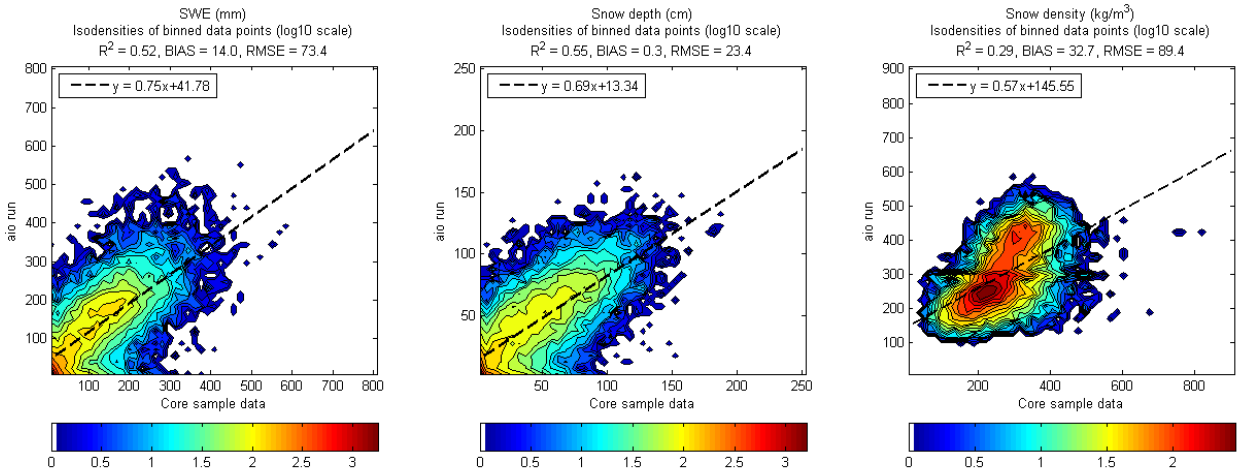

Figure 1.3: Comparaison des paramètres du couvert nival simulés par MRCC4 et mesurés (gauche : SWE ; centre : épaisseur de neige; droite : densité) (tiré de Langlois et al., 2013).

Ces erreurs induisent ainsi des imprécisions dans les prévisions hydrologiques (Gagnon et al., 2007) et possiblement météorologiques. Or, ces systèmes de prévisions font partie des principales mesures d'adaptation face aux éventuels changements climatiques appréhendés par la communauté scientifique. Il existe aussi un grand intérêt de connaître l'effet de la propagation de ces erreurs dans les prévisions futures.

1.1.2 Les micro-ondes passives pour l'estimation de l'équivalent en eau de la neige

La télédétection est de plus en plus utilisée pour observer l'évolution de la cryosphère et des couverts nivaux. Les données optiques et infrarouges (Moderate Resolution Imaging Spectroradiometer: MODIS, Advanced Very High Resolution Radiometer: AVHRR) permettent d'estimer l'étendue du couvert nival ainsi que l'albédo de la neige (Hall et al., 1995; Klein & Strove, 2002). Ces mesures ne donnent par contre pas d'information sur la quantité de neige présente et sont aussi limitées par la présence du couvert nuageux. Les données radar en bande C (Synthetic Aparture Radar : SAR) et Ku (QuickScat) permettent de cartographier l'étendue de la fonte de neige (Roy et al., 2010b; Nagler & Rott, 2000). D'autres parts, le projet CoreH2O (ESA, 2012) qui se base sur l'utilisation de deux radars (bande Ku et X) pour estimer le SWE à haute résolution sur le globe n'a pas été retenu par l'Agence Spatiale Européenne.

Plusieurs études ont démontré la sensibilité des MOP à la neige (Chang et al., 1987). Cette sensibilité réside principalement dans l'atténuation du signal par diffusion de volume causée par la discontinuité diélectrique entre les grains de neige et l'air (Bernier 1987). Lorsque la longueur

d'onde est comparable à la taille des grains (hautes fréquences : 37 GHz), la neige sèche absorbe très peu de radiation, ce qui permet à l'onde de pénétrer et de se diffuser, ce qui entraine une atténuation du signal (Amlien, 2008). Les fréquences plus basses interagissent peu avec la neige. L'atténuation dépend donc principalement de la fréquence, de la taille des grains de neige, de l'épaisseur ainsi que de la densité du couvert nival (voir le rappel théorique au Chap. 2).

Les mesures satellitaires MOP offrent aussi d'autres avantages intéressants. Des mesures de l'émission micro-onde de la surface terrestre sont disponibles depuis 1979, permettant des analyses représentatives des cycles climatiques. La répétitivité élevée du temps de passage (plus de 2 fois par jour dans les hautes latitudes) de ces capteurs en fait des outils attrayants pour l'étude globale des caractéristiques de la surface terrestre. La résolution spatiale de ces images est par contre généralement considérée comme grossière (entre 10 et 25 km^2).

Plusieurs algorithmes empiriques ont été développés pour estimer soit le SWE ou la hauteur de neige au sol à partir des mesures satellitaires MOP. La combinaison de deux différentes fréquences (37 GHz - 19 GHz), dont l'une est moins sensible à la neige (19 GHz), est souvent utilisée pour calculer des relations empiriques avec le SWE (voir Amlien, 2008 pour un aperçu de différents algorithmes). Certains algorithmes utilisent aussi la différence de polarisation spectrale (Aschbacher, 1989). Il a par contre été démontré que ces relations empiriques sont seulement valides pour des zones limitées et parfois inadéquates pour certains environnements comme la forêt boréale (Comtois-Boutet, 2007). Andreadis & Lettenmaier (2006) ont aussi constaté que l'utilisation des produits de SWE issus des MOP ne permettait pas d'améliorer les simulations hydrologiques.

L'utilisation de relations empiriques est souvent inadéquate à cause de la variation interannuelle de la métamorphose des grains de neige (Kelly & Chang 2003; Rosenfeld & Grody, 2000). La taille de grains est par contre un paramètre difficilement mesurable. La surface spécifique de la taille des grains de neige (SSA : *specific surface area*) définie comme le rapport entre la surface (S) et le volume (V_o) du grain de neige;

$$SSA = \frac{S}{V_o \cdot \rho_{ice}} \tag{1.1}$$

où ρ_{ice} est la densité de la glace (917 kg m^{-3}), est un paramètre qui permet de représenter la taille et la forme du grain en plus d'être maintenant mesurable de façon objective à partir de la réflectance dans l'infrarouge à ondes courtes (SWIR : *short-wave infrared*) (Gallet et al., 2009; voir Montpetit et al., 2012 à l'Annexe 4). Il a été montré que la SSA permet de bien représenter la taille de grains dans un modèle d'émission micro-onde de la neige en Antarctique (Brucker et al., 2011). Néanmoins, étant donné que la représentation des grains de neige dans les modèles d'émission micro-onde diffère du concept de la SSA, il est important de vérifier comment intégrer la SSA dans un modèle de transfert radiatif pour des neiges saisonnières. Aussi, dans le contexte d'un couplage MTR/CLASS pour quantifier l'effet de l'évolution de la taille des grains de neige sur l'émission micro-onde de la neige, un modèle de métamorphisme de la neige (modélisation de la SSA) doit donc être implémenté dans CLASS.

Ces relations sont aussi difficilement applicables en milieu forestier où la végétation masque une partie du signal provenant du sol (Chang *et al.* 1987; Goïta et al., 2003; Derksen et al., 2008). Peu de modèles sont disponibles pour considérer l'effet de la végétation pour les hautes fréquences sensibles à la neige (19 et 37 GHz). Certains modèles calculent la transmittance de la végétation (voir Sect. 2.2) pour les hautes fréquences en fonction du volume des troncs (Langlois et al., 2011; Kruopis et al. 1999). Ces relations sont par contre difficilement applicables au niveau satellitaire sur de grands territoires à cause du manque d'information spatialisée du volume des troncs. De plus, ces modèles négligent l'effet de diffusion de la végétation et considèrent donc une émissivité de la végétation à 1.

Les relations empiriques sont aussi limitées pour des SWE n'excédant pas 120 mm à cause de l'effet de saturation de la longueur de pénétration à 37 GHz (Rosenfeld & Grody et al., 2001). Un autre facteur important peut être la formation de croûtes de glace sur ou dans le couvert nival qui affecte radicalement le signal MOP (Montpetit et al., 2013; Rees et al., 2010). Les caractéristiques du sol (teneur en eau liquide, phase, température) ont aussi un effet sur les T_B, surtout aux plus basses fréquences, même lorsque le sol est couvert de neige (Kohn & Royer 2010).

La figure 1.4 montre ainsi que les différences de fréquences (T_B issues d'AMSR-E) normalement utilisées par les algorithmes empiriques de calcul du SWE ne montrent aucune régression claire avec les mesures de SWE en forêt boréale au nord du Québec. Dans une perspective d'utilisation de données MOP pour l'amélioration du SWE dans CLASS, une meilleure compréhension des différentes contributions doit donc être investiguée.

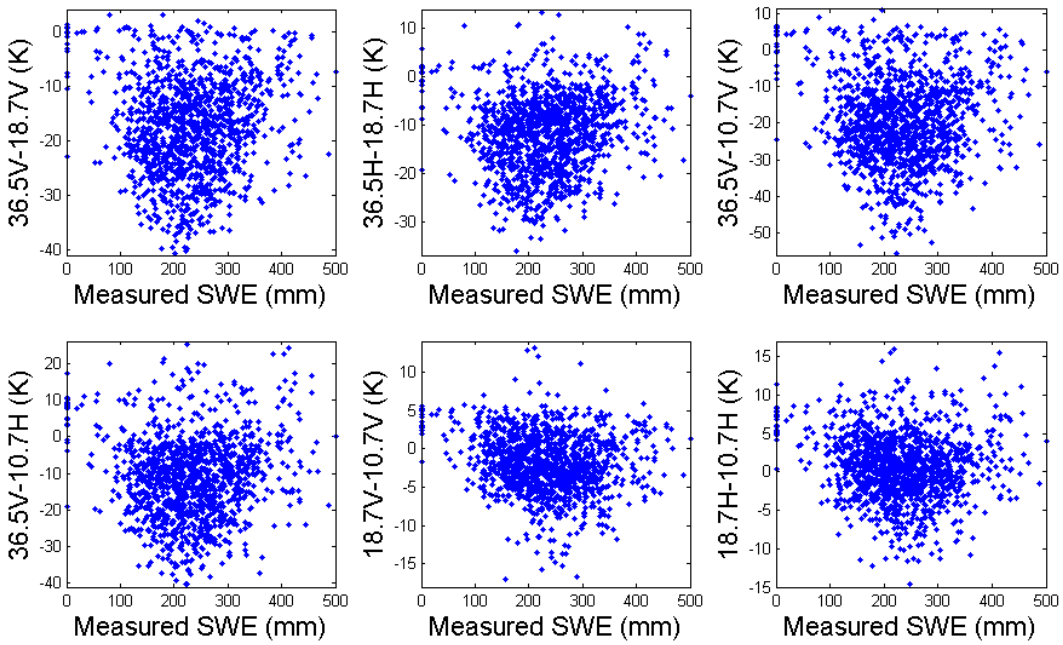

Figure 1.4: Comparaison des SWE mesurées (Hydro-Québec) avec différentes différences de fréquences issues d'AMSR-E.

Une solution pour considérer les différentes contributions au T_B en forêt boréale est l'utilisation d'un MTR, pour quantifier les contributions des différents éléments. Une fois ces contributions bien comprises et quantifiées, il sera éventuellement possible de développer des méthodes d'inversion ou d'assimilation (Langlois et al., 2012; Durand et al., 2009; Andreadis & Lettenmaier, 2006) pour améliorer les estimations de SWE dans CLASS à partir d'un couplage avec le MTR développé.

1.2 Objectif

L'objectif principal de la thèse est de coupler un modèle de transfert radiatif avec le schéma de surface CLASS afin de modéliser l'émission micro-onde hivernale en forêt boréale. L'étude vise à mieux modéliser et comprendre les effets des différentes contributions au signal dans une

perspective où ce couplage permettra d'améliorer les estimations du SWE à partir de données satellitaires. Ce projet s'insère dans une perspective d'application opérationnelle dans des systèmes d'assimilation établis comme le *Canadian Land data Assimiliation System* (CaLDAS) d'Environnement Canada.

Trois objectifs spécifiques permettront de répondre à l'objectif principal :

1. Paramétriser un MSEM (*Dense Media Radiative Transfer Theory – Multi Layer* : DMRT-ML) en fonction de la SSA
2. Développer un module de métamorphisme des grains (SSA) dans CLASS.
3. Paramétriser le modèle de transfert radiatif de la végétation (γ-ω) et du sol (QH) pour la forêt boréale.

Les trois objectifs constituent donc des outils nécessaires à la réalisation du couplage MTR/CLASS. La comparaison de simulations issues de MTR/CLASS avec une série temporelle continue de donnée satellitaires (AMSR-E) permettra ensuite de valider et de raffiner le couplage. Ce travail permettra ensuite d'évaluer le potentiel du couplage et des données satellitaires pour l'amélioration de l'estimation du SWE dans CLASS en forêt boréale.

1.3 Méthode générale et canevas de la thèse

La figure 1.5 montre l'organigramme des différents modèles et données nécessaires au couplage, tandis que la figure 1.6 montre les principaux sites d'études utilisés pour répondre aux différents objectifs. Les résultats de la thèse sont divisés en quatre chapitres qui représentent chacun un article. Chacun de ces articles répond ainsi à un objectif spécifique (Sect. 1.2) afin de permettre le couplage MTR/CLASS. Une dernière section Discussion compare les T_B simulées issues de MTR/CLASS comparées avec les observations d'AMSR-E. De cette comparaison, certains raffinements sont apportés aux différentes sections du MTR. Il est ensuite possible de vérifier la sensibilité des T_B au SWE et de discuter du potentiel de l'utilisation des T_B satellitaires pour l'estimation du SWE en forêt boréale à partir du MTR/CLASS.

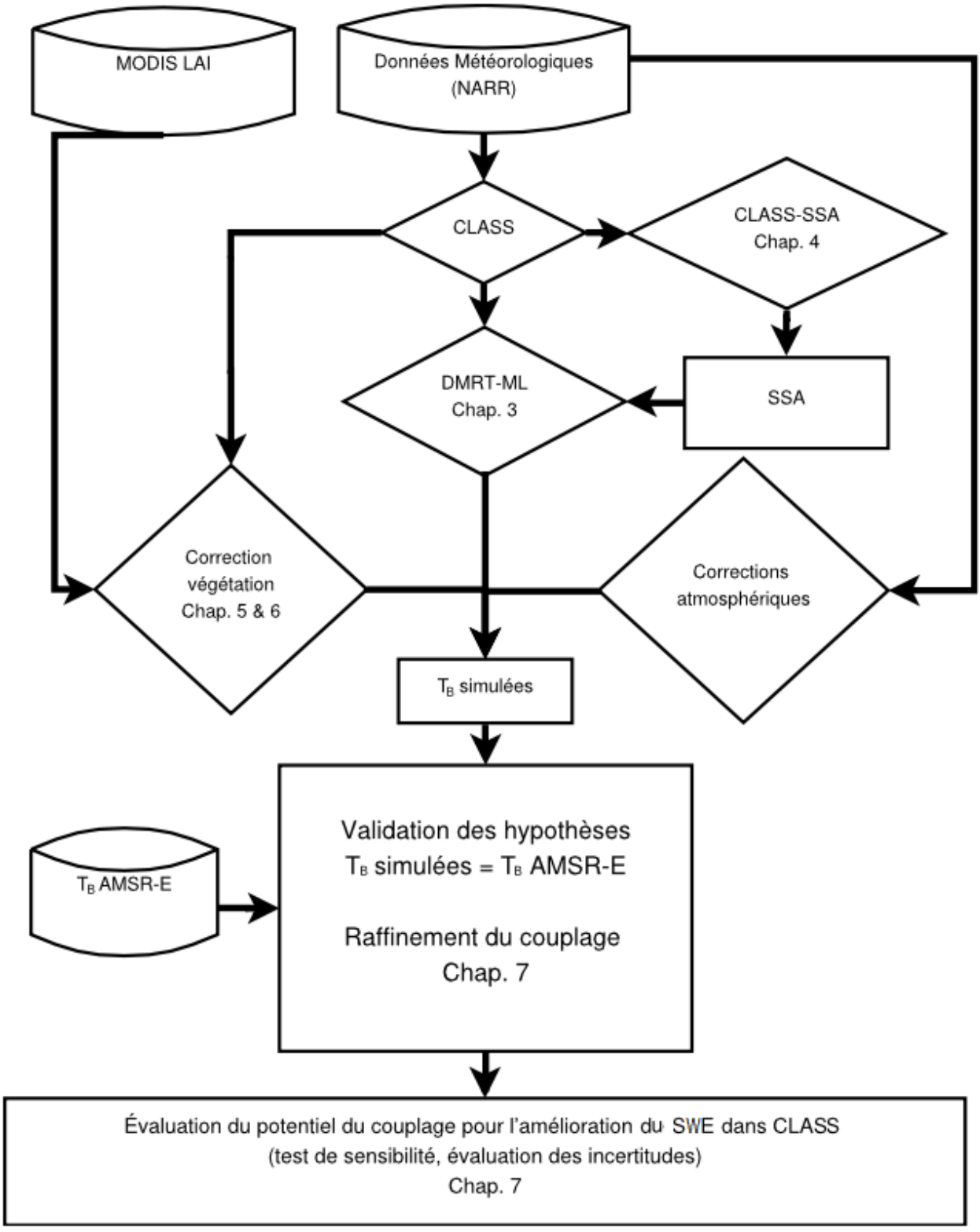

Figure 1.5: Organigramme du couplage MTR/CLASS indiquant la contribution de chacun des chapitres de cette thèse.

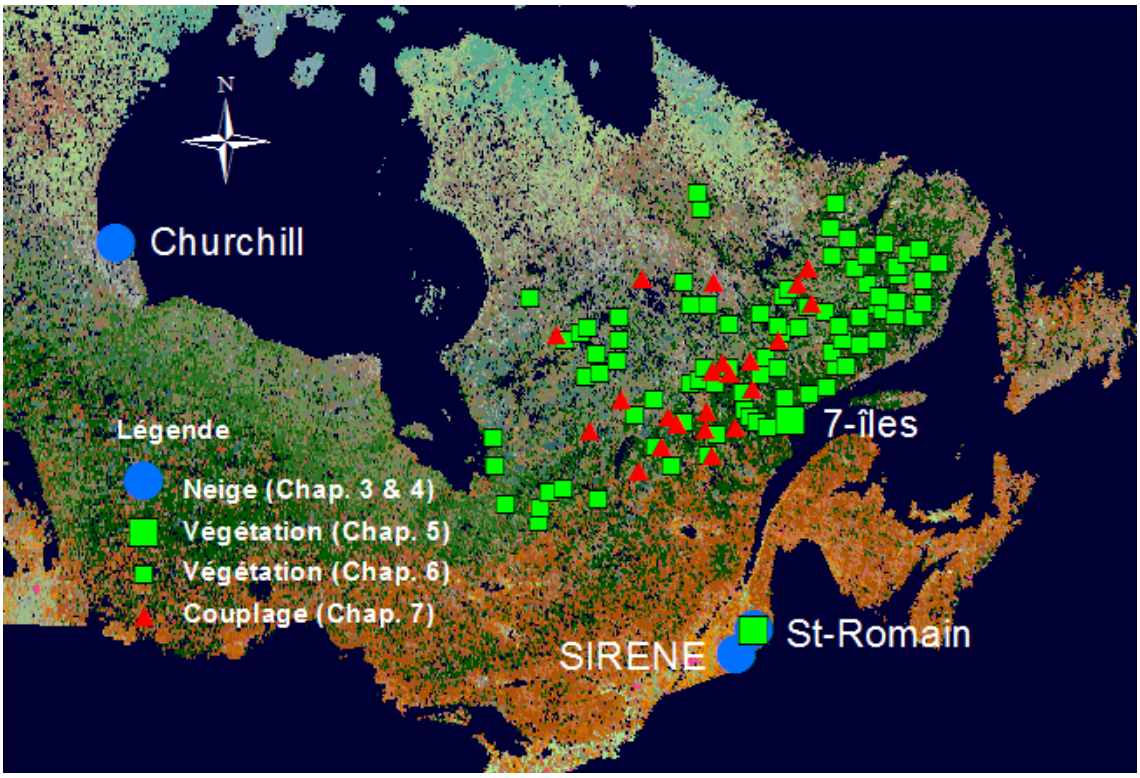

Figure 1.6 : Principaux sites d'études pour chacune des parties de la thèse (carte de fond : Land Cover of Canada 2005)

Dans l'optique où l'approche doit être appliquée globalement à la forêt boréale au Québec, les données météorologiques NARR (Mesinger et al., 2006) sont utilisées pour alimenter les modèles. NARR offre des données atmosphériques et de surface à une résolution temporelle de 3 heures de 1979 au présent (données fournies en temps réel). Les données sont issues du modèle atmosphérique Eta du National Centers of Environmental Prediction (NCEP) et de son système d'assimilation. Le système assimile ainsi un ensemble d'observations (dont les précipitations) pour corriger les principles variables du modèle. Il a été démontré que NARR permettait de bien alimenter les modèles de neige (Langlois et al., 2009) et il est considéré que NARR n'a pas de biais significatif. Les corrections atmosphériques sont toujours considérées dans les simulations avec le « *Millimiter-wave propagation model* » (MPM : Liebe, 1989) (voir Sect.2.3). Les données atmosphériques NARR (température et humidité des couches d'atmosphère) sont ainsi utilisées pour alimenter le modèle atmosphérique.

Le principal MSEM utilisé dans cette étude est DMRT-ML (Picard et al., 2013a; voir Sect. 2.1). Pour le premier objectif spécifique, au Chap. 3, sachant l'importance de la taille des grains dans l'émission micro-onde, une implémentation de l'intégration de la métrique SSA pour représenter

la taille des grains de neige dans DMRT-ML est évaluée sur 3 sites différents où des mesures radiométriques et de neige (SSA, densité et hauteur de neige) ont été prises (figure 1.6 et tableau 1.1). Sur ces mêmes sites, au Chap.4, CLASS-SSA, le module nécessaire pour la représentation du métamorphisme des grains de neige (objectif spécifique 2), est implémenté et validé à partir des données de SSA in situ.

Tableau 1.1 : Ensemble des données utilisées dans chacun des chapitres (une description détaillée de ces données est fournie dans chacun des chapitres)

	Chap. 3	**Chap. 4**	**Chap. 5**	**Chap. 6**	**Chap. 7**
Type de données (figure 1.6)	Neige	Neige	Végétation	Végétation	Couplage
Mesures et données utilisées	-Température - Densité - Hauteur - SSA - Données radiomètres (37 et 19 GHz)	- SSA - Hauteur	Données radiométriques - In situ hiver (St-Romain) - Aéroportées hiver (7-Îles) - AMSR-E (été)	- AMSR-E (été) - LAI (été et hiver) -Biomasse -Volume total	- AMSR-E (été et hiver) - SWE in situ (Hydro-Québec) - LAI MODIS (hiver)

Pour le troisième objectif spécifique, le Chap. 5 montre une première analyse de la paramétrisation du modèle γ-ω (voir Sect 2.2) principalement en milieu de forêt boréale dense pour quatre fréquences (37 GHz, 19 GHz, 10.7 GHz et 6.9 GHz) avec différents types de données radiométriques d'été et d'hiver (in situ, aéroportées, satellitaires : voir figure 1.6 et tableau 1.1). Afin de spatialiser les corrections de végétation, des relations entre le modèle γ-ω et différents paramètres structuraux de la forêt en été (Leaf area index : LAI, biomasse et volume total) dans le nord du Québec sont ensuite inversées à partir de données AMSR-E au Chap. 6 (voir figure 1.6 et tableau 1.1). Les paramètres de réflectivité du sol (QH) pour les forêts boréales y sont aussi calculés.

Le couplage MTR/CLASS est ensuite appliqué sur différents sites dans le nord du Québec où des mesures mensuelles de SWE ont été prises (base de données d'Hydro-Québec : figure 1.6 et tableau 1.1). Les simulations de CLASS (incluant CLASS-SSA) sont ainsi utilisées comme intrants dans le MTR (DMRT-ML, γ-ω) pour simuler les T_B. Les T_B simulées seront comparées avec les observations d'AMSR-E. De cette comparaison, quelques ajustements seront appliqués au MTR (émission du sol, γ-ω hiver, croûtes de glace). Une fois le couplage validé, il sera

possible d'évaluer l'effet des différentes incertitudes sur l'utilisation des données MOP satellitaires pour l'estimation du SWE. Des tests de sensibilité pourront permettre de mieux comprendre le rôle des principales composantes (grains de neige, végétation, croûtes de glace) sur le signal MOP en forêt boréale.

Chapitre 2: Cadre théorique

Cette section dresse un résumé global de l'effet des différentes contributions aux MOP en forêt boréale. Pour chacun des principaux éléments, une base théorique des modèles de transfert radiatif est d'abord présentée avant de présenter quelques tests de sensibilité issus de ces modèles. Par la suite, une description de différentes méthodes d'assimilation pour estimer le SWE à partir des MTR est donnée. Les simulations de modèles de transfert radiatif de cette section ne servent qu'à représenter les tendances générales, sachant que certains paramètres ne sont pas nécessairement optimisés dans les modèles. Cette section représente aussi un certain complément à la problématique où certaines difficultés reliées au modèle de transfert radiatif seront soulevées.

Le calcul des T_B mesurées en hiver par un capteur satellitaire en forêt boréale ($T_{Bforest}$) se traduit pour une fréquence et une polarisation données par (voir figure 1.2):

$$T_{B\,forest} = \left|(T_{B\,snow} + T_{B\,veg-r} + T_{B\,atm\downarrow-r-s}) \cdot \gamma + T_{B\,veg} + T_{B\,atm\downarrow-r-veg}\right| \cdot \gamma_{atm} + T_{B\,atm\uparrow}, \qquad (2.1)$$

où T_{Bsnow} est la température de brillance provenant de la surface couverte de neige sous la végétation, T_{Bveg} est la température de brillance émise par la végétation, $T_{Bveg\text{-}r}$ est la température de brillance émise par la végétation et réfléchie par la surface couverte de neige, $T_{Batm\downarrow\text{-}r\text{-}s}$ et $T_{Batm\downarrow\text{-}r\text{-}s}$ sont les T_B atmosphériques descendantes réfléchies respectivement par la surface et la végétation, γ_{atm} est la transmittance de l'atmosphère, et $T_{Batm\uparrow}$ est la température de brillance de l'atmosphère émise directement vers le capteur.

2.1 T_B sous la canopée

La T_B sous la canopée est constituée de T_{Bsnow} ainsi que du signal descendant réfléchi par la surface ($T_{B\downarrow\text{-}r}$: $T_{Batm\downarrow\text{-}r\text{-}s}$ + $T_{Bveg\text{-}r}$). À noter que le T_{Bsnow} considère l'émission du sol ainsi que l'émission et l'atténuation de la neige. Trois principaux modèles existent pour simuler la T_B d'une surface enneigée (T_{Bsnow}): DMRT-ML (Dense Media Radiative Transfer Theory – Multi-Layer: Picard et al., 2013a), Helsinki University of Thechnology (HUT n-layer : Lemmetyinen et al., 2012) et Microwave Emission Model of Layered Snowpacks (MEMLS : Wiesmann & Mätzler, 1999). Cette étude se concentre davantage sur DMRT-ML qui est une version opérationnelle de

la théorie DMRT (Tsang et al., 2001). L'avantage de la théorie DMRT est qu'elle permet de résoudre la constante diélectrique effective de la neige à partir des équations de Maxwell. DMRT-ML permet aussi de considérer un grand nombre de flux lors de la résolution du transfert radiatif (voir Picard et al., 2013). Dans le cadre de cette thèse, un module pour considérer l'émissivité du sol a été implémenté dans DMRT-ML afin de pouvoir simuler des neiges saisonnières (Picard et al., 2013a).

2.1.1 Neige

DMRT-ML considère que la neige est composée de sphères de glace. Le calcul de la constante diélectrique de la neige est résolu avec l'approximation quasi-cystalline de premier ordre et l'approximation de Percus-Yevick. La constante diélectrique effective (ε_{eff}) est calculée selon (Picard et al., 2013a) :

$$\varepsilon_{eff} = \varepsilon_b + (\varepsilon_{eff\,0} - \varepsilon_b)\left[(1 + \imath\frac{2}{9}(k_0 R_s)^3\sqrt{\varepsilon_{eff\,0}}\,\frac{\varepsilon_s - \varepsilon_b}{1} + \frac{\varepsilon_s - \varepsilon_b}{3\varepsilon_{eff\,0}}(1-f)\frac{(1-f)^4}{(1+2f - tf(1-f))^2}\right], \qquad (2.2)$$

où $k_0 = \pi/\lambda$ avec λ égal à la longueur d'onde, ε_s et ε_b sont respectivement les constantes diélectriques de la glace et de l'air, f est le volume fractionnel, ε_{ff0} est la constante diélectrique effective sans diffusion (voir Tsang et Kong, 2001) et R_s est le rayon des sphères de glace. t est égal à zéro lorsqu'il n'y a pas d'agrégation entre les sphères, ou égal à la plus grande solution de :

$$\frac{f}{12}t^2 - (\tau_s + \frac{f}{1-f})t + \frac{1 + f/2}{(1-f)^2} = 0, \qquad (2.3)$$

où τ_s est le paramètre d'agrégation (Shih et al., 1997). L'effet de l'agrégation entre les sphères de glace (*stickiness :* τ_s) sera étudié au Chap. 3. Finalement, les coefficients d'extinction (k_e), de diffusion (k_s) et d'absorption (k_a) de la neige peuvent être calculés avec :

$$k_e = 2k_0\Im\sqrt{\varepsilon_{eff}}\,, \qquad (2.4a)$$

$$k_s = \frac{2}{9} k_0^4 R_s^3 f \left| \frac{\varepsilon_s - \varepsilon_b}{1 + \frac{\varepsilon_s - \varepsilon_b}{3\varepsilon_{eff}}(1-f)} \right|^2 \frac{(1-f)^4}{(1+2f - tf(1-f))^2}, \quad (2.4b)$$

$$k_a = k_e - k_s, \quad (2.4c)$$

À noter que dans le cas de la glace bulleuse (glacier, glace de lac), il est possible d'inverser le diffuseur (bulle d'air) et la matrice de fond (glace) pour en calculer la constante diélectrique effective (Dupont et al., 2013).

DMRT-ML peut considérer une ou plusieurs couches de neige. La propagation de l'énergie électromagnétique entre les couches est ensuite calculée avec la méthode DISORT (DIscrete Ordinate Radiative Transfer Method) (Jin et al., 1994).

La figure 2.1 présente des tests de sensibilité effectués avec DMRT-ML considérant une seule couche de neige sur les trois principales variables affectant les T_B de la neige sèche: le rayon des sphères de glace (R_s), la hauteur de la neige et la densité de la neige. Il est à noter que le SWE n'est pas directement une entrée dans DMRT-ML, mais est considéré indirectement à travers la densité et la hauteur de neige. Comme mentionné précédemment, l'élément principal de diffusion dans la neige est la taille de grains. En effet, le coefficient de diffusion de la neige augmente en fonction du cube du rayon du grain de neige (eq. 2.4b). L'effet de la taille des grains est très important à 37 GHz, tandis qu'elle est pratiquement nulle à 10.7 GHz. La densité de la neige, diminuant la distance entre les sphères de glace et ainsi le volume fractionnel (f) lorsqu'elle augmente, a aussi un effet sur le coefficient de diffusion de la neige. Une fois de plus, l'effet est plus important à 37 GHz, mais reste présent à 10.7 GHz (≈10K). Pour sa part, la hauteur de neige augmente l'atténuation en augmentant la distance qu'une onde doit parcourir dans le couvert nival. À noter que pour une augmentation de la densité (donc du SWE), les T_B augmentent à 37 GHz pour les deux polarisations (Verticale : V; Horizontale: H), 10V et 19V, mais diminuent à 19H et 10H. Ceci montre que dans certains cas, une augmentation du SWE n'amène pas nécessairement une diminution des T_B. En fait, l'émission du couvert nival est influencée par la densité et la hauteur de neige, et non directement par le SWE. Sur la figure 2.1, l'effet de la densité est par contre exagéré parce que le rayon du grain est considéré comme constant alors que, généralement, la taille des grains augmente avec la densité de la neige (Dominé et al., 2007).

Cette remarque s'applique aussi pour l'analyse de l'effet de la taille des grains où la densité est considérée constante.

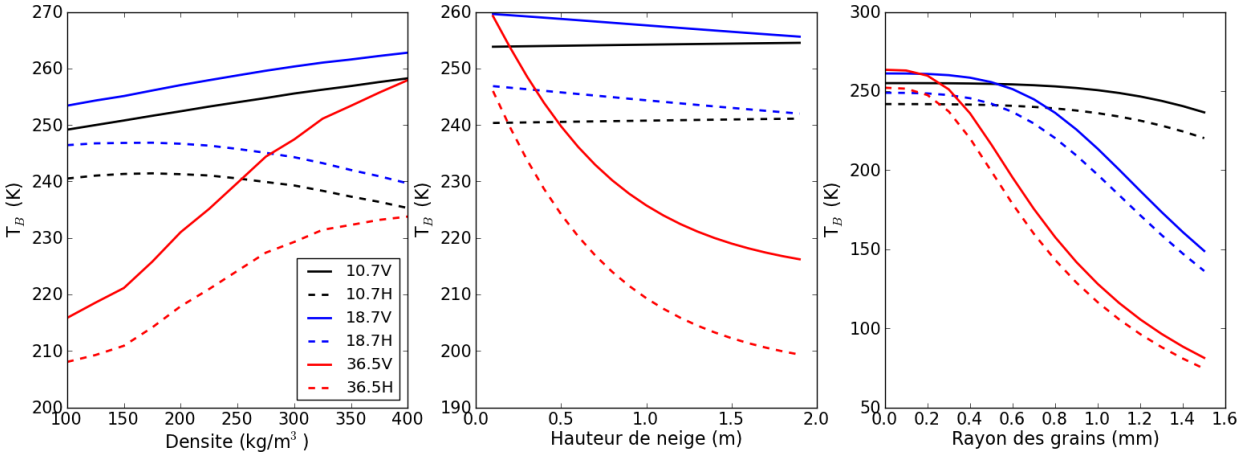

Figure 2.1: Tests de sensibilité sur les principales caractéristiques du couvert nival avec DMRT-ML considérant une seule couche de neige. La hauteur de neige = 0.5 m, densité de la neige = 250 kg m^{-3}, r_s = 0.5 mm, température de la neige = 260 K, température du sol = 270 K, humidité volumétrique du sol = 0.2, rugosité = 1 cm (modèle de réflectivité du sol de Wegmüller & Mätzler, 1999; voir Sect. 2.1.2).

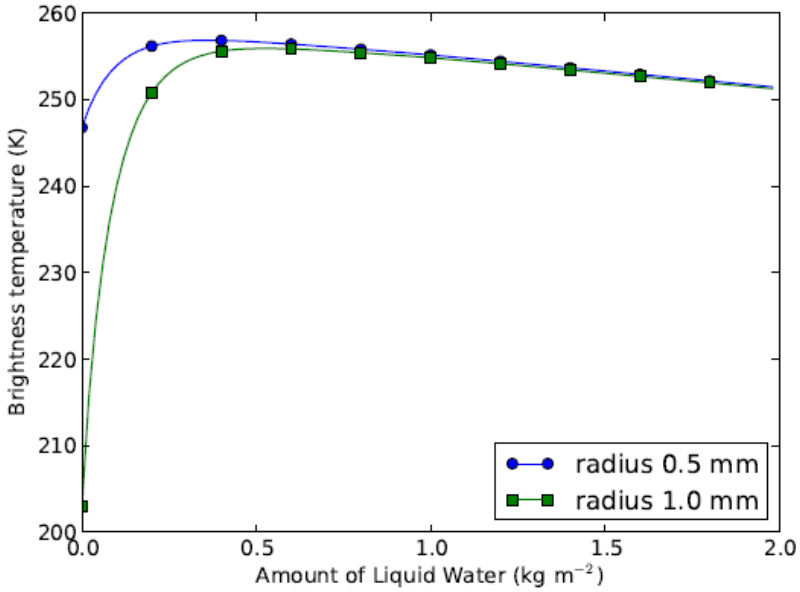

Figure 2.2: Température de brillance à 19H GHz en fonction de la teneur en eau liquide de la neige (valeur intégrée dans le premier 10 cm du couvert nival, en kg m^{-2}). La température de la neige = 273 K, la densité = 300 kg m^{-3}. Tiré de Picard et al. (2013a).

Un facteur important dans l'émission du couvert nival est la teneur en eau liquide de la neige (LWC). Ainsi, lorsque la neige fond et/ou qu'il y a des précipitations liquides, les T_B augmentent rapidement avec la hausse de l'émissivité de la neige (figure 2.2). Cette forte fluctuation du signal

est exploitée pour identifier les épisodes de fontes à partir de données satellitaires MOP (Picard et Fily, 2006; Takala et al., 2009). Par contre, la sensibilité aux autres paramètres, dont la hauteur de neige, s'en voit grandement diminuée, voire annihilée.

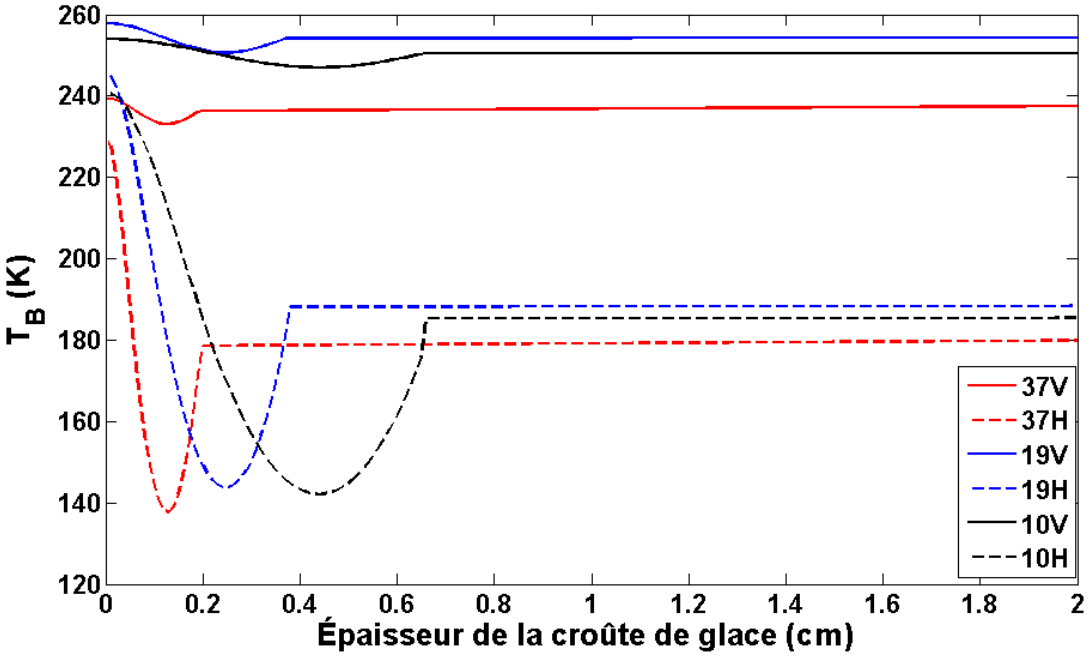

Figure 2.3: Tests de sensibilité sur l'effet de l'épaisseur d'une croûte de glace en surface avec MEMLS. La hauteur de neige = 0.5m, densité de la neige = 250 kg m^{-3}, R_s = 0.15 mm, température de la neige = 260 K, température du sol = 270 K, humidité volumétrique du sol = 0.2, rugosité = 1 cm (modèle de réflectivité du sol de Wegmüller & Mätzler, 1999; voir Sect. 2.1.2). Inspiré de Montpetit et al. (2013).

Un autre élément qui influence grandement le signal MOP de la neige est la présence de croûtes de glace qui se forment sur le couvert nival après des événements de pluie sur neige ou des cycles de fonte/regel (Grenfell & Putkonen 2008; Rees et al., 2010). Théoriquement, la glace pure ne diffuse pas la radiation puisqu'elle est constituée d'un seul milieu contrairement à la neige sèche qui est constituée de deux médiums, soit l'air et la glace. La figure 2.3 montre des simulations de T_B considérant la présence d'une croûte de glace en surface à l'aide du modèle MEMLS, où la croûte de glace est simulée par une couche ayant la densité de la glace pure (917 kg $^{-3}$) et une taille de grains nulle afin qu'il n'y ait pas de diffusion dans la couche (Montpetit et al., 2013). Le modèle montre que l'apparition d'une croûte de glace induit une chute rapide des T_B surtout en polarisation horizontale, créant une importante augmentation du rapport de polarisation, due au plus grand contraste diélectrique entre les milieux (glace-air et neige-air). L'effet de la croûte de glace varie davantage pour de faibles épaisseurs de croûtes de glace avant d'atteindre un plateau.

Ce phénomène est créé par l'effet de cohérence. Cet effet est causé par des réflexions multiples à l'intérieur d'une mince couche qui cause des interférences (constructives ou destructives) entre les multiples rayons se propageant à l'intérieur de la couche de glace lorsque l'épaisseur de celle-ci est plus faible que le quart de la longueur d'onde. Il est possible de simuler une croûte de glace dans DMRT-ML en mettant la densité d'une couche à 917 kg m^{-3}. Néanmoins, DMRT-ML ne prend pas en compte l'effet de cohérence, ce qui fait en sorte que l'épaisseur de la croûte de glace n'a aucun effet sur les T_B.

2.1.2 Sol

Un module d'émissivité du sol a été intégré à DMRT-ML pour simuler l'émission d'un sol rugueux sous la neige et/ou la végétation. À l'équilibre thermodynamique, l'émissivité pour une polarisation donnée (e_p) peut se définir comme (loi de Kirchoff) :

$$e_p = 1 - r_p \tag{2.5}$$

où r_p est la réflectivité. Deux modèles de sol ont été implémentés dans DMRT-ML (Wang et al., 1983; Wegmüller & Mätzler, 1999). Pour un sol homogène, les deux modèles calculent la réflectivité d'un sol qui dépend principalement de la rugosité de la surface et des coefficients de Fresnel. Pour les équations des deux modèles, voir Sect. 5.3.4, eq. 5.8 (Wang et al., 1983) et Sect. 3.4.1.3, eq. 3.3 - 3.4 (Wegmüller & Mätzler, 1999).

Les équations de Fresnel calculent la réflectivité d'un sol lisse (sans rugosité), en se basant sur la permittivité (ou constante diélectrique) du sol (qui dépend principalement du type de matériel, de l'humidité du sol, de sa température, ainsi que de la phase de l'eau) issue de relations empiriques (Dobson et al., 1985; Pulliainen et al., 1999; Mironov et al., 2010). La permittivité d'un sol est constituée d'une partie réelle (ε'), qui détermine les caractéristiques de propagations de l'énergie à travers le sol et la partie imaginaire (ε'') qui caractérise la perte d'énergie (Ulaby et al., 1982). La figure 2.4 (gauche) montre un changement rapide des T_B de 273 à 274 K à cause du changement de phase de l'eau qui affecte la constante diélectrique du sol selon le modèle de constante diélectrique de Pulliainen et al. (1999). Par contre, en utilisant des valeurs de constantes diélectriques de sols gelés mesurées (Hallikainen et al., 1985), cette variation est moins drastique

(figure 2.4, droite). Il y a aussi une diminution de l'émissivité de la surface lorsque l'humidité du sol augmente et ce phénomène diminue avec la fréquence. Il y a donc une plus grande sensibilité à l'humidité du sol aux basses fréquences. Pour sa part, l'effet de rugosité du sol tend à augmenter l'émissivité du sol en accentuant la diffusion résultant de l'augmentation de l'aire de la surface qui émet (Schmugge, 1985).

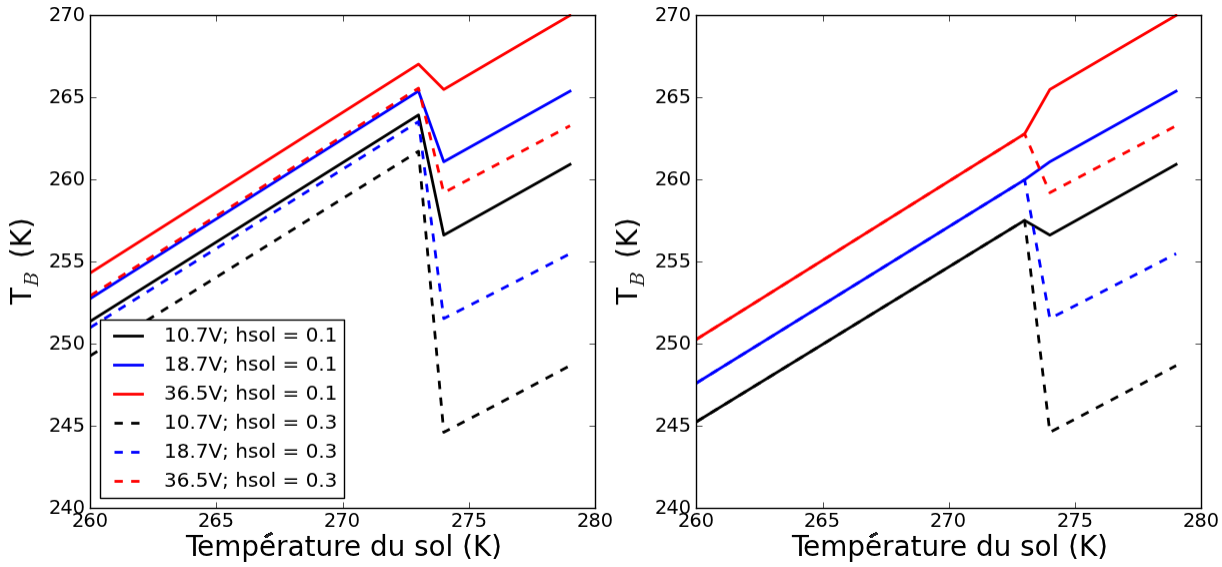

Figure 2.4: Tests de sensibilité sur l'effet de la température et l'humidité du sol sur les T_B pour des sols sans neige. Rugosité = 1 cm avec modèle de Wegmüller & Mätzler (1999). Gauche : constante diélectrique tirée du module HUT de Pulliainen et al. (1999); Droite : constante diélectrique en sol gelé issue de mesures (Hallikainen et al., 1985). hsol = humidité volumétrique du sol (cm^3 cm^{-3}).

Ces modèles de permittivité du sol ne considèrent par contre pas l'effet de transition de phase où il y a coexistence d'eau liquide et de glace dans le sol (Zhang et al., 2003). En effet, Mironov et al., (2010) ont montré que pour des sols organiques en toundra, de l'eau liquide pouvait être retrouvée jusqu'à -7 °C. Aussi, ces modèles considèrent des sols homogènes. Or, surtout pour les basses fréquences et pour des sols gelés ou très peu humides, la longueur de pénétration peut augmenter significativement et influencer l'émissivité du sol. Par exemple, Rautiainen et al., (2012) ont démontré qu'en bande L (1.4 GHz), le gel du sol en surface (5 premiers cm) n'affectait pas beaucoup les T_B. Ce phénomène est attribuable à la forte longueur de pénétration dans un sol gelé (faible permittivité) qui fait en sorte que le sol non gelé sous le sol gelé est mesuré par le capteur. Aussi, une autre difficulté réside dans le fait qu'au niveau des modèles de réflectivité, certains paramètres, dont la rugosité du sol, ne sont pas nécessairement connus en forêt boréale.

2.1.3 $T_{B\downarrow\text{-}r}$

Une surface couverte de neige réfléchit aussi une partie du rayonnement descendant ($T_{B\downarrow\text{-}r}$) provenant de l'atmosphère ou de la végétation. DMRT-ML permet de calculer cet effet en considérant une source isotopique. À partir de ce calcul, il est aussi possible de calculer la réflectivité de la surface couverte de neige (r_{neige}) avec :

$$r_{neige} = \frac{T_{Bsnow\text{-}\downarrow} - T_{Bsnow\text{-}sans\downarrow}}{T_{B\downarrow}} \tag{2.6}$$

où $T_{Bsnow\text{-}\downarrow}$ et $T_{Bsnow\text{-}sans\downarrow}$ sont respectivement les T_B calculées avec un $T_{B\downarrow\text{-}r}$ et sans $T_{B\downarrow\text{-}r}$.

2.2 Végétation

L'interaction de la végétation avec les micro-ondes est influencée principalement par le contenu en eau liquide de la végétation (biomasse) et sa structure (branche, feuille, tronc) (Pampaloni et al., 2004). La contribution de la végétation peut être définie par un modèle de transfert radiatif de la végétation simple à deux paramètres : τ-ω où τ est l'épaisseur optique de la végétation et ω représente la diffusion effective de la forêt. Étant donné que pour la plupart des capteurs MOP, l'angle de visé est constant (≈55°) le modèle peut considérer directement la transmissivité (γ) au lieu de l'épaisseur optique. Ce modèle définit le T_{Bveg} (voir eq. 2.1) selon :

$$T_{Bveg} = (1-\omega)(1-\gamma)T_{veg} \tag{2.7}$$

où T_{veg} est la température de la végétation. Dans le calcul du transfert radiatif, le γ permet ainsi principalement de partitionner la contribution provenant du sol (eq. 2.1 : $T_{Bsnow} \cdot \gamma$) et la contribution provenant de la végétation directement (eq. 2.7), alors que ω influence l'émission de la végétation. La figure 2.5 montre qu'en condition hivernale avec un sol couvert de neige à 37 GHz, une augmentation de ω conduit à une diminution des T_B à cause de la diminution de l'émissivité de la végétation. Le même comportement est généralement observé pour le γ, où une augmentation de la transmissivité fait en sorte que la contribution de la neige (faible T_B) est dominante. Par contre, pour de faibles transmissivités, cette tendance s'inverse à cause de l'augmentation du $T_{B\downarrow\text{-}r}$.

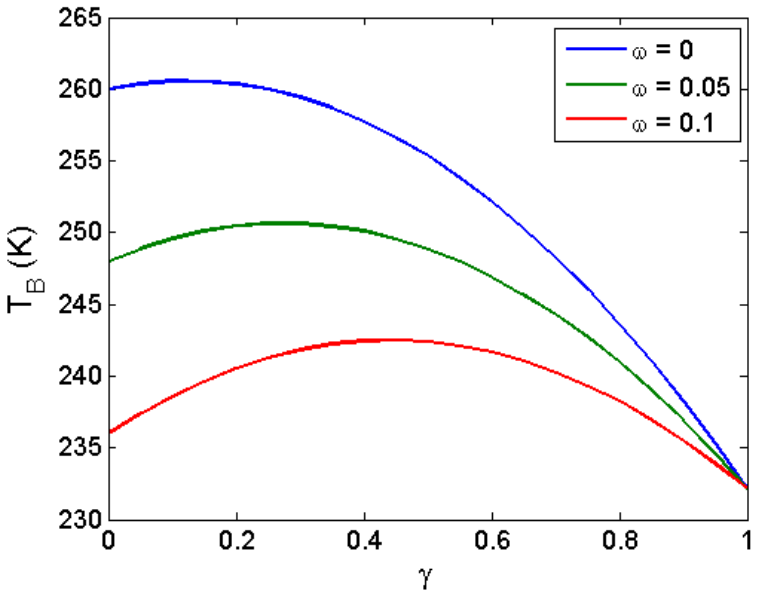

Figure 2.5: Tests de sensibilité sur l'effet des paramètres de végétation γ-ω sur les T_B à 37 GHz avec un sol couvert de neige (mêmes caractéristiques qu'à la figure 2.1). Température de la végétation = 260 K.

Le modèle τ-ω a été très étudié en bande L (1.4 GHz) dans le cadre de la mission *Soil Moisture and Ocean Salinity* (SMOS). Par contre, la paramétrisation du modèle est beaucoup moins connue pour les plus hautes fréquences en forêt boréale. Les valeurs de γ-ω varient aussi en fonction des caractéristiques et de la densité de la végétation. Dans la perspective d'un couplage appliqué spatialement sur la forêt boréale avec les données satellitaires, il est nécessaire de quantifier ces paramètres en fonction de données de paramètres structuraux de la végétation disponibles sur l'ensemble du territoire étudié. Le défi pour quantifier γ-ω réside aussi dans le découplage de la contribution de la végétation et du sol.

2.3 Atmosphère

Les mesures MOP offrent l'avantage d'être indépendantes de l'illumination et peu sensibles aux paramètres atmosphériques. Il reste que pour les hautes fréquences, les conditions atmosphériques peuvent néanmoins influencer les mesures. Quelques modèles permettent de calculer les contributions atmosphériques micro-ondes (Rosenkranz, 1998; Saunders et al., 1999; Kerr & Njoku, 1990; Liebe, 1989). Le modèle utilisé dans ce travail est le « *Millimiter-wave propagation model* » (MPM : Liebe, 1989) implémenté dans HUT (Pulliainen et al., 1999), un modèle semi-empirique permettant de simuler l'absorption, l'émission et la diffusion micro-onde d'une couche atmosphérique. En utilisant un minimum d'intrants (température, pression

barométrique et humidité de l'air), MPM calcule la transmissivité (γ_{atm}) et la température de brillance de chacune des couches atmosphériques. La température de brillance de la couche atmosphérique perçue par un capteur satellitaire ($T_{Batm\uparrow}$) devient (figure 2.6) :

$$T_{Batm\uparrow} = \int_{H1}^{H2} e_{atm}(z)T(z)e^{-k_{e-atm}(z,H)\sec(\theta)}dz \tag{2.8}$$

où θ est l'angle du capteur, z est la hauteur de la couche, $T(z)$ est la température de l'air, $e_{atm}(z)$ est l'émissivité de la couche, H_1 et H_2 représentent l'altitude du sol et du capteur satellitaire et $k_{e\text{-}atm}$ est l'épaisseur optique des couches atmosphériques. $k_{e\text{-}atm}$ est calculé à partir des coefficients d'absorption et de diffusion, tandis que e_{atm} est calculé en considérant le coefficient d'absorption intégré sur l'épaisseur de la couche (absorbance). À noter que pour calculer les T_B atmosphériques perçues au sol ($T_{Batm\downarrow}$), H_1 et H_2 sont inversés et la contribution du rayonnement cosmique (2.7 K) est prise en compte.

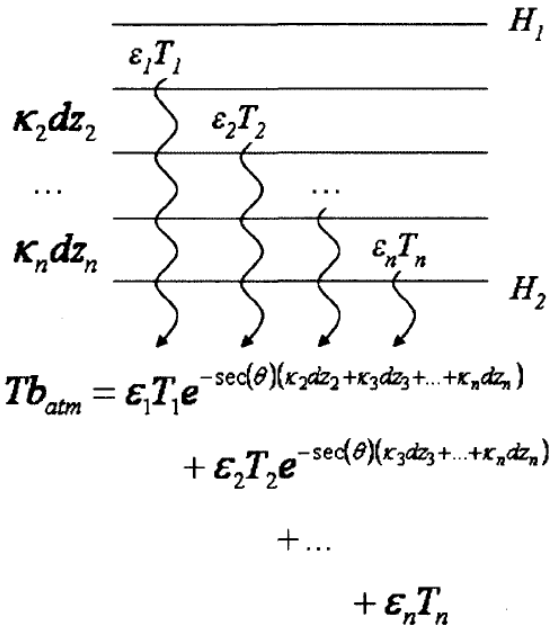

Figure 2.6: Schéma du modèle MPM. La contribution de chaque couche est atténuée par les couches atmosphériques successives. Tiré de Bergeron et al. (2012).

Dans cette étude, les paramètres atmosphériques sont calculés en utilisant les données des couches atmosphériques simulées par NARR. Pour $T_{Batm\downarrow}$ la contribution descendante

hémisphérique est calculée en considérant un angle effectif obtenu à partir de la transmittance calculée au nadir (selon Mätzler & Rosenkranz, 2007, voir eq. 5.3). Cet angle se trouve généralement entre 55° et 60° par rapport au nadir. Cette implémentation du couplage de MPM et de NARR a aussi été utilisée dans plusieurs autres travaux (Bergeron et al., 2013; Montpetit et al., 2013; Dupont et al., 2013; Picard et al., 2013b). La figure 2.7 montre que les $T_{Batm\downarrow}$ et les γ_{atm} sont grandement reliées à la vapeur d'eau précipitable intégrée sur l'ensemble de la couche atmosphérique. Les contributions atmosphériques sont donc généralement plus faibles en hiver ou pour des climats froids. Même si dans ce cas-ci, les $T_{Batm\downarrow}$ augmentent en fréquence, il existe néanmoins des spectres d'absorption de la vapeur d'eau, dont un autour de 22 GHz.

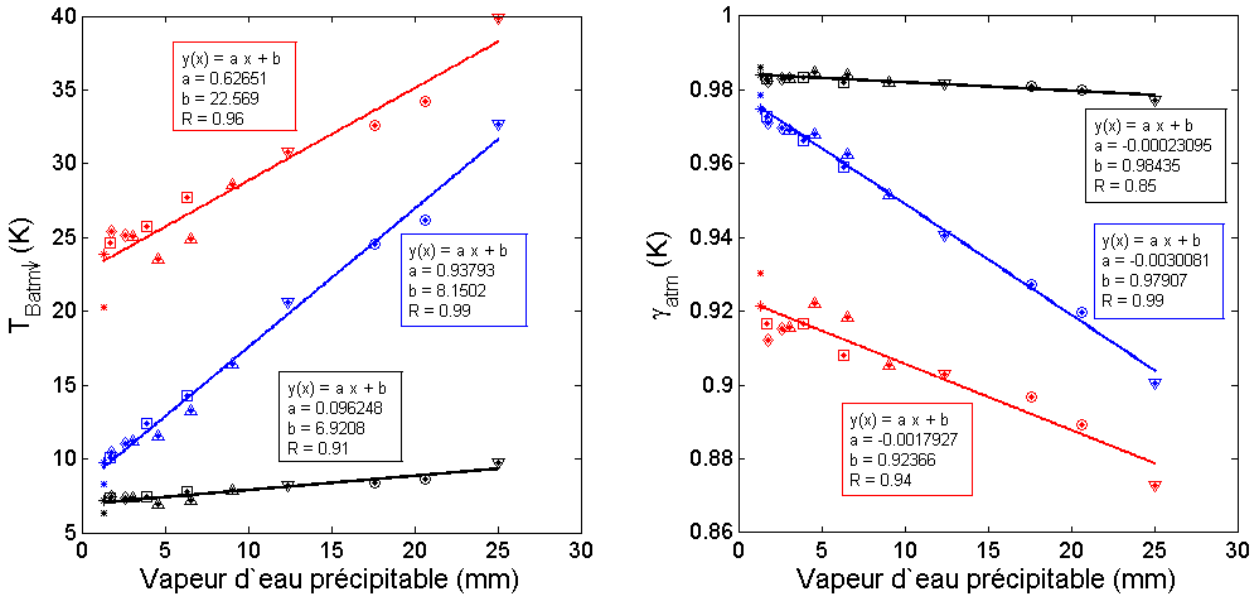

Figure 2.7: Relation entre la vapeur d'eau précipitable (NARR) et les simulations de $T_{Batm\downarrow}$ avec MPM alimentées par NARR. Rouge = 36.5 GHz; bleu = 18.7 GHz; noir = 10.7 GHz. * Baie James hiver, x calotte glaciaire Barnes hiver, □ Churchill, Manitoba hiver, ◊ arctique hiver, ▼ SIRENE été, Δ SIRENE hiver, ○ Sept-Îles été.

2.4 Méthodes d'inversion ou d'assimilation utilisant les MTR

Différentes méthodes ont été utilisées pour calculer des valeurs de variables clés, dont le SWE, à partir de MSEM et de données radiométriques. Cette section dresse quelques exemples d'inversion ou d'assimilation utilisant un MTR et les données radiométriques satellitaires pour estimer les SWE.

L'inversion consiste généralement à trouver la ou les valeurs optimales qui permettent de minimiser la différence entre les T_B simulées (issues du MTR) et les T_B mesurées par un capteur radiométrique. À partir de mesures de hauteurs de neige de stations météorologiques synoptiques, le projet GlobSnow (Takala et al., 2011; Pulliainen, 2006) inverse la taille de grains avec le modèle HUT et les données satellitaires MOP. Ces tailles de grains sont ensuite interpolées par krigeage, pour ensuite inverser les hauteurs de neige via une fonction coût sur l'ensemble du territoire avec les données MOP satellitaires. Vachon et al., (2010) ont appliqué une méthode semblable dans le Nord du Québec, où lorsque disponibles, les mesures nivométriques terrains sont utilisées pour inverser le coefficient d'extinction total dans le modèle HUT. Ce coefficient d'extinction est ensuite pris pour inverser les SWE à partir de données satellitaires. Ce type d'approche montre une certaine efficacité, mais demande néanmoins des mesures nivométriques au sol pour calibrer l'extinction reliée principalement aux grains de neige. Il a aussi été noté que GlobSnow montre certaines anomalies par rapport à d'autres produits de SWE disponibles (Langlois et al., 2013).

Pardé et al., (2007) proposent une méthode d'inversion où la taille de grains est considérée comme un paramètre libre. Avec HUT, une fonction coût est utilisée pour inverser la taille de grains et le SWE tout en considérant l'incertitude reliée à ces deux variables. Il a par contre été démontré que cette approche est influencée par les valeurs initiales utilisées (SWE et tailles de grains) ainsi que par l'incertitude considérée sur ces deux variables.

Les MTR permettent aussi de faire un lien entre les variables d'un modèle (modèle de neige par exemple) et les observations satellitaires. Le couplage d'un modèle de neige avec un MTR, comme proposé dans cette thèse, peut ainsi permettre de corriger certaines variables issues du modèle (dont le SWE). L'avantage de ces méthodes est qu'elles ne requièrent pas de mesures in situ. Langlois et al. (2012) ont ainsi couplé le modèle de neige SNOWPACK (Bartelt & Lehning, 2002) avec MEMLS. À partir de mesures radiométriques aéroportées, une correction par itération sur les tailles de grains simulées (ϕ) issues de SNOWPACK a d'abord été calculée pour minimiser la différence entre les T_B simulées (MEMLS alimenté par les simualtions SNOWPACK) et les T_B mesurées. Ensuite, à partir des mêmes données radiométriques une deuxième itération est effectuée sur le SWE afin de minimiser les T_B simulées et les T_B mesurées pour chaque site.

Il existe aussi des méthodes plus complexes, où un ensemble de paramètres sont considérés dans le système de données d'assimilation (Reichle, 2008). Le filtre de Kalman d'ensemble (EnKF) utilise le couplage d'un modèle de neige et d'un MTR pour l'assimilation de T_B afin de corriger le SWE estimé par un modèle de neige (Touré et al., 2011; Durand et al., 2009). Le filtre de Kalman d'ensemble est une variante du filtre de Kalman classique qui utilise l'approche statistique de Monte-Carlo pour analyser l'erreur du modèle en perturbant les données d'entrées (réplicats). L'algorithme utilise 2 phases : la première est la phase de propagation où le modèle de neige simule l'évolution d'un ensemble de variables d'états pour différents réplicats afin de calculer les matrices de covariances. La deuxième phase est l'analyse, où les valeurs d'états du modèle sont optimisées en considérant l'erreur dans la prédiction de la mesure et l'erreur dans les mesures des T_B. Une telle approche permet ainsi de considérer les différentes sources d'erreurs pour l'optimisation des variables. Il existe aussi des méthodes variationnelles, comme la méthode 3-D ou 4-D-var qui minimise une fonction coût sur l'espace et le temps (Le Dimet & Talagrand, 1986). Jia et al., 2013 ont montré l'efficacité d'une telle méthode pour l'inversion de l'humidité du sol, mais ont soulevé la limite de la méthode en saison hivernale à cause de la difficulté de bien représenter les effets reliés à la neige et au gel du sol.

Chapitre 3: Brightness Temperature Simulations of the Canadian Seasonal Snowpack Driven by Measurements of the Snow Specific Surface Area

« Simulations des Températures de Brillance des Couverts Niveaux Saisonniers Canadiens à partir de Mesures de Surface Spécifique de la Neige »

Auteurs : Roy, A., Picard, G., Royer, A., Montpetit, B., Dupont, F., Langlois, A., Derksen, C., Champollion, N.

Article publié dans le Journal *IEEE Transactions on Geoscience and Remote Sensing* (2013), vol. 51, p. 4692-4704.

Résumé:

La taille de grains est le paramètre qui affecte le plus l'émission micro-onde d'un couvert nival. La surface spécifique de la neige (snow specific surface area : SSA) est une métrique qui permet une mesure rapide et reproductible sur le terrain, tout en permettant de bien représenter la taille des grains de neige. Par contre, cette métrique ne peut pas être utilisée directement dans les modèles d'émission micro-onde de la neige (MSEM). L'objectif de cet article est d'évaluer la pertinence et l'adaptation nécessaire pour l'utilisation de la SSA dans deux MSEM: le Dense Media Radiative Theory – Multi Layer (DMRT-ML) et le Helsinki University of Technology model (HUT n-layer), en se basant sur des mesures radiométriques in situ. Les mesures de SSA utilisant la réflectance de la neige dans l'infrarouge à ondes courtes (*short-wave Infrared* : SWIR), ont été prises sur 20 snowpits dans différents environnements (gazon, toundra, tourbière sèche). Les résultats montrent que les deux modèles nécessitent un facteur de correction sur les valeurs de SSA pour minimiser l'erreur quadratique moyenne (RMSE) entre les températures de brillance mesurées et simulées. Pour DMRT-ML, le facteur de correction est dû à la simplification de la représentation de la neige, considérée comme des sphères de glace avec des rayons uniformes. Nous posons l'hypothèse que l'utilisation d'un facteur de correction est reliée à la distribution de la taille des grains et à l'agrégation (*stickiness*) entre les grains de neige. Pour HUT n-layer, l'utilisation de la SSA amène une sous-estimation de l'atténuation de la neige, particulièrement pour des couverts nivaux avec une fraction importante de givre de profondeur.

Cet article offre une bonne représentation de la taille des grains de neige pour DMRT-ML, ce qui est intéressant pour l'assimilation de données MOP dans les modèles de neige.

Mots-clés : Dense Media Radiative Theory-MultiLayer (DMRT-ML), Helsinki University of Technology model (HUT n-layer), mesures in situ de la neige, modèle d'émission micro-onde (MSEM), surface spécifique des grains de neige (SSA).

3.1 Présentation de l'article

Cet article a pour principal objectif de vérifier la pertinence et les adaptions à apporter pour l'utilisation de la SSA dans les MSEM DMRT-ML et HUT n-layer. Sachant l'importance de la taille des grains dans l'émission micro-onde, cet aspect est crucial dans la perspective d'un couplage entre un modèle de neige (CLASS) et un MTR (voir figure 1.5). L'étude calibre et valide l'intégration de la SSA dans les MSEM à partir d'une base de données de mesures radiométriques et de mesure de neige sèche in situ unique. L'étude a permis d'identifier un facteur de correction nécessaire à appliquer à la taille des grains dans DMRT-ML représentatif pour les neiges saisonnières. Plusieurs mesures ont été effectuées dans le cadre de ce doctorat, dont les mesures de réflectance de la neige dans l'infrarouge à ondes courtes avec l'instrument IRIS (*Infrared Integrated Sphere*), qui permettent ensuite de calculer la SSA (Montpetit et al., 2012, voir Annexe 4). L'utilisation de cette nouvelle métrique pour définir la taille des grains, dont la mesure est objective et reproductible sur le terrain (SSA), apporte une avancée dans le domaine. L'avantage de l'utilisation de la SSA réside aussi dans le fait que certains modèles simples permettent de modéliser la SSA pour représenter le métamorphisme des grains de neige au cours d'un hiver (voir Chap. 4). La nouvelle version du modèle de neige Crocus paramétrise aussi la SSA comme variable pronostique (Carmagnola et al., 2013). L'étude tente aussi de mieux comprendre les processus qui amènent la nécessité d'appliquer une correction à la taille de grains.

Brightness temperature simulations of the Canadian seasonal snowpack driven by measurements of the snow specific surface area

Alexandre Roy[a*]
Ghislain Picard[b]
Alain Royer[a]
Benoit Montpetit[a]
Florent Dupont[a-b]
Alexandre Langlois[a]
Chris Derksen[c]
Nicolas Champollion[b],

[a] Centre d'Applications et de Recherches en Télédétection (CARTEL), Université de Sherbrooke, 2500 boul. Université, Sherbrooke, Qc, Canada, J1K 2R1.
[b] UJF – Grenoble 1 / CNRS, Laboratoire de Glaciologie et Géophysique de l'Environnement (LGGE) UMR 5183, Grenoble, F-38041, France
[c] Climate Research Division, Environment Canada, Toronto, Ontario, Canada

Abstract

Snow grain size is the snowpack parameter that most affects the microwave snow emission. The specific surface area (SSA) of snow is a metric that allows rapid and reproducible field measurements and that well represents the grain size. However, this metric cannot be used directly in microwave snow emission models (MSEMs). The aim of this study is to evaluate the suitability and the adaptations required for using the SSA in two MSEMs: the Dense Media Radiative Theory-Multilayer model (DMRT-ML) and the Helsinki University of Technology model (HUT n-layer), based on in situ radiometric measurements. Measurements of the SSA, using snow reflectance in the short-wave infrared, were taken at 20 snowpits in various environments (e.g., grass, tundra and dry fen). The results show that both models required a scaling factor for the SSA values to minimize the root-mean-square error between the measured and simulated brightness temperatures. For DMRT-ML, the need for a scaling factor is likely due to the oversimplified representation of snow as spheres of ice with a uniform radius. We hypothesize that the need for the scaling factor is related to the grain size distribution of snow and the stickiness between grains. For HUT n-layer, using the SSA underestimates the attenuation by snow, particularly for snowpacks with a significant amount of depth hoar. This paper provides a reliable description of the grain size for DMRT-ML, which is of particular interest for the assimilation of satellite passive microwave data in snow models.

Keywords: DMRT-ML, HUT n-layer, microwave snow emission model, snow grains specific surface area, in situ measurements.

3.2 Introduction

The characterization of snow properties (e.g., accumulation, albedo, snow water equivalent, depth, melt, temperature) is a major challenge in the prediction of energy and water budgets in cold regions. Because the albedo of snow is initially very high, a change of its optical characteristics resulting from metamorphosis or changes in its spatial coverage lead to significant climatic feedbacks (Picard et al., 2012a, Klingaman et al., 2008; Vavrus, 2007). Water stored in the form of snow, potentially for many months before entering runoff, can also significantly affect soil moisture and rivers runoff, including the occurrence of flood events (Roy et al., 2010; Turcotte et al., 2007).

Passive microwave remote sensing is an appealing approach for characterizing the properties of snow at the synoptic scale; images are available at least twice a day for northern regions where meteorological stations and networks are generally sparse. Several studies have demonstrated the potential for using passive microwave measurements to estimate the snow water equivalent (SWE) (Chang et al., 1987; Kelly et al., 2003; Derksen et al., 2005; Pardé et al., 2007; Vachon et al., 2010) in mid-latitude zones where the snow cover is seasonal and several empirical algorithms based on linear relationships between the SWE and the spectral difference of brightness temperatures have been proposed (e.g., Singh and Gan, 2000). It has however been demonstrated that using constant empirical relationships is often inaccurate because of interannual variability in the seasonal metamorphosis of snow grains (Rosenfeld and Grody, 2000). One of the options to overcome this problem (see the review of Dietz et al., 2012) is to use a microwave snow emission model (MSEM) to understand the different contributions to the microwave signal. Different assimilation methods can then allow the coupling of a snow evolution model and an MSEM to correct the snow parameters by using brightness temperature observations (Durand et al., 2009; Toure et al., 2011; Takala et al., 2011; Durand and Liu, 2012; Langlois et al., 2012).

It has been shown that the snow grain size is one of the key parameters of snow emission. This has been illustrated through different radiative transfer models, e.g., Helsinki University of Technology (HUT: Pulliainen et al., 1999; Roy et al., 2004; Butt and Kelly, 2008; Kontu and Pulliainen, 2010), Dense Media Radiative Theory (DMRT: Tsang et al., 2000; Tedesco and Kim, 2006; Grody, 2008; Brucker et al., 2011a), and Microwave Emission Model of Layered

Snowpack*s* (MEMLS: Wiesmann and Mätzler, 1999; Durand et al., 2008; Toure et al., 2008; Langlois et al., 2012). However, the grain size is a parameter that is difficult to accurately characterize and measure in the field, and it is not measured operationally at weather stations. Even the definition of the snow grain size is ambiguous (Aoki et al., 2000; Mätzler, 2002); a widely-measured metric is the maximum diameter of grains D_{max} (Fierz et al., 2009). However, an accurate and objective measurement of this parameter is difficult to obtain given the wide variety of snow grain shapes. In addition, snow grains cannot always be clearly identified in the snow layer when the boundaries between grains are difficult to identify (Domine et al., 2008). For instance, Kontu and Pulliainen (2010) estimated that in their case, for a visual assessment (snow grains placed on a 1-mm grid) of the longest dimension of a grain D_{max}, the accuracy for grains larger than 1 mm is ± 0.5 mm and that for grains smaller than 1 mm is ± 0.25 mm.

In contrast, the specific surface area (SSA) of a snow grain, which represents the ratio of the area of ice per unit of mass of ice ($SSA = \frac{A}{\rho_{ice} V_o}$, units in m^2 kg^{-1}), is a well-defined parameter that represents the geometric characteristics of a porous medium such as snow (Domine et al., 2001). Methods based on snow reflectance in the short-wave infrared (SWIR) can now provide rapid and reproducible field measurements of the SSA (Gallet et al., 2009; Arnaud et al., 2011; Montpetit et al., 2012) with an accuracy within 12% compared with reference measurements made by methane adsorption (Domine et al., 2001).

In addition, significant progress has been made in modeling the evolution of the SSA in physical snow models (Legagneux et al., 2004; Flanner and Zender, 2006; Taillandier et al., 2007; Jacobi et al., 2010). These studies propose simple approaches to simulate the SSA, and they are straightforward to implement in a snow model. Often these models use, as their input, parameters that are already calculated by a traditional snow model. The SSA is also calculated in some existing snow models, such as CROCUS (Morin et al., 2012).

Thus considering that the measurement of the SSA is well-defined, its measurement is rapid and accurate and modeling the SSA is possible, it is important to examine the use of this snow microstructure metric in MSEM (Huang et al., 2012; Brucker et al., 2011a; Touré et al., 2008; Mätzler, 2002). However, the parameters representing the snow grain size in MSEM differ from the SSA concept, which is also different from the grain size measurements traditionally used

(Langlois et al., 2010). It thus appears necessary to adapt the MSEM to derive an effective grain size from SSA.

For Antarctica, Brucker et al. (2011a) used SSA measurements based on near-infrared (NIR) reflectance photography as input to a multilayer (ML) MSEM, namely DMRT-ML. They found that using the optical radius defined as:

$$R_{opt} = \frac{3}{\rho_{ice} SSA} \tag{3.1}$$

where ρ_{ice} is the ice density = 917 kg m^{-3}, was inadequate as input for their model based on DMRT theory. A scaling factor of $\phi = 2.85$ was applied to minimize the difference between the simulated brightness temperature (T_B) and data from the Advanced Microwave Scanning Radiometer for the Earth Observing System (AMSR-E):

$$R_{eff} = \frac{3}{\rho_{ice} SSA} \phi \tag{3.2}$$

where R_{eff} is the effective radius in the microwave range. The climatic conditions and the types of snow in Antarctica are different from the seasonal snow found in mid-latitude and sub-arctic environments so the relationship between SSA and R_{eff} may be different, and thus deserves further analysis in the context of seasonal snow. Furthermore, the soil emission may be a significant contribution to the signal emerging from the surface in environments with seasonal snow, while it is neglected in Antarctica (Brucker et al., 2011b) since snowpack depth is much larger than the microwave penetration depth at the frequencies considered here.

Kontu and Pulliainen (2010) proposed another approach to parameterize grain size in MSEM. They presented an empirical formula for calculating an effective diameter D_{eff} derived from D_{max}, which improves T_B simulations with the one-layer HUT model. The aim of their approach is to decrease the relative contribution of thick hoar layers (consisting of large grains at the bottom of the snowpack) in the calculation of the average snow grain size. This formula (with the same empirical coefficients) is also directly used in the HUT n-layer version, where it reduces the effect of large values on the observed grain size (Lemmetyinen et al., 2011). It should however be

noted that the empirical relation between grain sizes and the extinction coefficient was derived with grain sizes smaller than 1.6 mm (Hallikainen et al., 1987).

The objective of this study is to evaluate the performance of two well-known ML MSEMs, namely DMRT-ML and HUT n-layer, using SSA measurements and measured T_B at 18.7 GHz and 36.5 GHz. We first present the data, models and SSA adaptation method, followed by the results. In the discussion, we propose several physical explanations for the SSA adaptations. We also discuss various approaches for integrating the SSA values in both MSEMs.

3.3 Field sites and data description

Snowpit measurements were acquired for four types of land cover: open tundra, snow drifts on tundra, dry tundra fen, and mid-latitude open grassy sites. The first three sites were located close to the Churchill Northern Studies Centre (58.73 N, 93.81 W) in Manitoba, Canada. The data were collected during the Canadian CoReH20 Snow and Ice (CAN-CSI) campaign in the winter of 2010, which included four periods of intensive field sampling (beginning of January, mid-February, end of March, and mid-April). Full details of the campaign are provided in Derksen et al. (2012). During the winter of 2011, the grassy sites were located at the *Site interdisciplinaire de recherche en environnement extérieur* (SIRENE) experimental station at the Université de Sherbrooke (45.37 N, 71.92 W) and at St-Romain (80 km northeast of Sherbrooke) in Québec, Canada. The grassy sites have generally less aged snow. All snowpits were located in large open areas to avoid the effect of vegetation emission reflected by the snow, which could influence the radiometric measurements (Kruopis et al., 1999; Langlois et al., 2011; Roy et al, 2012). None of the snowpits had ice lenses, which can strongly influence the emissivity of the snow cover (Mätzler and Wegmüller, 1987; Rees et al., 2010; Montpetit et al., 2013).

T_B measurements in Churchill were taken for every snowpit at 19 and 37 GHz in vertical (V-pol) and horizontal (H-pol) polarizations at a height of approximately 2 m above the ground and at an angle of 53° with a PR-series field radiometer (Radiometrics Corp., Boulder, Colorado) close to the angle used by satellites. The footprint of the measurements at the snow surface of snow was approximately 0.6 m x 0.6 m. Radiometer calibration was based on one measurement taken with Eccosorb® at the ambient temperature (i.e., warm reference) and another measurement taken over a surface of liquid nitrogen (i.e., cold reference) (see Walker et al., 2002). In the worst case,

the measurement error for the calibration target was estimated as ± 2 K. Ambient and cold point measurements from before and after each measurement period (typically separated by 3 to 5 days) were used to produce a final calibrated T_B dataset. For the snowpits at SIRENE, the T_B measurements were taken at 19 and 37 GHz at an angle of 54° and at a height of approximately 1.5 m above the ground. The radiometers were calibrated before and after the winter season using ambient and cold targets.

For each site, profiles of the snow temperature, snow density, and SSA were taken at a vertical resolution of 5 cm in the footprint of the radiometric measurements. The density was measured with a 185-cm^3 density cutter, and the samples were weighed with a 100-g Pesola light series scale with an accuracy of 1 g. The temperature was measured with a Traceable 2000 digital temperature probe (± 0.1°C). The soil surface temperature was also measured. The SSA was measured with the shortwave InfraRed Integrating Sphere (IRIS) system (Montpetit et al., 2012: voir Annexe 4), which is based on the principle described in Gallet et al. (2009), which exploits the relationship between the SWIR snow reflectance and the SSA (Kokhanovsky and Zege, 2004). A snow sample obtained using a cylindrical snow sampler with a 10 cm diameter (parallel to the snow surface) and 6 cm long was placed directly under the opening of the integrating sphere in a closed box. The snow was then illuminated with a 1.33 μm laser and the signal reflected in the sphere was recorded by an InGaAs photodiode, which generates a voltage. Calibration with Lambertian targets with known reflectances (Spectralon: 0.06, 0.25 0.60, 0.79, and 0.98 at 1.33 μm) allowed the measured voltages to be related to the snow reflectance. From the reflectance, the SSA was calculated with the Kokhanovsky and Zege (2004) theoretical model as described by Montpetit et al. (2012). A summary of the average measurements of the 20 snowpits used is given in table 3.1.

Table 3.1: Average values for snowpit properties. Site type: tundra [1], drift tundra [2], dry tundra fen [3], and mid-latitude open grassy sites [4] (CH = Churchill, S-R = St-Romain, SIR = SIRENE). T_{snow} is the mean snowpack temperature; Density is the mean snowpack density; R_{opt} is the mean optical radius; T_{soil} is the soil surface temperature; T_B is the in situ radiometric measurement; Date is when the measurements were taken.

#	Site Type	Snow depth (m)	T_{snow} (K)	Density (kg/m3)	R_{opt} (mm)	T_{soil} (K)	T_B 37V	T_B 37H	T_B 19V	T_B 19H	Date
1	1 [CH]	0.37	259.4	235.4	0.24	267.9	177.7	169.4	243.1	220.3	09/02/2010
2	1 [CH]	0.48	255.2	261.4	0.36	269.6	150.3	140.2	223.1	204.0	24/03/2010
3	1 [CH]	0.45	258.7	229.8	0.38	270.3	149.5	140.5	220.2	204.4	24/03/2010
4	1 [CH]	0.44	252.5	284.6	0.29	269.8	164.4	155.3	222.5	205.8	26/03/2010
5	2 [CH]	0.70	257.3	311.4	0.21	270.3	218.7	201.0	250.7	224.0	10/02/2010
6	2 [CH]	1.18	269.4	372.6	0.22	272.7	223.2	208.7	247.6	222.0	18/03/2010
7	2 [CH]	0.82	265.3	284.0	0.21	271.8	211.9	199.4	236.6	224.6	20/03/2010
8	2 [CH]	0.91	267.1	324.8	0.23	272.5	201.4	190.2	230.0	211.0	20/03/2010
9	2 [CH]	0.83	268.3	292.8	0.25	272.9	207.5	188.7	237.7	203.2	20/03/2010
10	2 [CH]	1.74	266.0	380.3	0.17	272.8	244.9	227.7	251.2	231.6	22/03/2010
11	2 [CH]	1.80	266.8	367.8	0.18	272.9	227.3	206.6	241.4	203.4	22/03/2010
12	2 [CH]	1.50	266.4	380.9	0.20	272.7	222.2	198.4	243.2	213.8	22/02/2010
13	2 [CH]	1.19	265.8	351.4	0.18	272.5	223.5	196.3	245.9	222.4	22/03/2010
14	3 [CH]	0.51	258.5	308.4	0.21	269.7	195.4	180.8	237.7	210.9	13/02/2010
15	3 [CH]	0.34	258.6	262.7	0.20	267.2	185.3	170.0	241.2	214.8	13/02/2010
16	3 [CH]	0.57	259.3	328.0	0.28	270.1	180.6	165.2	218.3	187.3	23/03/2010
17	3 [CH]	0.19	259.1	263.2	0.38	264.6	150.9	139.6	216.4	185.0	23/03/2010
18	4 [SIR]	0.21	266.3	241.4	0.14	272.3	251.7	231.5	263.2	245.1	17/01/2011
19	4 [SIR]	0.33	271.6	254.6	0.17	273.0	250.5	226.3	262.9	243.2	27/01/2011
20	4 [S-R]	0.47	269.4	179.2	0.09	273.5	258.1	236.5	258.3	246.4	08/12/2010

3.4 Models and SSA adaptation approach

3.4.1 Models

This section describes the two MSEMs used in this study: DMRT-ML and HUT n-layer. The same soil emission model was used for the two models.

3.4.1.1 DMRT-ML

DMRT-ML (Picard et al., 2013) is a ML MSEM based on the DMRT theory (Tsang and Kong, 2001). Several studies have used this theory to examine the passive microwave emission from snow-covered ground (Tsang et al., 2000; Macelloni et al., 2001; Tedesco and Kim 2006; Grody, 2008; Tsang et al., 2008; Liang et al., 2008).

The DMRT theory assumes that the snow cover is composed of ice spheres. Permittivity is calculated using the first-order quasi-crystalline approximation and the Percus-Yevick approximation. It has been shown that the DMRT is in agreement with numerical solutions of the 3-D Maxwell equations up to a density of 275 kg m^{-3} (Liang et al., 2006; Tsang et al., 2008), which is a relatively low density for snow particularly when late in the snow season and at high latitudes.

The propagation of energy between the different snow layers is calculated with the Discrete Ordinate Radiative Transfer (DISORT) method (Jin 1994). In this study, the propagation of electromagnetic radiation was calculated for 32 streams. Brucker et al. (2010 and 2011a) used this model in a study on Antarctic snow. The version used in this study includes a soil reflectivity model (see Sect. 3.4.1.3), which is available online (http://lgge.osug.fr/~picard/dmrtml/).

3.4.1.2 HUT n-layer

The HUT n-layer model (Lemmetyinen et al., 2011) is an extension of the semi-empirical HUT model that calculates the emission of a one-layer snow cover (Pulliainen et al., 1999). The attenuation coefficient of snow is calculated using an empirical equation given the frequency and the grain size (D_{eff} is the microwave effective grain size, often derived from D_{max}, which is the longest diameter of the observed snow grain).

The ML model is based on a two-flux approximation for each layer. The model calculates the upwelling and downwelling fluxes for each layer before it calculates the upwelling emission at the surface of the snow cover.

3.4.1.3 Soil emission model

The Wegmüller and Mätzler (1999) model calculates the soil reflectivity for a rough surface. H-pol polarization reflectivity r_H is calculated as follows:

$$r_H = r_{H,Fresnel} \cdot \exp(-(k\sigma)^{\sqrt{-0.1\cos\theta}}) \tag{3.3}$$

where k is the wavenumber, σ is the standard deviation of the surface height (in meters), θ is the nadir angle (in degrees), and $r_{H,Fresnel}$ is the Fresnel coefficient. This equation is valid for θ smaller than 60°. The Fresnel coefficients were calculated using the soil permittivity calculated following Dobson et al. (1985). Because soil properties were not measured (except for soil temperature), soil moisture was set to 0.35 and the soil was considered as nonfrozen (soil temperature at the SIRENE site close to 0°C) and liquid water was present, whereas at the Churchill sites, soil temperatures was above the limit of -5°C to -7°C proposed by Mironov et al. (2010) for complete freezing of tundra soil. The reflectivity of the soil in V-pol r_V is derived from r_H as follows:

$$r_V = r_H \cdot (\cos\theta)^{0.655} \tag{3.4}$$

3.4.2 Grain size correction factor (ϕ) *and retrieval of soil parameters*

The overall approach for adapting the MSEM to an effective snow grain metric derived from SSA measurements consists of optimizing a constant and frequency-independent factor ϕ applied to the optical radius (eq. 3.2), following Brucker et al. (2011a). However, the Brucker et al. (2011a) study was in central Antarctica where the snow depth is several orders of magnitude deeper than the microwave penetration depth. In the case of a seasonal snowpack, the soil emission can be significant, and it depends on parameters that are rarely measured, such as the roughness parameter, soil moisture, and freezing state. Optimizing the grain size correction factor and the soil parameter(s) in one operation is not the most appropriate approach because the uncertainty in the observations and the model approximations will be compensated for by uncertainty and interdependences between the optimized parameters. A more physically-based approach consists of optimizing the factor ϕ by selecting the situations where the soil has the least contribution and using only the highest frequency at 37 GHz. The soil parameters are optimized in a second step using the opposite situation, that is, the shallowest snowpits and the lowest frequency at 19 GHz. The validation then includes all of the sites and both frequencies.

To find sites where the soil had a small contribution at 37 GHz [weak soil contribution (WSC)] a sensitivity test with DMRT-ML for the simulated T_B was carried out for a very rough soil (i.e., low soil reflectivity) and a very smooth soil (i.e., high soil reflectivity) with an initial value of $\phi =$

2.85 (Brucker et al., 2011a). Without a reference value for ϕ when using the SSA as a grain size parameter in HUT n-layer (no previous studies have been conducted on this specific topic), these same WSC sites were used for the analysis of the HUT n-layer model.

Once the sites were selected, there were three phases for each of the two MSEMs.

PHASE 1) Optimization of ϕ

This phase consisted of calculating ϕ (eq. 3.2) at 37 GHz in V-pol with an initial value for the soil roughness σ of 0.5 cm for WSC sites. Some studies consider a soil roughness of 1 cm (Wegmüller & Mätzler, 1999; Ferrazzoli et al., 2002), while the HUT model generally considers 0.3 cm (Pulliainen, 2006). Hence 0.5 cm can be considered as a plausible median value. By considering WSC at 37 GHz, we were able to properly optimize ϕ without compensating for errors related to the soil. Note that this approach applies a constant correction to each layer in the snowpack. An iterative process with an increment of 0.1 was used to calculate ϕ that minimized the root-mean-square error (RMSE) between the measured and simulated T_B at 37 GHz in V-pol for the WSC sites such that

$$RMSE_{\phi} = \sqrt{\frac{\sum_{i=1}^{N} (T_{\mathrm{B}\,sim;i}^{37V} - T_{\mathrm{B}\,mes;i}^{37V})^2}{N}} \tag{3.5}$$

where N is the total number of snowpits. Only the V-pol was used to avoid the increased sensitivity to the effect of snow stratification at H-pol (Durand et al., 2008). However, the values for H-pol were used for the validation in phase 3.

PHASE 2) Optimization of the soil parameters

Using the optimized factor ϕ, the surface roughness parameter σ for each site was optimized at 19 GHz (V-pol and H-pol) for the grassy sites (SIRENE and St-Romain) and the tundra sites (Churchill). To minimize the compensation of error between optimizations for phase 1 and 2, the sites used in phase 1 (WSC sites) were discarded in phase 2. Thus, only the sites where the soil contribution was more important were considered [strong soil contribution (SSC)]. We used an

increment of 0.01 cm to find the σ values that minimized the $RMSE_\sigma$ calculated as a function of the measured T_B ($T_{B\,mes}$) and the simulated T_B ($T_{B\,sim}$) in V-pol and H-pol as follows:

$$RMSE_\sigma = \sqrt{\frac{\sum_{i=1}^{N}(T_{\mathrm{B}\,sim;i}^{19V} - T_{\mathrm{B}\,mes;i}^{19V})^2 + (T_{\mathrm{B}\,sim;i}^{19H} - T_{\mathrm{B}\,mes;i}^{19H})^2}{2N}} \tag{3.6}$$

PHASE 3)

Using the optimized parameters for certain sites (ϕ for phase 1 and σ for phase 2), validation was performed for all sites, both frequencies, and both polarizations. Calculations of RMSE were used to evaluate the error.

3.5 Results

3.5.1 Identification of the sites where the soil had a low impact

To retrieve the ϕ factor at 37 GHz in V-pol, snowpits where the soil had a low impact had to be identified (WSC sites). To identify these WSC snowpits, we used an initial value of ϕ of 2.85 (Brucker et al. 2011a), and we calculated T_B with DMRT-ML for two extreme soil conditions: 1) smooth soil (or "cold soil") with a low reflectivity and σ = 0; and 2) rough soil (or "warm soil") with a high reflectivity and σ = 10 cm. The sites where the difference in T_B for both polarizations was smaller than 5 K were considered as WSC sites (see table 3.2). This selection process identified eleven WSC sites (2, 3, 6, 7, 8, 9, 10, 11, 12, 13, and 16).

3.5.2 Adaptation of measured SSA for DMRT-ML

PHASE 1)

Using a surface roughness of 0.5 cm, we calculated the ϕ that minimized the RMSE between the measured and simulated T_B at 37 GHz in V-pol (eq. 3.5) for the 11 WSC sites. Figure 3.1 shows that without a correction for R_{opt} there is a very large $RMSE_\phi$ of 63.0 K. It also shows that there is an optimal value for the correction factor corresponding to ϕ = 3.3 and a minimum $RMSE_\phi$ of 17.7 K. This value is slightly higher than that found by Brucker et al. (2011a). However the factor varies between ϕ =2.9 and ϕ = 3.7 for $RMSE_\phi$ more than 2 K over the minimum $RMSE_\phi$, thus showing the possible variation of ϕ.

Table 3.2: T_B (K) simulations for the DMRT-ML model with $\phi = 2.85$ and T_B at 37 GHz for a smooth soil T_B (σ_0: $\sigma = 0$ cm) and a rough soil T_B (σ_{10}: $\sigma = 10$ cm). Column 6 and 7 are the difference between these simulated T_B at V-pol and H-pol, respectively. The sites SSC sites are highlighted in gray.

Sites #	T_BV (σ_0)	T_BH (σ_0)	T_BV (σ_{10})	T_BH (σ_{10})	T_BV(σ_{10})-T_BV(σ_0)	T_BH(σ_{10})-T_BH(σ_0)
1	202.7	187.4	217.0	203.7	14.3	16.3
2	148.7	138.1	151.9	141.3	3.2	3.2
3	137.2	127.9	139.3	129.9	2.0	2.0
4	187.5	170.7	195.3	178.8	7.8	8.1
5	226.3	205.6	234.0	214.1	7.7	8.5
6	250.0	231.4	251.1	232.6	1.1	1.2
7	216.5	201.3	219.9	205.1	3.4	3.7
8	220.2	202.5	221.6	203.9	1.4	1.4
9	215.9	201.5	217.5	203.1	1.6	1.6
10	256.1	240.2	256.9	241.1	0.8	0.8
11	252.7	239.2	253.5	240.2	0.8	1.0
12	251.5	237.6	252.4	238.6	0.9	1.0
13	245.5	231.1	247.5	233.3	2.0	2.2
14	219.8	201.6	229.7	212.6	9.9	11.0
15	218.4	197.1	234.9	215.0	16.5	18.0
16	204.1	182.6	208.1	186.6	4.0	4.1
17	176.5	160.5	186.0	170.2	9.5	9.7
18	237.8	226.1	264.9	256.8	27.1	30.7
19	239.9	229.2	259.5	252.2	19.6	23.0
20	233.3	220.2	267.8	262.4	34.4	42.2

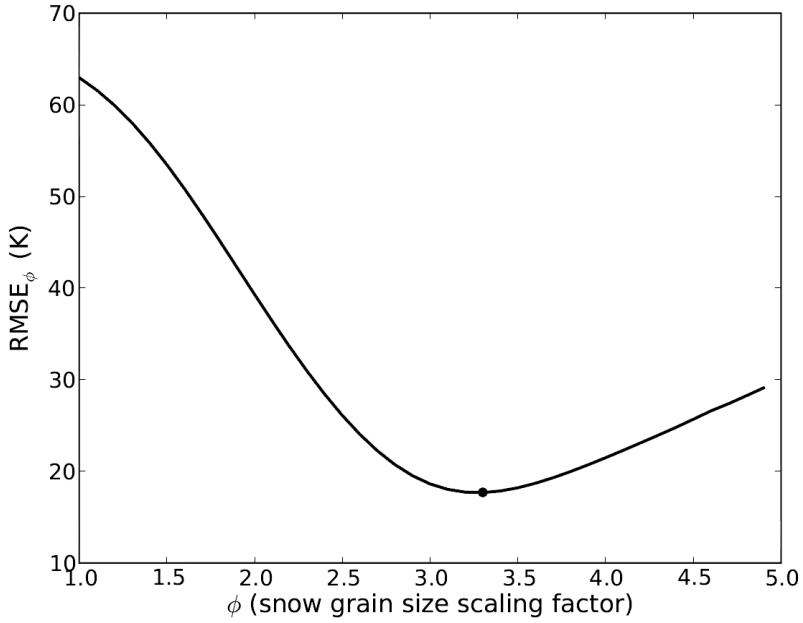

Figure 3.1: RMSEs (RMSE$_\phi$) for the DMRT-ML model simulations as a function of the grain size scaling factor ϕ, which was applied to the optical radius (eq. 3.2). RMSE$_\phi$ are calculated for all the 11 WSC sites at 37 GHz V-pol. (Black dot) The minimum RMSE$_\phi$ = 17.7 K is at $\phi = 3.3$.

PHASE 2)

In order to evaluate the ratio r_V/r_H in the soil model (eq. 3.4) using $\phi = 3.3$, the surface roughness of every site (σ) was then calculated separately by minimizing the residual error between the measurements and simulations at 19 GHz. Table 3.3 shows the optimal values for σ and the reflectivity values that minimized the differences between the simulated and measured T_B at 19 GHz in V-pol and in H-pol separately. There is large variability in the σ values between the different snowpits. The error related to modeling the snow, and more specifically the grain size, can nevertheless have a strong impact on the inverted roughness when the snow is deep and/or when the grains are large (greater effect of extinction) (see table 3.1). In one extreme case (site 11), it was impossible to converge towards the measured T_B at H-pol because the optimal soil reflectivity values were lower than the Fresnel coefficients (reflectivity of a plane surface), which is impossible with the selected soil emission model. A possible reason is an overestimation of the Fresnel coefficient due to uncertainty of the soil permittivity. Thus, the sites with deep snow cover or with large grains (WSC) were more influenced by the error related to the snow simulation (grain size) than by the soil roughness. Difference between simulated T_B for a low reflectivity of the soil (σ = 0) and a high reflectivity (σ = 10 cm) at 19 GHz are significantly lower for WSC sites (29.8 K) than for SSC sites (46.1 K). The roughness values calculated at these sites were thus strongly biased, but the impact on the T_B simulations was rather low.

Table 3.3 also shows that there was significant variation in the ratio r_V/r_H. The r_V/r_H values were lower for some locations, such as the SIRENE sites (0.39), while there was strong variability for all of the tundra sites (0.74 ± 0.20). The average r_V/r_H was very similar to that used in eq. 3.4 (0.71 for an incidence angle of 54°). The average ratio r_V/r_H for the SSC sites was relatively similar at 0.63 (table 3.3). However, for the grassy sites (all considered as SSC sites) the averaged ratio was significantly lower (0.47). These differences might impact the results mainly at 19 GHz where the soil contribution is generally larger.

Table 3.3: **Optimized DMRT-ML soil roughness (σ cm) for every site and reflectivity (r_V and r_H) at 19 GHz (soil moisture = 0.35). Column 6 is the ratio between r_V and r_H. The sites SSC sites are highlighted in gray.**

Sites #	σ_V (cm)	σ_H (cm)		r_V	r_H		r_V / r_H
1	0.474	0.153		0.080	0.136		0.59
2	0.137	0.093		0.114	0.146		0.78
3	1.133	0.754		0.065	0.087		0.74
4	0.009	0.032		0.178	0.179		0.99
5	0.732	0.319		0.065	0.104		0.63
6	0.052	0.013		0.127	0.186		0.68
7	0.119	0.427		0.124	0.107		1.16
8	0.008	0.039		0.178	0.165		1.08
9	0.137	0.001		0.113	0.258		0.44
10	0.090	0.103		0.119	0.136		0.87
11	< 0.001	-		0.205	0.426		0.48
12	0.011	< 0.001		0.169	0.284		0.59
13	0.139	0.044		0.117	0.178		0.65
14	0.072	0.020		0.121	0.180		0.67
15	0.179	0.088		0.096	0.137		0.70
16	< 0.001	< 0.001		0.221	0.284		0.78
17	0.001	< 0.001		0.187	0.271		0.69
18	2.383	0.500		0.032	0.076		0.42
19	2.324	0.295		0.034	0.095		0.36
20	1.396	0.842		0.057	0.088		0.65
	Mean r_v/r_h ratio						0.70
	Mean r_v/r_h ratio SSC sites (1, 4, 5, 14,15, 17, 18, 19, 20)						0.63

As a further step, a unique value for the surface roughness was optimized for the grassy sites and another for the Churchill sites using only the SSC sites, which were the sites that were not chosen for optimizing ϕ. The σ that minimized the RMSE for T_B at 19 GHz (eq. 3.6) was $\sigma = 0.78$ cm for the grassy sites (18, 19, 20), and $\sigma = 0.04$ cm for the tundra sites (1, 4, 5, 14, 15, 17) (figure 3.2). The curve for the grassy sites does not show a pronounced minimum RMSE mainly because the reflectivity varied less strongly as a function of the roughness for larger σ values (figure 3.2). It should be noted that the difference between both σ values may be due to the poor representation of soil moisture and texture which were considered identical for both sites. The optimized σ values should also be considered as an effective parameter (see Sect. 3.6.3).

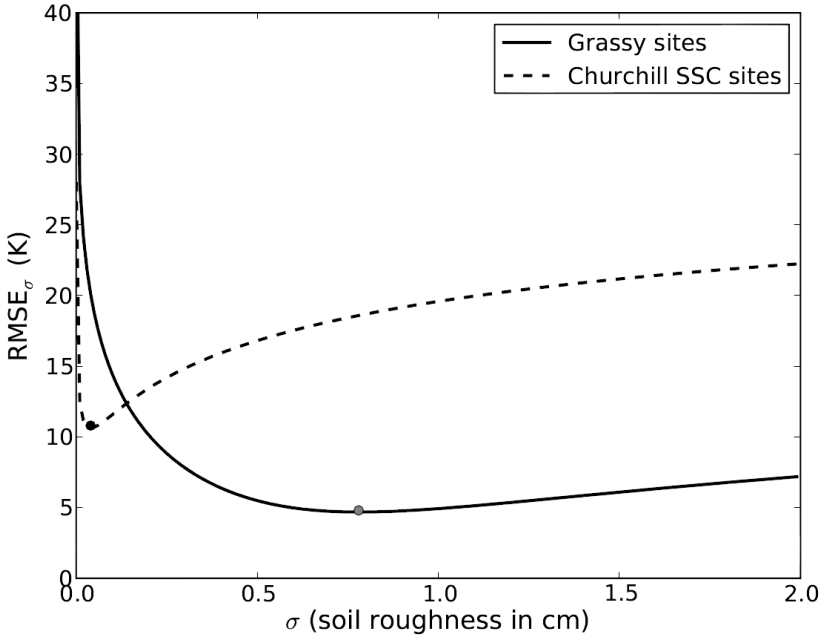

Figure 3.2: RMSE (RMSE$_\sigma$) for the optimization of the soil roughness parameter (σ) at 19 GHz using the DMRT-ML model. Grassy sites are represented by the solid line and tundra sites by the dashed line [(gray point) grassy: σ = 0.78 cm; (black point) tundra: σ = 0.04 cm]. RMSE$_\sigma$ is calculated from eq. 3.6.

PHASE 3)

Figure 3.3 shows the results for simulations using ϕ = 3.3 and the optimized soil roughness values. The RMSE at 37 GHz is higher that at 19 GHz for both polarizations (figure 3.3a). This difference is mainly due to sites where the wind had greatly increased the density of the topmost snow layers and the snow depth was the deepest. The smaller snow grains mainly at the surface (shallower penetration depth at 37 GHz) appear to cause an underestimation of the signal attenuation at these sites, which can result in a R_{eff} that is too low. Figure 3.3b shows that the simulated ratios of 19H-pol/19V-pol are slightly higher than measurements. This difference may be due to the soil ratio r_V/r_H (eq. 3.4) in the soil model, which was slightly lower for our sites (0.63 for SSC sites [see table 3.3] compared to the Wegmüller and Mätzler, 1999 model value of 0.71 calculated from eq. 3.4 for an incidence angle of 54). Figure 3.3(c) and (d) where simulated and measured T_B behaviors are similar, shows the coherency of simulations and indicates that the scaling factor of ϕ = 3.3 is valid at 37 GHz and 19 GHz.

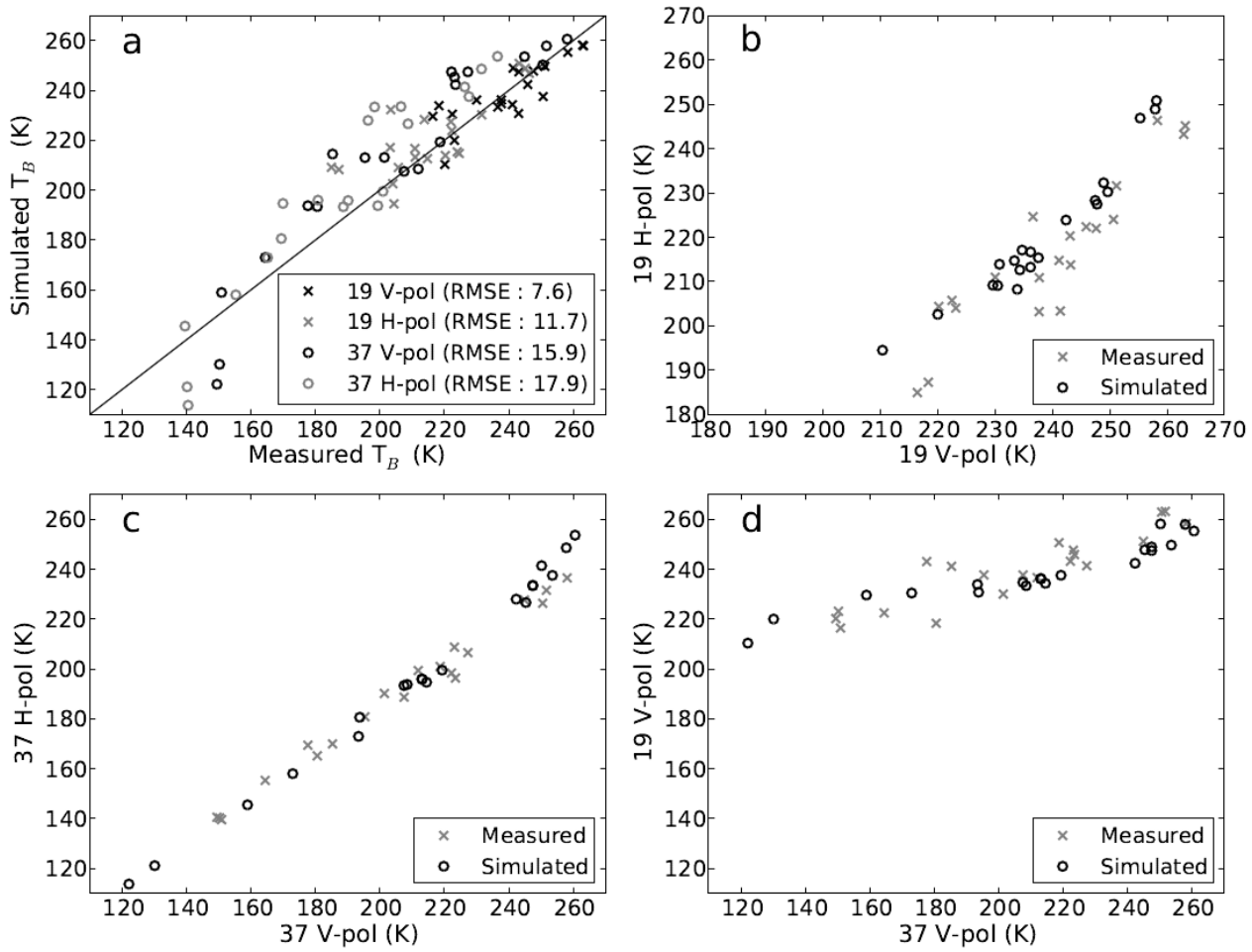

Figure 3.3: DMRT-ML model simulations for a grain size correction factor of $\phi = 3.3$ and optimized σ for all 20 snowpits at 19 and 37 GHz and two polarizations. (Upper left) Simulated brightness temperatures T_B compared to measured T_B. In the inset, the RMSE (in kelvin) for each frequency and polarization is given. (Upper right) T_B at 19 GHz H-pol versus T_B at 19 GHz V-pol. (Bottom left) T_B at 37 GHz H-pol versus T_B at 37 GHz V-pol. (Bottom right) T_B at 19 GHz V-pol versus T_B at 37 GHz V-pol.

The effect of the snow depth can be explained by the predominance of thick upper layers with small grains that caused the extinction to be underestimated. Kontu and Pulliainen (2010) proposed a correction for the maximum extent D_{max} that reduces the weight of large grains and increases the weight of small grains. In this paper, to test this approach, we applied a similar formulation to the optical radius R_{opt} in DMRT-ML such that

$$R_{eff} = a[1 - \exp(-bR_0)] \tag{3.7}$$

where a and b are empirical parameters. Because of the shallow penetration depth (mainly at 37 GHz) for sites with a deep snowpack, this approach tends to increase the extinction by the smallest grains at the top layers relative to the largest grains and thus decreases the simulated T_B.

Using the same previous 11 WSC sites, the parameters a and b were optimized (surface roughness was 0.5 cm). The values obtained were: a=1.1 and b=8.2. The surface roughness values were then optimized for the tundra sites (σ =0.04 cm) and the grassy sites (σ = 1.1 cm).

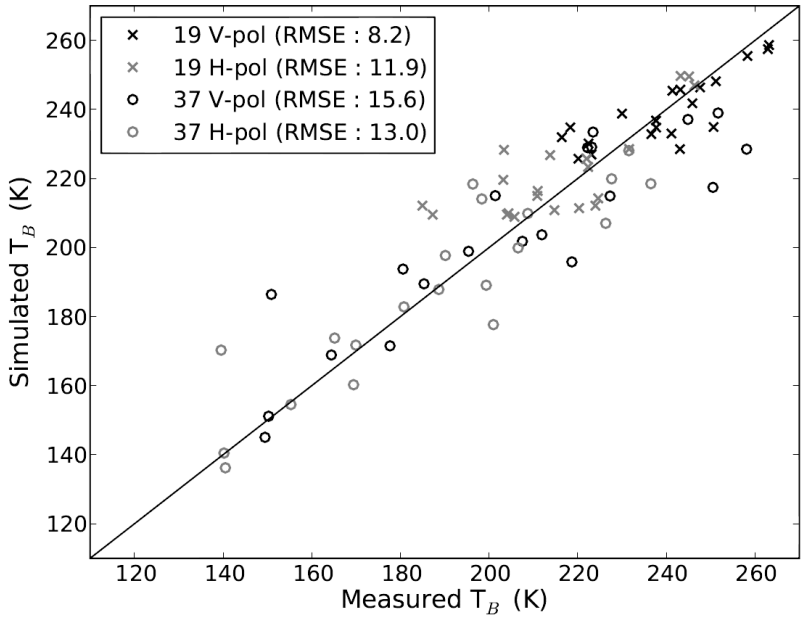

Figure 3.4: **DMRT-ML model simulations for a grain size correction with eq. 3.7 (a=1.1 and b=8.2) and optimized soil roughness for all 20 snowpits at 19 and 37 GHz and two polarizations. In the inset, the RMSE (in kelvin) for each channel is given.**

Figure 3.4 shows that giving a higher weight to the smallest grains using the approach in Kontu and Pulliainen (2010) improves the RMSE at 37 GHz, principally in H-pol. The improvements in H-pol mainly result from the improvement of the four sites where the T_B were the highest (10, 18, 19, and 20) (see table 3.1) and from two other sites with coarse grains. There was also an improvement at 37 GHz for the most dense snowpack. However, for the three grassy sites, the results were poorer at V-pol. The RMSEs at 19 GHz were also slightly poorer. These results show that the Kontu and Pulliainen (2010) approach for a ML model improves the simulations only under certain conditions. Part of this improvement may results because of the larger number of optimized parameters (two instead of one). This issue requires further investigation with a larger observational database.

3.5.3 Adaptation of measured SSA for HUT n-layer

Because there are no other studies that use the SSA as input data for HUT n-layer, it was difficult to choose an initial value for ϕ for HUT n-layer in order to identify WSC sites. The same WSC sites used for DMRT-ML were thus used to optimize ϕ for HUT n-layer.

PHASE 1)

For an initial value of the surface roughness (σ = 0.5 cm), the optimized factor using eq. 3.5 was ϕ = 3.7 (figure 3.5). This value is slightly sensitive to the choice of the initial value (for example, using an initial value of σ = 0.01 cm gives ϕ = 3.5, while it gives ϕ = 3.8 for σ = 50 cm). The choice of initial value of σ = 0.5 cm is based on previous studies. However, if we chose σ = 0.04 cm found at Churchill sites with DMRT-ML, we obtain ϕ = 3.5. The ϕ could thus slightly vary because of the initial σ value.

As for DMRT-ML, to analyze the r_V/r_H for the soil model (eq. 3.4) using ϕ =3.7, the surface roughness for every site (σ) was calculated separately. The results (not shown) were similar to those obtained with DMRT-ML with a mean ratio r_V/r_H of 0.63 for all sites and 0.62 for the SSC sites.

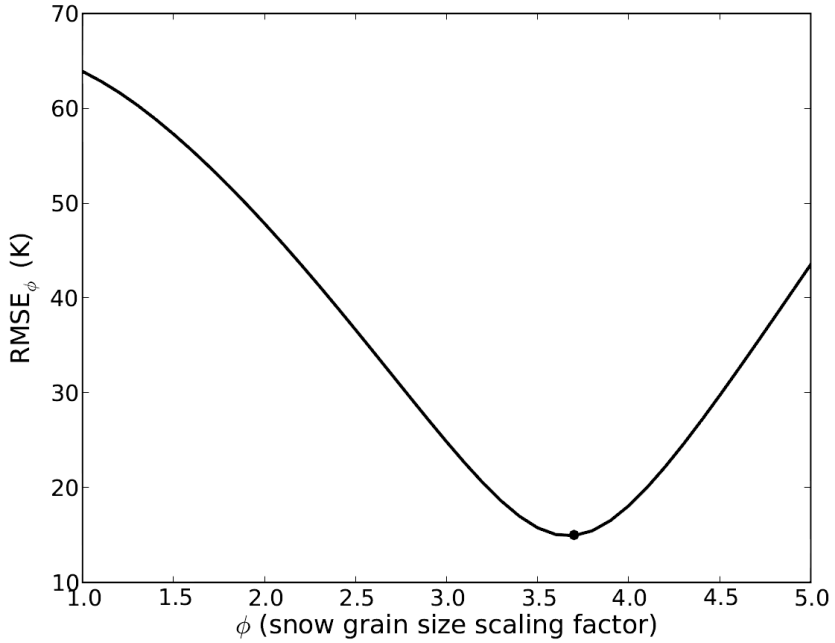

Figure 3.5: **RMSE (RMSE$_\phi$) for the HUT n-layer model simulations as a function of the grain size correction factor ϕ, which was applied to the optical radius (eq. 3.2). Results are shown for the 11 WSC sites. (Black dot) The minimum RMSE$_\phi$ was 15.0 K at ϕ = 3.7.**

The same SSC sites as for DMRT-ML were used to optimize σ for the grassy sites and the tundra sites. For the grassy sites, when minimizing the $RMSE_\sigma$ at 19 GHz (eq. 3.6), we obtained $\sigma = 0.94$ cm. For the soil parameters for the Churchill sites, the σ that minimized the $RMSE_\sigma$ was 0.06 cm. Thus, the σ values that we obtained were again very similar to those obtained using DMRT-ML. Using the σ values derived from HUT n-layer in DMRT-ML, leads to small differences in RMSE at 19 GHz at V-pol (0.1 K) and H-pol (0.5 K) compared to using values derived from DMRT-ML (Sect. 3.4.2 phase 1). This shows that, by using two different snow models, we obtained almost the same soil parameters. This supports the reliability of the results for the soil parameters, the independence of the models, and the scaling factor for the snow grains.

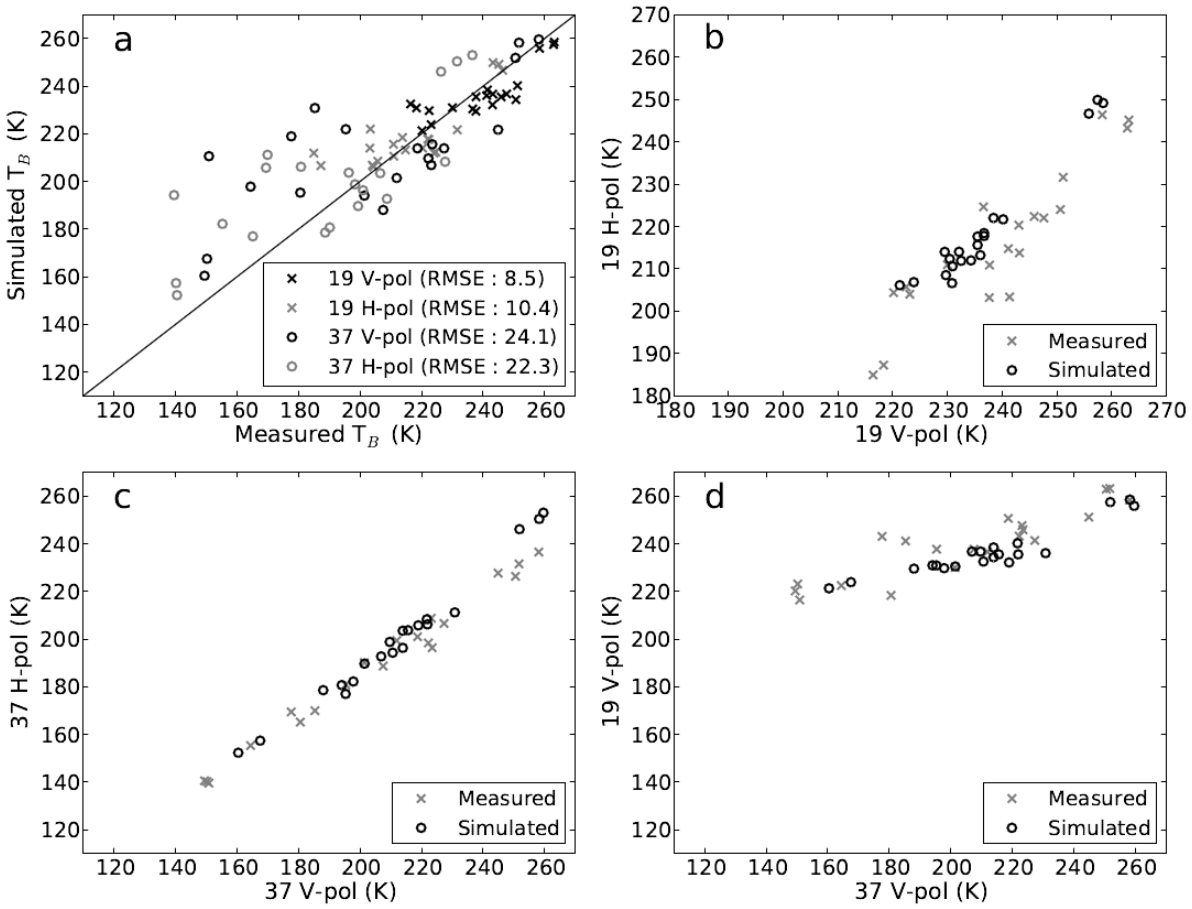

Figure 3.6: HUT n-layer model simulations for a grain size correction factor of $\phi = 3.7$ and optimized σ for all 20 snowpits at 19 and 37 GHz and two polarizations. In the inset, the RMSE (in kelvin) for each channel is given. (Upper left) Simulated brightness temperatures T_B compared to measured T_B. (Upper right) T_B at 19 GHz H-pol versus T_B at 19 GHz V-pol. (Bottom left) T_B at 37 GHz H-pol versus T_B at 37 GHz V-pol. (Bottom right) T_B at 19 GHz V-pol versus T_B at 37 GHz V-pol.

Figure 3.6a shows, however, that the RMSEs at 37 GHz are much higher than with DMRT-ML. HUT n-layer overestimated T_B, especially for sites where the T_B was the lowest (containing the largest grains). It thus seems that the extinction by large grains was underestimated. This problem is probably due to the fact that HUT n-layer was initially designed to use D_{max} for the grain size parameter. Even with a scaling factor, the R_{opt} will tend to underestimate the grains with a large D_{max} because the relationship between SSA and D_{max} is not linear (Langlois et al., 2011). Figure 3.6(b) is similar to figure 3.3. Hence it shows the possible high soil ratio r_V/r_H (eq. 3.4) in the soil model. Figures 3.6(c) and d also show similarity with figure 3.3. It indicates that the higher RMSE caused by attenuation underestimation is not reflected in HUT n-layer polarization and frequency coherency.

3.6 Discussion

3.6.1 Physical basis for ϕ in the DMRT model

The parameter ϕ introduced in this study and in Brucker et al. 2011a, which was adjusted in order to minimize the difference between the microwave observations and simulations, had a value much greater than unity and was different between the two studies (2.85 versus 3.3). Indeed, to use SSA measurements to drive DMRT-ML, as well as models based on the DMRT in general, it is important to understand the source of ϕ and to link its variability to measurable characteristics of snow. First, it is important to emphasize that, in agreement with the analysis by Durand et al. (2008), measurement errors for other snowpack parameters having an influence on T_B (e.g., density, depth, stratigraphy) cannot explain an RMSE as high as 63 K that was obtained with ϕ = 1 (figure 3.1). In the following, we explore the possible sources influencing the magnitude of ϕ. Second, we discuss the difference between ϕ from this study and from measurements taken in Antarctica (Brucker et al., 2011a).

The DMRT version used in this study assumes small homogeneous spheres, i.e., with R_o much smaller than the wavelength (Tsang & Kong. 2001). These spheres all have the same radius, are randomly distributed, and are not necessarily in contact. If this was an accurate description of the microscopic structure of snow, then R_{eff} in DMRT-ML would be equivalent to the radius of the spheres composing our hypothetical snow, and we would obtain ϕ = 1. However, this study shows a significant departure of ϕ from unity that cannot be completely explained by measurement errors in the physical quantities of snow or in the microwave brightness

temperature. It is thus clear that the difference between the microstructure of natural snow and the representation used in the DMRT is the principal cause of the high values of ϕ. Two possible sources are discussed here, namely, the cohesion between the grains (stickiness) and the heterogeneity of snow grain size.

The position of snow grains is not random and independent because, among other things, the grains must physically touch each other to ensure the cohesion of the snow. In DMRT, this characteristic is modeled by using an attractive force between the spheres, which is parameterized by the stickiness factor (τ_s) (see Tsang et al., 2000). The resulting aggregation of grains forms clusters that interact with microwaves as objects that are larger than the spheres of which they are actually composed. This causes an increase in the scattering, which is compatible with the high value of ϕ that is obtained when clustering is neglected. To test this hypothesis, DMRT-ML was modified to take into account stickiness in the simple case of "short range", i.e., the size of clusters are smaller than the wavelength. For 20 sites at 37 GHz and with the soil parameters optimized for DMRT-ML, a two-parameter (ϕ_{sticky} and τ_s) optimization was carried out by a two parameters space exploration (an increment of 0.1 for ϕ and 0.01 for τ_s). The values that gave the lowest RMSE were $\phi_{\text{sticky}} = 2.6$ and $\tau_s = 0.44$ (figure 3.7). These results show that stickiness could explain, in part, the value of $\phi = 3.3$ that was previously calculated. Figure 3.7 also shows that for a range of RMSE of + 1 K over the minimal RMSE (14.5 K-15.5 K) we found a solution at $\phi_{\text{sticky}} = 1.4$ and $\tau_s = 0.13$, which is an interesting result that is discussed in more detail below. Note that the validity of the calculations for $\tau_s <\approx 0.3$ is not guaranteed for the "short range" version of the stickiness implemented in DMRT-ML (Tsang et al., 2001; Picard et al., 2013). In conclusion, even if the stickiness seems to be a pertinent physical explanation, in practice, its introduction poses difficulties because it is not a measurable quantity for natural snow and its optimization is not unequivocal, even in the simplified case that we considered here by using a constant value for the entire snowpack.

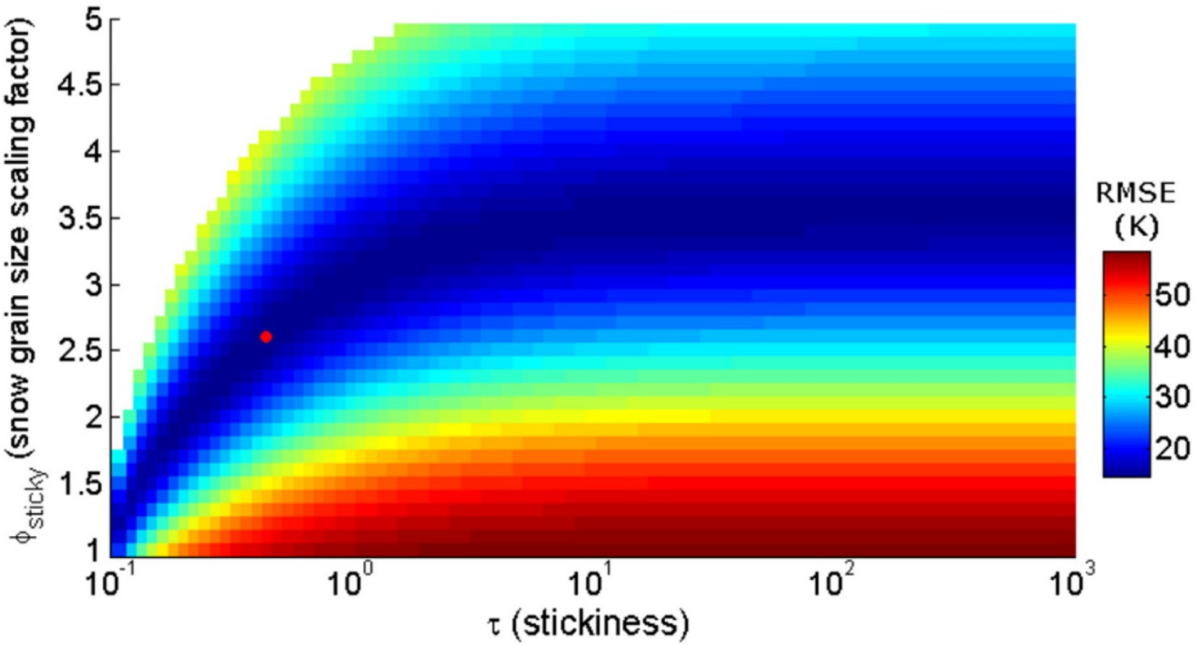

Figure 3.7: **RMSE (in kelvin) between DMRT-ML model T_B simulations and T_B measured as a function of the grain size correction factor ϕ_{sticky} and stickiness τ_s (logarithmic scale). (White) Invalid result from DMRT-ML. (Red point) Minimum RMSE for $\phi_{sticky} = 2.6$ and $\tau_s = 0.44$.**

Another factor that can explain the high value of ϕ is the heterogeneity of snow grains, particularly their size. This factor is important because the dependence of scattering on particle size is strongly nonlinear in the small particle range (for spheres and the frequencies examined in this study, it varies with the cube of the radius) (e.g., Jin, 1994). As a result, large particles scatter much more than small particles. Thus, a collection of spheres with variable sizes has, in general, a larger scattering coefficient than a collection with the same SSA composed of identical spheres. In other words, the equivalent volume to surface area sphere approach that is valid in optics (Grenfell and Warren, 1999) is not valid in the microwave range (Jin, 1994).

To test the impact of the grain size distribution, we calculated the scattering and absorption coefficients (without stickiness) for sizes following the Rayleigh distribution in DMRT-ML; this distribution has a short upper tail, which permits the convergence of the calculation (West et al., 1993). For this case, we obtained an optimal $\phi_{distribution}$ of 2.4, which is a factor of 1.4 lower than the monodisperse case of $\phi = 3.3$ and confirms the result of Jin (1994). The precise value of $\phi_{distribution}$ depends on the distribution chosen, which poses problems similar to stickiness because the grain size distribution may be variable depending on the type of snow, is difficult to measure

in the field, may pose conceptual difficulties because the snow grains are not spherical, and sometimes may be hardly identifiable as individual grains.

The combination of the two factors described here seems to explain the high factor of 3.3. In fact by setting $\tau_s = 0.13$, the product of ϕ_{sticky} and $\phi_{\text{distribution}}$ is 3.1, which is close to 3.3. However, this simple product is not rigorous and the accurate calculation of the scattering and absorption coefficients for a size distribution of sticky spheres is not trivial (Tsang & Kong 2001) and it is not implemented in DMRT-ML.

It is quite possible that other factors contribute to the coefficient ϕ, such as the grain shape. To address this, our future research will determine whether ϕ varies depending on the type of snow, as suggested by the different ϕ obtained in the present study and in Brucker et al. (2011a). In fact, the parameters for the stickiness and the distribution of snow grain sizes may vary from one type of snow to another and have an influence on ϕ. However, the difference obtained in both studies is not sufficiently large to exclude the uncertainty in the SSA or T_B measurements. Indeed, the study in Antarctica used satellite-derived T_B from kilometers-wide pixels compared to the point measurements of snow properties and T_B used in this paper.

These are only qualitative explanations, and yet, given that the minimization previously obtained with $\phi = 3.3$ is reasonable from an assimilation perspective, the use of a fixed ϕ in the range of 2.8-3.5 is currently the most acceptable option.

3.6.2 Analysis of ϕ for HUT n-layer

The results obtained with the HUT n-layer model show that the SSA may not be a suitable parameter. As a semiempirical model, HUT n-layer was parameterized as a function of measurements of D_{max}. This difference in the conceptual characterization of snow grains may thus explain the higher RMSE with the HUT n-layer model compared to DMRT-ML, especially for sites where there was a considerable fraction of depth hoar. It could also explain the higher value of $\phi = 3.7$ compared to $\phi = 3.3$ with DMRT-ML. Furthermore, we showed that the ϕ of HUT n-layer was slightly sensitive to soil parameterization. This sensitivity might be caused by the fact that the attenuation of large grains is underestimated by HUT n-layer at Churchill sites (as also illustrated in Derksen et al., 2012) leading to an overestimation of the soil contribution.

By using the σ value derived from DMRT-ML, ϕ value decreases to 3.5, while the RMSE remains almost the same. A simple adaptation of the HUT n-layer model to use the SSA as input is therefore not appropriate. It is thus necessary to find a parameterization of the model that is suitable.

3.6.3 Soil parameters

For the tundra sites, our study showed that the soil roughness had a low impact on T_B at 37 GHz. Even for sites where the snow depth was relatively shallow (< 50 cm), the attenuation by snow grains (principally by depth hoar) was sufficiently high to attenuate most of the contribution from the soil.

At 19 GHz, even if the grain size was the dominant factor, it was still necessary to take the soil into consideration. The average soil parameters for the grassy and tundra sites were retrieved for the case where the snow grain size had a low impact. There can nevertheless be considerable microvariability in the soil conditions (e.g., roughness, moisture, soil type and litter) even within the same site (Grant et al., 2009, Saleh et al., 2006, Schmugge et al., 1988). Furthermore, considering the same soil moisture and texture for every site may lead to incorrect estimates of the soil permittivity property because of the Fresnel soil reflectivity. The calculated surface roughness becomes more like the average effective soil parameters for each site rather than true measureable roughness; further investigation will be needed to better understand the representation of this parameter. In addition, as shown in table 3.3, the ratio r_V/r_H considered as constant in the roughness model of Wegmüller and Mätzler (1999), may be different from one site to another, as grassy sites exhibited a lower ratio.

3.6.4 Synthesis of the results

Several parameterizations for MSEM as a function of SSA measurements were evaluated in this study and are summarized in table 3.4. In terms of the average RMSE for the two frequencies and the two polarizations, the Kontu and Pulliainen (2010) approach, which was originally developed for HUT but applied to DMRT-ML in this study, led to a slight improvement in the average RMSE compared with an approach with a fixed ϕ (table 3.4). The approaches with stickiness and the size distribution also led to an improvement of the average RMSE. The Kontu and Pulliainen (2010) approach with the HUT n-layer model was not presented because the optimization of the *a*

and b coefficients converged to a result equivalent to $\phi = 3.7$. The Kontu and Pulliainen (2010) approach tends to increase the underestimation of extinction for large grains and thus overestimates the T_B on snowpits having a large proportion of depth hoar.

Table 3.4: RMSE for HUT n-layer and different configurations of the DMRT-ML model. In parenthesis, the correction applied to the snow grains is shown (ϕ: eq. 3.2; Kontu: eq. 3.7; τ_s: with stickiness; Rayleigh: Rayleigh grain size distribution).

Models and approaches	37V	37H	19V	19H	Mean RMSE
DMRT-ML ($\phi = 3.3$)	15.9	17.9	7.6	11.7	13.3
DMRT-ML (Kontu: 1.1-8.2)	15.6	13.0	8.2	11.9	12.2
DMRT-ML ($\phi_{sticky} = 2.6$; $\tau_s = 0.44$)	14.5	16.0	7.9	10.8	12.3
DMRT-ML ($\phi = 2.4$; Rayleigh)	14.3	16.2	7.6	11.2	12.3
HUT n-layer ($\phi = 3$ .7)	24.1	22.3	8.5	10.4	16.3

3.7 Conclusion

The size of the scatterers in snow is the main parameter influencing the passive microwave emission. The objective of this study was to parameterize two radiative transfer models (i.e., DMRT-ML and HUT n-layer) using snow SSA measurements to characterize grain size and ground-based radiometer measurements at 19 and 37 GH to evaluate the models.

For DMRT-ML, we found that a value of $\phi = 3.3$ minimized the RMSE between the simulated and measured T_B. This factor may be explained, in part, by the grain size distribution and the stickiness between grains that tends to form clusters with a large effective size. This study showed that at 37 GHz, the model had a very low sensitivity to the soil parameters for most snowpacks, especially for the deepest snowpacks or those with depth hoar. At 19 GHz, although the transparency of the snow was higher, the grain size extinction has an important contribution. The approach of Kontu and Pulliainen (2010), which gives a higher weight to small grains, led to an 8% decrease of the RMSE but required an optimization of two parameters instead of one. For HUT n-layer, a simple adaptation for the SSA does not allow good estimates of the extinction mostly at 37 GHz, particularly for sites containing coarse grains.

Our results show that a grain size metric derived from SSA for snow applied to DMRT-ML led to an average RMSE (19 and 37 GHz) of approximately 13 K. The results are comparable to other studies where the variety of types of snow and the range of measured T_B were more limited (Derksen et al., 2012: 12.0 K; Kontu and Pulliainen, 2010: 9.3 K; Lemmetyinen et al., 2010:

13.1K). For HUT n-layer, we obtained higher overall RMSE (16.3 K), mainly due to the 37 GHz results (23.2 K).The results were derived from a unique dataset that included precise snow measurements (e.g., SSA) for various types of snow cover, as well as co-located in situ radiometric measurements. An analysis of a much larger database from new field measurements may refine the optimization of ϕ and provide a better understanding of the physical basis of this parameter.

Acknowledgements

This project was carried out in part during a visit of the first author to the Laboratoire de Glaciologie et Géophysique de l'Environnement (CNRS/Université Joseph Fourier). The study was funded by the Fond Québécois de la Recherche sur la Nature et les Technologies (FQRNT) through the Global Environmental and Climate Change Centre (GEC3) and the Coopération Permanente de Coopération Franco-Québécoise (CPCFQ). We also thank the National Sciences and Engineering Research Council of Canada (NSERC), Environment Canada – Climate Research Division, and the Canadian Space Agency for their financial support as well as the French Programme National de Télédétection Spatiale. The authors would like to thank the Churchill Northern Studies Centre (CNSC) and the Environment Canada staff that participated in the project for their collaboration and support, J. Lemmetyinen for providing the HUT n-layer model, and the two reviewers who helped in improving the quality of the manuscript.

References

T. Aoki, M. Fukabori, A. Hachikubo, Y. Tachibana, and F. Nishio, "Effects of snow physical parameters on spectral albedo and bidirectional reflectance of snow surface," *Journal of Geophysical Research D: Atmospheres*, vol. 105, no. D8, pp. 10219-10236, Jan., 2000.

L. Arnaud, G. Picard, N. Champollion, F. Domine, J.-C. Gallet, E. Lefebvre, M. Fily and J.M. Barnola, "Measurement of vertical profiles of snow specific surface area with a 1 cm resolution using infrared reflectance: Instrument description and validation," *Journal of Glaciology*, vol. 57, no. 201, pp. 17-29, Feb. 2011.

L. Brucker, G. Picard, L. Arnaud, J.-M. Barnola, M. Schneebeli, and H. Brunjail, "Modeling time series of microwave brightness temperature at dome C, antarctica, using vertically resolved snow temperature and microstructure measurements," *Journal of Glaciology*, vol. 57, no. 201, pp. 171-182, Feb. 2011a.

L. Brucker, A. Royer, G. Picard, A. Langlois, and M. Fily, "Hourly simulations of the microwave brightness temperature of seasonal snow in Quebec, Canada, using a coupled snow evolution-emission model," *Remote Sensing of Environment*, vol. 115, pp. 1966-1977, Aug. 2011b.

L. Brucker, G. Picard, and M. Fily, "Snow grain-size profiles deduced from microwave snow emissivities in Antarctica," *Journal of Glaciology*, vol. 56, no. 197, pp. 514-526, Aug. 2010.

M. Butt, and R. Kelly, "Estimation of snow depth in the UK using the HUT snow emission model," *International Journal of Remote Sensing*, vol. 29, no. 14, pp. 4249-4267, Jul. 2008.

A.T.C. Chang, J.L. Foster, and D.K. Hall "Nimbus-7 SMMR derived global snow cover parameters," *Annals of Glaciology*, vol. 9, pp. 39-44, 1987.

C. Derksen, P. Toose, J. Lemmetyinen, J. Pulliainen, A.Langlois, N. Rutter, and M. Fuller, "Evaluation of passive microwave brightness temperature simulations and snow water equivalent retrievals through a winter season." *Remote Sensing of Environment*, vol. 117, pp. 236–248, Feb. 2012.

C. Derksen, A. Walker, and B. Goodison, "Evaluation of passive microwave snow water equivalent retrievals across the boreal forest-tundra transition of western Canada," *Remote Sensing of Environment*, vol. 96, pp. 315-327, Jun. 2005.

A.J. Dietz, C. Kuenzer, U. Gessner, and S. Dech, "Remote sensing of snow – a review of available methods," *International Journal of Remote Sensing*, vol. 33, no. 13, pp.4094-4134, Jul., 2012.

M.C. Dobson, F.T. Ulaby, M.T. Hallikainen, and M.A. El-Rayes, "Microwave dielectric behavior of wet soil-part II : dielectric mixing models," *IEEE Transanctions on Geoscience and Remote Sensing*. vol. GE-23, no. 1, pp. 35-46, Jan. 1985.

F. Domine, M. Albert, T. Huthwelker, H. Jacobi, A.A Kokhanovsky, Lehning, M., G. Picard and W.R. Simpson, "Snow physics as relevant to snow photochemistry," *Atmospheric Chemistry and Physics*, vol. 8, no. 2, pp. 171–208, Jan., 2008.

F. Domine, A. Cabanes, A. Taillandier, and L. Legagneux, "Specific surface area of snow samples determined by CH4 adsorption at 77 K and estimated by optical microscopy and scanning electron microscopy," *Environmental Science and Technology*, vol. 35, no. 4, pp. 771-780, Feb. 2001.

M. Durand, and D. Liu, "The need for prior information in characterizing snow water equivalent from microwave brightness temperatures," *Remote Sensing of Environment*, vol.126, pp. 248-257, Nov. 2012.

M. Durand, E.J. Kim, and S.A. Margulis, "Radiance assimilation shows promise for snowpack characterization," *Geophysical Research Letters*, vol. 36, L02503, Jan. 2009.

M. Durand, E.J. Kim, and S.A. Margulis, "Quantifying uncertainty in modeling snow microwave radiance for a mountain snowpack at the Point-Scale, including stratigraphic effects," *IEEE Transactions on Geoscience and Remote Sensing*, vol. 46, no. 6, pp. 1753–1767. Jun. 2008.

P. Ferrazzoli, L. Guerriero, and J.-P.Wigneron, "Simulating L-band emission of forests in view of future satellite applications," *IEEE Transactions on Geoscience and Remote Sensing*, vol. 40, no. 12, pp. 2700–2708, Dec. 2002.

C. Fierz, R.L. Armstrong, Y. Durand, P. Etchevers, E. Greene, D.M. McClung, K. Nishimura, P.K. Satyawali, and S.A. Sokratov, *The International Classification for Seasonal Snow on the Ground.* IHP-VII Technical Documents in Hydrology N°83, IACS Contribution N°1, UNESCO-IHP, Paris, 2009.

M.G. Flanner, and C.S Zender, "Linking snowpack microphysics and albedo evolution," *Journal of Geophysical Research*, vol. 111, D12208, Jun. 2006.

J. Gallet, F. Domine, C. Zender, and G. Picard, "Measurement of the specific surface area of snow using infrared reflectance in an integrating sphere at 1310 and 1550 nm," *The Cryosphere*, vol. 3, pp. 167-182, Aug. 2009.

J.P. Grant, A.A. Van de Griend, M. Schwank, and J.-P. Wigneron, "Observations and modeling of a pine forest floor at L-band," *IEEE Transactions on Geoscience and Remote Sensing*, vol. 47, no. 7, Jul. 2009.

T.C. Grenfell, and S.G. Warren, "Representation of a nonspherical ice particle by a collection of independent spheres for scattering and absorption of radiation," *Journal of Geophysical Research*, vol. 104, no. D24, pp. 697–31, Jul. 1999.

N. Grody, "Relationship between snow parameters and microwave satellite measurements: Theory compared with Advanced Microwave Sounding Unit observations from 23 to 150 GHz," *Journal of Geophysical Research*, vol. 113, D22108, Nov. 2008.

M.T. Hallikainen, F.T. Ulaby, and T.E. Van Deventer, "Extinction behavior of dry snow in the 18- to 90- GHz range," *IEEE Transactions on Geoscience and Remote Sensing*, vol. GE-25, no. 6, pp. 737-745, Nov. 1987.

C. Huang, S.A Margulis, M.T. Durand, and K.N. Musselman, "Assessment of snow grain-size model and stratigraphy representation impacts on snow radiance assimilation: forward modeling evaluation," *IEEE Transactions on Geoscience and Remote Sensing*, vol. 50, no. 11, pp. 4551-4564, Nov. 2012.

H.-W. Jacobi, F. Domine, W.R. Simpson, T.A. Douglas, and M. Sturm, "Simulation of the specific surface area of snow using a one-dimensional physical snowpack model: implementation and evaluation for subarctic snow in Alaska," *The Cryosphere*, vol. 4, pp. 35–51, Jan. 2010.

Y. Jin, *Electromagnetic scattering modelling for quantitative remote sensing*. *World Scientific*. 1994.

R.E. Kelly, A.T.C. Chang, L. Tsang, and J.L. Foster, "A prototype AMSR-E global snow area and snow depth algorithm," *IEEE Transactions on Geoscience and Remote Sensing*, vol. 41, no. 2, pp. 230-242, Feb. 2003.

N.P. Klingaman, B. Hanson, and D.J. Leathers, "A teleconnection between forced great plains snow cover and European winter climate," *Journal of Climate*, vol. 21, pp. 2466-2483, Jun. 2008.

A.A Kokhanovsky, and E.P. Zege, "Scattering optics of snow," *Applied Optics*, vol. 43, no. 7, pp. 1589-1602, Mar. 2004.

A. Kontu, and J.T. Pulliainen, "Simulation of spaceborne microwave radiometer measurements of snow cover using in situ data and brightness temperature modeling," *IEEE Transactions on Geoscience and Remote Sensing*, vol. 48, no. 2, pp. 1031-1044, Mar. 2010.

N. Kruopis, J. Parks, A. Arslan, H. Alasalmi, J. Koskinen, and M. Hallikainen, "Passive microwave measurements of snow-covered forest areas in EMAC'95," *IEEE Transactions on Geoscience and Remote Sensing*, vol. 37, no. 5, pp. 2699–2705, Sep. 1999.

A. Langlois, A. Royer, C. Derksen, B. Montpetit, F. Dupont, and K. Goïta, "Coupling of the snow thermodynamic model SNOWPACK with the microwave emission model for layered snowpacks (MEMLS) for subartic and artic snow water equivalent retrievals," *Water Resources Research*, vol. 48, W12524, doi:10.1029/2012WR012133, Dec. 2012.

A. Langlois, A. Royer, F. Dupont, A. Roy, K. Goïta, and G. Picard, "Improved corrections of forest effects on passive microwave satellite remote sensing of snow over boreal and subarctic regions," *IEEE Transactions on Geoscience and Remote Sensing*, vol. 49, no. 10, pp. 3824-3837, Oct. 2011.

A. Langlois, A. Royer, B. Montpetit, G. Picard, L. Brucker, L. Arnaud, P. Harvey-Collard, M. Fily, and K. Goïta, "On the relationship between snow grain morphology and in-situ near infrared calibrated reflectance photographs," *Cold Regions Science and Technology*, vol. 61, pp. 34-42, Apr. 2010.

L. Legagneux, A.-S. Taillander, and F. Domine, "Grain growth theories and the isothermal evolution of the specific surface area of snow," *Journal of Applied Physics*, vol. 95, no. 11, pp. 6176-6184, Jun. 2004.

J. Lemmetyinen, J. Pulliainen, A. Rees, A. Kontu, Y. Qiu, and C. Derksen, "Multiple-layer adaptation of HUT snow emission model : comparison with experimental data," *IEEE Transactions on Geoscience and Remote Sensing*, vol. 48, no. 7, pp. 2781-2794, Jul. 2010.

D. Liang, X. Xu, L. Tsang, K.M. Andreadis and E.G. Josberger, "The effects of layers in dry snow on its passive microwave emissions using dense media radiative transfer theory based on the quasicrystalline approximation (QCA/DMRT)," *IEEE Transactions on Geoscience and Remote Sensing*, vol. 46**,** no. 11, pp. 3663–3671, Nov. 2008.

D. Liang, K. Tse, Y. Tan, L. Tsang and K.H. Ding, "Scattering and emission in snow based on QCA/DMRT and numerical Maxwell model of 3Dimensional simulations (NMM3D)," *In Proceedings of the IEEE 9th Specialist Meeting on Microwave Radiometry and Remote Sensing of the Environment (MicroRad 2006), 28 February–3 March 2006, San Juan, Puerto Rico*, Piscataway, NJ, Institute of Electrical and Electronics Engineers, pp. 197–202, 2006.

G. Macelloni, S. Paloscia, P. Pampaloni and M. Tedesco, "Microwave emission from dry snow: a comparison of experimental and model results," *IEEE Transactions on Geoscience and Remote Sensing*, vol. 39, no. 12, pp. 2649–2656, Dec. 2001.

C. Mätzler, "Relation between grain-size and correlation length of snow," *Journal of Glaciology*, vol. 48, no. 162, pp. 461-466, Jun. 2002.

C. Mätzler and U. Wëgmuller, "Dielectric properties of fresh-water ice at microwave frequencies," *Journal of Physics D: Applied Physics*, vol. 20, pp. 1623-1630, Dec. 1987.

V.L. Mironov, R.D. De Roo, and I.G. Savin, "Temperature-dependable microwave dielectric model for an artic soil". *IEEE Transactions on geoscience and Remote Sensing*, vol. 48, no. 6. pp. 2544-2556, Jun. 2010.

B. Montpetit, A. Royer, A. Langlois, P. Cliche, A. Roy, N. Champollion, G. Picard, F. Domine, R. Obbard, " New short wave infrared albedo measurements for snow specific surface area retrieval," *Journal of Glaciology*, vol. 58, no. 211, Sep. 2012.

B. Montpetit, A. Royer, A. Roy, A. Langlois, and C. Derksen, "Snow microwave emission modeling of ice lenses within the snowpack using the microwave emission model for layered snowpacks (MEMLS)," *IEEE Transactions on Geoscience and Remote Sensing*, available online, doi:10.1109/TGRS.2013.2250509 .

S. Morin, F. Domine, A. Dufour, B. Lejeune, B. Lesaffre, J.-M. Willemet, C.M. Carmagnola, H.-W. Jacobi, "Measurements and modeling of the vertical profile of specific surface area of an alpine snowpack," *Advances in Water Resources*, vol. 55, pp. 111-120, doi:10.1016/j.advwatres.2012.01.010, Jan. 2013.

M. Pardé, K. Goïta, A. Royer, "Inversion of a passive microwave snow emission model for water equivalent estimation using airborne and satellite data," *Remote Sensing of Environment*, vol. 111, pp. 346-356, Nov. 2007.

G. Picard, F. Domine, G. Krinner, L. Arnaud, and E. Lefebvre, "Inhibition of the positive snow-albedo feedback by precipitation in interior Antartica," *Nature Climate Change*, vol. 2, pp.795-798, Jul. 2012.

G. Picard, L. Brucker, A. Roy, F. Dupont, M. Fily, A. Royer, C. Harlow, "Simulation of the microwave emission of multi-layered snowpacks using dense media radiative transfer theory: the DMRT-ML model", *Geoscientific Model Development*, vol. 6, pp.1061-1078, Jul. 2013.

J. Pulliainen, “Mapping of snow water equivalent and snow depth in boreal and sub-arctic zones by assimilating space-borne microwave radiometer data and ground-base observations,” *Remote Sens. Environ.*, vol. 101, pp. 257–269, 2006.

J.T. Pulliainen, J. Grandell, and M.T. Hallikainen, “HUT snow emission model and its applicability to snow water equivalent retrieval,” *IEEE Transactions on Geoscience and Remote Sensing*, vol. 37, no. 3, pp. 1378-1390, May 1999.

A. Rees, J. Lemmetyinen, C. Derksen, J.T. Pulliainen, and M. English, “Observed and modelled effects of ice lens formation on passive microwave brightness temperatures over snow covered tundra,” *Remote Sensing of Environment*, vol. 114, pp. 116-126, Jan. 2010.

S. Rosenfeld, and N. Grody, “Anomalous microwave spectra of snow cover observed from Special Sensor Microwave/Imager measurements”, *Journal Geophysical Research*, vol. 105, no. D11, pp. 14913–14925, Jun. 2000.

A. Roy, A. Royer, R. Turcotte, ”Improvement of springtime streamflow simulations in a boreal environment by incorporating snow-covered area derived from remote sensing data,” *Journal of Hydrology*, vol. 390, pp. 35-44, Aug. 2010.

A. Roy, A. Royer, J.-P. Wigneron, A. Langlois, J. Bergeron, P.Cliche, ”A simple parameterization for a boreal forest radiative transfer model at microwave frequencies,” *Remote Sensing of Environment*, vol. 124, pp. 371-383, Sep. 2012.

V. Roy, K. Goïta, A. Royer, A.E. Walker, and B.E. Goodison, “Snow water equivalent retrieval in a Canadian boreal environment from microwave measurements using the HUT snow emission model,” *IEEE Transactions on Geoscience and Remote Sensing*, vol. 42, no. 9, pp. 1850-1859, Sep. 2004.

K. Saleh, J.-P. Wigneron, P. de Rosnay, J.-C. Calvet, M.-J. Escorihuela, Y. H. Kerr, and P. Waldteufel, “Impact of rain interception by vegetation and mulch on the L-band emission of natural grass,” *Remote Sensing of Environment*, vol. 101, no. 1, pp. 127–139, Mar. 2006.

T. J. Schmugge, J. R. Wang, and G. Asrar, “Results from the push broom microwave radiometer flights over the Konza Prairie in 1985,” *IEEE Transactions on Geoscience and Remote Sensing*, vol. 26, no. 5, pp. 590–596, Sep. 1998.

P.R. Singh, and T.Y. Gan, “Retrieval of snow water equivalent using passive microwave brightness temperature data,” *Remote Sensing Environment*, vol. 74, no. 2, pp. 275–286, Nov. 2000.

A.-S. Taillandier, F. Domine, W.R. Simpson, M. Sturm, and T.A Douglas, “Rate of decrease of the specific surface area of dry snow : Isothermal and temperature gradient conditions,” *Journal of Geophysical Research*, vol. 112, F03003, Jul. 2007.

M. Takala, K. Luojus, J. Pulliainen, C. Derksen, J. Lemmetyinen, J-P Kärnä, and J. Koskinen, ”Estimating northern hemisphere snow water equivalent for climate research through assimilation of space-borne radiometer data and ground-based measurements”, *Remote Sensing of Environment*, vol. 115, no.12, pp. 3517-3529, Dec. 2011.

M. Tedesco, and E.J. Kim, “Intercomparison of electromagnetic models for passive microwave remote sensing of snow,” *IEEE Transactions on Geoscience and Remote Sensing*, vol. 44, no. 10, pp. 2654–2666, Oct. 2006.

A.M. Toure, K. Goïta, A. Royer, E.J. Kim, M. Durand, S.A. Margulis, and H. Lu, “A case study of using a multilayered thermodynamical snow model for radiance assimilation,” *IEEE Transactions on Geoscience and Remote Sensing*, vol. 49, no. 8, pp. 2828-2837, Aug. 2011.

A.M. Toure, K. Goïta, A. Royer, C. Mätzler and M. Schneebeli, “Near-infrared digital photography to estimate snow correlation length for microwave emission modeling,” *Applied Optics*, vol. 47, no. 36, pp. 6723–6733, Dec. 2008.

L. Tsang, J.A. Kong, K.-H. Ding, and C.O. Ao, *Scattering of electromagnetic waves: numerical simulations*. New York, Wiley, 2001.

L. Tsang, and J.A. Kong, *Scattering of electromagnetic waves: advanced topics*. New York, Wiley, 2001.

L. Tsang, C.-T. Chen, A.T.C. Chang, J. Guo, and K.-H. Ding, “Dense media radiative transfer theory based on quasicrystalline approximation with application to passive microwave remote sensing of new snow,” *Radio Science*, vol. 35, no. 3, pp. 731–749, Jan. 2000.

L. Tsang, D. Liang, X. Xu, and P. Xu. “Microwave emission from snowpacks: modeling the effects of volume scattering, surface scattering and layering,” *In Proceedings of 10th Specialist Meeting on Microwave Radiometry and Remote Sensing of the Environment (MicroRad 2008),* Firenze,Italy, Mar. 11-14, 2008, pp.1-4.

R. Turcotte, L.G. Fortin, V. Fortin, J.P. Fortin, and J.P. Villeneuve, “Operational analysis of spatial distribution and the temporal evolution of the snowpack water equivalent in southern Québec, Canada,” *Nordic Hydrology*, vol. 38, pp. 211-234, 2007.

F. Vachon, K. Goïta, D. De Sève, and A. Royer, “Geophysical inversion of a physical-based model combined with *in situ* data assimilation for snow water equivalent monitoring,” *IEEE Transactions on Geoscience and Remote Sensing*, vol. 48, no. 1, pp. 59-71, Jan. 2010.

S. Vavrus, “The role of terrestrial snow cover in the climate system,” *Climate dynamic*, vol. 29, pp. 73-88, Feb. 2007.

A. Walker, “Snow cover variations over the Mackenzie river basin from SSM/I passive 37 microwave satellite data,” *Annals of Glaciology*, vol. 34, pp. 8-14, 2002.

U. Wegmüller and C. Mätzler, “Rough bare soil reflectivity model,” *IEEE Transactions on Geoscience and Remote Sensing*, vol. 37, no. 3, May 1999.

R.L. West, L. Tsang, and P. Winebrenner, "Dense medium radiative transfer theory for two scattering layers with a Rayleigh distribution of particle sizes," *IEEE Transactions on Geoscience and Remote Sensing*, vol. 31, no. 2, pp. 426–437, Mar. 1993.

A. Wiesmann, and C. Mätzler, "Microwave Emission Model of Layered Snowpacks," *Remote Sensing of Environment*, vol. 70, pp. 307-316, Dec. 1999.

3.8 Discussion

Le travail démontre qu'il est possible d'utiliser la SSA comme métrique dans DMRT-ML. Par contre, un facteur ϕ doit être appliqué afin de ne pas sous-estimer l'atténuation de la neige. Il a été démontré qu'un facteur fixe de $\phi = 3.3$ permet de bien représenter l'effet de la taille des grains pour des neiges saisonnières. En effet, dans le cadre de l'étude, le $\phi = 3.3$ permet d'optimiser les simulations sur un ensemble de snowpits (20) avec des types de neige saisonnière différents (spatialement et temporellement). La nécessité de ce facteur pourrait être due à la distribution des grains de neige qui n'est pas monodisperse dans le couvert nival (pas toutes des sphères de mêmes dimensions), ainsi qu'à l'adhésion entre les particules (*stickiness*) qui fait en sorte que la taille de grains effective augmente. Les résultats motivent aussi l'utilisation de DMRT-ML au lieu de HUT n-layer, étant donné que HUT semble sous-estimer l'atténuation en présence de givre de profondeur.

Comme CLASS est un modèle de neige à une couche, il est aussi nécessaire de vérifier le comportement de DMRT-ML avec une seule couche de neige (densité et R_{opt} moyens pondérés par la hauteur de chaque couche de neige). La même méthodologie que dans l'article du présent chapitre (voir Sect. 3.4.2) a été effectuée, mais considérant une couche de neige. Le tableau 3.5 montre ainsi que le même $\phi = 3.3$ est retrouvé avec DMRT-ML à une couche avec des RMSEs légèrement plus élevés (0.5 K). Aussi, en utilisant une couche, l'approche de Kontu & Pulliainen (2010) donne une RMSE moyenne de 11.5 K, presque 2 K plus bas que DMRT-ML multicouche. Sans confirmer ni affirmer que l'une ou l'autre des méthodes est meilleure, ces résultats semblent démontrer qu'un modèle à une couche permet de bien représenter l'émissivité micro-onde d'un couvert nival. Dans le cadre du couplage, le modèle de neige à une couche de CLASS devrait permettre de bien simuler l'émission micro-onde de la neige.

Tableau 3.5: RMSE pour différentes configurations du modèle DMRT-ML (dont à 1 couche).

	37V	**37H**	**19V**	**19H**	**Mean RMSE**
DMRT-ML (ϕ=3.3)	15.9	17.9	7.6	11.7	13.3
DMRT-ML (Kontu : 1.1-8.2)	15.6	13.0	8.2	11.9	12.2
DMRT-ML (ϕ_{sticky}=2.6 ; τ_s=0.44)	14.5	16.0	7.9	10.8	12.3
DMRT-ML (ϕ=2.4 ; Rayleigh)	14.3	16.2	7.6	11.2	12.3
DMRT 1-layer (ϕ=3.3)	17.1	17.5	7.9	12.6	13.8
DMRT 1-layer (Kontu : 1.3-4.7)	13.3	12.3	7.9	12.3	**11.5**

L'étude s'inscrit aussi dans le cadre d'un effort pour mieux comprendre le rôle de la taille de grains dans les MSEMs. Le tableau 3.6 montre les différentes valeurs de ϕ obtenues avec différents modèles et différents types de neige. Un fait intéressant est la similitude du ϕ retrouvé pour une neige saisonnière sur la calotte glaciaire Barnes (Dupont et al., 2013). Comme discuté dans l'article, le type de neige différent retrouvé en Antarctique peut expliquer les différences plus importantes. Les variations peuvent aussi être reliées à l'instrument servant à mesurer la SSA. Dans le cas de MEMLS, en utilisant exactement la même base de données que dans l'article ci-dessus, une valeur ϕ =1.3 a été obtenue (Montpetit et al., 2013). Cette valeur, beaucoup plus près de l'unité, peut s'expliquer par le fait que MEMLS utilise la longueur de corrélation (calculée à partir de la taille de grains et de la fraction de glace de la neige).

Tableau 3.6: Synthèse de différentes valeurs de ϕ pour différents MSEMs et différents types de neige.

MSEM	**Sites**	**Instrument**	ϕ	**Références**
MEMLS	Canada: Arctique, Subarctique, Sud du Québec	IRIS SWIRcam DUFISSS	1.3	Montpetit et al. (2013)
DMRT-ML	Dome C Antarctique	IR photos	2.8	Brucker et al. (2011)
	Dome C Antarctique	POSSSUM	2.3	Picard et al. (2013b)
	Calotte glaciaire Barnes, Arctique Canadien	IRIS POSSSUM	3.5	Dupont et al. (2013)
	Canada: Arctique, Subarctique, Sud du Québec	IRIS DUFISSS	3.3	Roy et al. (2013a)
HUT n-layer	Canada: Arctique, Subarctique, Sud du Québec	IRIS DUFISSS	3.7	Roy et al. (2013a)

- POSSSUM: Profiler Of Snow Specific Surface area Using SWIR reflectance Measurement (Arnaud et al., 2011)
- SWIRcam: Short-wave InfraRed camera (Montpetit et al., 2013)

Dans la suite du travail, le modèle DMRT-ML à une couche est utilisé. Étant donné qu'une taille de grains simulée par un modèle de neige (modèle CLASS-SSA, Chap.4) sera utilisée, il apparait que le facteur de correction ϕ pourrait différer de celui correspondant aux mesures (tableau 3.5).

Chapitre 4: Snow Specific Surface area Simulation Using the One-layer Snow Model in the Canadian Land Surface Scheme (CLASS)

« Simulation de la Surface Spécifique de la Neige avec le Modèle de Neige à une Couche de CLASS »

Auteurs : Roy, A., Royer, A., Montpetit, B., Bartlett, P. A., Langlois, A.

Article publié dans le Journal *The Cryosphere* (2013), vol.7, p.961-975.

Résumé:
La taille de grains est un paramètre clé pour modéliser l'émission micro-onde ainsi que le bilan de surface d'énergie à cause de son influence sur l'albédo de la neige et sur la conductivité et la diffusivité thermique. Un modèle de SSA est implémenté dans le modèle de neige à une couche de CLASS. En condition sèche, ce modèle multicouche « *offline* » (CLASS-SSA) simule la diminution de la SSA en se basant sur l'âge de la neige, la température de la neige et le gradient de température, tandis qu'en condition humide, il considère la teneur en eau liquide (LWC) dans le couvert nival pour simuler le métamorphisme humide. Les simulations du modèle ont été comparées avec des mesures in situ obtenues sur différents sites (alpin, arctique et subarctique) constitués de différents types de neige. Les SSA modélisés offrent une bonne similitude par rapport aux mesures, avec des RMSE de 8.0 m^2 kg^{-1} en comparant chacun des points entre eux et une RMSE de 5.1 m^2 kg^{-1} pour les valeurs moyennes (pondérées à la hauteur des couches) de SSA dans le couvert nival. Le modèle reste néanmoins limité en condition de neige humide, car l'aspect une couche du modèle CLASS donne seulement une valeur intégrée d'eau liquide dans la neige. Ces simulations de SSA sont d'un grand intérêt pour l'assimilation de T_B micro-ondes passives ainsi que pour l'étude des bilans d'énergie et de masse et leur rétroaction sur le climat.

Mots clés: Taille des grains de neige, CLASS, métamorphisme de la neige.

4.1 Présentation de l'article

Comme mentionné précédemment, étant donné que la taille de grains est une variable clé dans l'émission micro-onde du couver nival, il est nécessaire d'inclure un module de métamorphisme

des grains de neige dans CLASS afin de permettre le couplage entre DMRT-ML et CLASS. Cette implémentation n'est par contre pas directe dans le cas d'un modèle à une couche, étant donné que les processus affectant l'évolution de la SSA créent une stratification des couches de neige. L'étude développe ainsi un modèle de SSA « *offline* » dans CLASS (CLASS-SSA) sans rien changer au modèle CLASS. Le modèle CLASS-SSA est ainsi contrôlé par les sorties de SWE, de densité de la neige et de hauteur de la neige de CLASS et garde toujours les caractéristiques moyennes (1 couche) de CLASS. Une telle approche simplifie grandement le problème par rapport à l'ajout d'un modèle complet multicouche dans CLASS, étant donné que seulement la SSA est calculée et que tous les bilans d'énergies et de masse restent intouchés. Il y a donc une forte simplification en termes d'implémentation, mais aussi en termes de validation. De plus, les principaux modèles climatiques et météorologiques Canadiens ne devraient pas migrer vers des modèles de neige multicouches dans un avenir rapproché (Bélair, communication personnelle). Étant donné que les erreurs issues des simulations de neige sont souvent reliées davantage aux données entrantes (précipitations), un modèle multicouche plus complexe n'apporterait pas nécessairement de meilleurs résultats. L'une des limites de CLASS-SSA est le métamorphisme lors de conditions en neige humide. Cette faiblesse a par contre été constatée principalement sur le site de Col de Porte en milieu alpin, où les conditions de neige humide sont particulièrement importantes. Les températures moyennes de janvier y sont beaucoup plus élevées (-1.63°C) qu'en forêt boréale (-18.7°C) où les événements de neige mouillée sont plus isolés et plus courts.

L'implémentation d'un module de calcul de la SSA dans CLASS (CLASS-SSA) permet ainsi de pouvoir alimenter DMRT-ML de tous les paramètres nécessaires (dont l'évolution de la taille de grains au cours d'un hiver) afin de simuler les T_B d'un couvert nival. L'étude permet aussi de bien connaître les incertitudes reliées au modèle et les limites associées. Il a par contre été démontré que les simulations de SSA montrent un biais par rapport aux mesures. Ainsi, il faudra vérifier l'ajustement du facteur de correction à appliquer sur les SSA (ϕ) qui pourrait être différent de ceux trouvés au Chap. 3 dans le cadre du couplage entre CLASS-SSA et DMRT-ML en forêt boréale.

Les intérêts d'une telle approche sont nombreux. En effet, la microstructure de la neige influence aussi l'albédo de la neige ainsi que la conductivité thermique de la neige. Sachant la grande sensibilité des modèles à l'albédo de la neige (Langlois et al., 2013; Wang et al., submitted),

Ouranos et Environnement Canada sont intéressés à paramétriser l'albédo de la neige de leur modèle à 1 couche à partir de SSA simulées .

Snow specific surface area simulation using the one-layer snow model in the Canadian LAnd Surface Scheme (CLASS)

A. Roy[a*],
A. Royer[a],
B. Montpetit[a],
P. A. Bartlett[b],
A. Langlois[a]

[a] Centre d'Applications et de Recherches en Télédétection (CARTEL), Université de Sherbrooke, 2500 boul. Université, Sherbrooke, QC, Canada, J1K 2R1.

[b] Climate Processes Section, Environment Canada, Toronto, ON, Canada

Abstract

Snow grain size is a key parameter for modeling microwave snow emission properties and the surface energy balance because of its influence on the snow albedo, thermal conductivity and diffusivity. A model of the specific surface area (SSA) of snow was implemented in the one-layer snow model in the Canadian LAnd Surface Scheme (CLASS) version 3.4. This offline multilayer model (CLASS-SSA) simulates the decrease of SSA based on snow age, snow temperature and the temperature gradient under dry snow conditions, while it considers the liquid water content of the snowpack for wet snow metamorphism. We compare the model with ground-based measurements from several sites (alpine, arctic and subarctic) with different types of snow. The model provides simulated SSA in good agreement with measurements with an overall point-to-point comparison root mean square error (RMSE) of 8.0 m^2 kg^{-1}, and a RMSE of 5.1 m^2 kg^{-1} for the snowpack average SSA. The model, however, is limited under wet conditions due to the single-layer nature of the CLASS model, leading to a single liquid water content value for the whole snowpack. The SSA simulations are of great interest for satellite passive microwave brightness temperature assimilations, snow mass balance retrievals and surface energy balance calculations with associated climate feedbacks.

Keywords: Snow grain size, CLASS, snow metamorphism.

4.2 Introduction

Snow grain size is of particular interest for microwave snow emission models, the surface energy balance (albedo and turbulent fluxes) and atmospheric-snow chemistry interactions (Domine et al., 2008). At high microwave frequencies (generally measured at 19 GHz and 37 GHz), snow grain size is an important variable affecting snowpack extinction and scattering properties (Kontu and Pulliainen, 2010; Grody, 2008; Durand et al., 2008; Roy et al., 2004). Thus, snow grain size must be considered in microwave snow emission models (MSEM) for the retrieval of snow properties from satellite passive microwave observations (Langlois et al., 2012; Huang et al., 2012; Pardé et al., 2007). Hence, in passive microwave applications, prior information such as snow grain size from a snowpack physical model is required for snow water equivalent (SWE) estimates (Durand and Liu, 2012). The surface albedo is also sensitive to the snow grain size and its vertical profile (Wiscombe and Warren 1980; Jin et al., 2008; Lyapustin et al., 2009, Aoki et al., 2011). Gardner and Sharp (2010) found that the broadband albedos of snowpacks show a logarithmic relationship with specific surface area (SSA). The thermal properties of snow, such as snow conductivity and diffusivity, are also related to snow microstructure (Domine et al., 2008; Adams and Sato, 1993). Surface albedo and snow conductivity are thus key parameters for modeling the surface energy balance in order to understand the impact of snow cover on global and regional climate dynamics (Armstrong and Brun, 2008). They also have a major impact on the prediction of the snow water equivalent as well as the timing of melt onset (Franz et al., 2010).

However, many snow evolution models do not take into account snow grain size. The Canadian LAnd Surface Scheme (CLASS : Verseghy 1991; Verseghy et al., 1993) is used in the Canadian global circulation models (Scinocca et al., 2008) and the Canadian Regional Climate Model (CRCM: Music and Caya, 2007; Caya and Laprise, 1999); it includes a one-layer snow model which does not simulate snow grain metamorphism. This is a major limitation for the assimilation of passive microwave brightness temperature (T_B) data for the improvement of snow simulations. In the context of data assimilation, where physical and emission models of snow are coupled, estimates of snow grain size are needed (Durand et al., 2009; Toure et al., 2011; Langlois et al., 2012). The implementation of snow grain metamorphism within CLASS is thus of particular interest for assimilation purposes. This implementation is not, however, straightforward in a one-layer snow model because snow metamorphism depends on many

variables, such as snow age and the temperature gradient, which lead to a stratification of snow layers with different grain sizes. Thus, a major difficulty is that the vertical stratification is not considered in single-layer physical snow models. This study aims to address this issue, as simply as possible, using the CLASS one-layer snow evolution model. Even if one layer snow models are less physically correct then multi-layered models (Brun et al., 1992; Bartlelt et al., 2002; Bougamont et al., 2005, Ettema et al., 2010, Niwano et al., 2012), the SnowMIP experiments have shown that CLASS performs relatively well (Brown et al. 2006; Rutter et al., 2009). Furthermore, in climate and meteorological models, the errors in snow simulations are often related to the precipitation inputs. Hence, in these contexts, a more complex multi-layer model would not necessarily produce better results.

Grain size is a parameter that is difficult to characterize accurately and measure in the field. The specific surface area (SSA), which represents the ratio of the surface area per unit of mass, is a well-defined parameter representing the geometric characteristics of a porous medium, such as snow (Dominé et al., 2001). Methods based on snow reflectance in the shortwave infrared (SWIR) can now provide rapid and reproducible field measurements of SSA (Gallet et al., 2009; Arnaud et al., 2011; Montpetit et al., 2012), which can be related theoretically, to grain size. SSA can be related to the radius of a monodisperse collection of ice spheres, each having the same surface area to volume ratio, called the optical radius (R_{opt}):

$$R_{opt} = \frac{3}{\rho_{ice} SSA} \tag{4.1}$$

Recent studies have shown that SSA offers a reliable representation of snow grain size in the context of microwave snow emission modeling (MSEM) (Roy et al., 2013, Montpetit et al., 2013, Brucker et al., 2011). These studies showed that a scaling factor on R_{opt} derived from SSA is required to simulate brightness temperatures in order to palliate oversimplification of snow grain representation in models. From a good representation of snow grain size in the snowpack for microwave emission simulations, it is possible to determinate which part of the signal is attributable to snow grain and which is attributable to other snow characteristic of interest like SWE.

Considering the importance of snow grain size and the advances made in snow microstructure characterization with the SSA metric, many studies have developed approaches to model the evolution of SSA throughout the winter season. Cabanes et al. (2003) first proposed an empirical exponential decay function of time and temperature for snow SSA. Legagneux et al. (2003) show, using laboratory experiments under isothermal conditions, that the decreasing trend of SSA was best fitted using a logarithmic function. That trend is also confirmed with X-ray microtomography measurements (Flin et al., 2004; Kaempfer and Schneebeli, 2007; Chen and Baker, 2010). Taillandier et al. (2007), using methane adsorption SSA measurements (Domine et al., 2001) in a taiga environment, proposed empirical relationships for the decrease of SSA as a function of time based on the snow age, snow temperature and the temperature gradient within the snowpack. A similar approach relating SSA to snow type (fresh snow, recognizable particles, aged and rounded crystals, aged and faceted crystals, and depth hoar) and snow density was developed by Domine et al. (2007). Jacobi et al. (2010) implemented these last two approaches in the Crocus multi-layer snow model (Brun et al., 1992). With the model based on snow type and density (Domine et al., 2007), SSA was overestimated in surface snow, but this was mainly because Crocus underestimated density, as this model does not take into account the upward water vapor flux induced by the large temperature gradient in the subarctic snowpack (Taillandier et al., 2006); however, a generally good agreement between SSA simulations and measurements (methane adsorption) was observed when the SSA was calculated based on prognostic equations using snow age (Taillandier et al., 2007). Flanner and Zender (2006) developed a physically-based model to predict the evolution of dry snow SSA. The model considers the snow temperature, temperature gradient and snow density and uses two adjustable parameters for the distribution of crystal sizes and for the irregularity in particle spacing. A weakness of most of these previous approaches is that the wet snow metamorphism is not taken into account, whereas water within the snowpack leads to a drastic decrease of SSA (wet snow metamorphism) due to rapid rounding and an increase in the size of snow grains (Brun, 1989). However, Flanner et al. (2007) did implement wet snow metamorphism following Brun (1989) in the model of Flanner and Zender (2006). Note that wind can also have complex effect on snow grains, by enhancing the rate of SSA decrease (Cabanes et al., 2003) or on the contrary, lead to an increase in SSA (Domine et al., 2009). Morin et al. (2013) compared SSA deduced from the R_{opt} values simulated by Crocus with SSA measured from SWIR reflectance (Gallet et al., 2009) in an alpine environment. They showed qualitative agreement between measured and simulated SSA and that

its simulation is difficult under wet snow conditions mostly because of the difficulty in simulating adequately the vertical profile of liquid water content in the snowpack.

The main objective of this study is to evaluate an offline SSA model implemented in the one-layer CLASS snow model for different northern climate environments. More specifically, the SSA model is a multi-layer snow model driven by CLASS outputs to simulate the evolution of SSA in the different snow layers. The evolution of SSA is computed using the model of Taillandier et al. (2007) based on snow aging, for dry snow, and the equation of Brun (1989) for wet snow metamorphism. The simulated SSA values are compared with measured SSA derived from SWIR reflectance (Montpetit et al., 2012 ; Gallet et al., 2009) for five different sites (two northern mid-latitude, Arctic tundra, taiga and Alpine) throughout the winter season. The model is developed in a perspective of passive microwave applications for SWE retrievals at a large scale, but could be used for other applications such as snow albedo estimates. The study also provides an additional validation of the Taillandier et al. (2007) equations using new sets of accurate in situ SSA measurements for different environments.

4.3 Method

4.3.1 CLASS-SSA model

The CLASS-SSA model operates in an "offline" mode, meaning that it uses the CLASS simulated state variables to simulate the SSA evolution, without feedback on the snowpack evolution. The CLASS snow model is a one-layer model (a detailed description of the snow model in CLASS is given in Bartlett et al., 2006 and Brown et al., 2006). Version 3.4 of the stand-alone driver for CLASS (Verseghy, 2009), which allows running the model using meteorological data, was used in this study. CLASS has been designed to run at a time step of 30 minutes or less, to ensure numerical stability of the modeled prognostic variables (Verseghy, 2009). In this study, CLASS is run at a time step of 30 minutes. In our case, the meteorological data used to drive the CLASS model (precipitation rate, air temperature, wind speed, air humidity, and incoming shortwave and longwave radiation) were derived from in situ measurements or from the North American Regional Reanalysis (NARR) data (Mesinger et al., 2006) (more details on driving data are provided in Sect. 4.3.2). The use of NARR data is motivated by the necessity to run the model at a large scale in the perspective of passive

microwave space-borne applications. The thermal conductivity of snow was calculated from snow density using the empirical relationship described in Sturm et al. (1997).

The offline SSA model is a multilayer model, where layer evolution is constrained by snow density, snow depth and SWE from CLASS simulations. Figure 4.1 shows the flowchart of CLASS-SSA. The SSA evolution of dry snow is based on the logarithmic relationship for snow aging developed by Taillandier et al. (2007). The CLASS-SSA model adds snow layers when snowfall occurs. Consecutive precipitation (precipitation occurring during two or more consecutive time steps) is however considered as one precipitation event and contributes to the same layer. The initial SSA ($SSA_{initial}$) was set to 73.0 m^2 kg^{-1} (the mean SSA value for fresh snow measured by Domine et al., 2007: the $SSA_{initial}$ value is discussed in Sect. 4.5), and the density of each new snow layer was set to the fresh snow density calculated by CLASS (Hedstrom and Pomeroy, 1998). However, because we want the CLASS-SSA model to be coherent with the CLASS snow model, the snow parameters (SWE, snow depth and snow density) of the CLASS-SSA model are corrected during the snowpack evolution in order to match the corresponding values simulated by CLASS. Thus, prior to each time step, a correction factor is applied to the SWE value of every snow layer to fit the multilayer model SWE with the CLASS simulation. A densification routine is then implemented, mostly to estimate the position and thickness of each layer within the snowpack. The same densification model as the one used in CLASS (Bartlett et al., 2006) is applied to every layer. After compaction is applied to each layer, if the summed multilayer snow depth is lower than the snow depth simulated by CLASS, a correction factor is applied to the thickness of the top snow layer so that the summed multilayer snow depth corresponds to the snow depth simulated by CLASS (figure 4.1). However, in this context, the top layer cannot be less than 100 kg m^{-3}. If it reaches 100 kg m^{-3}, densification is applied to the second layer and so on. In this case, the correction is applied only to the top layers to avoid an unrealistic thickening of the dense bottom layers. On the other hand, if the sum of the snow depths for all the layers is higher than the snow depth simulated by CLASS, a correction is applied to all the layers, but the density of any layer cannot exceed the maximum snow density estimated by CLASS. Thus, when the snowpack melts, the density of every layer increases due to the decreasing thickness, leading to wet densification.

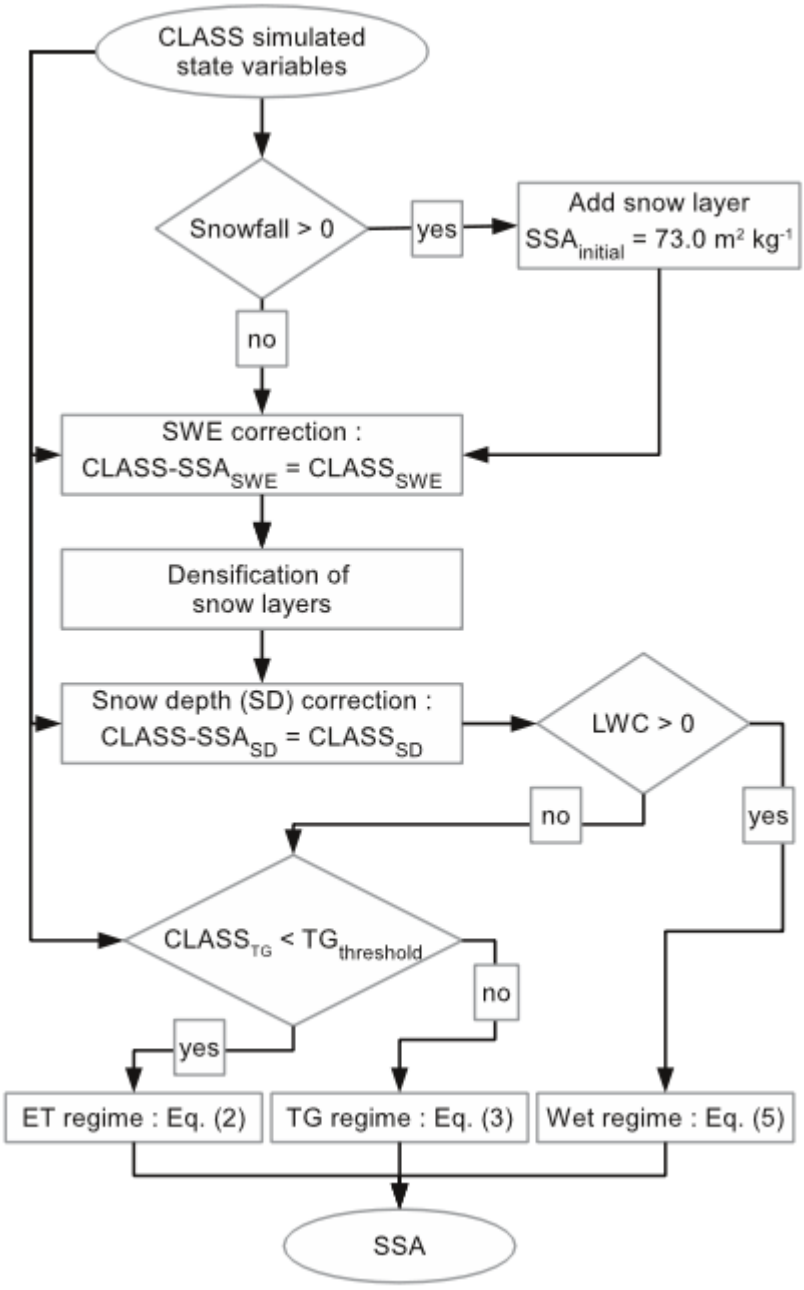

Figure 4.1: CLASS-SSA model flow chart.

The SSA evolution for each snow layer is then calculated considering the model of Taillandier et al., (2007) (figure 4.1). The model parameterizations for SSA evolution are based on snow age and snow temperature (T_{snow}). Two algorithms are available, depending on the temperature gradient regime: one for equi-temperature (ET) metamorphism,

$$SSA(t) = [0.629 \cdot SSA_{initial} - 15.0 \cdot (T_{snow} - 11.2)] - [0.076 \cdot SSA_{initial} - 1.76 \cdot (T_{snow} - 2.96)] \cdot \ln\{t + e^{\frac{-0.371*SSA_{initial} - 15.0*(T_{snow} - 11.2)}{0.076*SSA_{initial} - 1.76*(T_{snow} - 2.96)}}\} \quad (4.2)$$

and the other for strong temperature gradient (TG) metamorphism;

$$SSA(t) = [0.659 \cdot SSA_{initial} - 27.2 \cdot (T_{snow} - 2.03)] - [0.0961 \cdot SSA_{initial} - 3.44 \cdot (T_{snow} + 1.90)] \cdot \ln\{t + e^{\frac{-0.341*SSA_{initial} - 27.2*(T_{snow} - 2.03)}{0.0961*SSA_{initial} - 3.44*(T_{snow} + 1.900)}}\} \quad (4.3)$$

where t is the age of the snow layer in hours. Note that in eq. 4.2 and 4.3, SSA is in $cm^2\ g^{-1}$. T_{snow} is the snow layer temperature (°C) calculated by linearly interpolating the air temperature and the CLASS simulated snow-soil interface temperature. Air temperature appears more accurate and representative than the surface (skin) temperature for estimating the snowpack temperature gradient. Figure 4.2 shows a rapid decrease in the SSA over the first few days, which is related to destructive metamorphism when snow crystals lose most of their complicated shape and break up into smaller grains with less total surface area (Sommerfeld and Lachapelle 1970). This metamorphic process is faster in warmer snow (higher T_{snow}) (Colbeck, 1983). After a few days, the decrease in SSA slows down earlier in the ET regime when compared with the TG regime. The process of constructive metamorphism is dominant when the temperature gradient induces water vapor transport from warm to cold temperatures causing rapid grain growth from vapor deposition at the bottom of the snow grains (Colbeck, 1983). Hence, in the absence of that mechanism in ET conditions, the decrease in SSA slows and SSA rapidly reaches its minimum value.

According to eq. 4.2 and eq. 4.3 the rate of SSA decrease for a given time step (ΔSSA) depends on snow age, snow temperature, temperature gradient and $SSA_{initial}$. Based on Jacobi et al. (2010), we calculate the ΔSSA from eq. 4.2 and 4.3 according to:

$$\Delta SSA = SSA(t + \Delta t) - SSA(t) \quad (4.4)$$

where Δt corresponds to the time step (0.5 hours). The ΔSSA is then subtracted from the model's previous SSA value. Jacobi et al. (2010) used a temperature gradient threshold ($TG_{threshold}$) of 15 K m^{-1} to distinguish between ET and TG conditions, which will be evaluated in this study. Taillandier et al. (2007) also suggested a minimum value for SSA, because the logarithmic equation for SSA can lead to unrealistic low values. The minimal SSA value is set to 8.0 m^2 kg^{-1}, as proposed by Taillandier et al., (2007).

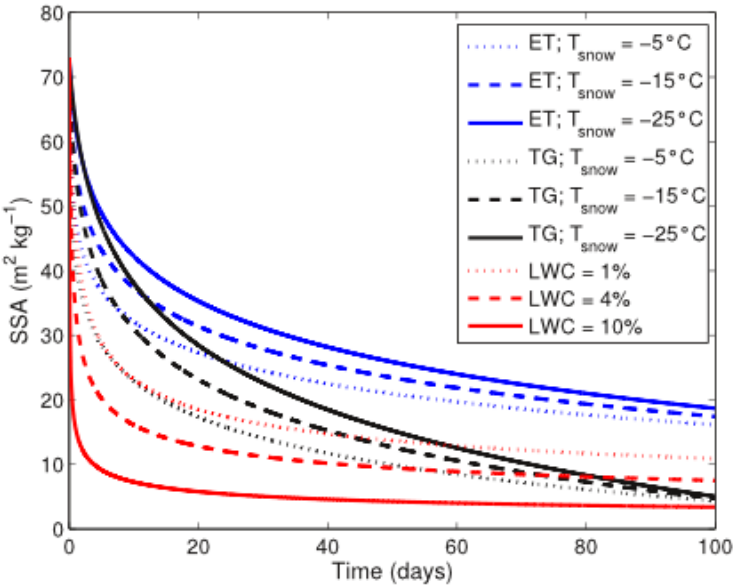

Figure 4.2: **SSA evolution as a function of the temperature gradient regime (ET or TG with LWC=0) and snow temperature (T_{snow}) from eqs. 4.2 and 4.3, as well as a function of liquid water content (LWC) from eq. 4.5.**

Nevertheless, the parameterization reported by Taillandier et al. (2007) does not take into account metamorphism during wet snow conditions. The equation of Brun (1989), derived from experimental measurements, provides a way to simulate the evolution of snow grain volume under wet snow conditions with respect to the liquid water content of the snowpack. The equation of Brun (1989) can be expressed with optical radius growth (ΔR_{opt}) as:

$$\Delta R_{opt} = \frac{C_1 + C_2 LWC^3}{{R_{opt}}^2 \cdot 4\pi} \tag{4.5}$$

where C_1 and C_2 are empirical coefficients (C_1 = 1.1x10^{-3} mm day^{-1}, C_2 = 3.7x10^{-5} mm day^{-1}) and LWC is the liquid water content in mass percentage. Note that in the experiment of Brun (1989),

the empirical relationship was based on the volume equivalent sphere deduced from the measured mean convex snow grain radius, which is a definition closely related to the SSA. Figure 4.2 shows that the SSA decrease is more pronounced when LWC increases in the snowpack. In this study, when the CLASS liquid water content is greater than zero, the model-derived SSA value is converted into its equivalent R_{opt} using eq. 4.1 in order to apply eq. 4.5, and then reconverted to SSA. Furthermore, because the LWC distribution is not homogeneous within the snowpack, even though CLASS uses a single LWC value for the whole snowpack, here the LWC is first distributed in the top 10 cm. If the LWC in the top 10 cm is greater than 10% in mass, the excess water is distributed to the rest of the snowpack. The 10% limit can thus be considered as the water retention capacity. This value was chosen because 10% in mass is the value where, in the experiment of Brun (1989), LWC reaches the irreducible water content and percolation occurs, leading to a saturation of grain growth rate increase for high LWC. However, the liquid water retention capacity of CLASS for the whole snowpack was kept at 4%.

4.3.2 Sites and data

Snowpit measurements were conducted at five sites. Measurements were taken during the winter of 2010-2011 at the first two sites, which were located in an open mid-latitude northern environment. The sites were at the *Site interdisciplinaire de recherche en environnement extérieur* (SIRENE) experimental station at the Université de Sherbrooke (45.37 °N, 71.92 °W) and at St-Romain (45.45 °N, 71.02 °W; 80 km northeast of Sherbrooke) in Québec, Canada. Mean January temperature at Sherbrooke is -11.9°C and the cumulated precipitation is 294.3 cm of snowfall, generally from November to April (National Climate Data, Environment Canada). Temperatures are generally slightly colder at St-Romain and cumulated snowfall higher because of the higher altitude (≈ 150 m over Sherbrooke). Two other sites were located close to the Churchill Northern Study Centre (58.73 °N, 93.81 °W) in Manitoba, Canada: one in an arctic dry fen (tundra) and the other in a taiga environment (black spruce forest). Churchill has a subarctic climate with a mean January temperature of -26.7°C and accumulated snowfall of 191cm generally from October to May (National Climate Data, Environment Canada). The data were collected during the Canadian CoReH20 Snow and Ice (CAN-CSI) campaign in the winter of 2010, which included four periods of intensive field sampling (January, February, March, and April). Further details of the campaign are provided in Derksen et al. (2012). The last is the meteorological research station Col de Porte (CDP; 45.17 °N, 5.46 °E), near Grenoble, France, in

the French Alps at an elevation of 1325 m. The daily average mean temperature for January is -1.63°C and the mean total cumulated snowfall from December to April is 557 cm. Measurements were carried out during the winter of 2009-2010 (see Morin et al., 2013 and Morin et al., 2012 for more details).

At the first four sites, SSA profiles were taken at a vertical resolution of 5 cm. The SSA was measured with the shortwave InfraRed Integrating Sphere (IRIS) system (Montpetit et al., 2012), which is based on the principle described by Gallet et al. (2009), which exploits the relationship between the SWIR snow reflectance and the SSA (Kokhanovsky and Zege, 2004). The density was measured with a 185 cm^3 density cutter, and the samples were weighed with a 100 g Pesola light series scale with an accuracy of 1 g. The temperature was measured with a Traceable 2000 digital temperature probe. Liquid water content of snow was also measured with the Snow Fork (Toikka Engineering Ltd., Espoo, Finland) at the Churchill Arctic fen site during wet conditions on April 13 and 16 2010. At the Col de Porte site, 16 SSA profiles were taken using the Dual Frequency Integrating Sphere for Snow SSA instrument (DUFISSS: Gallet et al., 2009), also based on the relationship between the SWIR reflectance and the SSA. Note that from late February onwards, warm conditions led to several snowmelt events, which caused a significant decrease in the snow SSA values. Hence, a distinction is made between dry snow conditions at Col de Porte (7 sets of data from January 6 to February 16) and wet snow conditions (9 sets of data from February 25 to April 20). The total snow depth and snow density profiles were also measured (Morin et al., 2013) and ultrasonic snow depth observations were acquired at SIRENE and Col de Porte.

NARR data (Mesinger et al., 2006) (2 m air temperature and air humidity, precipitation, 10 m wind speed, surface shortwave and longwave radiation) were used to force the CLASS model at the first four sites. Langlois et al. (2009) show that the NARR product delivers reliable input data for snowpack modeling. Forcing data from the NARR nearest neighbor pixel of each site was employed. As NARR provide data on a three-hour time step, the variables were interpolated to a 30-minute time step, except for precipitation which maintained a three-hour interval. To initialize the starting conditions, the CLASS model was run starting the year prior to the winter in this study: from October 1 2009 to June 1 2011 at SIRENE and St-Romain; from October 1 2008 to June 1 2010 at Churchill. At the Col de Porte site, meteorological variables (air temperature,

humidity, windspeed, precipitation and incoming shortwave and longwave radiation) recorded with an hourly time resolution throughout the snow season of 2009-2010 (from 20 September 2009 to 10 May 2010) were interpolated to a 30-minute time-step and used to drive the CLASS model (see Morin et al, 2012 for more details on the Col de Porte meteorological data).

4.4 Results

4.4.1 CLASS snow parameter evaluation

First, an analysis of the one-layer CLASS snow model simulations was conducted. Simulated snow density, total snow depth and SWE were compared with all measurements taken in snow pits where SSA profiles were measured. Figure 4.3 shows that the simulation accuracy varied from one site to another. Snow density is generally accurate except at Col de Porte, where the density was overestimated. The overestimation is probably due to the high densification of snow under wet conditions with CLASS. For snow depth, there is an underestimation for the Churchill sites. Since there were underestimates at both forest and fen sites, NARR precipitation is probably the main cause. In fact, the cumulated NARR precipitation from the beginning of the snow season to the first snowpit measurement in February at the dry fen is lower (97.1 mm) than the snowpit measured SWE (157.3 mm). However, other phenomena such as blowing snow and interception by vegetation could lead to differences between the simulated and measured SWE (consequently snow depth as well). Comparisons between continuous ultrasonic snow depth observations at SIRENE and Col de Porte also show that errors in diagnosing precipitation phase at the beginning of the snow season lead to an offset of snow depth (overestimation at SIRENE) (figure 4.4a). That sensitivity to precipitation phase in CLASS is also demonstrated in Langlois et al. (submitted). Figure 4.4b shows that underestimation of melt events at the beginning of the season also lead to positive offset in the snow depth. However, the snow depth RMSE is comparable to what was found with CLASS 3.1 in the Snow Model Intercomparison Project (Brown et al., 2006). The overall SWE RMSE is 64.7 mm, which is close to what was found in Langlois et al. (submitted) between modeled (CRCM) and observed SWE values for northern Québec. There is a good correlation between the measured and simulated SWE for the SIRENE and Col de Porte sites, where there is, however, a consistent overestimation. However, the SWE is underestimated at St-Romain and both Churchill sites.

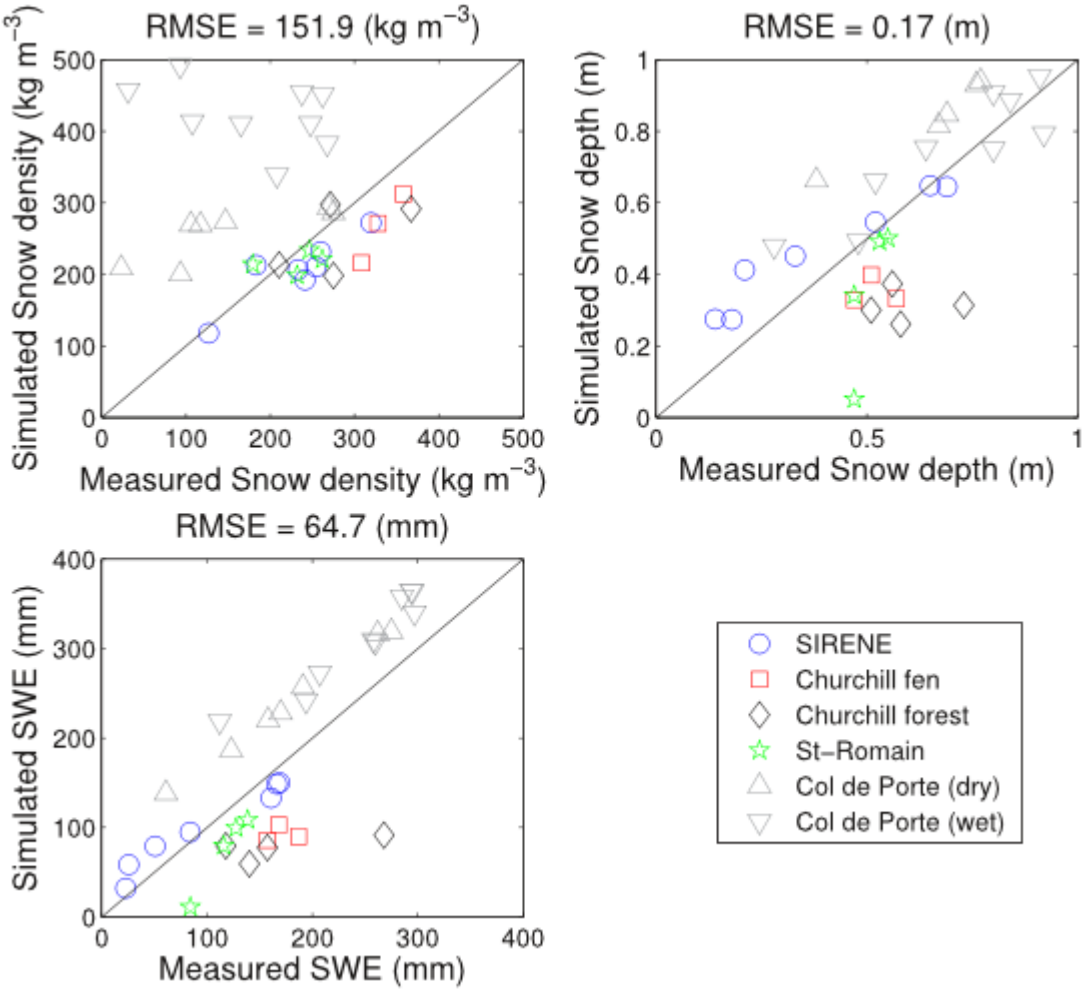

Figure 4.3: **Comparison of CLASS simulated snow properties with field measurements at different sites. Dry and wet sites at Col de Porte are separated.**

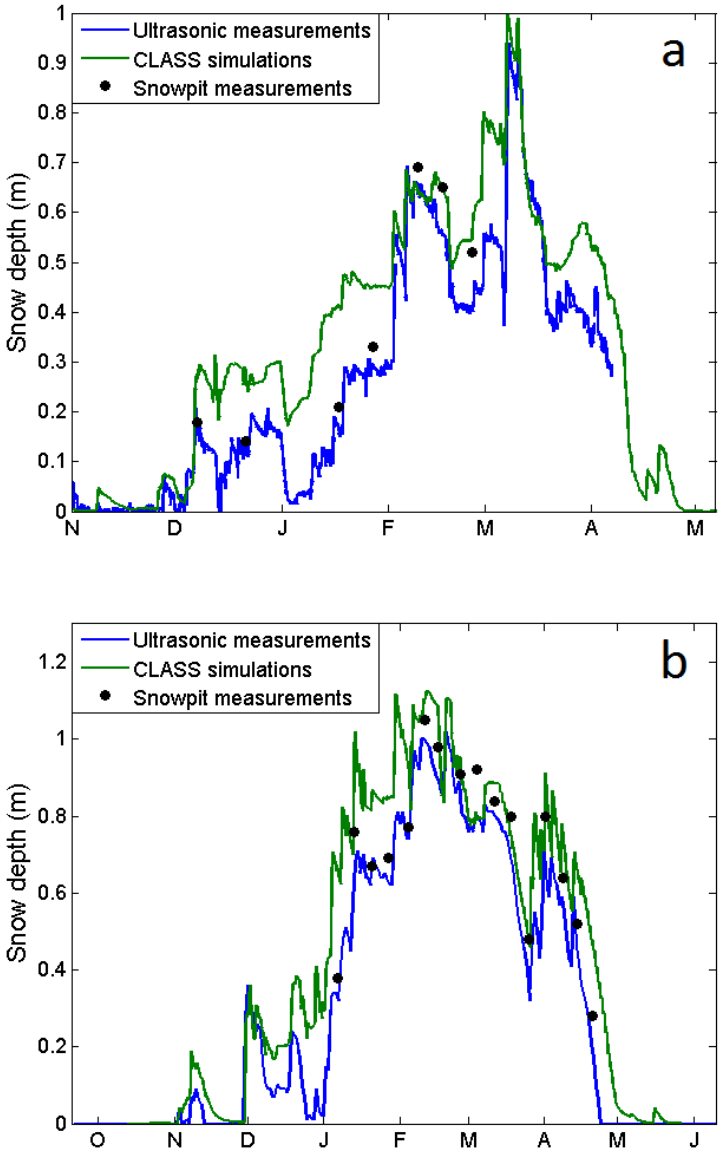

Figure 4.4: CLASS snow depth simulations compared with Ultrasonic measurements at a) SIRENE and b) Col de Porte. Black dots are the snow depths from snowpit measurements.

4.4.2 CLASS-SSA model evaluation and validation

In this study, SSA is considered for the evaluation and validation, because measurements of shortwave infrared reflectance of snow are related to SSA (see Sect. 4.3.2). To evaluate the CLASS-SSA simulations, an analysis of the $TG_{threshold}$ was first conducted. However, differences between the simulated and measured snow depths (figures 4.3 and 4.4), caused problems when relating measured SSA to its corresponding simulated SSA for a given snow depth in the snowpack. A correction was applied to the measured snow depth in order to match the simulated snow depth; this caused the measured profiles to be stretched or compressed. The root mean

square error values between the simulated and measured SSA ($RMSE_{SSA}$) were calculated at the first four sites for different $TG_{threshold}$ values. The Col de Porte sites where wet snow metamorphism dominated were excluded because wet metamorphism has a strong influence on SSA evolution that is not related to the $TG_{threshold}$. Figure 4.5 shows that, for $TG_{threshold}$ values between 10 K m^{-1} and 20 K m^{-1}, the $RMSE_{SSA}$ for the 5 sites is relatively constant. The minimum $RMSE_{SSA}$ value (7.3 m^2 kg^{-1}) for the 5 sites is $TG_{threshold}$ = 16 K m^{-1}, which is close to the 15 K m^{-1} value used by Jacobi et al. (2010). This value is also consistent with Taillandier et al. (2007), who proposed that the $TG_{threshold}$ should be between 9 K m^{-1} and 20 K m^{-1}. The SIRENE site reached a minimum RMSE at $TG_{threshold}$ = 14 K m^{-1}, whereas the RMSE at both Churchill sites slightly increased with $TG_{threshold}$. The RMSE at St-Romain and the dry snow Col de Porte sites slightly decreased from 10 K m^{-1} to 25 K m^{-1} before reaching a constant value (figure 4.5).

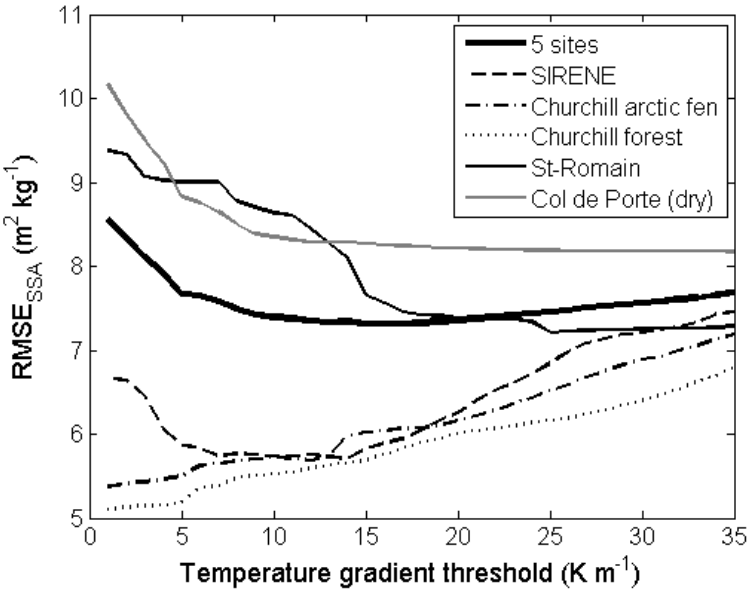

Figure 4.5: **$RMSE_{SSA}$ between the measured SSA and the simulated SSA using CLASS-SSA as a function of the temperature gradient threshold ($TG_{treshold}$).**

The minimum RMSE was at $TG_{threshold}$ = 16 K m^{-1} and was thus used to simulate SSA with CLASS-SSA at the 5 sites (figure 4.6). Previous studies have generally defined the TG threshold for depth hoar formation between 10 K m^{-1} and 20 K m^{-1} (Taillandier et al., 2007; Colbeck, 1983; Marbouty, 1980). However, it should be noted that the formation of faceted snow crystals has been observed at low growth rates under low gradient thresholds (Domine et al., 2003; Flin and Brzoska, 2008). Pinzer and Schneebeli (2009) proposed that alternating temperature gradients also leads to formation of rounded grains, similar to those observed in ET metamorphism.

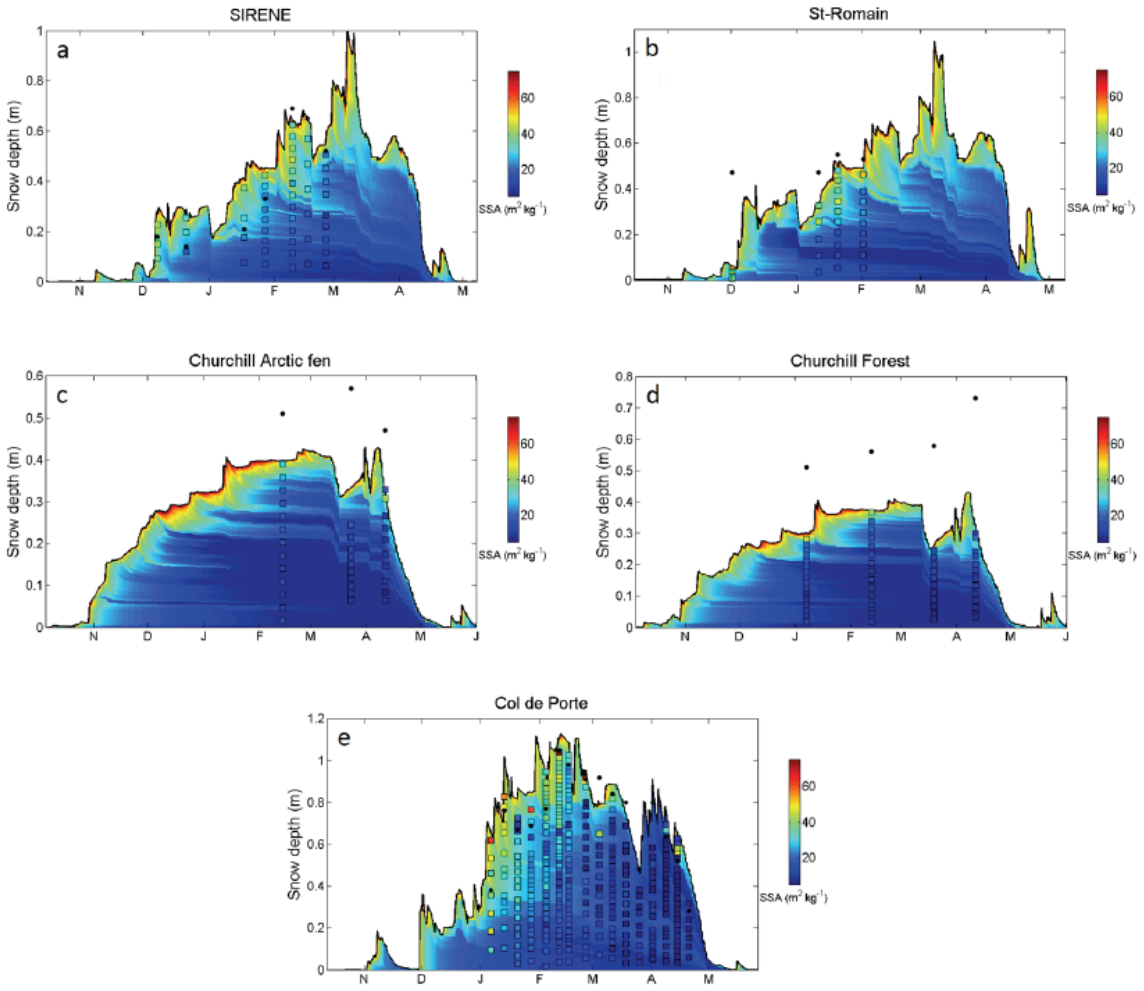

Figure 4.6: **Seasonal profile of simulated SSA at five sites (a = SIRENE; b = St-Romain; c = Churchill Arctic fen; d = Churchill Forest; e = Col de Porte) compared to SSA measurements (square: where the measured SSA profiles were adjusted to the simulated snow depth, see text). The measured profiles are stretched or compressed to fit with simulated snow depth. Black dots correspond to the measured snow depths.**

However, overall comparisons show good agreement between simulated and measured SSA (figure 4.6). More specifically, the SIRENE and St-Romain results show similar patterns with a gradient from low SSA at the bottom to higher SSA coming from fresh precipitation at the top. Nevertheless, there is a low SSA layer that appeared in mid-December caused by a melt event. This layer was observed as a melt ice-crust layer of 3 cm with low SSA (measured with a SWIR camera: Montpetit et al., 2012) during the snowpit measurements, but SSA was not measured with IRIS because it is difficult to extract this kind of snow (i.e., crusts) with the IRIS instrument. For the Churchill sites, both measured and simulated SSA are low near the bottom (≈ 25 cm), which is related to the formation of depth hoar in the presence of a high temperature gradient. However, the simulated SSA values in the top layers are generally higher than the measurements.

This may be due to the underestimation of the snow depth at the beginning of the season causing an underestimation of the relative thickness of the bottom layers with low SSA within the snowpack, which leads to an overestimation of the top layer thickness (figures 4.6c and d). Underestimation of the April measurements at both sites should, however, be attributed to an underestimation of snow LWC by CLASS during the spring melt, which limited the decrease of simulated SSA by wet metamorphism. In fact, LWC as measured with the Snow Fork on April 13 and 16 at the Churchill Arctic fen site suggests a strong underestimation by CLASS (0.2% vs 3.8% on April 13 and 1.0% vs 15.5% on April 16, for CLASS and the Snow Fork, respectively). The issue with LWC is discussed in Sect. 4.5. The Col de Porte site illustrates the difference between the first seven dry sets of data showing good agreement, and the second period, starting on February 25, when wet snow becomes predominant in the snowpack, giving a systematic overestimation of the SSA.

The comparison of the simulated SSA values to their corresponding measurements gives a RMSE of 8.0 m^2 kg^{-1}, which represents an error of 42.3% (figure 4.7). Part of the error could be attributed to the fact that we did not necessarily compare the same snow layers due to different positions between the simulated and measured points. The correction applied to the simulated snow depth profile might be a factor, but the high variability within a SSA profile might also be a source of error. The simulated SSA variations are also strong within the snowpack, mainly for high SSA, where the evolution is faster (see figure 4.2). Considering the mean depth-averaged SSA weighted by the snow layer thickness, the RMSE decreases significantly to 5.1 m^2 kg^{-1} representing an error of 25.7%. Furthermore, the coefficient of determination (R^2) increases from 0.60 to 0.84. As mentioned previously, another major source of error corresponds to the influence of wet conditions, as observed at the Col de Porte site after the mid-season. In fact, by removing data for this wet period, the depth-averaged RMSE decreases to 4.1 m^2 kg^{-1} (17.5%). As mentioned in Morin et al. (2013), even with a multi-layer model, limitations on the precision of LWC simulations exacerbate the difficulty of modeling snow grain evolution under wet conditions. The weakness of the model under wet snow conditions will be analyzed below in the Discussion (Sect. 4.5). The SSA at St-Romain and at Col de Porte (dry snow period) are underestimated by the model, while at the Churchill sites SSA is slightly overestimated due to the high simulated SSA in the top layers (figures 4.6c and d).

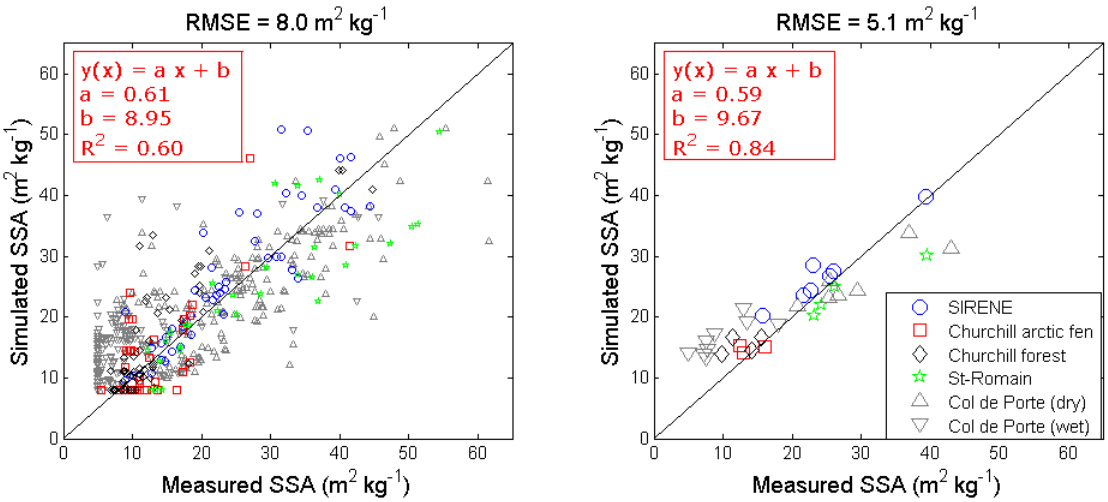

Figure 4.7: **Measured vs simulated SSA comparison (left panel shows all points; right panel shows the one-layer average). The RMSE in averaged SSA (right panel) without the wet points is 4.1 m^2 kg^{-1}.**

4.5 Discussion

The simulation of a stratified phenomenon such as SSA using a one-layer snow model such as CLASS requires certain assumptions and simplifications of the physics within the snowpack. These assumptions may induce errors in estimates of the SSA evolution. Here, we discuss the different elements that may impact the precision of the model and how they may influence the estimates. It is thus possible to identify the conditions under which CLASS-SSA is more limited and propose possible improvements. We then consider the proposed model's application, mainly in the context of passive microwave simulations.

4.5.1 Sources of errors

An assumption made in the CLASS-SSA approach is that the temperature profile of the snowpack is linear. In general, the temperature variations will be larger in the top layers responding to the variations in air temperature, while the bottom layers are less affected as the air temperature fluctuations do not reach these layers because of the low snow thermal conductivity (Armstrong and Brun, 2008; Vionnet et al., 2012). Hence, in cold weather like in Churchill, the linearity of the temperature profiles is likely to induce underestimated snow layer temperatures. This phenomenon could also partly explain why the SSA of top layers, at both Churchill sites, is overestimated, considering that the SSA decrease is more pronounced with higher snow temperatures. Furthermore, the linearity of the temperature gradient would generally underestimate the local temperature gradient in the top layers and overestimate the local temperature gradient in the bottom layers. However, in the North during winter, this diurnal

temperature cycle is generally in most cases less pronounced than over temperate or mountainous regions (Leathers et al., 1998). Furthermore, using a linear gradient throughout a dry and relatively shallow snowpack (below about 1 to 1.5 m depth) appears thus as a satisfactorily hypothesis in most cases over Northern areas. Kondo and Yamazaki (1990) demonstrated that a linear temperature profile can be successfully employed in a snowmelt model.

As shown through the wet metamorphism simulation, CLASS-SSA is limited by the modeling of snow parameters in CLASS. Hence, the use of a one-layer model giving a LWC for the entire snowpack becomes a limitation. Furthermore, there might be an underestimation of LWC by CLASS. Measurements of LWC with the Snow Fork at the Churchill Arctic fen site, suggests a strong underestimation by CLASS. Moreover, raising the limit of the simulated snowpack water retention capacity from 4% to 10% did not improve the simulated LWC and the SSA calculation under wet conditions in Col de Porte because the CLASS LWC rarely reaches the retention capacity. Part of the problem was, however, resolved by distributing the LWC mostly in the top layers, but the SSA evolution under wet conditions remains a weakness. Table 4.1 shows that the bias is significantly reduced when wet metamorphism is modeled with snowpack liquid water distributed in the top 10 cm at the Col de Porte wet sites compared with a wet metamorphism considering a uniform LWC or compared to no wet metamorphism. We also tested simulations by drastically increasing the total LWC artificially in CLASS (if LWC > 0 then LWC = 10%), such conditions significantly reduce the simulated SSA, as expected, with a bias of -2.6 m^2 kg^{-1} for Col de Porte wet snow condition data (table 4.1). This last case confirms that the problem comes from an underestimation of LWC in CLASS under warm conditions.

Table 4.1: **SSA bias and RMSE at Col de Porte wet sites for different configurations of CLASS-SSA wet metamorphism.**

Model Configurations	**RMSE (m^2 kg^{-1})**	**Bias (m^2 kg^{-1})**
No wet metamorphism	15.9	13.4
Uniform LWC (CLASS)	12.6	10.1
LWC distributed in the top 10 cm (CLASS-SSA configuration)	9.4	6.8
Drastic increase of LWC (if LWC > 0 then LWC = 10%)	6.7	-2.6

Snow depth errors from CLASS might also impact CLASS-SSA simulations. In fact, as shown for both Churchill sites (figures 4.6c and d), a bias in snow precipitation can impact the

representation of the thickness of a given snow layer. Thus, in this study, part of the SSA error could be related to uncertainties in the NARR precipitation data (Langlois et al., 2009).

Other phenomena not parameterized in the CLASS snow model, such as blowing snow, could influence the simulated snow depth (Liston and Hiemstra, 2011). In open areas (four of our five sites), strong wind shear stress could have exceeded the snow particle resistance to dislocation (Li and Pomeroy 1997). Hence, a less cohesive top snow layer with lower SSA could be removed almost completely in an open arctic region like Churchill (Baggaley and Hanesiak, 2005). Furthermore, the snow thermal conductivity strongly varies between the tundra, where the snowpack has a high conductivity due to hard wind slabs, compared to taiga and forest snowpacks which have three to four times lower thermal conductivity due to lower wind compaction and depth hoar development (see Gouttevin et al., 2012). These differences impact the snow temperature and temperature gradient and are not represented in CLASS-SSA.

In the CLASS-SSA model, the $SSA_{initial}$ value is fixed at 73.0 m^2 kg^{-1}. This value was chosen based on freshly fallen snow SSA measurements (sampled, at the most, 24 hours after the snowfall) from methane adsorption by Domine et al. (2007). However, this study shows a range of 33.1 to 155.8 m^2 kg^{-1} with a standard deviation of ± 26.2 m^2 kg^{-1} based on 63 samples. Freshly fallen snow SSA is rarely modeled as it depends on the type of solid precipitation, which depends on the meteorological conditions (air temperature, wind, type of clouds, atmospheric stratification) when the snowflake is formed. Domine et al. (2007), however, proposed freshly fallen snow SSA values based on four types of fresh snow that can be related to density. As CLASS calculates the fresh snow density from the air temperature using the equation from Hedstrom and Pomeroy (1998), we implemented $SSA_{initial}$ values based on the Domine et al. (2007) relationship. However, this implementation did not change the results significantly; a slight increase in RMSE from 8.0 to 8.3 m^2 kg^{-1} was found. Figure 4.8 shows that $SSA_{initial}$ has a relatively low impact on simulations. The sensitivity to $SSA_{initial}$ values appears to be more important for the snowpack where measurements were taken mostly at the beginning of the season (SIRENE and St-Romain). A precise dynamic parameterization of freshly fallen SSA could probably improve the results, mostly for snow with high SSA at the beginning of the snow season.

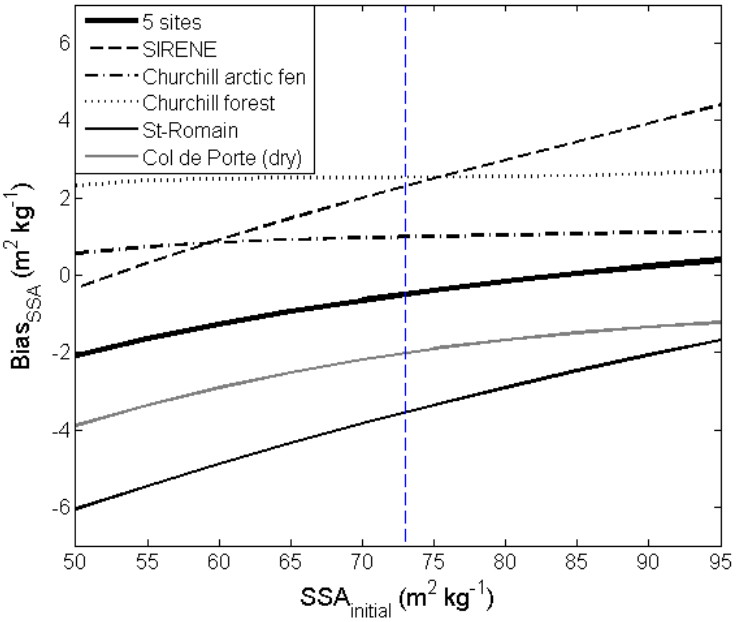

Figure 4.8: Bias between the measured SSA and the simulated SSA using CLASS-SSA as a function $SSA_{initial}$ (the vertical dotted blue line represents the $SSA_{initial}$ set in CLASS-SSA at 73.0 m^2 kg^{-1}). La même figure, mais avec les RMSE, est donnée à l'Annexe 1.

4.5.2 Comparison with other models

Despite the above simplifications, the CLASS-SSA model simulates SSA with a reasonable accuracy for a wide range of snow types. Our RMSE of 8.1 m^2 kg^{-1} (figure 4.7) is comparable to the result obtained at Col de Porte by Morin et al. (2013) from internal computation of the optical radius in Crocus (6.37 m^2 kg^{-1}) and the method of Domine et al., (2007) based on the density and snow type (8.08 m^2 kg^{-1}). Snow data from the 2010 winter season at Col de Porte provide a unique and very accurate time series of SSA measurements (Morin et al., 2013). Figure 4.9 shows a comparison of temporal snowpack averaged SSA values at Col de Porte for CLASS-SSA, the Crocus model (Morin et al. 2013), and the measurements. When the snowpack is dry, both models underestimate the SSA. On February 25 and after, when wet conditions occur, CLASS-SSA overestimates the SSA due an underestimation of the snowpack LWC, while Crocus still underestimates the SSA. For this dataset, CLASS-SSA simulations seem comparable to or better than Crocus in dry conditions. However, in wet conditions, Crocus better simulates the decrease in SSA as LWC increases (figure 4.9). Hence, Crocus seems to capture better the dynamic of the SSA evolution. Note that Jacobi et al. (2010) obtained, from 162 snow SSA measurements at a taiga site, an RMSE of 8.6 m^2 kg^{-1} with the implementation of the Taillandier et al. (2007) approach within Crocus, whereas the implementation of Domine et al. (2007) results

in a RMSE of 16.2 m^2 kg^{-1} (the results were highly affected by the underestimation of snow density by Crocus).

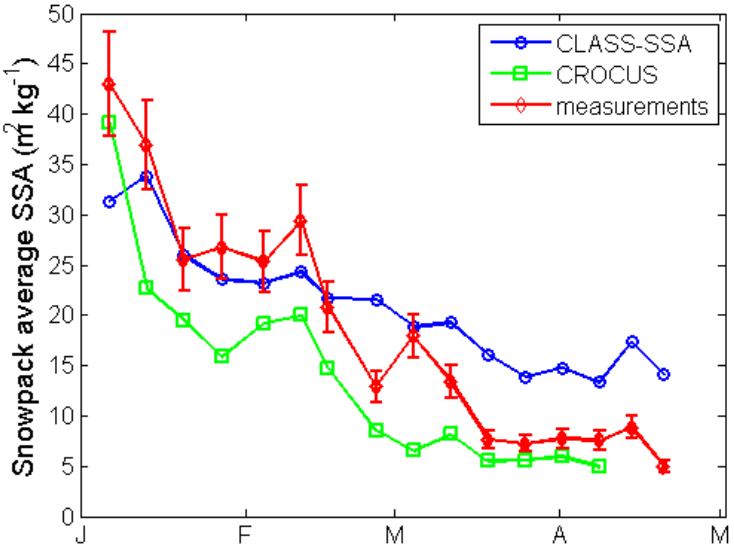

Figure 4.9: **Snowpack-averaged SSA evolution with time at Col de Porte for CLASS-SSA, Crocus and the measurements. The last Crocus value was excluded because the simulations give no snow on ground. Error bars on measurements are the measurements accuracy (12%: Gallet et al., 2009).**

4.5.3 R_{opt} analysis for MSEM

In the context of using the simulated SSA to assimilate microwave brightness temperatures (T_B), we now examine the impact of errors generated by the proposed approach in terms of T_B error. As mentioned in Sect. 4.2, the DMRT MSEM calculates T_B from R_{opt} derived from SSA. Figure 4.10 shows the comparison between R_{opt} derived from measured SSA and R_{opt} derived from simulated SSA. As the relationship between SSA and R_{opt} is not linear (eq. 4.1), we see that for individual points (figure 4.10 left), the differences between simulated and measured R_{opt} are more important for larger grains. This is caused by the fact that for low SSA, a given variation of SSA leads to a larger change in the simulated R_{opt} (a change of SSA from 10 to 8 m^2 kg^{-1} leads to change R_{opt} from 0.327 to 0.409 mm). R_{opt} is then much more sensitive to error in SSA for larger grains. It also partly explains the fact that the error for wet snow in Col de Porte is large. For mean R_{opt} values over the snowpack, there is a RMSE of 0.043 mm and R^2 of 0.84, comparable to SSA results, if the wet snowpacks are excluded. There is however a small positive bias of 0.034 mm mainly caused by strong influence of large grains in the averaging.

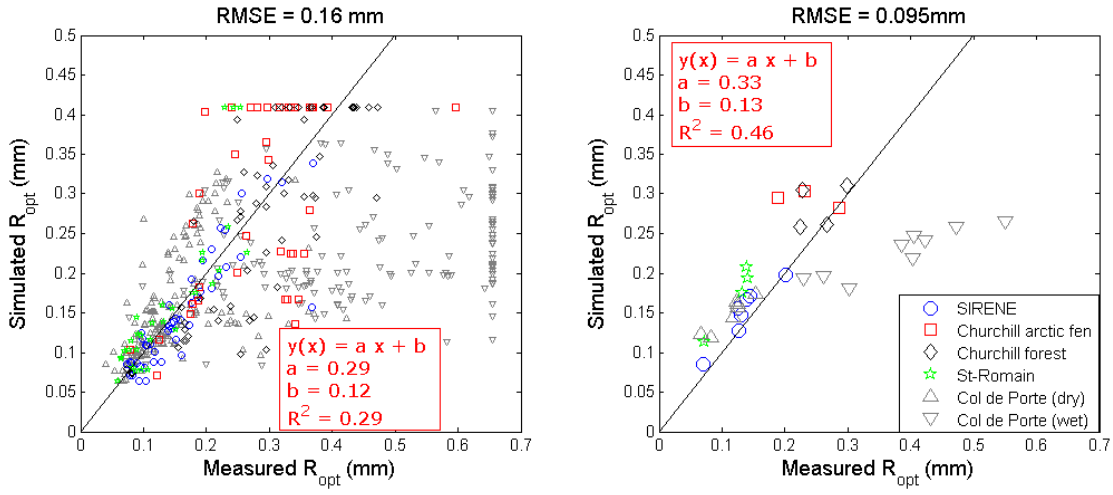

Figure 4.10: **Measured vs simulated R_{opt} derived from SSA (eq. 4.1) comparison (left panel shows all points; right panel shows the one-layer average). The RMSE in averaged R_{opt} (right panel) without the wet points is 0.043mm.**

Moreover, the density stratification is another parameter that should be considered when modeling the radiative transfer within the snowpack (e.g. Picard et al., 2013). In our case, the densification routine in CLASS-SSA is only used to calculate the depth and the position of every snow layer, and not necessarily to calculate a precise density. The simulated densities might differ from real densities. An example is the decrease of densification at the bottom snow layer when depth hoar formation occurs that is not taken into account in the SSA offline model. The correction of densities in the top layers (see Sect. 4.3.1) might also lead to low densities in the top layers. Here, to attenuate the effects of these simplifications in the T_B simulations, we consider a bulk snowpack characterized by an effective snow grain effective radius R_{eff} calculated from the averaged R_{opt} following the form suggested by Kontu & Pulliainen (2010):

$$R_{eff} = a[1 - \exp(-bR_{opt})] \tag{4.6}$$

where a=1.3 and b=4.7. These empirical parameters were fitted from simulations using averaged R_{opt} derived from measured SSA compared to ground-based radiometric measurements, but for the bulk snowpack (see Roy et al., 2013).

Simulations with the DMRT-ML (Picard et al., 2013) were conducted to analyze the effect of the R_{opt} error on T_B simulations. The T_B simulations are conducted employing single-layer averaged R_{eff} values (eq. 4.6) ± the derived RMSE of R_{opt} (±0.043 mm). Considering a snowpack of 0.5 m

with a bulk density of 250 kg m^3, an error of 0.043 mm in R_{opt} leads to maximum variations of T_B of the order of ± 23.3 K at 36.5 GHz and ± 2.7 K at 18.7 GHz. We thus see the high sensitivity of 36.5 GHz to grain size given an error that could be significant in some cases (high depth hoar layer), while the proposed simple approach can be applied for T_B simulations at 18.7 GHz with acceptable accuracy. Such a sensitivity analysis would benefit from further development as many combinations of snowpack parameters and conditions could occur.

4.5.4 Model applications

The simulation of snowpack parameters, such as SWE, at individual sites using an operational land-surface scheme designed for use in large-scale climate models, could include large errors, as illustrated in figure 4.3. These errors could result from uncertainties in the meteorological forcing data, model parameters, as well as the nonlinearity and scaling effects of the processes modeled (e.g. Andreadis et al., 2008). The proposed model opens opportunities to couple CLASS with MSEM for improving SWE estimates. Data assimilation offers the potential to merge information on snow variables from satellite observations and land-surface model simulations. CLASS-SSA was developed mainly for passive microwave T_B assimilation in CLASS to improve estimates of snow parameters. The model employed in this study provides a good estimate or "first guess" of the snow grain size and a description of the snow type at a given time during the snow season. Inversion approaches, where parameters (snow depth, snow density) are retrieved by minimizing the differences between simulated and measured brightness temperatures (Langlois et al., 2012; Vachon et al., 2010; Pardé et la., 2007) will benefit from SSA simulations by taking into account the important effect of snow metamorphism on the microwave signal. The "first guess" could also be used as a state initial condition in more complex data assimilation system approaches (Toure et al., 2011 ; Durand et al., 2009; Reichle, 2008) because the grain-size parameterization is no longer the dominant source of uncertainty. Grain size can be considered as one of many sources of uncertainty, but with known likely error or variation. Hence the CLASS-SSA model can be applied to improve SWE estimates at large scales from satellite-borne passive microwave information. From this perspective, as mention previously (Sect. 4.5.3), attention needs to be paid to the effect of the conversion of SSA to R_{opt} on the uncertainty related to the grain size simulation depending on the type of grains. In fact, considering eq. 4.1, errors in SSA with large grains (low SSA, such as depth hoar) will lead to higher variation of R_{opt} than for smaller grains (high SSA) (see Morin et al, 2013).

The proposed methodology could also be implemented a hydrology land-surface scheme (HLSS) such as the one developed in the framework of Environment Canada's community environmental modeling system: MESH. MESH evolved from the WATCLASS model which links a hydrological routing model (WATFLOOD) (Pietroniro et al., 2006) to the Canadian Land Surface Scheme (CLASS). It is used as a basis for coupling horizontal surface hydrology (river routing) with both weather and climate atmospheric models (see discussion by Teutschbein and Seibert, 2010).

Furthermore, snow surface albedo (mostly in the infrared) is driven by snow grain size. Hence, the use of SSA estimated with CLASS-SSA could lead to improved estimates of snowpack albedo, which are derived from a physically-based model. Pure snow albedo (no impurities) could be related to the SSA using a simple optical equation model suggested by Kokhanovsky and Zege (2004). Based on the simple radiative transfer model of Gardner and Sharp (2010), an error of 8.0 m^2 kg^{-1} in SSA leads to an uncertainty in the broadband albedo calculation of around ±3% for small grains (30 m^2 kg^{-1}) to around 6% for large grains (10 m^2 kg^{-1}). It should be noted that the grains at the top of the snowpack that drive the broadband surface albedo are generally smaller (mostly in dry conditions) and thus less affected by grain uncertainty.

4.6 Conclusions

This study analyzes the coupling of a SSA evolution model with a one-layer snow model from the Canadian LAnd Surface Scheme (CLASS). The simulated SSA values were compared with a unique SSA database for five different sites, representing four different climatic environments including a wide range of snow types. Based on the SSA decrease due to snow aging in snow layers (Taillandier et al. 2007), the CLASS-SSA model is an offline multi-layer parameterization driven by CLASS single-layer snow model outputs. The CLASS-SSA model also considers wet metamorphism using the equation of Brun (1989) based on the liquid water content of snow.

Despite the limits of a simple one-layer snow model, it provides SSA with an overall RMSE of 8.0 m^2 kg^{-1} for individual layers, and a depth-averaged RMSE of 5.1 m^2 kg^{-1} for the snowpack SSA. The model, however, shows weaknesses in the wet snow metamorphism regime, which is mostly due to a low bias in the snow model simulations of LWC within the snowpack.

The proposed implementation of the SSA model in an off-line mode and driven by a one-layer snow model offers a simple, computationally efficient and versatile approach. It would not be difficult to implement for other models as it only needs six basic inputs that are normally available from snow models (snow depth, SWE, snow density, LWC, soil-snow interface temperature, air temperature). This approach is thus applicable for other one-layer snow models (Turcotte et al., 2007; Bélair et al., 2003), but also for multi-layer models where SSA is not explicitly modeled, such as the Snow-Atmosphere-Soil Transfer (SAST) energy balance snow physics model (Sun et al., 1999).

Future work will evaluate the use of these SSA simulations for satellite passive microwave brightness temperature assimilations and surface snow albedo calculations.

Acknowledgements

The authors would like to thank the National Sciences and Engineering Research Council of Canada (NSERC) and Environment Canada for their financial support. All of our colleagues who helped us during the field campaigns in France and Canada are also gratefully acknowledged. We thank Samuel Morin, (Météo-France – CNRS, CNRM-GAME/Centre d'Études de la Neige), for providing the Col de Porte dataset and valuable suggestions on the manuscript. We thank Diana Verseghy (Climate Processes Section, Environment Canada) for providing the CLASS model code. We also thank Ghislain Picard and Florent Domine for their helpful comments and the two reviewers who helped to improve the quality of the manuscript.

References

Adams, E. and Sato, A.: Model for effective thermal conductivity of a dry snow cover composed of uniform ice spheres, Annals of Glaciology, 18, 300–304, 1993.

Andreadis, K. M., Liang, D., Tsang, L., Lettenmaier, D.P., and Josberger, E. G.: Characterization of errors in a coupled snow hydrology microwave emission model, Journal of Hydrometeorology, 9, 149–164, 2008.

Aoki, T., Kuchiki, K., Niwano, M., Kodama, Y., Hosaka, M., and Tanaka, T.: Physically based snow albedo model for calculating broadband albedos and the solar heating profile in snowpack for general circulation models, Journal of Geophysical Research, 116, D11114, 2011.

Armstrong, R. and Brun, E.: Snow and climate: physical processes, surface energy exchange and modeling, Cambridge University Press, 2008.

Arnaud, L., Picard, G., Champollion, N., Domine, F., Gallet, J. C., Lefebvre, E., Fily, M., and Barnola, J. M.: Measurement of vertical profiles of snow specific surface area with a 1 cm resolution using infrared reflectance: instrument description and validation, Journal of Glaciology, 57, 17–29, 2011.

Baggaley, D. G. and Hanesiak, J. M.: An empirical blowing snow forecast technique for the Canadian arctic and the Prairie provinces, Weather and Forecasting, 20, 51–62, 2005.

Bartelt, P., Lehning, M.: A physical SNOWPACK model for the Swiss avalanche warning Part I: numerical model, Cold region Science and Technology, 35, 123-145, 2002.

Bartlett, P. A., MacKay, M. D., and Verseghy, D. L.: Modified snow algorithms in the Canadian land surface scheme: Model runs and sensitivity analysis at three boreal forest stands, Atmosphere-ocean, 44, 207–222, 2006.

Belair, S., Brown, R., Mailhot, J., Bilodeau, B., and Crevier, L.: Operational implementation of the ISBA land surface scheme in the Canadian regional weather forecast model. Part II: Cold season results, Journal of Hydrometeorology, 4, 371–386, 2003.

Bougamont, M., Bamber, J.L., and Greuell, W.: A surface mass balance model for the Greenland ice sheet, 110 (F4), 2003-2012, 2005.

Brown, R., Bartlett, P., MacKay, M., and Verseghy, D.: Evaluation of snow cover in CLASS for SnowMIP, Atmosphere-Ocean, 44, 223–238, 2006.

Brucker, L., Picard, G., Arnaud, L., Barnola, J.-M., Schneebeli, M., Brunjail, H., Lefebvre, E., Fily, M.: Modelling time series of microwave brightness temperature at Dome C, Antarctica, using vertically resolved snow temperature and microstructure measurements, Journal of Glaciology, 57, 171-182, 2011.

Brun, E.: Investigation on wet-snow metamorphism in respect of liquid-water content, Annals of Glaciology, 13, 22–26, 1989.

Brun, E., David, P., Suduland, M., and Brunot, G.: A numerical model simulate snow-cover stratigraphy for operational avalanche forecasting, Journal of Glaciology, 38, 14-22, 1992.

Cabanes, A., Legagneux, L., and Domine, F.: Rate of evolution of the specific surface area of surface snow layers, Environmental Science & Technology, 37, 661–666, 2003.

Caya, D. and Laprise, R.: A semi-implicit semi-Lagrangian regional climate model: The Canadian RCM, Monthly Weather Review, 127, 341–362, 1999.

Chen, S. and Baker, I.: Evolution of individual snowflakes during metamorphism, Journal of Geophysical Research, 115, D21114, 2010.

Colbeck, S.: Theory of metamorphism of dry snow, Journal of Geophysical Research, 88, 5475–5482, 1983.

Derksen, C., Toose, P., Lemmetyinen, J., Pulliainen, J., Langlois, A., Rutter, N., and Fuller, M.: Evaluation of passive microwave brightness temperature simulations and snow water equivalent retrievals through a winter season, Remote Sensing of Environment, 117, 236–248, 2012.

Domine, F., Cabanes, A., Taillandier, A., and Legagneux, L.: Specific surface area of snow samples determined by CH4 adsorption at 77 K and estimated by optical microscopy and scanning electron microscopy, Environmental Science & Technology, 35, 771–780, 2001.

Domine, F., Lauzier, T., Cabanes, A., Legagneux, L., Kuhs, W., Techmer, K., and Heinrichs, T.: Snow metamorphism as revealed by scanning electron microscopy, Microscopy Research and Technique, 62, 33–48, 2003.

Domine, F., Taillandier, A.-S., and Simpson, W. R.: A parameterization of the specific surface area of seasonal snow for field use and for models of snowpack evolution, Journal of Geophysical Research, 112, F02031, 2007.

Domine, F., Albert, M., Huthwelker, T., Jacobi, H.-W., Kokhanovsky, A. A., Lehning, M., Picard, G., and Simpson, W. R.: Snow physics as relevant to snow photochemistry, Atmospheric Chemistry and Physics, 8, 171–208, 2008.

Domine, F., Taillandier, A.-S., Cabanes, A., Douglas, T.A., and Sturm, M.: Three examples where the specific surface area of snow increased over time, The Cryosphere, 3, 31-39, 2009.

Durand, M., Kim, E. C., and Margulis, S.: Quantifying uncertainty in modeling snow microwave radiance for a mountain snowpack at the point-scale, including stratigraphic effects, IEEE Transactions on Geoscience and Remote Sensing, 46, 1753–1767, 2008.

Durand, M., Kim, E., and Margulis, S.: Radiance assimilation shows promise for snowpack characterization, Geophysical Research Letters, 36, L02503, 2009.

Durand, M. and Liu, D.: The need for prior information in characterizing snow water equivalent from microwave brightness temperatures, Remote Sensing of Environment, 126, 248-257, 2012.

Ettema, J., van den Broeke, M.R., van Meijgaard, E., van de Berg, W., Bamber, J.L., Box, J.E., Bales, R.C.: Higher surface mass balance of the Greenland ice sheet revealed by high-resolution climate modeling, Geophysical Research Letters, 36, L12501, 2009.

Flanner, M. and Zender, C.: Linking snowpack microphysics and albedo evolution, Journal of Geophysical Research, 111, D12208, 2006.

Flanner, M., Zender, C., Randerson, J., and Rasch, P.: Present-day climate forcing and response from black carbon in snow, Journal of Geophysical Research, 112, D11202, 2007.

Flin, F., Brzoska, J., Lesaffre, B., Coléou, C. and Pieritz, R.: Three-dimensional geometric measurements of snow microstructural evolution under isothermal conditions, Annals of glaciology, 38, 39-44, 2004.

Flin, F. and Brzoska, J.: The temperature-gradient metamorphism of snow: vapour diffusion model and application to tomographic images, Annals of Glaciology, 49, 17–21, 2008.

Franz, K., Butcher, P., and Ajami, N.: Addressing snow model uncertainty for hydrologic prediction, Advances in Water Resources, 33, 820–832, 2010.

Gallet, J., Domine, F., Zender, C., and Picard, G.: Measurement of the specific surface area of snow using infrared reflectance in an integrating sphere at 1310 and 1550 nm, The Cryosphere, 3, 167–182, 2009.

Gardner, A., and Sharp, M.: A review of snow and ice albedo and the development of a new physically based broadband albedo parameterization, Journal of Geophysical Research, 115, F01009, 2010.

Gouttevin, I., Menegoz, M., Domine, F., Krinner, G., Koven, C., Ciais, P., Tarnocai, C., and Boike, J.: How the insulating properties of snow affect soil carbon distribution in the continental pan-arctic area, Journal of Geophysical Research, 117, G02020, 2012.

Grody, N.: Relationship between snow parameters and microwave satellite measurements: Theory compared with Advanced Microwave Sounding Unit observations from 23 to 150 GHz, Journal of Geophysical Research, 113, D22108, 2008.

Hedstrom, N. and Pomeroy, J.: Measurements and modelling of snow interception in the boreal forest, Hydrological Processes, 12, 1611–1625, 1998.

Huang, C., Margulis, S., Durand, M., and Musselman, K.: Assessment of Snow Grain-Size Model and Stratigraphy Representation Impacts on Snow Radiance Assimilation: Forward Modeling Evaluation, IEEE Transactions on Geoscience and Remote Sensing, 50, 4551-4564, 2012.

Jacobi, H., Domine, F., Simpson, W., Douglas, T., and Sturm, M.: Simulation of the specific surface area of snow using a one-dimensional physical snowpack model: implementation and evaluation for subarctic snow in Alaska, The Cryosphere, 4, 35–51, 2010.

Jin, Z., Charlock, T. P., Yang, P., Xie, Y., and Miller, W.: Snow optical properties for different particle shapes with application to snow grain size retrieval and MODIS/CERES radiance comparison over Antarctica, Remote Sensing of Environment, 112, 3563–3581, 2008.

Kaempfer, T. and Schneebeli, M.: Observation of isothermal metamorphism of new snow and interpretation as a sintering process, Journal of Geophysical Research, 112, D24101, 2007.

Kokhanovsky, A. A. and Zege, E. P.: Scattering optics of snow, Applied Optics, 43, 1589–1602, 2004.

Kondo, J., and Yamazaki T.: A prediction model for snowmelt, snow surface temperature and freezing depth using a heat balance method, Journal of Applied Meteorology, 29, 375-384, 1990.

Kontu, A. and Pulliainen, J.: Simulation of spaceborne microwave radiometer measurements of snow cover using in situ data and brightness temperature modeling, IEEE Transactions on Geoscience and Remote Sensing, 48, 1031–1044, 2010.

Langlois, A., Brucker, L., Kohn, J., Royer, A., Derksen, C., Cliche, P., Picard, G., Willemet, J. M., and Fily, M.: Simulation of snow water equivalent (SWE) using thermodynamic snow models in Québec, Canada, Journal of Hydrometeorology, 10, 1447–1463, 2009.

Langlois, A., Royer, A., Derksen, C., Montpetit, B., Dupont, F., Goïta, K.: Coupling the snow thermodynamic model SNOWPACK with the microwave emission model of layered snowpacks for subarctic and arctic snow water equivalent retrievals, Water Ressources Research, 48, W12524, 2012.

Langlois, A., Bergeron, J., Brown, R., Royer, A., Harvey, R., Roy, A., Wang, L., Thériault, N.: Evaluation of CLASS 2.7 and 3.5 simulations of snow cover from the Canadian Climate model (CRCM4) over Québec, Canada, Journal of Hydrometeorology, submitted (AMSJHM-S-13-00073).

Leathers D. J., Palecki, M.A., Robinson, D.A., and Dewey, K.F.: Climatology of the daily temperature range annual cycle in the United States , Climate Research, 9, 197-211,1998.

Legagneux, L., Lauzier, T., Domine, F., Kuhs, W., Heinrichs, T., and Techmer, K.: Rate of decay of specific surface area of snow during isothermal experiments and morphological changes studied by scanning electron microscopy, Canadian Journal of Physics, 81, 459–468, 2003.

Li, L. and Pomeroy, J.: Estimates of threshold wind speeds for snow transport using meteorological data, Journal of Applied Meteorology, 36, 205–213, 1997.

Liston, G. and Hiemstra, C.: The changing cryosphere: Pan-Arctic snow trends (1979-2009), Journal of Climate, 24, 5691-5712, 2011.

Lyapustin, A., Tedesco, M., Wang, Y., Aoki, T., Horif, M., and Kokhanovsky, A. A.: Retrieval of snow grain size over Greenland from MODIS, Remote Sensing of Environment, 113, 1976–1987, 2009.

Marbouty, D.: An experimental study of temperature gradient metamorphism, Journal of Glaciology, 26, 303–312, 1980.

Mesinger, F., DiMego, G., Kalnay, E., Mitchell, K., Shafran, P., Ebisuzaki, W., Jovic, D., Woollen, J., Rogers, E., and Berbery, E.: North American regional reanalysis, Bulletin of the American Meteorological Society, 87, 343–360, 2006.

Montpetit, B., Royer, A., Langlois, A., Cliche, P., Roy, A., Champollion, N., Picard, G., Domine, F., and Obbard, R.: New shortwave infrared albedo measurements for snow specific surface area retrieval, Journal of Glaciology, 58, 941-952, 2012.

Montpetit, B., Royer, A., Roy, A., Langlois, L., Derksen, D.: Snow microwave emission modeling of ice lenses within a snowpack using the microwave emission model for layered snowpacks, IEEE Transactions on Geoscience and Remote Sensing, available online, doi:10.1109/TGRS.2013.2250509, 2013.

Morin, S., Domine, F., Dufour, A., Lejeune, Y., Lesaffre, B., Willemet, J., Carmagnola, C., and Jacobi, H.: Measurements and modeling of the vertical profile of specific surface area of an alpine snowpack, Advances in Water Resources, 55, 111-120, doi:10.1016/j.advwatres.2012.01.010, 2013.

Morin, S., Lejeune, Y., Lesaffre, B., Panel, J.-M., Poncet, D., David, P., and Sudul, M.: An 18-yr long (1993-2011) snow and meteorological dataset from a mid-altitude mountain site (Col de Porte, France, 1325 m alt.) for driving and evaluating snowpack models, Earth System Science Data, 4, 13–21, 2012.

Music, B. and Caya, D.: Evaluation of the hydrological cycle over the Mississippi River basin as simulated by the Canadian Regional Climate Model (CRCM), Journal of Hydrometeorology, 8, 969–988, 2007.

Niwano, M., Aoki, T., Kuchiki, K., Hosaka, M., Kodama, Y.: Snow metamorphism and albedo process (SMAP) model for climate studies: Model validation using meteorological and snow impurity data measured at Sapporo, Japan, Journal of Geophysical Research, 117, F03008, 2012.

Pardé, M., Goïta, K., and Royer, A.: Inversion of a passive microwave snow emission model for water equivalent estimation using airborne and satellite data, Remote Sensing of Environment, 111, 346–356, 2007.

Picard, G., Brucker, L., Roy, A., Dupont, F., Fily, M., Royer, A: Simulation of the microwave emission of multi-layered snowpacks using the dense media radiative transfer theory: the DMRT-ML model, Geoscience Model Development, 6, 1061-1078, 2013.

Pietroniro, A., Leconte, R., Toth, B., Peters, D.L., Kouwen, N., Conley, F.M., and Prowse, T.: Modelling climate change impacts in the Peace and Athabasca catchment and delta III – Integrated model assessment, Hydrological Processes. 20(19), 4231-4235, 2006.

Pinzer, B. and Schneebeli, M.: Snow metamorphism under alternating temperature gradients: Morphology and recrystallization in surface snow, Geophysical Research Letters, 36, L23503, 2009.

Reichle, R.: Data assimilation methods in the Earth sciences, Advances in Water Resources, 31, 1411–1418, 2008.

Roy, V., Goïta, K., Royer, A., Walker, A., and Goodison, B.: Snow water equivalent retrieval in a Canadian boreal environment from microwave measurements using the HUT snow emission model, IEEE Transactions on Geoscience and Remote Sensing , 42, 1850–1859, 2004.

Roy, A., Picard, G., Royer A., Montpetit, B., Dupont, F., Langlois, A., Derksen, C., Champollion, N.; Brightness temperature simulations of the Canadian seasonal snowpack driven by measurements of the snow specific surface area, IEEE Transactions on Geoscience and Remote Sensing, available online, doi:10.1109/TGRS.2012.2235842, 2013.

Rutter, N. and 50 others authors: Evaluation of forest snow processes models (SnowMIP2), Journal of Geophysical Research, 114, D06111, 2009.

Scinocca, J., McFarlane, N., Lazare, M., Li, J., and Plummer, D.: The CCCma third generation AGCM and its extension into the middle atmosphere, Atmospheric Chemistry and Physics Discussions, 8, 7883–7930, 2008.

Sommerfeld, R. and LaChapelle, E.: The classification of snow metamorphism, Journal of Glaciology, 9, 3–17, 1970.

Sturm, M., Holmgren, J., König, M., and Morris, K.: The thermal conductivity of seasonal snow, Journal of Glaciology, 43, 26–41, 1997.

Sun, S., Jin, J., and Xue, Y.: A simple snow-atmosphere-soil transfer model, Journal of Geophysical Research, 104, 19587–19597, 1999.

Taillandier, A.-S., Domine, F., Simpson, W. R., Sturm, M., Douglas, T. A., and Severin, K.: Evolution of the snow area index of the subarctic snowpack in central Alaska over a whole season. Consequences for the air to snow transfer of pollutants, Environmental Science & Technology, 40, 7521-7527, 2006.

Taillandier, A.-S., Domine, F., Simpson, W. R., Sturm, M., and Douglas, T. A.: Rate of decrease of the specific surface area of dry snow: Isothermal and temperature gradient conditions, Journal of Geophysical Research., 112, F03003, 2007.

Teutschbein, C., and Seibert, J.: Regional climate models for hydrological impact studies at the catchment scale: a review of recent modeling strategies, Geography Compass, 4 (7), 834–860, 2010.

Toure, A., Goïta, K., Royer, A., Kim, E., Durand, M., Margulis, S., and Lu, H.: A Case study of using a multilayered thermodynamical snow model for radiance assimilation, IEEE Transactions on Geoscience and Remote Sensing, 9, 2828-2837, 2011.

Turcotte, R., Fortin, L.-G., Fortin, V., Fortin, J.-P., and Villeneuve, J.-P.: Operational analysis of the spatial distribution and the temporal evolution of the snowpack water equivalent in southern Québec, Canada, Nordic Hydrology, 38, 211–234, 2007.

Vachon, F., Goïta, K., De Sève, D., Royer, A.: Inversion of a snow emision model calibrated with in situ data for snow water equivalent monitoring, IEEE Transactions on Geoscience and Remote Sensing, 48, 59-71, 2010.

Verseghy, D.: CLASS- A Canadian land surface scheme for GCMs, I. Soil model, International Journal of Climatology, 11, 111–133, 1991.

Verseghy, D., McFarlane, N., and Lazare, M.: CLASS- A Canadian land surface scheme for GCMs, II. Vegetation model and coupled runs, International Journal of Climatology, 13, 347–370, 1993.

Verseghy, D.: CLASS - The Canadian Land Surface Scheme (Version 3.4) : Technical Documentation (Version 1.1), 2009.

Vionnet, V., Brun, E., Morin, S., Boone, A., Faroux, S., Le Moigne, P., Martin, E., and Willemet, J.: The detailed snowpack scheme Crocus and its implementation in SURFEX v7, Geoscientific Model Development, 5, 773–791, 2012.

Wiscombe, W. and Warren, S.: A model for the spectral albedo of snow. I: Pure snow, Journal of the Atmospheric Sciences, 37, 2712–2733, 1980.

Chapitre 5: A Simple Parameterization for a Boreal Forest Radiative Transfer Model at Microwave Frequencies

« Paramétrisation Simple d'un Modèle de Transfert Radiatif Micro-onde en Forêt Boréale »

Auteurs : Roy, A., Royer, A., Wigneron, J.-P., Langlois, A., Bergeron, J., Cliche, P.

Article publié dans le Journal *Remote Sensing of Environment* (2012), vol. 124, p. 371-383.

Résumé:

L'impact de la canopée forestière sur les mesures micro-ondes passives est important, mais peu documenté, particulièrement pour les forêts boréales denses. L'objectif de l'étude est d'évaluer la paramétrisation de l'émissivité d'une forêt de conifères denses à quatre fréquences AMSR-E (37, 19, 10.7 et 6.9 GHz). Le modèle de transfert radiatif τ-ω est utilisé, mais en considérant la transmissivité (γ) à un angle d'incidence de 55° pour l'épaisseur optique (τ). L'approche d'inversion se fait en 3 étapes : 1) des mesures aéroportées à haute résolution à 19 et 37 GHz ont été utilisées pour inverser les paramètres effectifs de la forêt (γ-ω), sachant l'émission de la surface neige-sol à partir de pixels où la forêt est absente, 2) ces valeurs sont ensuite comparées avec des données radiométriques in situ sur différents sites où des mesures de T_B ont été prises au-dessus et en dessous de la canopée, 3) ces valeurs de γ-ω sont ensuite utilisées sur une base de données AMSR-E d'été en forêt boréale dense. Les valeurs obtenues à partir des données aéroportées sont cohérentes avec les mesures in situ, ainsi qu'avec les données satellitaires. Nous avons trouvé qu'aux fréquences d'AMSR-E, les valeurs de transmissivité diminuent en fréquence de 0.67 à 0.41. L'albédo de diffusion (ω) peut-être considéré indépendant en fréquence avec $\omega \approx 0.064 \pm 0.005$. Une paramétrisation de l'émissivité du sol en forêt boréale (modèle QH) aux différentes fréquences est aussi proposée. Nous discutons ensuite de ces nouvelles valeurs de γ-ω ainsi que de la paramétrisation du sol, en mettant les résultats en perspective avec la littérature. Les résultats sont particulièrement intéressants pour différentes applications en télédétection basées sur les micro-ondes passives en forêt boréale, comme l'estimation de l'humidité du sol ainsi que la caractérisation de la neige sous la canopée.

5.1 Présentation de l'article

En forêt boréale, la canopée forestière masque une partie du signal provenant du sol et émet du rayonnement. Ainsi, pour simuler les T_B à l'aide du couplage MTR/CLASS, une prise en compte de la végétation est nécessaire (figure 1.5). L'objectif de cet article est donc de paramétriser le modèle γ-ω pour une forêt boréale dense. L'étude utilise une base de données multiéchelles (in situ, aéroportée, satellitaire) et multi-temporelle (été et hiver) pour inverser les paramètres de végétation ainsi que les paramètres de réflectivité du sol (Sect. 2.1.2). Les sites de forêts denses ont été priorisés dans cette partie de l'étude pour s'assurer d'avoir une contribution maximale de la végétation. De plus, les conifères représentent le peuplement le plus important de la forêt boréale. L'étude s'est donc concentrée sur la forêt de conifère dense. Cette étude se veut surtout une première analyse afin de mieux comprendre les interactions végétation-sol en termes de signal MOP.

Ce travail soulève la difficulté de découpler l'effet du sol et de la végétation en tentant de paramétriser quatre variables. Par contre, l'indépendance de γ-ω en polarisation démontrée dans l'étude, permet de considérer deux mesures (polarisation horizontale et verticale) pour inverser les deux paramètres de végétation, ce qui permet une meilleure convergence. En accord avec la littérature, il semble aussi que H_R ainsi que ω puissent être considérés constants en fréquence. L'étude soulève aussi la difficulté de comparer des mesures prises à différentes échelles à cause de l'incertitude reliée aux mesures de paramètres structuraux, mais aussi à l'ambigüité de savoir ce que le radiomètre voit en réalité aux différentes échelles. Par exemple, au niveau satellitaire, il y a toujours des clairières ou des ouvertures dans un pixel, tandis que les mesures in situ sont très sensibles à l'endroit où pointe le radiomètre dans la forêt à cause du fort contraste entre les T_B des troncs et les T_B de l'atmosphère (trouées).

Cette étude offre ainsi d'importantes nouvelles informations et connaissances sur la paramétrisation du modèle γ-ω dans la forêt boréale pour quatre fréquences (37, 19, 10.7 et 6.9 GHz). Dans le cadre du couplage MTR/CLASS sur l'ensemble de la forêt boréale, les Chaps. 6 et 7 traiteront des relations entre γ et des paramètres structuraux de la végétation pour la spatialisation. Des paramètres Q_R, H_R et ω représentatifs de l'ensemble de la forêt boréale seront aussi inversés. À noter que des corrections ont été apportées à la figure 5.6b (explication des mesures manquantes) et à la figure 5.7 (correction des axes) par rapport à l'article publié.

A simple parameterization for a boreal forest radiative transfer model at microwave frequencies

Alexandre Roy[a*], Alain Royer[a], Jean-Pierre Wigneron[b], Alexandre Langlois[a], Jean Bergeron[a], Patrick Cliche[a]

[a] Centre d'applications et de recherches en télédétection, Université de Sherbrooke, 2500 boul. Université, Sherbrooke, Qc, Canada, J1K 2R1.

[b] INRA, UR 1263 EPHYSE, F-33140 Villenave d'Ornon, France.

Abstract

The impact of forest cover on passive microwave measurements is important but not well documented, particularly for dense boreal forests. The objective of this study was to evaluate a parameterization of the forest emissivity, for dense needleleaf forests at four *Advanced Microwave Scanning Radiometer for the Earth Observing System* (AMSR-E) frequencies (37, 19, 10.7, and 6.9 GHz). The τ-ω radiative transfer model was used, but considering transmissivity (γ) at an incident nadir angle of 55° for the optical thickness (τ). The approach was as follows: 1) high resolution airborne data at 19 and 37 GHz were used to derive the equivalent or effective forest parameters (γ-ω) knowing the contribution of the snow-soil emission from non-forested pixels, 2) these γ-ω values were verified using winter radiometric in situ measurements from different forest sites where the brightness temperature (T_B) values above and under the canopy were considered, 3) these γ-ω values were applied and the frequency was extended on a large AMSR-E summer dataset for dense boreal forest sites. The airborne-derived values were consistent with in situ measurements as well as with satellite-based observations. We found that at AMSR-E frequencies, transmissivity values spectrally decreased from 0.67 to 0.41 for frequencies from 6.9 to 37 GHz. The single scattering albedo (ω) can be considered frequency independent at $\omega \approx 0.064 \pm 0.005$. A soil parameterization (QH model) at different frequencies was also proposed for boreal forests. We discuss these new γ-ω values and the soil parameterization within the context of the relevant literature. The results are of particular interest for various remote sensing applications based on passive microwave sensor observations over boreal forests, such as the retrieval of soil moisture and the monitoring of snow characteristics under the canopy.

Keywords: single scattering albedo, transmissivity, boreal forest, AMSR-E, passive microwave brightness temperatures, QH soil parameterization, airborne.

5.2 Introduction

The forest canopy and the surface state under forested areas, such as the soil moisture and snow cover, are key parameters in surface-climate interactions. The forest itself can have feedback effects on climate through phenological shifts or changes in biomass growth resulting from climate change (Penuela et al., 2009; McMahon et al., 2010). In addition, soil moisture that is directly linked to changes in the precipitation rate can also impact climate change (Hirschi et al., 2010). Consequently, poor estimates of soil moisture can significantly decrease the prediction skill of climate models (Ni-Meiste et al., 2006). Another important variable in near-surface climate processes is the snow cover under forested areas (e.g. Betts et al., 2001). Forest cover can significantly modify snow evolution that, in turn, impacts the hydrology of these areas (see Andreadis et al., 2009; Roy et al., 2010).

Passive microwave measurements from satellites are a promising tool for deriving surface characteristics in natural and forested ecosystems (Kerr et al., 2001). For these ecosystems, several studies have evaluated the potential of passive microwave observations for monitoring soil moisture (Njoku et al., 2003; Paloscia et al., 2006; Grant et al., 2007; Cano et al., 2010, Kurum et al., 2011), litter moisture content (Saleh et al., 2006; Grant et al., 2007; Guglielmetti et al., 2008), and snow (e.g. Mätzler, 1987; Kelly et al., 2003; Derksen, 2008).

Satellite passive microwave measurements can also be used to monitor the vegetation canopy. This could provide useful information about the vegetation biomass or the plant water content (Jackson and Schmugge, 1991; Jackson et al. 2004; Calvet et al., 1994; Wigneron et al., 1997), water interception effects (Saleh et al., 2006), and vegetation phenology linked to the carbon cycle (e.g. Jones et al., 2011). All of these objectives require a good parameterization of the vegetation canopy at the scale of the radiometer's field-of-view (Van de Griend and Wigneron, 2004a, b).

The forest canopy has a strong impact on microwave measurements through the attenuation of the signal emitted from the surface (soil or snow) and by emitting its own energy both toward the satellite and the ground (Ferrazzoli et al., 2002; Pampaloni, 2004). The careful decoupling of the forest canopy signal from the surface signal in observations of the brightness temperature (T_B) is of particular importance in microwave radiometry. Complex models that separately consider the scattering/absorption effects of the crown and trunk layers have been developed (Ferrazzoli and Guerriero, 1996; Karam, 1997, Kurum et al., 2011). However, these methods are less suitable for studies at *Advanced Microwave Scanning Radiometer for the Earth Observing System* (AMSR-E) spatial resolutions because they need precise information about the vegetation, which is not available at AMSR-E footprint sizes. Thus, in general, simplified radiative transfer models are used for applications based on spaceborne-observations. A simplified radiative transfer model called the τ-ω model is the most commonly used; it characterizes the forest canopy considering the optical thickness of the vegetation τ (or the transmissivity γ) and the single scattering albedo ω (Mo et al., 1982; Ulaby et al., 1986; Wigneron et al., 2004).

The transmissivity γ_p can be defined in terms of the optical depth such that $\gamma_p = \exp(-\tau_p/\cos\theta)$, where θ is the angle at nadir and the subscript p is for the polarization. The term γ (the subscript p is hereafter omitted for simplicity) will be used in this study instead of τ because the viewing angle of the AMSR-E is constant at 55°. The τ-ω model is a widely used empirical 0^{th}-order radiative transfer model that only accounts for radiation scattered by the canopy in the forward direction. In the model, a vegetation layer lying above the soil surface is considered as a plane parallel absorbing and scattering medium characterized by a constant temperature and the equivalent or effective vegetation parameters γ-ω (Ferrazzoli et al., 2002 ; Pampaloni, 2004).

This 0^{th}-order model, which neglects the scattering source function, is physically less correct than single-scattering or multiple scattering solutions of the radiative transfer equations (see the review of Matzler et al., 2006). However, this model is very tractable for retrieval applications and widely used in the scientific community (thus allowing a comparison with other studies of our retrieved values for the model parameters). Moreover, as long as the γ and ω parameters are considered as effective or equivalent parameters (as opposed to physical parameters), several studies based on comparisons with complex modeling approaches showed that accurate simulations of the vegetation-covered surfaces could be performed based on a simplified 0^{th}-order

approach (Ferrazzoli.et al., 2002, Kurum et al., 2012). For instance, Kurum et al. (2012) showed that ω can, in fact, be considered as an effective parameter that accounts for all processes taking place within the canopy including multiple scattering.

The main limitation of microwave applications lies in the poor documentation of γ-ω and soil reflectivity for numerous ecosystems, including for boreal forests. Some studies have derived γ values as a function of the stem volume in boreal forests for 19 and 37 GHz using airborne data by neglecting ω (Kruopis et al., 1999; Langlois et al., 2010a). These studies reported different values and also diverged from the values obtained from ground-based radiometer measurements (Pardé et al., 2005). At lower frequencies (6.6 and 10.7 GHz), Pellarin et al. (2006) derived γ from a relationship with the Leaf Area Index (LAI) using a factor (b_v). They retrieved forest parameters (b_v-ω) by testing all possible combinations for the b_v factor, ω, and soil parameters leading to the best agreement between simulated and measured Scanning Multichannel Microwave Radiometer's (SMMR) T_B for 12 different areas. They obtained values of ω=0.06 at 10.7 and 6.6 GHz for Siberian coniferous forest, while for Canadian coniferous forests they obtained ω = 0.06 at 10.7 GHz and ω = 0.08 at 6.6 GHz. However, the optimum value for the combined coniferous site was ω = 0.06 for both frequencies. The optimum b_v factor for both frequencies and both sites was $b_v = 0.2$. Using ground-based measurements (incident angle = 60°) from a deciduous forest, Santi et al. (2009) obtained γ values ranging from around 0.1 for trees with leaves to 0.4 for defoliated trees for 37 GHz, 6.8 GHz, and 10 GHz; at 1.4 GHz, γ values varied from 0.25 to 0.5. Guglielmetti et al. (2007) also showed similar values at 1.4 GHz and 11.4 GHz. These two studies also showed a predominant contribution from branches and leaves and a minor effect from trunks. Few values of ω have been estimated: Meissner and Wentz (2010) obtained a slight increase of $\omega \approx 0.055$ at 6.9 GHz to $\omega \approx 0.07$ at 37 GHz for a tropical forest at AMSR-E frequencies (but assuming the transmissivity was 0); in the *Soil Moisture and Ocean Salinity* (SMOS) project, a value of ω = 0.08 was used for needleleaf forests at 1.4 GHz (SMOS, 2011); Grant et al. (2008) obtained ω = 0.07 over mature coniferous and deciduous canopies from in situ measurements at the L-band. Jones et al. (2011) set ω at 0.05 in order to retrieve the variability of the vegetation optical depth from AMSR-E data.

With increasing biomass in the vegetation layer, the attenuation of the surface microwave emission is expected to increase with higher scattering by the vegetation, especially at higher

frequencies. An improved quantification and understanding of these attenuation γ and scattering ω effects are required for the accurate retrieval of snow and soil properties as well as for the analysis of the canopy. The main difficulty in retrieving these parameters from T_B is decoupling the effects of both ω and γ, on one hand, and soil parameterization on the other hand (Van de Griend and Wigneron, 2004a, b; Pellarin et al., 2006; Grant et al., 2008). Setting ω to a fixed value in order to retrieve γ (or the canopy optical depth) (e.g., Jones et al., 2011) or deriving a γ value from the LAI canopy in order to retrieve the surface (soil or snow) parameter under the canopy (e.g. Pellarin et al., 2006) could both potentially lead to inaccurate estimates depending on the type of vegetation (forest) considered. Furthermore, changes in the soil parameterization can also lead to obtaining different vegetation parameters (Pellarin et al., 2006). Thus, incorrect estimates could result in erroneous partitioning of the contributions from the surface and the canopy. Parameters must thus be retrieved simultaneously with datasets that adequately constrain the retrieval in order to avoid the indetermination associated with an infinite number of solutions.

The objective of this study was to derive γ and ω for a dense needleleaf boreal forest at the AMSR-E spatial scale using three different datasets: winter airborne measurements, in situ winter radiometric measurements, and summer AMSR-E satellite data. The multi-scale and multi-data approach allowed us to resolve the soil-vegetation decoupling. The study was mostly conducted with the aim of correcting the influence of vegetation on the retrieved soil characteristics at AMSR-E frequencies. The attenuation effect of vegetation at different microwave frequencies was also evaluated to verify the usefulness of AMSR-E data for monitoring surface characteristics under dense boreal forests. The values of γ and ω were then compared with other studies and the component of each element contributing to the signal received by the sensor (soil, vegetation, and atmosphere) was evaluated and discussed.

5.3 Methods

In this section, we first present the radiative transfer model used in the study. Second, we describe the method applied to derive the vegetation parameters with the airborne winter dataset and to derive the soil parameters with the summer satellite data. The approach was as follows: 1) high resolution airborne data were used to derive the γ-ω forest parameters knowing the contribution of the snow-soil emission from forest-free pixels, 2) these γ-ω values were compared to winter in situ measurements from different forest sites where T_B values above and under the

canopy were considered, 3) these γ-ω values were applied to AMSR-E summer data for dense boreal sites with fitted soil parameters. Each step is described in detail below.

5.3.1 Radiative transfer model

The T_B measured over a forest canopy $T_{Bforest}$ (neglecting the atmosphere) is often modeled using the simplified radiative transfer model generally called the τ-ω model (see Ferrazzoli et al., 2002 where the coefficients were fit to the outputs of a discrete physical model, or see Grant et al., 2008). The model was presented as

$$T_{\mathrm{B}\,forest} = T_{B\,surface} + T_{B\,veg} + T_{B\,veg-r}\,. \tag{5.1}$$

From eq. 5.1, we further defined

$$T_{B\,surface} = \gamma\, e_{surface} T_{surface}, \tag{5.1a}$$

$$T_{B\,veg} = (1-\omega)(1-\gamma)T_{veg}\,, \tag{5.1b}$$

$$T_{B\,veg-r} = \gamma(1-\omega)(1-\gamma)(1-e_{surface})T_{veg}\,, \tag{5.1c}$$

where $e_{surface}$ is the emissivity of the surface under the forest canopy, $T_{surface}$ is the surface temperature (K), and T_{veg} is the vegetation temperature (K). Thus, $T_{\mathrm{B}surface}$ refers to the emission of the surface under the canopy attenuated by the forest; $T_{\mathrm{B}veg}$ is the direct emission from the forest; $T_{\mathrm{B}veg\text{-}r}$ is the downwelling forest emission reflected by the surface.

From a satellite perspective, such as the AMSR-E, the atmospheric contributions must be taken into consideration such that

$$T_{\mathrm{B}\,forest} = [T_{\mathrm{B}surface} + T_{\mathrm{B}veg} + T_{\mathrm{B}veg-r} + T_{\mathrm{B}atm\downarrow-r-s} + T_{\mathrm{B}atm\downarrow-r-veg}]\ \gamma_{atm} + T_{\mathrm{B}atm\uparrow}\,, \tag{5.2}$$

and

$$T_{\mathrm{B}atm\downarrow-r-s} = T_{\mathrm{B}atm\downarrow}\gamma^2(1-e_{surface})\,, \tag{5.2a}$$

$$T_{\mathrm{B}atm\downarrow-r-veg} = \omega(1-\gamma)T_{\mathrm{B}atm\downarrow}, \tag{5.2b}$$

where $T_{\mathrm{B}atm\downarrow}$ and $T_{\mathrm{B}atm\uparrow}$ are respectively the downwelling and upwelling brightness temperatures, and γ_{atm} is the atmospheric transmissivity. The terms $T_{\mathrm{B}atm\downarrow\text{-}r\text{-}s}$ and $T_{\mathrm{B}atm\downarrow\text{-}r\text{-}veg}$ are respectively the $T_{\mathrm{B}atm\downarrow}$ reflected by the surface and the forest canopy. The term $\omega(1-\gamma)$ in eq. 5.2b represents the forest reflectivity derived from Kirchoff's law taking into consideration forest emissivity as $(1-\omega)(1-\gamma)$.

The atmospheric parameters ($T_{\mathrm{B}atm\downarrow}$, $T_{\mathrm{B}atm\uparrow}$, and γ_{atm}) were modeled using the atmospheric model implemented in the Helsinki University of Technology (HUT) snow emission model (Pulliainen et al., 1999). The atmospheric model was driven with the air temperature and air moisture of the atmospheric layer above the surface from the 29 North American Regional Reanalysis (NARR) atmospheric layers (Sect. 5.3.4). The model considers the radiative transfer through the atmospheric layers and provides values of $T_{\mathrm{B}atm\downarrow}$ and γ_{atm} over the canopy level and $T_{Batm\uparrow}$ at the satellite sensor level. For the terms $T_{\mathrm{B}atm\downarrow\text{-}r\text{-}v}$ and $T_{\mathrm{B}atm\downarrow\text{-}r\text{-}s}$, the values corresponding to the integrated signal coming from all directions have to be considered. This hemispherical downwelling contribution was derived from an effective angle θ_{eff} that was defined following the relation of Mätzler and Rosenkranz (2007) considering γ_{atm} at nadir where

$$\theta_{eff} = 59.936 - 34.081 \cdot -\ln(\gamma_{atm\text{-}nad}) + 67.105 \cdot (-\ln(\gamma_{atm\text{-}nad}))^2 - 78.331 \cdot (-\ln(\gamma_{atm\text{-}nad}))^3 + 34.371 \cdot (-\ln(\gamma_{atm\text{-}nad}))^4 \tag{5.3}$$

Therefore, $\gamma_{atm\text{-}nad}$ was calculated with NARR atmospheric data and the HUT atmospheric model to derive θ_{eff} (eq. 5.3) and, afterward, $T_{\mathrm{B}atm\downarrow}$. Values for $T_{\mathrm{B}atm\uparrow}$ and γ_{atm} were calculated with the same model for an angle of 55° (AMSR-E angle).

For an airborne sensor, the attenuation effect of the atmosphere is negligible and the radiative transfer model can be simplified to

$$T_{B\,forest} = T_{B\,surface} + T_{B\,veg} + T_{B\,veg-r} + T_{B\,atm\downarrow-r-s} + T_{B\,atm\downarrow-r-veg}\,. \tag{5.4}$$

5.3.2 Airborne winter dataset

The 19 and 37 GHz airborne data were collected on 19 February, 2008, during the Canadian International Polar Year project (IPY) called *Variability and Change in the Canadian Cryosphere* which took place in northern Québec, Canada (see Langlois et al., 2010 for more detail). The radiometer installation on the National Research Council's Twin Otter aircraft as well as the calibration procedure and associated uncertainty for the IPY airborne campaign is described in Derksen et al. (2010). The radiometer's stability depended on the frequency and varied somewhat between missions, but the overall precision was estimated at ± 2 K at 19 GHz and < 1 K at 37 GHz. The ground field of view at a 54° angle of incidence was approximately 120 m by 200 m. The flight lines were conducted from Sept-Iles to Kangirsuk; the aircraft completed a series of loops called a "cloverleaf" pattern approximately every 40 km over each sampling site. Each site included in situ sampling of snow properties and forest characteristics (Langlois et al., 2010). Snowpits were also dug, and a temperature profile was measured at 3 cm intervals using a Traceable 2000 digital temperature probe (± 0.1°C).

For this study, two of the cloverleaf flight patterns above the dense boreal forest were chosen (figure 5.1). The γ-ω values for the forest canopy were retrieved from the airborne 19 and 37 GHz observations using eq. 5.4. The selection of T_B ($T_{Bsurface}$ over forest-free surfaces or $T_{Bforest}$ over forested surfaces) was based on the Land Cover Map of Canada 2005; the Canadian Centre for Remote Sensing (Natural Resources Canada, Ottawa, Canada) produces this map (Latifovic et al., 2004). As described by Langlois et al. (2011), the $T_{Bforest}$ values were associated with the two cloverleaf airborne T_B located in class 1 (Evergreen needleleaf forest, closed tree canopy: crown cover > 60%) or 6 (Evergreen needleleaf forest, open tree canopy: crown cover 25-60%) for 609 values. The term $T_{Bsurface}$ was derived by taking the average T_B of snow (T_{Bsnow}) over open areas (according to the Land Cover Map). The airborne measured $T_{Bforest}$ ranged from 230.5 to 256.9 at 19V, 192.0 to 254.7 at 19H, 212.7 to 257.1 at 37 V, and 199.3 to 256.2 at 37H. The mean T_{Bsnow} values were respectively 237.6, 223.0, 211.9, and 201.5. We found that the T_{Bsnow} values were coherent; they showed lower T_B values over open areas than over the forest canopy, lower values at 37 GHz compared to 19 GHz (higher scattering for higher frequency) (Mätzler and Wiesmann, 1999), and also lower values at H polarization compared to V polarization (effect of stratification within the snowpack) (Durand et al., 2008). To estimate the value of $e_{surface}$, T_{Bsnow} was divided

by the average measured T_{snow}. The values of T_{veg}, as well as the atmospheric parameters, were derived using the NARR data (see Sect. 5.3.4).

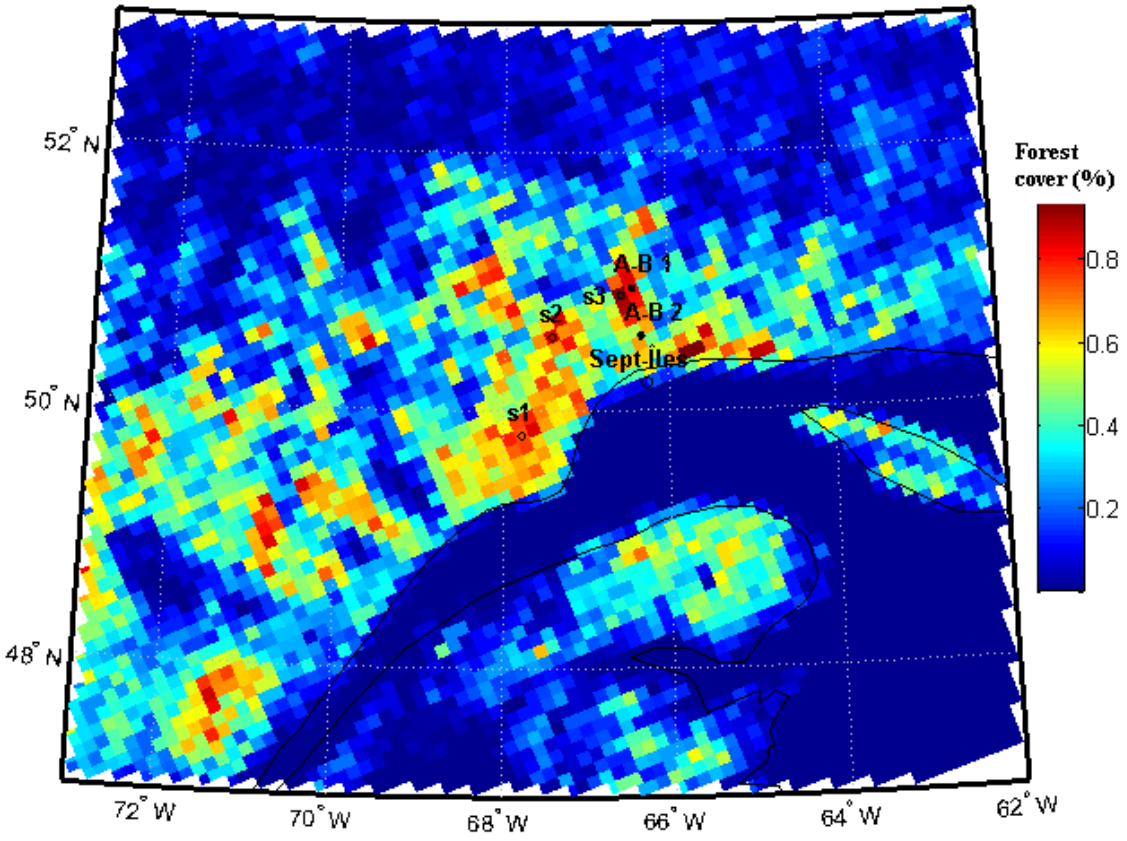

Figure 5.1: The study sites in Quebec, southeastern Canada (s=AMSR-E; A-B = airborne). The colorbar shows the dense boreal forest cover from the Land Cover Map of Canada (2005) (class 1) on a 12.5 km EASE-grid.

The boreal forest in the study region was mostly populated with black spruce (*Picea mariana*). Black spruce trees have a horizontal branch structure with shoots that are mostly oriented parallel to the plane of the branches (Leblanc et al., 1999). Figure 5.2 shows a picture of a typical black spruce forest close to the Sept-Iles meteorological station.

Figure 5.2: A photograph of a typical black spruce forest near the Sept-Iles meteorological station.

5.3.3 In situ measurements

Radiometric measurements were carried out for similar natural coniferous (*Abies balsamea* and Picea *rubens*) plots with different densities in St-Romain (45.76ºN, 71.04ºW), Québec, during the winter of 2010 using surface-based passive microwave radiometers (Radiometrics Corp.). The soil was covered by snow during the measurements. Tree diameter-breast-height (DBH), height, density, and species were measured at each sampling site. The DBH is the outside bark diameter at breast height (1.37 m) above the forest floor on the uphill side of the tree. Tree measurements were taken individually within a 10 m diameter sampling zone. The dry biomass was calculated for each tree using the equations proposed by Ter-Mikaelian and Korzukhin (1997) for different types of vegetation (DBH-dependent). The stem volume (SV, in $m^3 \cdot ha^{-1}$) was then calculated from the estimated dry biomass, the basal volume, and the mass specific to each species; the SV was summed up for the sampling zone.

For the in situ measurements, the radiometers were pre- and post-calibrated during the winter using warm (ambient temperature microwave absorber) and cold (liquid nitrogen) targets. The setup for the in situ microwave measurements is shown in figure 5.3. Three radiometric measurements were carried out at each site with an incident nadir angle of 55°: (a) downward looking from the top of the trees ($T_{\mathrm{B}up}$: labeled as 1 in figure 5.3); (b) upward observations from the soil level ($T_{\mathrm{B}down}$: labeled as 2 in figure 5.3); (c) and downward-looking observations close to the soil below the trees ($T_{\mathrm{B}surface\text{-}forest}$: labeled as 3 in figure 5.3) in the footprint of the first measurement.

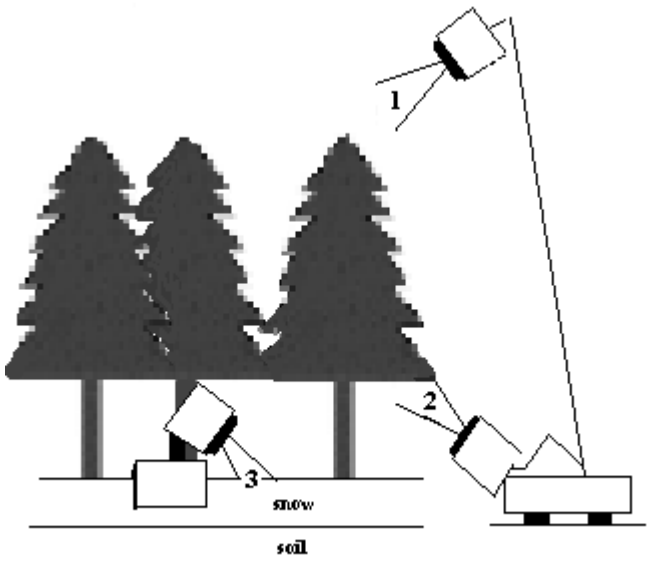

Figure 5.3: The setup for the in situ microwave measurements of a coniferous forest.

Considering that $T_{\mathrm{B}surface\text{-}forest}$ measured $T_{\mathrm{B}surface}$, $T_{\mathrm{B}veg\text{-}r}$ and $T_{\mathrm{B}atm\downarrow\text{-}r\text{-}s}$, under the canopy, eq. 5.4 was simplified to represent $T_{\mathrm{B}up}$ (above the canopy) with $T_{\mathrm{B}surface\text{-}forest}$ as:

$$T_{\mathrm{B}up} = T_{\mathrm{B}surface\text{-}forest} \cdot \gamma + T_{\mathrm{B}veg} + T_{\mathrm{B}atm\downarrow\text{-}r\text{-}veg} \tag{5.5}$$

while $T_{\mathrm{B}down}$ (under the canopy) was modeled considering the tree emission, sky emission, and the soil emission reflected by the forest:

$$T_{\mathrm{B}down} = T_{\mathrm{B}veg} + T_{\mathrm{B}surface\text{-}forest} \cdot \omega(1-\gamma) + T_{\mathrm{B}atm\downarrow}\gamma \tag{5.6}$$

From these two equations, only γ-ω remained unknown and was inverted using measured T_{Bup}, T_{Bdown}, and $T_{Bsurface\text{-}forest}$ values. Retrieved vegetation parameters were then compared with the calculated stem volume at each site.

5.3.4 AMSR-E summer dataset

Three sites with dense needleleaf forests located near the Sept-Iles (Quebec, Canada) meteorological station (50°13'N; 66°16'W) were selected for the AMSR-E observations (figure 5.1). The selection of these sites was based on the Land Cover Map resampled on a 12.5 km by 12.5 km AMSR-E grid. The pixels with eight neighbors that contained the highest percentage of Land cover class 1 were selected. While the three sites showed percentages of class 1 over 65%, the total forest coverage was higher than 90% (figure 5.1). The forest covers that were not class 1 were mainly class 6. The Leaf Area Index (LAI) was also calculated from the 8-day LAI product derived from MODIS AQUA (MYD15A2) (Yang et al., 2006). The LAI was used for the purpose of comparison to calculate γ at 6.9 and 10.7 GHz using the method of Pellarin et al. (2006) and at 1.4 GHz using SMOS (2011). The average value of the LAI over the study period (see below) was considered. The stem volumes were also derived from the Système d'Information ÉcoForestier (SIEF) database produced by Québec's ministère des Ressources naturelles et de la Faune. The SIEF vector SV values were merged with the Land cover class to associate a SV value with each class. Table 1 shows that the three selected sites had an equivalent amount of dense forest cover. These forest sites were exceptionally dense at the scale of the AMSR-E pixels and sufficiently homogeneous to avoid strong variations that could occur with variations in the AMSR-E swath footprint between orbit passes.

Table 5.1: Vegetation characteristics at the three AMSR-E selected sites.

	% of class 1 in the central pixel	Average % of class 1 in the central pixel and its neighbouring pixels	Average % of forest cover in the central pixel and its neighbouring pixels	SV m^3 ha^{-1}	LAI
Site1	84.4	65.9	92.8	84.0	1.85
Site2	84.6	73.2	91.8	78.4	2.40
Site3	93.4	68.3	90.4	85.9	2.07

The AMSR-E/Aqua L2A Global Swath Spatially-Resampled Brightness Temperatures, which are available from the National Snow and Ice Data Center (NSIDC), were used in this study. The spatial resolution with a 37 km footprint (Res. 2) was used for all frequencies (10.7, 18.7, and

36.5 GHz) except for 6.9 GHz where only the spatial resolution at a 56 km footprint (Res. 1) was available. Only the ascending pass was used (about 13h00 local time) to avoid night-time dew effects (Lin and Minnis, 2000).

The study was carried out from 1 July to 1 October for the years 2005 and 2008. These years were chosen because July 2005 and August 2008 were particularly dry, and August 2005 was particularly wet (table 5.2). Using these datasets, we obtained a strong contrast in the soil conditions while the vegetation characteristics remained almost unchanged. This contrast may have helped to separate the soil from the forest contributions. In order to avoid rain and cloud effects on T_B (Lin and Minnis, 2000), we excluded days when the recorded daily precipitation measured at the Sept-Iles meteorological station exceeded 5 mm. The total number of points for the whole summer dataset was 447 (3 sites and 149 days). The ranges for the AMSR-E brightness temperatures ($T_{Bforest}$ from eq. 5.2) for all frequencies and polarizations are shown in table 3.

Table 5.2: Monthly cumulated precipitation measured at the Sept-Iles meteorological station.

	July	August	September
2005	33.3mm (1st most dry*)	155.8 mm (7th most wet*)	104.7mm
2008	112.1 mm	46.1mm (8th most dry*)	124.3mm

* based upon the last 60 years (http://www.climat-quebec.qc.ca/)

Table 5.3: Ranges of values for measured AMSR-E $T_{Bforest}$, and calculated $T_{Batm\uparrow}$.

	AMSR-E $T_{Bforest}$	$T_{Batm\uparrow}$
6.9V	276-254	6-8
6.9H	266-239	6-8
10V	281-259	7-11
10H	273-249	7-11
19V	288-263	13-45
19H	282-255	13-45
37V	289-265	26-48
37H	284-258	26-48

Several variables characterizing the atmosphere and the surface were obtained from the NARR data (Mesinger et al., 2006). The NARR horizontal resolution is 0.3° (≈32 km) and the temporal resolution is 8 times daily (every 3 hours). In this paper, we used the NARR near-surface air temperature for T_{veg}, the 0-10 cm soil temperature for $T_{surface}$, and the temperature/air moisture of the 29 atmospheric layers for the atmospheric contributions. Estimates of soil moisture were also obtained from the NARR data referred to as 1-10 cm soil moisture. It is known that the NARR

soil moisture data contains some uncertainty (Mesinger et al., 2006; Luo et al., 2007). However, figures 5.4a and b shows that these soil moistures are realistic and consistent with precipitation measurements from the Sept-Iles meteorological station. Even if a few discrepancies exist, the large number of days considered in this study would compensate for a few days where the soil moisture might not be totally accurate.

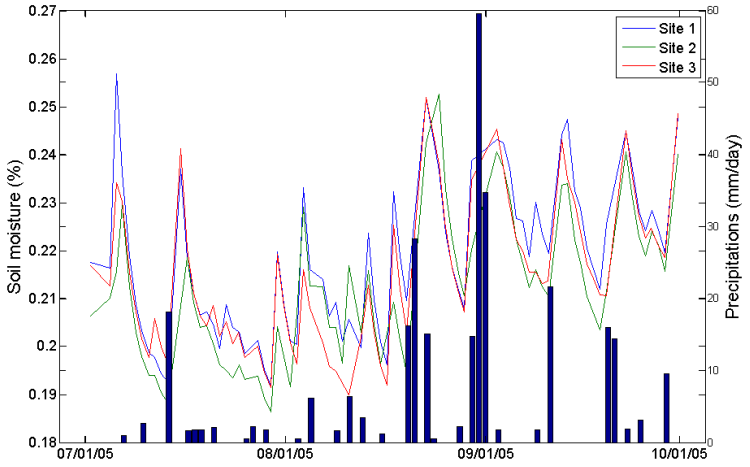

Figure 5.4a: The NARR soil moisture data versus daily precipitation data for the Sept-Iles meteorological station (2005).

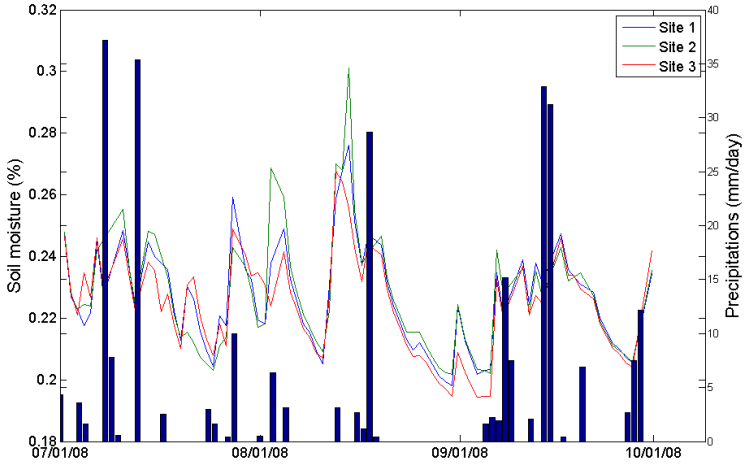

Figure 5.4b: Same as figure 5.4a, but for 2008.

Surface emissivity ($e_{surface}$) was modeled using the approach:

$$e_{surface} = 1 - r_{surface} \tag{5.7}$$

where $r_{surface}$ is the reflectivity of the surface, which is written as a function of the reflectivity of a plane surface ($r_{Fresnel\text{-}P}$ and $r_{Fresnel\text{-}O}$, with subscripts P and O representing H or V polarizations) using the QH model by Wang et al. (1983):

$$\mathrm{r_{surface}} = [(1 - Q_R) \cdot \mathrm{r_{Fresnel\text{-}P}} + Q_R \cdot r_{\mathrm{Fresnel\text{-}O}}] \cdot \exp(-H_R) \tag{5.8}$$

In this equation, H_R parameterizes the intensity of the roughness effects, and Q_R parameterizes the polarization mixing ratio effects (these parameters are labeled as QH parameters hereafter for simplicity). The $r_{Fresnel}$ was calculated considering the dielectric constant estimation proposed by Dobson et al. (1985).

The variables used in the retrieval procedures for airborne and AMSR-E datasets are summarized in table 5.4.

Table 5.4: **Variables used for γ-ω retrievals for both datasets.**

Variables	Airborne winter	AMSR-E summer
γ and ω	Unknowns	Airborne-derived values
$\boldsymbol{T_{Bsurface}}$	Forest-free airborne values (i.e. T_{Bsnow})	- $e_{surface}$ - NARR soil 0-10 cm temperature
$\boldsymbol{e_{surface}}$	T_{Bsnow}/T_{snow}	QH models (unknowns) : - NARR soil 0-10 cm temperature and moisture
$\boldsymbol{T_{veg}}$	NARR near-surface air temperature	NARR near-surface air temperature
$\boldsymbol{T_{Batm}\uparrow}$ & $\boldsymbol{\gamma_{atm}}$	Not applicable	HUT atmospheric model (Pulliainen et al., 1999)
$\boldsymbol{T_{Batm}\downarrow}$	HUT atmospheric model (Pulliainen et al., 1999) - 29 NARR layers air temperature/moisture - Mätzler et Rosenkranz (2007) for θ_{eff}	HUT atmospheric model (Pulliainen et al., 1999)

5.3.5 Combined dataset retrieval procedure

First, the root mean square errors (RMSE, unit K) between the simulated and measured T_B for the airborne datasets were calculated for all possible combinations of the different γ-ω couple values

with an iteration step of 0.001 for the γ values between 0 and 1 and ω between 0 and 0.3. For each case, at a given frequency and polarization, we thus obtained a three dimensional matrix that included the RMSE as the third variable. Among all the generated values, the γ-ω couple giving the lowest RMSE for both polarizations was then retrieved independently for each frequency. This approach implies that we considered $\gamma_H = \gamma_V$ and $\omega_H = \omega_V$, which is supported by many studies (Owe et al., 2001; Ferrazzoli et al., 2002; Pellarin et al., 2006; Kurum et al 2012). These assumptions were also confirmed by in situ γ-ω derived for the coniferous sites (see Sect. 5.4.2) where the polarization differences of γ and ω were very small (< 8%). Applying these retrieved vegetation parameters at 19 and 37 GHz to AMSR-E sites, a three dimensional matrix was calculated for different QH soil parameters (iteration step of 0.01 between 0 and 0.8) at the three AMSR-E sites. As previously done, the QH couple giving the lowest RMSE for both polarizations was retrieved independently for each frequency.

Based on the assumptions that H_R and ω were spectrally constant, it was then possible to retrieve Q_R and γ values at 6.9 and 10.7 GHz. An iteration on Q_R was independently done for 10.7 and 6.6 GHz to find the Q_R value that gave $\gamma_V = \gamma_H$. The assumption of a spectrally constant ω was based on Pellarin et al. (2006), who found ω = 0.06 at 6.6 and 10.7 GHz for a coniferous forest, and Meissner and Wentz (2010), who showed that the increase of ω from 6.9 to 19 GHz is rather small (0.015). Based on Pampaloni and Paloscia (1986) and Ulaby et al. (1983), Sahoo et al. (2008) also used a constant value of ω at 10.7 and 19.7 GHz. A comparison of the retrieved values with other studies also showed that the term ω, which is seen as an "effective" single scattering albedo, can be estimated to be spectrally constant. For H_R, Wang et al. (1983) showed frequency independency from 1.4 to 10.7 GHz, while Prigent et al. (2000) and Wigneron (unpublished data from ground-based measurements) showed with the PORTOS-93 dataset (Wigneron et al., 1995) that H_R values are similar at 23 and 36 GHz.

5.4 Results

5.4.1 Retrieval of γ-ω from the airborne winter dataset

First, the γ-ω values were retrieved from the 609 airborne winter $T_{Bforest}$ measurements. The RMSE between the simulated T_B and the airborne T_B at 19 and 37 GHz were calculated for values of γ varying from 0 to 1 with an increment of 0.01 and ω varying from 0 to 0.3 over the same increment. The RMSE values were plotted on a γ-ω axis graph; figure 5.5 shows the results at

vertical (V) and horizontal (H) polarizations at 19 and 37 GHz. The results indicated that, for both frequencies and polarizations, curves could provide solutions corresponding to all of the γ-ω couples that minimized the RMSE between the simulated and measured T_B (figure 5.5). For both frequencies, the H and V polarizations had solution curves (all ω values given the minimum RMSE for each γ) that intersected close to ω ≈ 0.064.

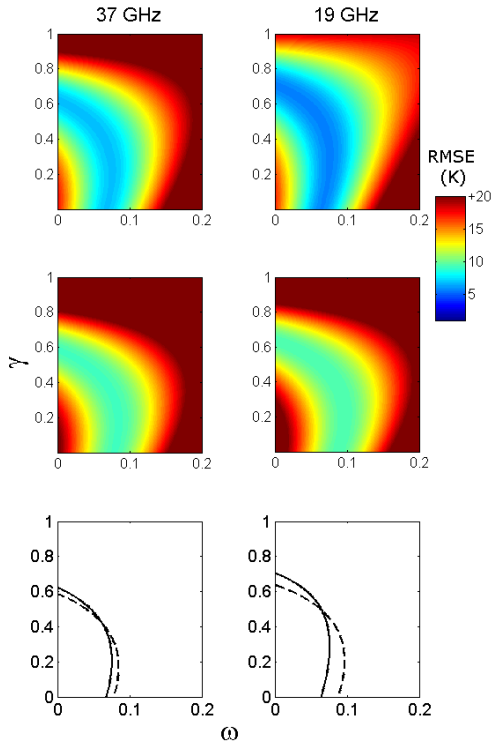

Figure 5.5: Airborne results at 37 and 19 GHz. Top: RMSE at V polarization; Middle: RMSE at H polarization; Bottom: solution curves (solid line is the V polarization and dotted line is the H polarization).

Thus, given $\omega_H = \omega_V$, a unique γ-ω solution was found for both frequencies (table 5.5). This result also showed that ω was almost constant (0.062 and 0.065) for both frequencies, confirming the hypothesis made in this study. Moreover, γ is lower at 37 GHz (0.423) than at 19 GHz (0.497), which is in agreement with the theoretical consideration that there is an increase of the penetration depth with decreasing frequency (Ulaby et al., 1986). The highest RMSE values at H polarization were probably due to the impact of snow layering (snow grain size/morphology, density, and ice lenses) that was more important at H than V polarization (e.g. Durand et al., 2008); consequently, variations in the snow emissivity at H polarization may have introduced a larger variability in the retrieved forest parameters.

Table 5.5: γ-ω and RMSE airborne dataset solutions considering $\omega_H = \omega_V$.

	37 GHz	**19 GHz**
γ	0.423	0.497
ω	0.062	0.065
RMSE V	6.84 K	5.66 K
RMSE H	9.23 K	9.37 K

5.4.2 Comparison of the airborne-derived γ-ω values with the in situ radiometric data

The retrieved γ-ω values obtained from the airborne dataset (table 5.5) were compared with γ-ω values calculated from three in situ radiometric measurements for different coniferous forest plots. To compare γ values from airborne measurements, we had to take into account the variation in forest density between these sites. We used the mean stem volume parameter to characterize the forest stands. The mean stem volume (82.8 m^3 ha^{-1} ±3.9) of the three AMSR-E sites was considered representative of the measured airborne $T_{Bforest}$ (see figure 5.1). For both frequencies, considering all the in situ calculated γ (V and H polarizations) values and measured stem volumes, a fit was modeled using the empirical relationship as suggested by Kruopis et al. (1999):

$$\gamma = a + (1-a)\exp(-b \cdot SV) \tag{5.9}$$

where *a* and *b* are the model constants fitted by a linear least squares regression. Figure 5.6a and b shows that the γ values derived from the airborne dataset were in agreement with the calculated in situ values. At 37 GHz, the airborne-derived γ was slightly higher than the exponential fit, while the γ value at 19 GHz was, however, higher than the exponential fit (but note that there was no measurement between 20 and 140 m^3 ha^{-1} to adequately force the model fit).

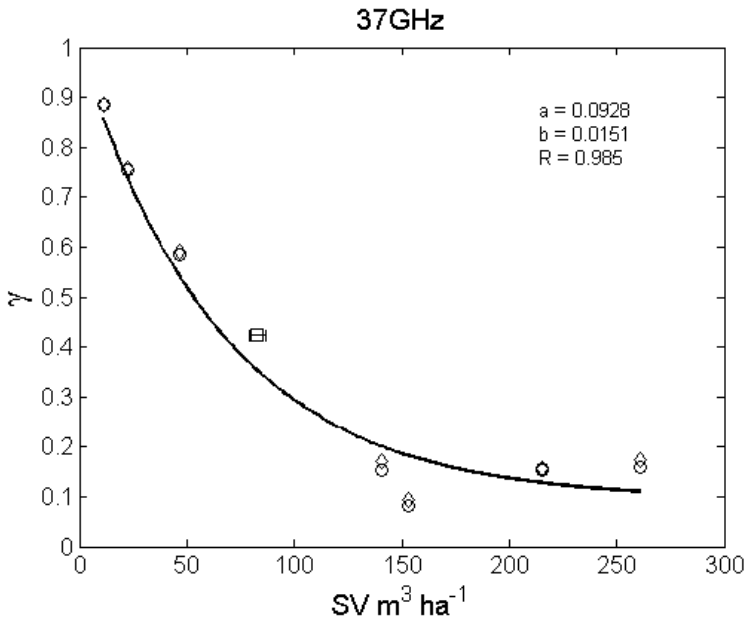

Figure 5.6a: We present γ as a function of the stem volume (SV) at 37 GHz. Circles = in situ V polarization; diamonds = in situ H polarization; squares = airborne (H and V polarization); solid line = eq. 5.9 fit.

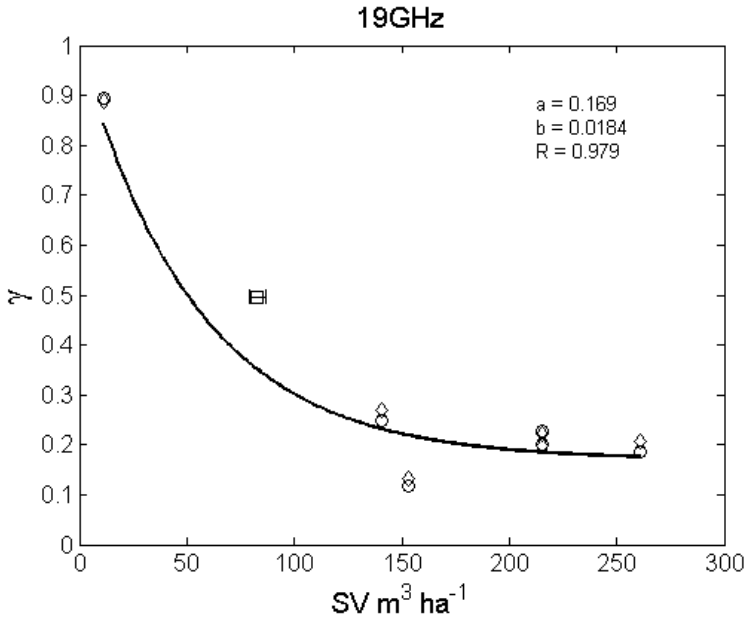

Figure 5.6b: Same as figure 5.6a but for 19 GHz (less radiometric data were taken at 19 GHz because of a failure of the radiometer).

Variations of ω values derived from in situ site measurements ranged between 0.110 ± 0.052 and 0.081 ± 0.049 (table 5.6), which was higher than the airborne-derived values (0.064). If we consider only the forest plots where SV < 200 m^3 ha^{-1}, the mean ω decreased to 0.082 ± 0.025 (table 5.6), which was closer than the airborne-derived data (table 5.5). The low in-situ mean ω value at 19H (0.057) and high mean value at 19V (0.115) were explained by the important

differences between H and V retrieved ω obtained at the site where the SV was very low (11.3 m^3 ha^{-1}) (ω_H = 0.001 ; ω_V = 0.193). Without that site, the mean values would be ω_{19V} = 0.076 and ω_{19H} = 0.085.

Table 5.6: Mean ω values for in situ data at St-Romain.

	37V	37H	19V	19H
ω	0.092 ±0.042	0.081 ±0.049	0.110 ±0.052	0.086 ±0.054
ω (SV<200)	0.091 ±0.052	0.068 ±0.056	0.115 ±0.071	0.057 ±0.052

The results obtained with the in situ measurements showed the coherence between the airborne and in situ results. However, the low number of in situ measurements reduced the applicability of the dataset for general model fitting. The in situ measurements also introduced some uncertainties due to the high heterogeneity at the radiometer field-of view scale. For example, the measurements of the T_{Bdown} were highly sensitive to clumping in the canopy, which caused high contrast in the measurements (very low T_{Batm} compared to high T_{Bveg}).

5.4.3 Soil parameterization from the AMSR-E dataset at 37 and 19 GHz

The airborne dataset was used to derive γ-ω for a dense boreal forest. However, in the radiative transfer equation (eq. 5.2), $e_{surface}$ remained an unknown at the satellite scale. Assuming that the vegetation characteristics were constant during the winter and summer, it was possible to retrieve soil parameters QH considering the airborne γ-ω values. Thus, the QH couple that minimized the sum of RMSE in V and H polarizations for each frequency independently were found at the three AMSR-E sites. Figure 5.7 shows that there was a convergence for both frequencies with values of Q_R = 0.10 and H_R = 0.52 at 37 GHz and Q_R = 0.19 and H_R = 0.67 at 19 GHz. Results also showed that the obtained RMSE were lower than 2 K. Analysis of the soil reflectivity derived from the QH values and a comparison with other studies are discussed in section 5.5.

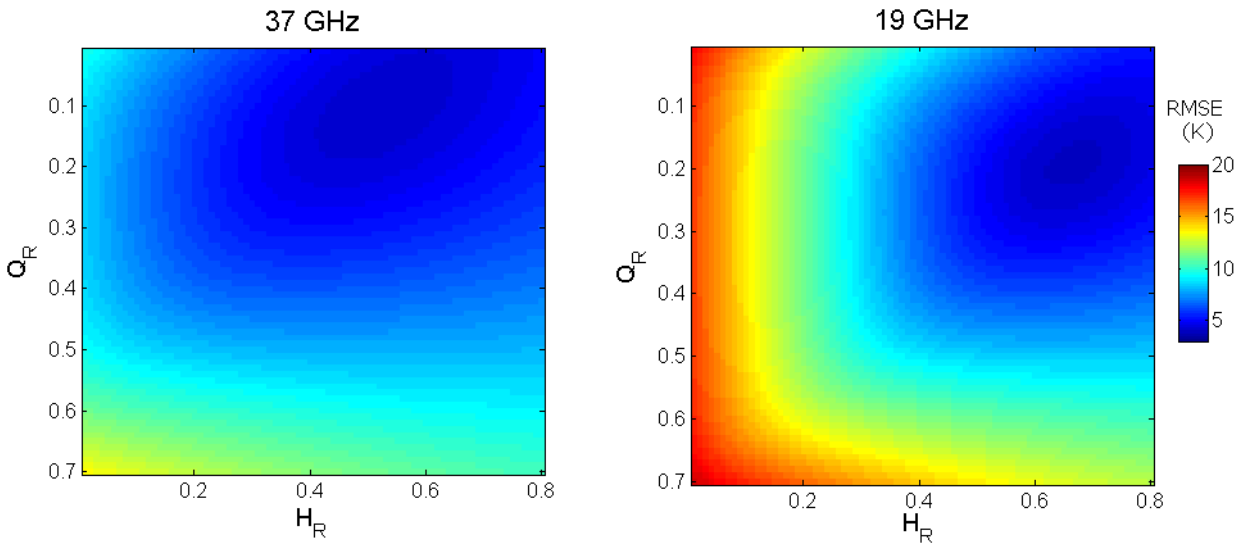

Figure 5.7: **RMSE (H+V) for different QH values at 19 and 37 GHz for the three AMSR-E sites (figure corrigée par rapport à la version dans l'article).**

By separately considering these optimized parameters (γ-ω and QH) for the three sites, calculated RMSE between the measured and simulated T_B remained lower than 2.3 K for both frequencies and polarization (table 5.7), thus confirming the robustness of the approach. Solution curves of γ-ω were also traced for the three AMSR-E sites considering only the optimized soil parameters (figure 5.8). Site 2 gives solution curves that intersect at the γ and ω values that were slightly higher compared to sites 1 and 3. These differences might be due to small differences in the vegetation characteristics between the AMSR-E sites because the LAI and the stem volume slightly diverged for site 2 compared with sites 1 and 3 (see table 5.1). However, the mean standard deviations of ω and γ were estimated from this variability between the sites (ω_{37} = 0.005; ω_{19} = 0.004; γ_{37} = 0.017; γ_{19} = 0.020), which showed a good coherence between the sites. However, some of the difference between each site might also have been due to differences in soil characteristics. The 37 GHz at the V polarization behavior also showed that the solution curves crossed ω = 0 (figure 5.8) at very high γ values (>0.95), which confirmed that neglecting ω might induce error in radiative transfer simulations of the forest canopy.

Table 5.7: **RMSE between measured and simulated brightness temperatures (K) on AMSR-E sites considering optimized parameters (γ-ω and QH).**

	37V	**37H**	**19V**	**19H**	**10.7V**	**10.7H**	**6.9V**	**6.9H**
Site 1	1.97	1.88	1.86	1.92	1.69	1.84	2.18	2.54
Site 2	2.18	2.19	1.92	2.21	1.87	2.13	3.13	5.67
Site 3	2.04	2.13	1.91	2.12	1.90	2.51	2.27	2.60

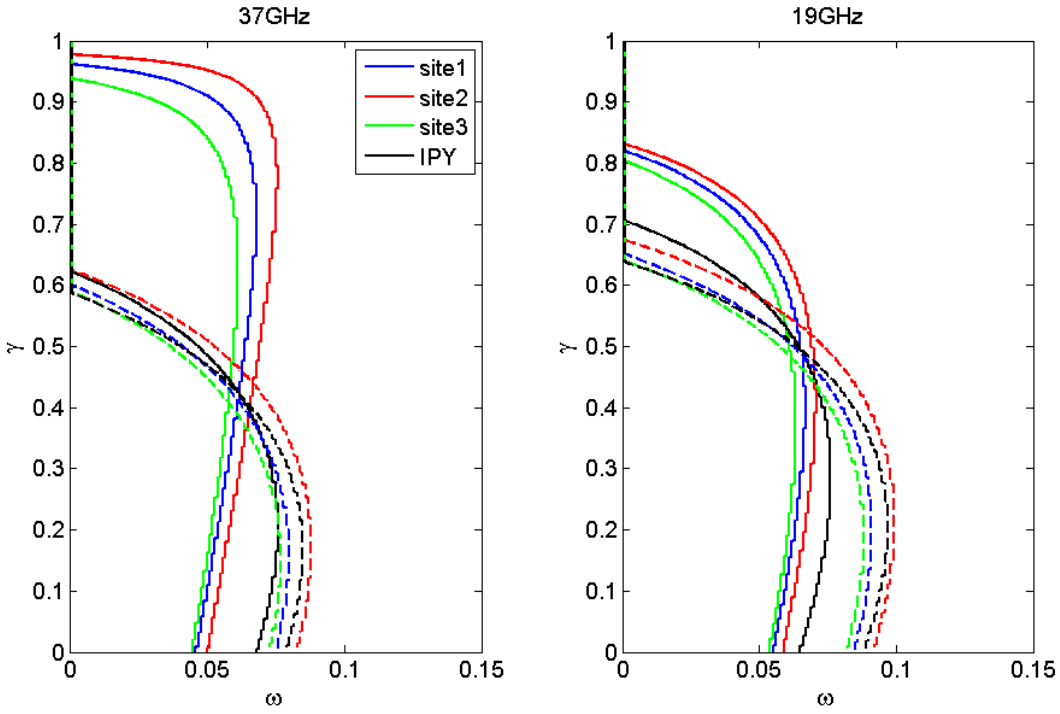

Figure 5.8: Solution curves (RMSE) for the three AMSR-E sites with optimized QH (solid line = V polarization and dotted line = H polarization). The airborne-derived IPY curve is reported (figure 5.5).

5.4.4 AMSR-E parameterization at 10.7 and 6.9 GHz

By considering H_R and ω to be spectrally constant (Wang et al., 1983; Prigent et al., 2000), a value of Q_R was found that gave $\gamma_V = \gamma_H$ at 10.7 and 6.9 GHz. Thus, with ω = 0.0635 and H_R = 0.595 (mean value of H_{R19} and H_{R37}) at the three AMSR-E sites the best γ_V and γ_H (γ that minimized the RMSE) were calculated with Q_R values ranging from 0 to 0.7 with an increment of 0.01. Figure 5.9 shows that there was a solution for both frequencies where $\gamma_V = \gamma_H$ giving values of γ = 0.62 and Q_R = 0.30 at 10.7 GHz and γ = 0.69 and Q_R = 0.31 at 6.9 GHz. These retrieved values were then separately applied to the three AMSR-E sites. The results showed that the RMSE values that were obtained were comparable to those obtained with 37 and 19 GHz (under 2.6 K), except for 6.9 at site 2 (table 5.7). The difference might be due to the fact that the 6.9 GHz resolution is coarser, which can increase the heterogeneity (open areas, small lakes) within a pixel. The difference might also be due to the fact that as was said previously, site 2 represented different forest characteristics. Mean standard deviations of $\gamma_{10.7}$ (± 0.018) and $\gamma_{6.9}$ (± 0.048) were also calculated by optimizing γ for each of the three sites independently considering the obtained values of Q_R (0.30 at 10.7 GHZ and 0.31 at 6.9 GHz).

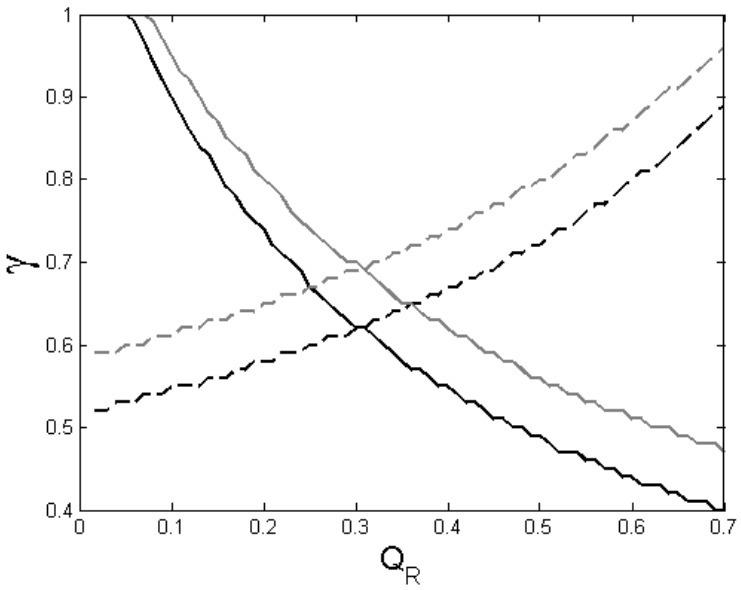

Figure 5.9: **The variation in γ as a function of Q_R at 6.9 GHz (gray) and 10.7 GHz (black) with ω=0.0635 (solid line is for the V polarization and dotted line is for the H polarization).**

Derived γ-ω and QH for dense boreal forests at AMSR-E scale for the four frequencies and both polarizations are summarized in table 5.8.

Table 5.8: Synthesis of derived forest and soil parameterization at four AMSR-E frequencies.

	37 GHz	19 GHz	10.7 GHz	6.9 GHz
γ	0.423** (± 0.017)	0.497** (± 0.020)	0.62 (±0.018)	0.69 (± 0.048)
ω	0.062** (± 0.005)	0.065** (± 0.004)	0.0635*	0.0635*
Q_R	0.10	0.19	0.30	0.31
H_R	0.52	0.67	0.595*	0.595*

* Value derived considering frequency independency

** Value derived from airborne dataset

5.4.5 Analysis of atmospheric, vegetation, and surface contributions

Using the γ-ω values, each contribution from eq. 5.2 (atmospheric, vegetation, and surface) was calculated and analyzed for all frequencies of the AMSR-E summer dataset (figure 5.10). Direct emission from the vegetation T_{Bveg} contributed almost half of the signal received by the sensor at 37 GHz, and it decreased with the frequency to around 90 K (≈ 35%) for lower frequencies. The values for $T_{Bv\text{-}r\text{-}s}$ were weak and relatively constant at all frequencies, but they were not negligible as the values varied between 2.7 and 13.0 K. The $T_{Batm\uparrow}$ values were low but not negligible at lower frequencies; values almost reached 30 K (≈10%) at 37 GHz. The terms corresponding to the reflected atmospheric contributions ($T_{Batm\downarrow\text{-}r\text{-}v}$ and $T_{Batm\downarrow\text{-}r\text{-}s}$) were generally lower than 1 K and

could be neglected because their values were lower than the RMSE obtained with the simulations. This analysis showed that the T_{Bveg} contribution was more important than T_{Bsurf} at higher frequencies (19 and 37 GHz).

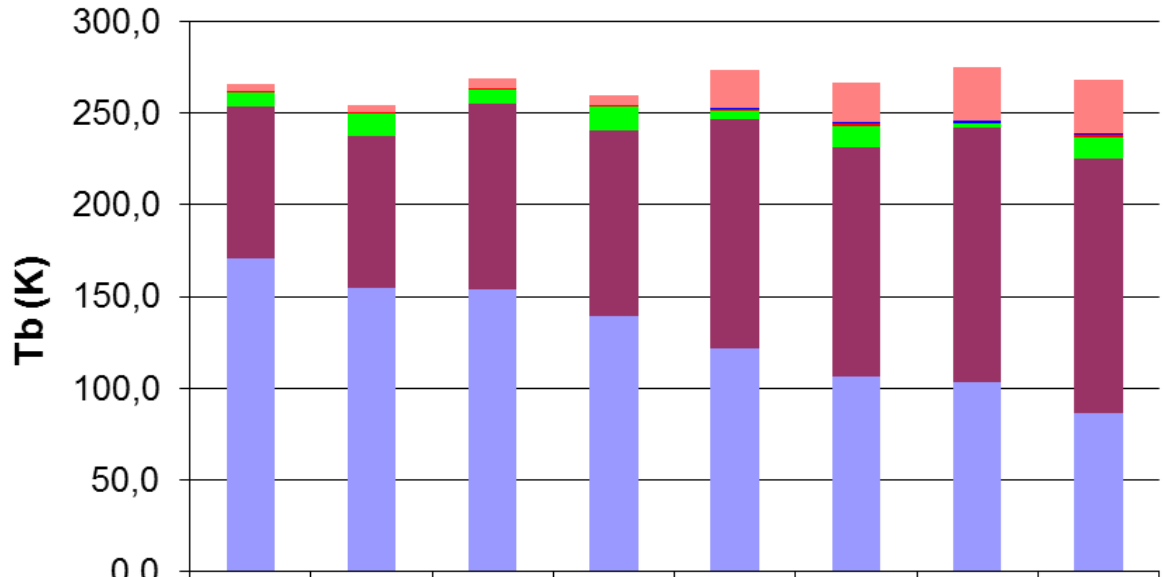

	6.9V	6.9H	10.7V	10.7H	18.7V	18.7H	36.5V	36.5H
Tbatm↑	3,7	3,7	5,3	5,3	21,3	21,3	29,2	29,2
Tbatm↓-r-v *	0,1	0,1	0,2	0,2	0,8	0,8	1,1	1,1
Tbatm↓-r-s *	0,4	0,7	0,4	0,7	0,5	1,1	0,3	1,1
Tbv-r-s *	7,6	12,2	7,7	13,0	4,8	12,0	2,7	11,8
Tbveg *	83,1	83,1	101,2	101,2	125,1	125,1	138,8	138,8
Tbsurf *	170,6	154,7	154,0	139,3	121,4	106,2	103,0	86,3

Figure 5.10: Simulated contribution of the mean T_B received by the AMSR-E sensor for the whole AMSR-E summer dataset (*these terms were multiplied by γ_{atm} to calculate the effective contributions at the sensor). See eq. 5.2 for definitions of each component.

5.5 Discussion

Figures 5.11 and 5.12a and b summarize the derived values for ω and γ respectively, including a comparison with other published values.

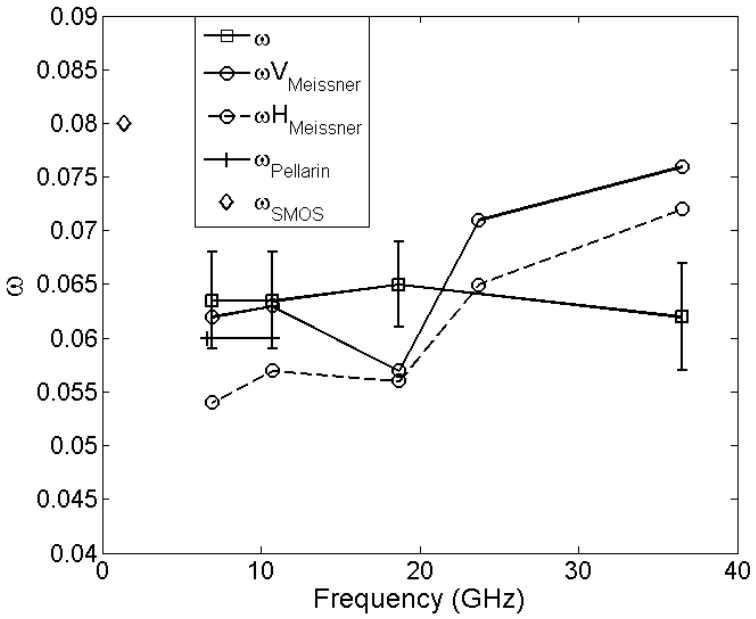

Figure 5.11: A comparison of ω values: □ = present study; ○ = Meissner & Wentz al. (2010) for a tropical forest; + = Pellarin et al. (2006) for a coniferous forest; and ◊ = SMOS (2011) for a needleleaf forest.

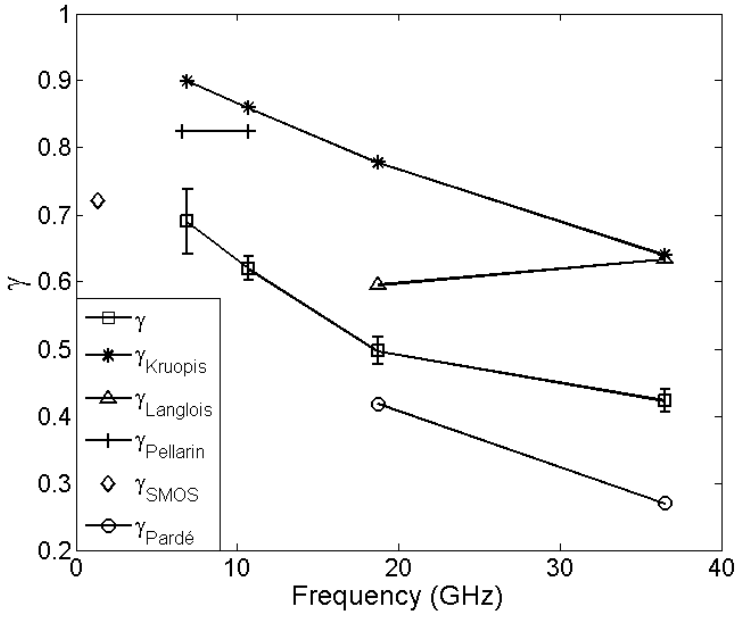

Figure 5.12a: A comparison of γ values at V polarization: □ = present study; * = Kruopis et al. (1999) for a boreal forest in Finland; Δ = Langlois et al. (2011); + = Pellarin et al. (2006) for a coniferous forest; ◊ = SMOS (2011) for a needleleaf forest; and o = Pardé et al. (2005) for ground-based boreal forest measurements.

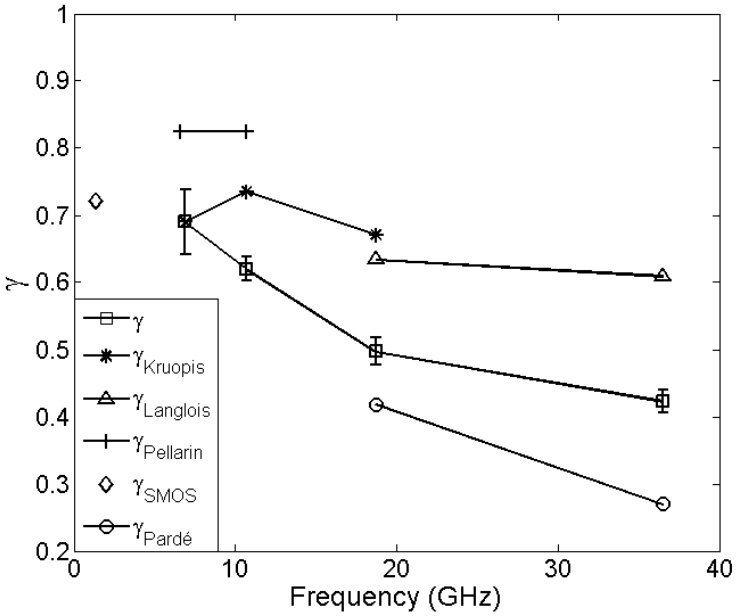

Figure 5.12b: Same as figure 5.12a but for H polarization.

At field scale, the effect of the vegetation structure may have a strong impact on the values for the vegetation model parameters (γ, ω) (Wigneron et al., 1995: 2007). Conversely, several studies suggest that ω values are typically polarization-independent for coarse-scale observations of natural vegetation (Owe et al., 2001; Pellarin et al., 2006). The present study was carried out using three types of observations, and we found that the retrieved values of ω were mainly polarization-independent. For theoretical and effective models, Kurum et al. (2012) found at L-band very small differences between ω_V and ω_H (less than 10%) at high incident angles (>45°) with pine plot measurements. For a coniferous forest, Pellarin et al. (2006) demonstrated that $\omega_H = \omega_V = 0.06$ at low frequencies (6.9 and 10.7 GHz), which is very close to the value found in this study at 19 and 37 GHz. In the *Soil Moisture and Ocean Salinity* (SMOS) projects, the value of 0.08 for needleleaf forests at 1.4 GHz was chosen (SMOS, 2011), while Grant et al. (2008) used ω=0.07, which are also close to the value of ω found in this study (figure 5.11). These results suggest that ω might be mostly frequency-independent for boreal forests.

The γ values derived from the three distinct datasets considered in this study are shown in figures 5.12a and b for V and H polarizations respectively. In general, it appears from this analysis that assuming ω = 0 in order to retrieve γ from the radiometric measurements of the canopy led to larger values of γ (figure 5.12a and b). Our proposed values were smaller than those obtained with ω = 0 by Langlois et al. (2011) and Kruopis et al. (1999). In fact, figure 5.5 shows that if

considering ω = 0, the derived γ values were much higher (over 0.6) for both frequencies and both polarizations. This phenomenon was also observed at the L-band (Grant et al., 2008). Thus, neglecting ω would cause an overestimation of the soil contribution in the satellite measured T_B in the radiative transfer model.

The results we obtained were also consistent with theory, where γ values decrease with frequency. We observed an increase of the penetration depth with decreasing frequency. The values obtained at 10.7 and 6.9 GHz calculated from the mean LAI for the AMSR-E sites (see table 5.1) were lower than those obtained by Pellarin et al. (2006). However, the values obtained in this study were more consistent with the value used in the SMOS project (also derived from the LAI values). A linear relationship could be traced between 1.4 and 19 GHz (figure 5.12a and b). As Pellarin et al. (2006) pointed out, the values that they obtained were very sensitive to the selection of the soil parameterization.

The transmissivity values derived from ground-based measurements at 19 and 37 GHz by Pardé et al. (2005) appear to be lower than those obtained in this study at both polarizations (fig. 5.12a and b). The Pardé et al. (2005) study was based on in situ radiometric measurements with the antenna pointing toward the sky through the canopy. The authors neglected ω following the approach suggested by Matzler et al. (1994); the emissivity of the canopy was considered as (1-γ) instead of (1 - γ)·(1 - ω) as used in this study, which would lead to an underestimation of γ. Furthermore, the term emitted from the ground and reflected by the canopy to the radiometer was also neglected; this assumption leads to an overestimation of the canopy emission. However, Santi et al. (2009) obtained low γ values for a deciduous forest by considering ω from 1.4 to 37 GHz. Guglielmetti et al. (2007) also showed that the canopy was mainly opaque in the foliated state of a broadleaf forest at 11.4 GHz. It is difficult to make a direct comparison between our work and these last two studies because the tree species were different. However, the low values that they obtained also showed that the forest volume on an AMSR-E footprint is not as high as an in situ dense mature forest plot. At coarse satellite resolution, there are always open areas (table 5.1) as opposed to a completely dense and closed canopy that can occur at a high resolution.

Soil reflectivity values derived from optimized QH models were analyzed (table 5.8). Figure 5.13 shows that reflectivity values for mean AMSR-E site 1 conditions (soil moisture and temperature) decreased with frequency, which was consistent with the theory (Ulaby et al., 1986). The frequency dependency was, however, higher at V than at H polarization. That was translated by a decrease of Q_R with frequency (increasing of the polarization mixing ratio from 0.1 at 37 GHz to 0.31 at 6.9 GHz), which was the inverse of the Wang et al. (1983) findings between 1.4 and 10.7 GHz. However, Shi et al. (2005) indicated that the effect of roughness on the effective reflectivity at large angles of incidence differs in both magnitude and direction for the two different polarizations. The same phenomenon was also observed for an L-band surface emission study at large angles of incidence (Shi et al., 2002). As a result, this phenomenon significantly affects on the relationship of the surface reflectivity, especially on the polarization ratio V/H, which was represented by Q_R in the QH model. The value of $H_R \approx 0.6$ indicated a rough surface if we compared it with QH values obtained for in situ measurements of bare soil (37 GHz in Prigent et al., 2000; 10.7 and 6.9 GHz in Wang et al., 1983). It is, however, difficult to compare our values with in situ measurements of bare soil as the derived QH values in this study were parameters that represented effective surface roughness (including litter and microtopography) and can hardly be related to a geometric roughness. Grant et al. (2009) also showed that the presence of litter and grass on soil significantly decreases the reflectivity in the L-band.

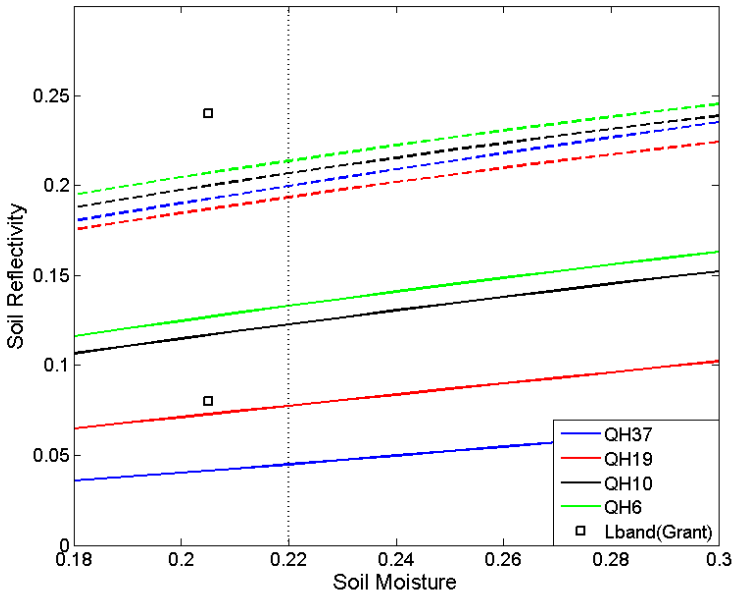

Figure 5.13: Soil reflectivity values as a function of soil moisture (vertical black dotted line is the mean soil moisture for the AMSR-E sites; solid lines are for V polarization; dashed lines are for H polarization).

The use of winter and summer datasets to invert vegetation parameters implied that the vegetation parameters were considered constant. With evergreen needleleaf forests, the structure of the tree remains practically unchanged during winter. However, there might be a change in the vegetation water content of trees during the winter, which could have an impact on the dielectric constant. It is, however, not possible to evaluate the impact of this phenomenon.

5.6 Conclusions

Precise forest parameterizations are essential for AMSR-E applications for boreal forests. This study compared a large T_B AMSR-E dataset with theoretical simulations of forest and soil emissions over three homogeneous dense boreal sites in southeastern Canada. Soil moisture and atmospheric conditions taken from NARR data, which show an important seasonal variability, were used to simultaneously retrieve the transmissivity (γ) and single scattering albedo (ω) values of the forest cover. The simplified so-called τ-ω radiative transfer model was used. In order to decouple the vegetation contribution from the soil, a 19 and 37 GHz winter dataset was used to derive a γ-ω couple, and then was used to retrieve soil model parameters at the AMSR-E resolution using the QH model. The derived ω values were relatively low ($\approx 0.064 \pm 0.005$). By considering ω to be spectrally constant and $\gamma_V = \gamma_H$, we retrieved γ values of 0.423 ± 0.017, 0.497 ± 0.020, 0.62 ± 0.018, and 0.69 ± 0.048 at 36.5, 18.7, 10.7, and 6.9 GHz respectively. We showed that considering $\omega = 0$ led to abnormally high γ values. We also found that Q_R decreased with frequency at the AMSR-E angle.

With the AMSR-E dataset, the minimum RMSE between the simulated and measured T_B were approximately 2 K at 3 sites neglecting the values obtained at site 2 at 6.9 GHz. These results demonstrated the potential for characterizing the surface through a dense forest canopy using passive microwave radiometry by considering both the effects of attenuation γ and diffusion ω generated by the canopy.

Developing an accurate correction for the contribution of forests opens the door to opportunities for the application of radiance assimilation for surface temperature, snow water equivalent, and soil moisture corrections over forested areas. It will be possible to approach radiance assimilation with land surface schemes, for example, at the level of the surface under the canopy instead of

considering satellite T_B. This approach simplified the problem and reduced the uncertainty of the assimilated radiance. The transmissivity values also showed the semi-transparency of the forest cover for frequencies from 6.9 to 37 GHz, which confirmed the possibility of monitoring the surface under the forest with passive microwaves at the AMSR-E frequencies. The suggested spectral variation of γ-ω values can be useful for innovative satellite applications such as WindSat (Gaiser et al., 2004). The relatively low variations in γ-ω parameterizations at low frequencies (1.4, 6.9, and 10.7 GHz channels) could be of interest for the Soil Moisture and Ocean Salinity (SMOS) mission (Kerr et al., 2001) or for future satellites such as Soil Moisture Active Passive (SMAP, NASA) (Entekhabi et al., 2008).

For a spatialization of boreal forest corrections, future work will need to identify the variation of γ and ω with regard to forest biomass at 19 and 37 GHz at the satellite scale. We plan to investigate possible relationships between γ and LAI as Pellarin et al. (2006) did at 6.6 and 10.7 GHz. Macelloni et al. (2001) also showed relationships between T_B and forest parameters such as LAI. The results obtained in this study showed the potential of using distinct datasets for the γ-ω retrievals, which might be of interest for various ecosystems other than boreal forests.

Acknowledgments

The authors thank the Natural Sciences and Engineering Research Council of Canada (NSERC) for their financial support. We also thank Environment Canada for the International Polar Year (IPY) field campaign support (Anne Walker, P.I.), including the airborne microwave measurements. We are grateful to the National Snow and Ice Data Center (NSIDC) for the AMSR-E data, the Land Processes Distributed Active Archive Center (LP DAAC) for the LAI product, and the National Center for Environmental Prediction (NCEP) for the North American Regional Reanalysis (NARR) data. We also thank J. Pulliainen for providing the Helsinki University of Technology (HUT) emission model and Y. Kerr for the helpful comments on this work.

References

Andreadis, K.M., Storck, P., & Lettenmaier, D.P. (2009). Modeling snow accumulation and ablation processes in forested environments. *Water Resources Research*. 45. W05429. doi:10.1029/2008WR007042.

Betts, A., Ball, J., & McCaughey, J. (2001). Near-surface climate in the boreal forest. *Journal of Geophysical Research*. 106(D24). 33529-33541.

Calvet, J.-C., Wigneron, J.-P., Mougin, E., Kerr, Y.H., & Brito, J.L. (1994). Plant water content and temperature of the Amazon forest from satellite microwave radiometry. *IEEE Transactions on Geoscience and Remote Sensing*. 32. 397-408.

Cano, A., Saleh, K., Wigneron, J.-P., Antolín, C., Balling, J.E., Kerr, Y.H., Kruszewski, A., Millán-Scheiding, C., Schmidl Søbjærg, S., Skou, N., & López-Baeza, E. (2010). The SMOS Mediterranean Ecosystem L-Band characterisation EXperiment (MELBEX-I) over natural shrubs. *Remote Sensing of Environment*. 114 (4). 844-853.

Derksen, C., Toose, P., Rees, A., Wang, L., English, M., Walker, A. & Sturm, M. (2010). Development of a tundra-specific snow water equivalent retrieval algorithm for satellite passive microwave data. *Remote Sensing of Environment*. 114. 1699-1709.

Derksen, C. (2008). The contribution of AMSR-E 18.7 and 10.7 GHz measurements to improved boreal forest snow water equivalent retrievals. *Remote Sensing of Environment*. 112. 2701-2710.

Dobson, M.C., Ulaby, F.T., Hallikainen, M.T. & El-Rayes, M.A. (1985). Microwave dielectric behaviour of wet soil part II : dielectric mixing models. *IEEE Transactions on Geoscience and Remote Sensing*. GE-23 (1). 35-46.

Durand, M., Kim, E.J., & Margulis, S.A. (2008). Quantifying uncertainty in modeling snow microwave radiance for a mountain snowpack at the point-scale, including stratigraphic effects. *IEEE Transactions on Geoscience and Remote Sensing*. 46(6). 1753-1767.

Entekhabi, D., Jackson, T.J., Njoku, E., O'Neill, P., & Entin, J. (2008). Soil moisture active/passive (SMAP) mission concept. *Proceeding SPIE 7085. 70850H.* doi: 10.1117/12.795910.

Ferrazzoli, P., Guerriero, L. & Wigneron, J.-P. (2002). Simulating L-band emission of forests in view of future satellite applications. *IEEE Transactions on Geoscience and Remote Sensing*. 40(12), 2700–2708.

Ferrazzoli, P. & Guerriero, L. (1996). Passive microwave remote sensing of forests : A model investigation. *IEEE Transactions on Geoscience and Remote Sensing*. 34, 433-443.

Gaiser, P.W., St-Germain, K.M., Twarog, E.M., Poe, G. A., Purdy, W., Richardson, D., Grossman, W., Jones, W.L., Spencer, D., Golba, G., Cleveland, J., Choy, L., Bevilacqua, R.M. & Chang, P.S. (2004). The WindSat spaceborne polarimetric microwave radiometer: Sensor

description and early orbit performance. *IEEE Transactions on Geoscience and Remote Sensing*. 42(11). 2347–2361.

Grant, J.P., Wigneron, J.-P., Van de Griend, A.A., Kruszewski, A., Schmidl Søbjærg, S. & Skou, N.(2007). A Field Experiment on Microwave Forest Radiometry - L-band signal behaviour for varying conditions of surface wetness. *Remote Sensing of Environment*. 109. 10–19.

Grant, J.P., Saleh, K., Wigneron, J.-P., Guglielmetti, M., Kerr, Y.H., Schwank, M., Skou, N., & Van de Griend, A. (2008). Calibration of the L-MEB model over a coniferous and a deciduous forest. *IEEE Transactions on Geoscience and Remote Sensing*. 46(3). 808-818.

Grant, P.G., Van de Griend, A.A., Schwank, M. & Wigneron, J.-P. (2009). Observations and modeling of a pine forest floor at L-band. *IEEE Transactions on Geoscience and Remote Sensing*. 47(7). 2024-2034.

Guglielmetti, M., Schwank, M., Mätzler, C., Oberdörster, C., Vanderborght, J. & Flühler, H. (2007). Measured microwave radiative transfer properties of a deciduous forest canopy. *Remote Sensing of Environment*. 109(4). 523-532.

Guglielmetti, M., Schwank, M., Mätzler, C., Oberdörster, C., Vanderborght, J. & Flühler, H. (2008). FOSMEX: Forest Soil Moisture Experiments With Microwave Radiometry. *IEEE Transactions on Geoscience and Remote Sensing*. 46(3). 2008.

Hirschi, M., Seneviratne, S.I., Alexandrov, V., Boberg, F., Boroneant, C., Christensen, O.B., Formayer, H., Orlowsky, B., & Stepanek, P. (2010). Observational evidence for soil-moisture impact on hot extremes in southeastern Europe. *Nature Geoscience*, 4(17), doi:10.1038/ngeo1032.

Jackson, T.J., & Schmugge, T.J. (1991). Vegetation effects on the microwave emission of soils. *Remote Sensing of Environment*. 36. 203-212.

Jackson, T.J., Chen, D., Cosh, M., Li, F., Anderson, M., Walthall, C., Doriaswamy, P., & Hunt, E.R. (2004). Vegetation water content mapping using Landsat data derived normalized difference water index for corn and soybeans. *Remote Sensing of Environment*. 92. 475–482.

Jones, M.O., Jones, L.A., Kimball, J.S. & McDonald, K.C. (2011). Satellite passive microwave remote sensing for monitoring global land surface phenology. *Remote Sensing of Environment*, 115, 1102-1114.

Karam, M.A. (1997) A physical model for microwave radiometry of vegetation. *IEEE Transactions on Geoscience and Remote Sensing*. 35. 1045-1058.

Kelly, R.E., Chang, A.T., Tsang, L., & Foster, J.L. (2003). A prototype AMSR-E global snow area and snow depth algorithm. *IEEE Transactions on Geoscience and Remote Sensing*. 41. 230–242.

Kerr, Y.H., Waldteufel, P., Wigneron, J.-P., Martinuzzi, J.M., Font, J. & Berger, M. (2001). Soil moisture retrieval from space: the soil moisture and ocean salinity (SMOS) mission. *IEEE*

Transactions on Geoscience and Remote Sensing. 39. 1729–35.

Kruopis, N., Praks, J., Arslan, A.N., Alasalmi, H.M., Koskinen, J.T., Hallikainen, M.T. (1999). Passive Microwave measurements of snow-covered forest area in EMAC'95. *IEEE Transactions on Geoscience and Remote Sensing*. 37. 2699-2705.

Kurum, M, Lang, R.H., O'Neill, P.E., Joseph, A.T., Jackson, T.J. & Cosh, M.H. (2011). A first-order radiative microwave radiometry of forest canopies at L-band. *IEEE Transactions on Geoscience and Remote Sensing*. 49(9). 3167-3179.

Kurum, M., O'Neill, P.E., Lang, R.H., Joseph, A.T., Cosh, M.H. & Jackson, T.J. (2012). Effective tree scattering and opacity at L-band. *Remote Sensing Environment*. 118. 1-9.

Langlois, A., Royer, A., Dupont, F., Roy, A., Goïta, K., & Picard, G. (2011). Improved corrections of forests effects on passive microwave satellite remote sensing of snow over boreal and subartic regions. *IEEE Transactions on Geoscience and Remote Sensing*. 49(10). 3824-3837.

Langlois, A., Royer, A. & Goïta, K. (2010). Analysis of simulated and spaceborn passive microwave brightness temperature using in situ measurements of snow and vegetation properties.. *Canadian Journal of Remote Sensing*. 36(S1). S135-S148.

Latifovic, R., Zhu, Z.-L., Cihlar, J., Giri, C. & Olthof, I. (2004). Land cover mapping of North and Central America – Global Land Cover 2000. *Remote Sensing Environment*. 89(1). 116-127.

Leblanc, S., Bicheron, P., Chen, J., Leroy, M. & Cihlar, J. (1999). Investigation of directional reflectance in boreal forests with an improved four-scale model and airborne POLDER data. *IEEE Transactions on Geoscience and Remote Sensing*. 37(3). 1396-1414.

Lin, B., & Minnis, P. (2000). Temporal variations of land surface microwave emissivities over the atmospheric radiation measurement program southern great plains site. *Bulletin of American meteorological society*. 39. 1103-1116.

Luo, Y., Berbery, E.H., Mitchell, K.E., & Betts, A.K. (2007). Relationships between land surface and near-surface atmospheric variables in the NCEP North American Regional Reanalysis. *Journal of Hydrometeorology*. 8(6). 1184-1204.

Macelloni, G., Paloscia, S., Pampaloni, P., & Ruisi, R. (2001). Airborne multifrequency L- to Ka-band radiometric measurements over forest, *IEEE Transactions on Geoscience and Remote Sensing*. 39. 2507–2513.

Mätzler, C. (1987). Applications of the Interaction of Microwaves with the Natural Snow Cover. *Remote Sensing Reviews*. 2. 259-392.

Mätzler, C. (1994). Microwave transmissivity of a forest canopy: Experiments made with a beech. *Remote Sensing of Environment*. 48. 172–180.

Mätzler, C. & Wiesmann, A. (1999) Extention of the microwave emission model of layered snowpacks to coarse-grained snow. *Remote Sensing of Environment*. 70. 317-325.

Mätzler, C. (2006). Comparison of emission models for covered surfaces. *In* Mätzler, C., Rosenkranz, P.W., Battaglia, A. & Wigneron, J.-P. (eds.) Thermal Microwave Radiation - Applications for Remote Sensing. IET Electromagnetic Waves Series 52. London. UK. 227-240.

Mätzler, C., & Rosenkranz, P.W. (2007). Dependance of microwave brightness temperature on bistatic surface scattering : model functions and application to AMSU-A, *IEEE Transactions on Geoscience and Remote Sensing*. 45. 2130–2138.

McMahon, S.M., Parker, G.G. & Miller, D.R. (2010). Evidence for a recent increase in forest growth. *Proceedings of the National Academy of Sciences*. 107. 3611–3615.

Meissner, T., & Wentz, F. (2010). Intercalibration of AMSR-E and WINDSAT brightness temperature measurements over land scenes, *presented at the 11th Specialist Meeting on Microwave Radiometry and Remote Sensing of the Environment (MicroRad 2010)*, 1-4 March 2010, Washington, DC, USA.

Mesinger, F. & 18 Coauthors. (2006). North American Regional Reanalysis. *Bulletin of American meteorological society*. 87(3). 343–360.

Mo, T., Choudhury, B.J., Schmugge, T.J., Wang, J.R. & Jackson, T.J. (1982). A model for microwave emission from vegetation-covered fields. *Journal of geophysical Research*. 87. 11229.

Ni-Meister, W., Houser, P.R. & Walker J.P. (2006). Soil moisture initialization for climate prediction: Assimilation of scanning multifrequency microwave radiometer soil moisture data into a land surface model, *Journal of Geophysical Research*. 111. D20102. doi:10.1029/2006JD007190.

Njoku, E.G., Jackson, T.J., Lakshmi, V., Chan, T.K. & Nghiem, S.V. (2003). Soil moisture retrieval from AMSR-E. *IEEE Transactions on Geoscience Remote Sensing*. 41(2). 215-229.

Owe, M., de Jeu, R., & Walker, J.P. (2001). A methodology for surface soil moisture and vegetation optical depth retrieval using the microwave polarization difference index. *IEEE Transactions on Geoscience and Remote Sensing*. 39(8). 1643-1654.

Paloscia, S., Macelloni, G. & Santi, E. (2006). Soil moisture estimates from AMSR-E brightness temperatures by using a dual-frequency algorithm. *IEEE Transactions on Geoscience and Remote Sensing*. 44(11). 3135-3144.

Pampaloni, P. (2004). Microwave radiometry of forests. *Waves Random Media*.
14. 275−298.

Pampaloni, P., & Paloscia, S. (1986) Microwave emission and plant water content : A comparison between field measurements and theory. *IEEE Transactions on Geoscience and Remote Sensing*. 24. 900-905.

Pardé, M., Goïta, K., Royer, A. & Vachon, V. (2005). Boreal forest transmissivity in the microwave domain using ground-based measurements. *IEEE Geoscience Remote Sensing Letters*. 2(2). 169-171.

Pellarin, T., Kerr, Y.H. & Wigneron, J.-P. (2006). Global simulations of brightness temperature at 6.6 and 10.7 GHz over land based on SMMR data set analysis, *IEEE Transactions on Geoscience and Remote Sensing*. 44. 2492-2505.

Penuelas, J., Rutishauser, T., & Filella, I. (2009). Phenology feedbacks on climate change. *Science*. 324. 887−888.

Prigent, C., Wigneron, J.-P., Rossow, B. & Pardo-Carrion, J.R. (2000). Frequency and angular variations of land surface microwave emissivities: can we estimate SSM/T and AMSU emissivities from SSM/I emissivities?. *IEEE Transactions on Geoscience and Remote Sensing*. 38(5). 2373-2385.

Pulliainen, J., Hallikainen, M. & Grandell, J. (1999). Hut snow emission model and its applicability to snow water equivalent retrieval. *IEEE Transactions on Geoscience and Remote Sensing*. 37. 1378–1390.

Roy, A., Royer, A., Turcotte, R. (2010). Improvement of springtime streamflow simulations in a boreal environment by incorporating snow-covered area derived from remote sensing data. *Journal of hydrology*. 390. 35-44.

Sahoo, A.K., Houser, P.R., Ferguson, C., Wood, E.F., Dirmeyer, P.A., Kafatos, M. (2008) Evaluation of AMSR-E soil moisture results using the in-situ data over the Little river experimental watershed, Georgia. *Remote Sensing of Environment*. 112. 3142-3152.

Saleh, K., Wigneron, J.-P., de Rosnay, P., Calvet, J.-C., Escorihuela, M.-J., Kerr, Y.H., & Waldteufel, P. (2006). Impact of rain interception by vegetation and mulch on the L-band emission of natural grass. *Remote Sensing of Environment*. 101. 127–139.

Santi, E., Paloscia, S., Pampaloni, P. & Pettinato, S. (2009). Ground-based microwave investigations of forest plots in Italy. *IEEE Transactions on Geoscience and Remote Sensing*. 47. 3016-3025.

Shi, J., Jiang, L., Zhang, L., Chen, K.-S., Wigneron, J.-P. & Chanzy, A. (2005). A parametrized multifrequency-polarization surface emission model. *IEEE Transactions on Geoscience and Remote Sensing*. 43(12). 2831-2841.

Shi, J., Chen, K.S., Li, Q., Jackson, T.J., O'Neill, P.E., & Tsang, L. (2002). A parametrized surface reflectivity model and estimation of bare surface soil moisture with L-band radiometer. *IEEE Transactions on Geoscience and Remote Sensing*. 40(12). 2674-2686.

SMOS (2011) SMOS level 2 processor for soil moisture ATBD for the SMOS level 2 soil moisture processor development continuation project. Issue 3.4. Submitted by Array Systems Computing Inc. Prepared by : CBSA, UoR, TV and INRA. 24 january 2011.

Ter-Mikaelian, M.T. & Korzukhin, M.D. (1997). Biomass equations for sixty-five North America tree species. *Forest ecology management*. 97(1). 1-24.

Ulaby, F.T., Moore, R.K. & Fung, A.K. (1986). Microwave Remote Sensing. vol. 3. Artech house. Norwood. MA.

Ulaby, F.T., Razani, M., & Dobson, M.C. (1983) Effects of vegetation cover on the microwave radiometric sensitivity to soil moisture. *IEEE Transactions on Geoscience and Remote Sensing*. 21. 51-61.

Van de Griend, A.A. & Wigneron, J.-P. (2004a). On the measurement of microwave vegetation properties: some guidelines for a protocol. *IEEE Transactions on Geoscience and Remote Sensing*. 42(10). 2277-2289.

Van de Griend A.A. & Wigneron, J.-P. (2004b). The b-Factor as a function of frequency and canopy type at H polarization. *IEEE Transactions on Geoscience and Remote Sensing*. 42(4). 786-794.

Wang, R.W., O'Neill, P.E, Jackson, T.J. & Engman, E.T. (1983) Multifrequency measurements of the effects of soil moisture, soil texture and surface roughness. *IEEE Transactions on Geoscience and Remote Sensing*. GE-21(1). 44-51.

Wigneron, J.-P., Chanzy, A., Calvet, J.-C. & Bruguier, N. (1995). A simple algorithm to retrieve soil moisture and vegetation biomass using passive microwave measurements over crop fields. *Remote Sensing of Environment*. 51. 331-341.

Wigneron, J.-P., Guyon D., Calvet J.-C., Courrier, G. & Bruguier, N. (1997). Monitoring coniferous forest characteristics using a multi-frequency (5-90GHz) microwave radiometer. *Remote Sensing of Environment*. 60. 299-310.

Wigneron, J.-P., Pardé, M., Waldteufel, P., Chanzy, A., Kerr, Y.H., Schmidl S. & Skou, N. (2004). Characterizing the dependence of vegetation model parameters on crop structure, view angle and polarization at L-Band. *IEEE Transactions on Geoscience and Remote Sensing*. 42. 416-425.

Wigneron, J.-P., Kerr, Y.H., Waldteufel, P., Saleh, K., Esorihuela, M.-J., Richaume, P., Ferrazzoli, P., de Rosnay, P., Gurney, R., Calvet, J.-C., Grant, J.P., Guglielmetti, M., Hornebuckle, B., Mätzler, C., Pellarin, T. & Schwank, M. (2007). L-band microwave emission of the biosphere (L-MEB) model : description and calibration against experimental data sets over crop fields. *Remote Sensing of Environment*. 107. 639-655.

Yang, W.Z., Tan, B., Huang, D., Rautiainen, M., Shabanov, N.V., Wang, Y., Privette, J.L., Huemmrich, K.F., Fensholt, R., Sandholt, I., Weiss, M., Ahl, D.E., Gower, S.T., Nemani, R.R., Knyazikhin, Y. & Myneni, R.B. (2006). MODIS leaf area index products: from validation to algorithm improvement. *IEEE Transactions on Geoscience and Remote Sensing*. 44(7). 1885-1898.

5.7 Discussion

Lors de la paramétrisation de la végétation et du sol au niveau des pixels AMSR-E, dans ce chapitre, nous posons l'hypothèse que les paramètres de végétation restent les mêmes pour des conditions d'été et d'hiver. Une analyse plus détaillée de la transmissivité en été est présentée au Chap. 6, et confirme l'ordre de grandeur des paramètres estimés dans ce Chap. 5. Cependant au Chap. 7, nous montrerons qu'il semble qu'il y ait en fait une diminution de l'émissivité (augmentation de ω) en hiver par rapport à l'été. Une discussion plus approfondie est donnée au Chap. 7 (Sect. 7.4.2) sur les différences de paramétrisation de la végétation avec les changements de saisons.

Chapitre 6: Relationship Between Forest Microwave Transmissivity and Structural Parameters for the Canadian Boreal Forest

« Relation entre la Transmissivité Micro-Onde et des Paramètres Structuraux de la Forêt Boréale Canadienne»

Auteurs : Roy, A., Royer, A., Hall, R. J.

Article soumis dans le Journal *Geoscience and Remote Sensing Letters*

Résumé: Cet article propose des relations entre la transmissivité micro-onde de la forêt boréale et quatre différents paramètres structuraux de végétation : Leaf Area Index (LAI) d'été et d'hiver dérivé de MODIS, ainsi que la biomasse (t ha^{-1}) et le volume total (m^3 ha^{-1}) (nouvelles bases de données pour le Nord du Québec, Canada). Ces relations ont été dérivées à partir de données AMSR-E d'été en prenant en compte l'effet de la diffusion sur l'émission de la canopée. Les RMSEs entre les T_B simulées et les observations AMSR-E sont d'environ 5 K. Les résultats de cette étude permettent d'appliquer des corrections de végétation pour l'estimation de paramètres de surface clé sous la canopée en forêt boréale.

6.1 Présentation de l'article

Le chapitre précédent (Chap. 5) montre l'importance de la considération de ω dans la paramétrisation de l'émissivité de la végétation en forêt boréale. Par contre, l'étude limitée à des sites de forêts boréales denses ne permet pas de spatialiser les corrections de végétation. Ainsi, dans ce chapitre, à partir de données AMSR-E et NARR (pour le sol) d'été, les valeurs de γ-ω ainsi que les paramètres de réflectivité du sol QH sont inversés sur un ensemble de sites en forêt boréale avec différentes densités de végétation. Les valeurs de γ sont ensuite comparées avec trois types de données de paramètres structuraux de la végétation dont deux provenant d'une nouvelle base de données du Service Canadien des Forêts. Les meilleures relations sont trouvées avec les LAI moyens d'hiver. Ce point semble démontrer qu'aux fréquences étudiées, la transmissivité en forêt boréale en été est davantage reliée aux conifères, tandis que le sous-bois a peu d'influence.

Ces relations de transmissivité de forêt boréale d'été seront ensuite utilisées dans le MTR/CLASS pour simuler les T_B en été comme en hiver (Chap. 7). Initialement, étant donné que la structure de la végétation reste relativement identique en hiver comme en été, nous posions l'hypothèse que les paramètres d'été trouvés dans cette étude étaient applicables à la forêt en hiver. Or, au Chap. 7 il sera montré que nous trouvons un biais positif des T_B simulées par rapport aux observations AMSR-E qui augmente avec la végétation lorsque les paramètres d'été sont utilisés. De ce fait, les paramètres γ-ω seront inversés pour des conditions hivernales.

Relationship between forest microwave transmissivity and structural parameters for the Canadian boreal forest

Alexandre Roy[a]
Alain Royer[a]
Ronald J. Hall[b]

[a] Centre d'Applications et de Recherches en Télédétection (CARTEL), Université de Sherbrooke, 2500 boul. Université, Sherbrooke, Qc, Canada, J1K 2R1.
[b]Canadian Forest Service, Natural Resources Canada,

Abstract:

This letter proposes relationships between boreal forest microwave transmissivity and four forest structural parameters: summer and winter Leaf Area Index (LAI) from MODIS, biomass (t ha^{-1}), and total volume (m^3 ha^{-1}) for northern Québec, Canada. These relationships were derived for summer AMSR-E datasets that took into account the effects of canopy emission and scattering. Root mean square error results between brightness temperature simulations and ASMR-E observations are approximately 5 K. Results reported in this study can be used as forest correction equations for key surface parameter retrievals under the boreal forest canopy, such as soil moisture or snow depth/water equivalent.

Keywords: boreal forest transmissivity, AMSR-E, Leaf Area Index, biomass, total volume

6.2 Introduction

The boreal forest is the world's second largest forest biome [1]. Just south of the Arctic Circle, the boreal forest stretches across the Northern Hemisphere in a large, circumpolar eco-climatic region that is always snow covered during the winter months. These regions have a significant impact on the seasonal and annual climatology of much of the Northern Hemisphere [2] as well as on hydrological cycles [3]. However, most of these regions are located in remote areas where the sparse network of meteorological stations and field observations are not sufficient to generate spatially accurate information on climatological attributes. Passive microwave measurements, which provide synoptic coverage more than twice a day in northern regions can be used to derive information about surface characteristics given their sensitivity to soil moisture through its effects on the dielectric constant and hence emissivity of soil [4]. Furthermore, the presence of snow is an important scatterer at higher frequencies (18.7 and 36.5 GHz) that consequently reduces the signal coming from the surface [5]. These data are appealing sources of information to improve

the monitoring of surface parameters, particularly in remote areas dominated by forests such as the Canadian boreal forest.

A major limitation from using microwave data in a boreal forest environment, however, is the attenuation of the ground surface emission by the tree canopy. Depending on its frequency (from 36.5 to 6.9 GHz), the surface emission under a dense boreal canopy in winter can represent 40% to 70% of the total signal [6], [7]. Thus, the signal must be corrected for vegetation attenuation, and for the emission from the vegetation itself. The τ–ω vegetation radiative transfer model [8], which is the most commonly used model for applications based on spaceborne observations such as AMSR-E, represents the optical thickness (τ) of the vegetation and its scattering albedo (ω). However, most studies dealing with forest transmissivity at AMSR-E frequencies have neglected the forest scattering by considering ω = 0 [9], [10], bringing an overestimation of forest emissivity [11]. Furthermore, they related transmissivity to stem volumes, which is a forest structural parameter rarely available at large spatial scales.

Moreover, the difficulty in retrieving these two vegetation parameters (τ–ω) is that the total measured brightness temperature also depends upon soil conditions; there are thus two imbricated aspects that must be taken into account by modeling the vegetation and the soil effects. The soil emission is related to soil moisture, which is assumed to be known in this study, and also to soil textural and structural properties (as surface roughness enhances soil emission) and both can be estimated using a simple semi-empirical soil emissivity model based on two best-fit parameters QH [12].

The objective of this study is to relate the microwave transmissivity of the boreal forest canopy in a region located in northern Québec to three forest structural parameter products: LAI, biomass and total volume. The results of this work are also intended to find ω and QH values over the boreal region of northern Québec. The relationships generated are provided for the spatial correction of the boreal forest microwave transmissivity. In the context of forest-covered surfaces remote sensing using AMSR-E microwave brightness temperature (T_B), the proposed models provide new values that account for the forest canopy contributions.

6.3 Description of sites and data

6.3.1 Sites

The study area is located within the boreal forest of northern Québec (>50° latitude). Image pixels from the 1-km-pixel Land Cover Map of Canada 2005 were resampled to a 12.5 km by 12.5 km AMSR-E EASE-grid from which pixels with eight neighbours that contained more than 80% coniferous land cover were selected. A threshold of 75% coniferous cover was considered for latitudes >54°. If two or more neighbouring pixels reached that limit, only the pixel with the highest percentage of coniferous cover was chosen. Hence, 85 sites satisfying the above-mentioned conditions were selected (figure 6.1).

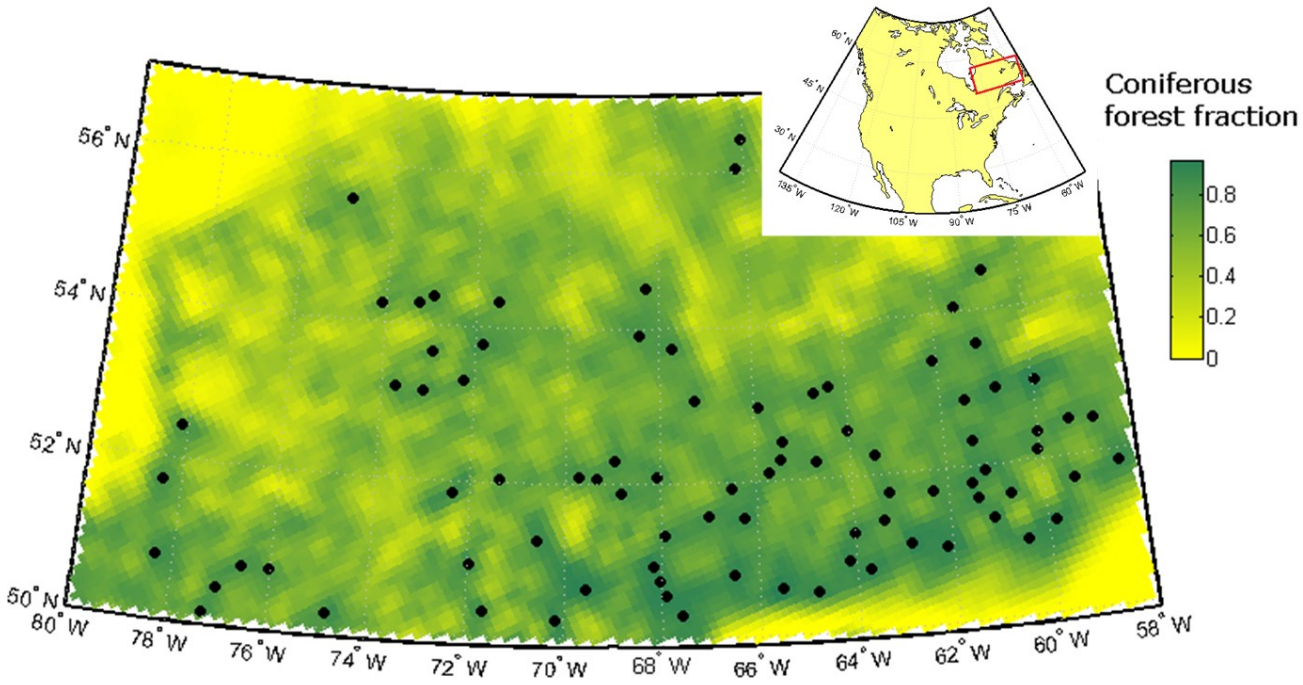

Figure 6.1: The 85 study sites (black dots) and the mean boreal coniferous forest fraction derived from the Land Cover Map of Canada (2005) on a 12.5 km EASE-Grid and its 8 neighbour pixels. Only points above 50° latitude were chosen.

6.3.2 Data

6.3.2.1 AMSR-E data

The AMSR-E/Aqua L2A Global Swath Spatially-Resampled Brightness Temperatures, provided by the National Snow and Ice Data Center (NSIDC), were used in this study. The AMSR-E data consisted of a nominal spatial resolution with a 37-km footprint that was analyzed at the 10.7, 18.7 and 36.5 GHz frequencies, and a 56-km footprint used at 6.9 GHz. Both ascending (about 13:00 local time) and descending (about 3:00 local time) passes were used. The study used data

within the time period from July 1st to August 31st for 2005 and 2008 respectively. These years encompassed a wide range of soil moisture and were chosen to obtain a strong contrast in the soil conditions (see [6]).

6.3.2.2 LAI MODIS

The 8-day LAI product derived from MODIS TERRA (MOD15A2: [13]) was resampled to the AMSR-E EASE-Grid. The average LAI was computed as the mean of all MODIS LAI values within each AMSR-E EASE-Grid pixel. Then, the "summer" average value from July 1st to August 31st for 2005 and 2008 was calculated to generate an LAI value considered representative of the summer conditions for a given site (LAI_{summer}). The "winter" average value from January 1st to February 27th was computed to determine an LAI value representative of the winter conditions (LAI_{winter}).

6.3.2.3 Canadian Forest Service biomass and total volume products

The Earth Observation for Sustainable Development of Forests (EOSD) project was a collaborative undertaking by the Canadian Forest Service and Canadian Space Agency, in partnership with the Provinces/Territories, several universities and non-governmental organizations to generate a circa year 2000 land cover map of the forested areas of Canada [14]. The EOSD land cover map identifies vegetated and non-vegetated areas from which total volume and above ground biomass (AGB) were estimated for areas dominated by coniferous, deciduous and mixed forest types. A pixel level integration process was implemented whereby forest age from the Canada Forest Inventory, site quality based on temperature and moisture, and the ecozone were used with the forest land cover to generate estimates of total volume and AGB [15]. The individual tree dry biomass equations applied to the field data which was then scaled to a plot and ha^{-1} basis was derived from Lambert et al. [16]. These were employed by the generation of volume-to-biomass functions reported by Boudewyn et al. [18]. An estimate of AGB was also assigned to vegetated areas classified as shrub and herb based on look-up tables developed from ground data within strata described by the ecozone and vegetation type [15]. These maps were initially aggregated to a 1 km spatial resolution and subsequently resampled to generate average values within a 12.5 x 12.5 km on the EASE-grid. The spatial footprint for biomass was larger than the total volume due to the absence of tree cover in areas classified as shrub and herb. An assessment of the EOSD biomass map was undertaken across six regions

spanning multiple ecological zones across Canada. A detailed forest inventory data was available, which resulted in an average coefficient of determination (R^2) of 0.8 with biases ranging between 7 to 57 t ha^{-1} [15].

6.4 Radiative transfer model and transmissivity inversion

The forest radiative transfer model used in this study is the well-known τ-ω model [8]. Given a constant viewing angle by AMSR-E at 55°, τ can be defined in terms of transmissivity (γ), such that $\gamma = \exp(-\tau/\cos\theta)$, where θ is the viewing angle. From the γ-ω model, the brightness temperature of a forested area ($T_{Bforest}$) from a satellite perspective can be represented as follows (see [6], for details):

$$T_{B\,forest} = [\gamma\ e_{surface}T_{surface} + (1-\omega)(1-\gamma)T_{veg} + \gamma(1-\omega)(1-\gamma)(1-e_{surface})T_{veg} + T_{B\,atm\downarrow}\gamma^2(1-e_{surface}) + \omega(1-\gamma)T_{B\,atm\downarrow}]\ \gamma_{atm} + T_{B\,atm\uparrow} \quad (6.1)$$

where T_{surf} is the surface (soil) temperature (K), e_{surf} is the surface emissivity, T_{veg} is the temperature of the vegetation (taken as air temperature), $T_{Batm\downarrow}$ and $T_{Batm\uparrow}$ are respectively the downwelling and upwelling atmospheric brightness temperatures, and γ_{atm} is the atmospheric transmissivity. Surface variables needed in the model were obtained from North American Regional Reanalysis (NARR) data [18]. Over the 81 sites, the NARR soil humidity ranges from 0.16 to 0.38 ($m^3 \cdot m^{-3}$). The atmospheric contributions were also derived using NARR temperature/humidity 29 atmospheric layers and [19] models. The e_{surf} term can be calculated from the QH soil reflectivity model [12].

In (eq. 6.1), only the forest parameters (γ-ω) and soil reflectivity parameters (QH: e_{surf}) are unknown. See [6] for more detail on how these different components contributed to the processing of $T_{Bforest}$. In particular, it appears that both these contributions are linked together and cannot be decoupled. Thus, for each site and each frequency (6.9, 10.7, 18.7 and 36.5 GHz), an iterative process was carried out on γ (by steps of 0.01) and Q_R (step of 0.05) to find the γ and Q_R that minimized root mean square errors (RMSE) between the simulated and measured T_B at horizontal and vertical polarizations (γ is considered constant for both polarizations as demonstrated and assumed in previous studies, e.g. see [6]; [20]). That direct iteration process is conducted for different ω (step of 0.01) and H_R (step of 0.05) values considered as constant in

frequency. Hence, the mean optimal RMSE (best γ and Q_R) of every site and at every frequency/polarization were calculated for each ω-H_R couple. The optimized γ values found for each site (considering optimal ω-H_R) were compared with forest structural parameters (LAI, biomass and total volume). The transmissivity was linked to the forest structural parameters (FSP) by an exponential fit of the form [9]:

$$\gamma(FPS) = a + (1-a)\cdot\exp(-b\cdot FPS)\,. \tag{6.2}$$

6.5 Results and discussion

Figure 6.2 shows that for different values of ω and H_R, the mean optimized RMSE for γ and Q_R at each site and frequencies were found at ω = 0.05 and H_R = 0.4. The ω-H_R two dimensional graph (figure 6.2) shows that the optimal solution does not appear sensitive to H_R when 0.04 < ω < 0.06 and these were in the range of values previously reported (see [6]). These parameters must be considered as effective parameters that accounts for mixing effects of variable dielectric and physical properties of both soil and vegetation within the pixel (see [21]).

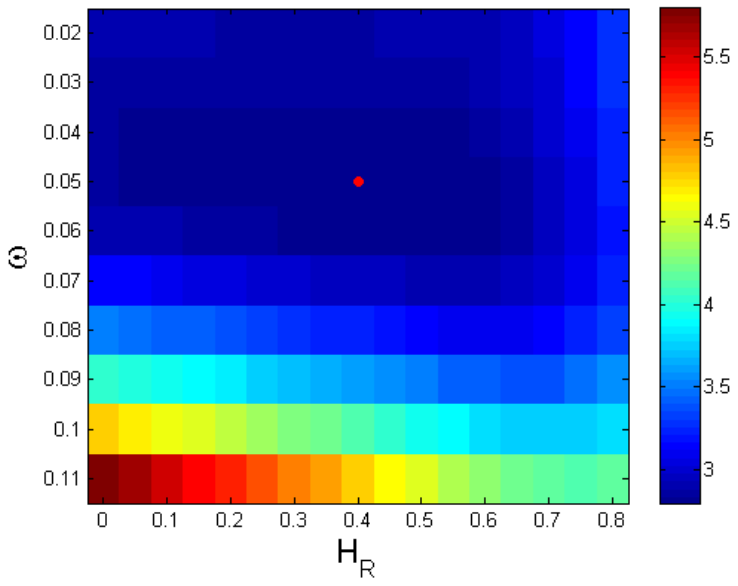

Figure 6.2: RMSE (in kelvin, color scale) between simulated and AMSR-E measured T_B as a function of the roughness soil parameter (H_R) and the boreal forest scattering albedo (ω) at the four frequencies. (Red point) Minimum RMSE for H_R = 0.4 and ω = 0.05.

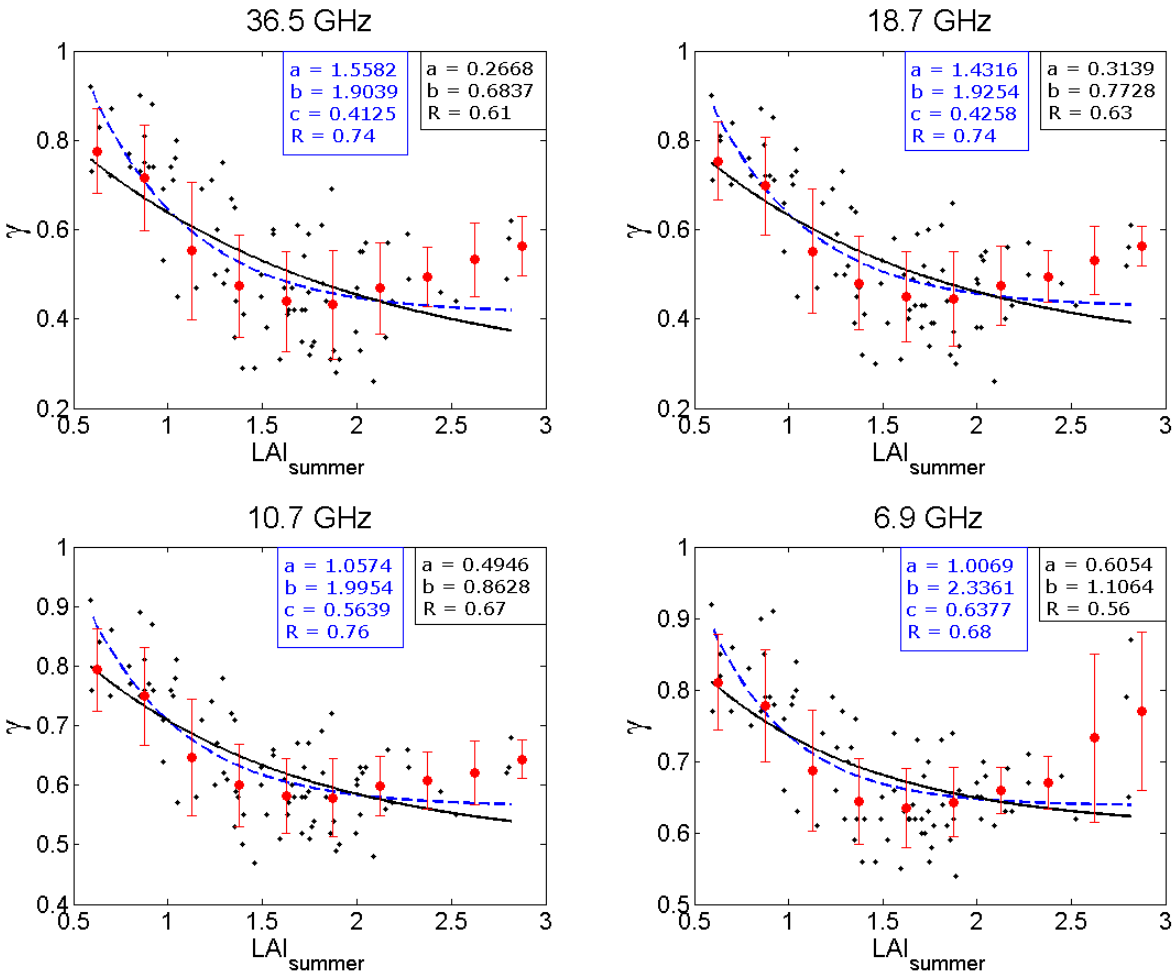

Figure 6.3: Optimized γ as a function of LAI_{summer} at the four frequencies. (Black dots) Individual points. (Red points) Mean values for an interval of 0.25 for LAI. Two fits over all the blacks dots were tested: eq. 6.2 (black line) and $\gamma(FPS) = a \cdot \exp(-b \cdot FPS) + c$ (dotted blue line), which gave the best fit.

When the calculated transmissivity values, derived using ω = 0.05 and H_R = 0.4, were compared with each forest structural parameter, we observed nonlinear relationships between the calculated transmissivity represented by optimized γ and LAI_{summer} (figure 3). It appears that the exponential relationship suggested by Kruopis et al. [9] (eq. 6.2) tends to underestimate the transmissivity for low LAI_{summer}. This result occured because eq. 6.2 passes through γ = 1 for a LAI_{summer} = 0, while figure 6.3 shows that LAI_{summer} is found to be approximately 0.5 for γ = 1. A similar equation [$\gamma(FPS) = a \cdot \exp(-b \cdot FPS) + c$] provides a better fit to these data. At LAI_{summer} > 2.0, however, the transmissivity increases slightly with LAI. This phenomenon may be related to the presence of understory vegetation. Within the boreal forest, many stands are relatively open, which results in relatively low values for coniferous LAI. During the summer when the deciduous foliage and shrubs become visible within canopy openings in the understory, the LAI would rise

significantly, while the transmissivity related mostly to tree branches [22] remains stable. Figure 6.4 shows that if considering LAI_{winter} (i.e., when the understory is mostly buried under snow) with the same T_B summer datasets, there is no increase in γ for higher LAI. Furthermore, the fact that LAI_{winter} leads to a better fit using the exponential relationship (eq. 6.2), suggests that the gap between $LAI_{summer} = 0$ and $\gamma = 1$ in figure 6.3 could also be caused by shrubs and understory vegetation that contribute to the LAI values in summer while having a very low influence on γ.

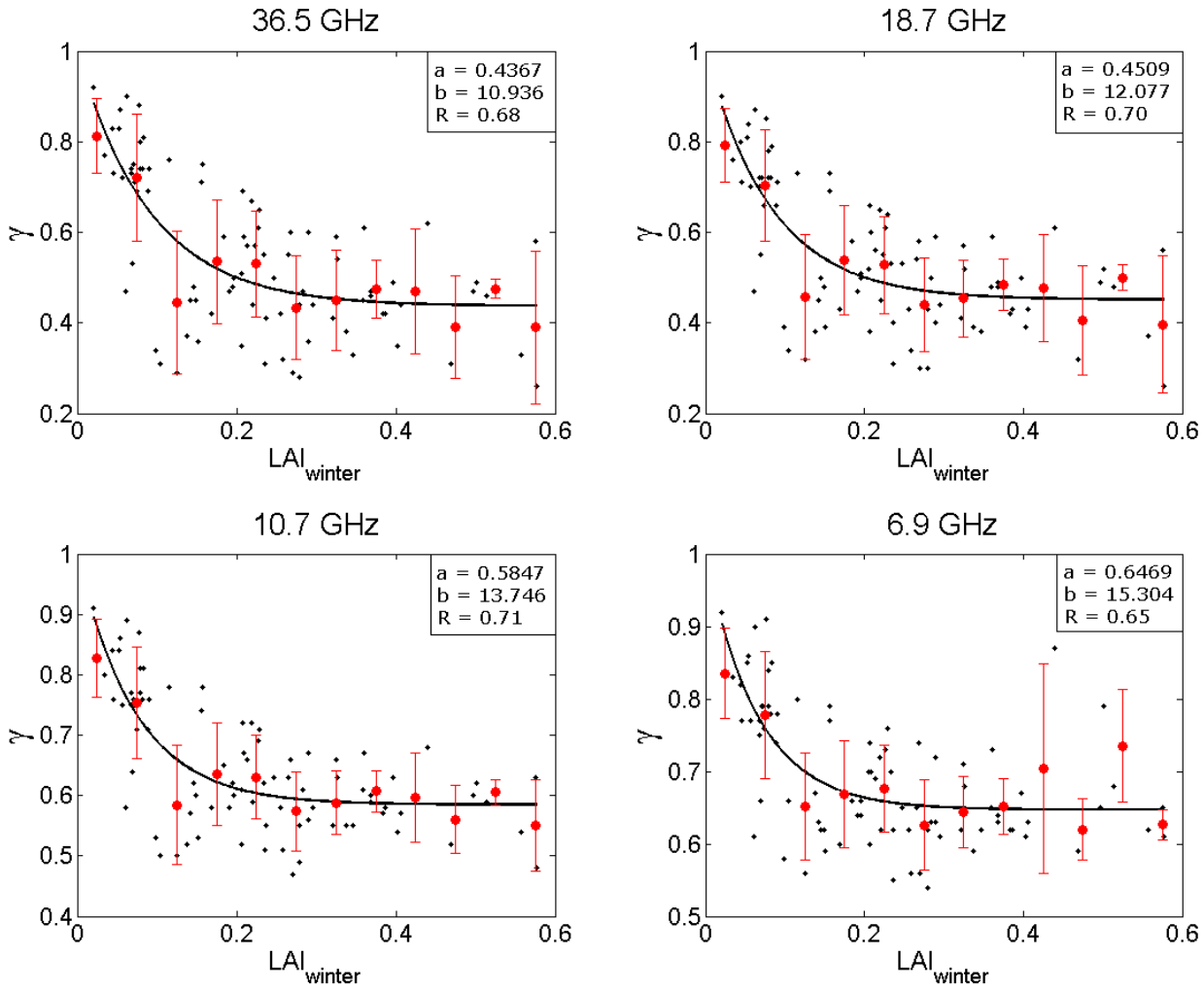

Figure 6.4: Optimized γ as a function of LAI_{winter} at the four frequencies. (Black dots) Individual points. (Red points) Mean values for an interval of 0.05 for LAI. (Black line) Exponential function fit from eq. 6.2 estimated from all the black dots.

The relationships between γ and forest biomass were similar at lower frequencies (10.7 and 6.9 GHz) but the fit seems to overestimate the transmissivity for high biomass at 36.5 and 18.7 GHz, which show a more linear trend (figure 6.5). For total volume (figure 6.6), there is less coherence for the low values of total volume, where the first interval shows lower values than the 2nd and 3th

intervals. The correlation coefficients of biomass and total volume are generally lower than those for LAI. Note also that, as expected, all the relationships show that transmissivity increases with decreasing frequencies.

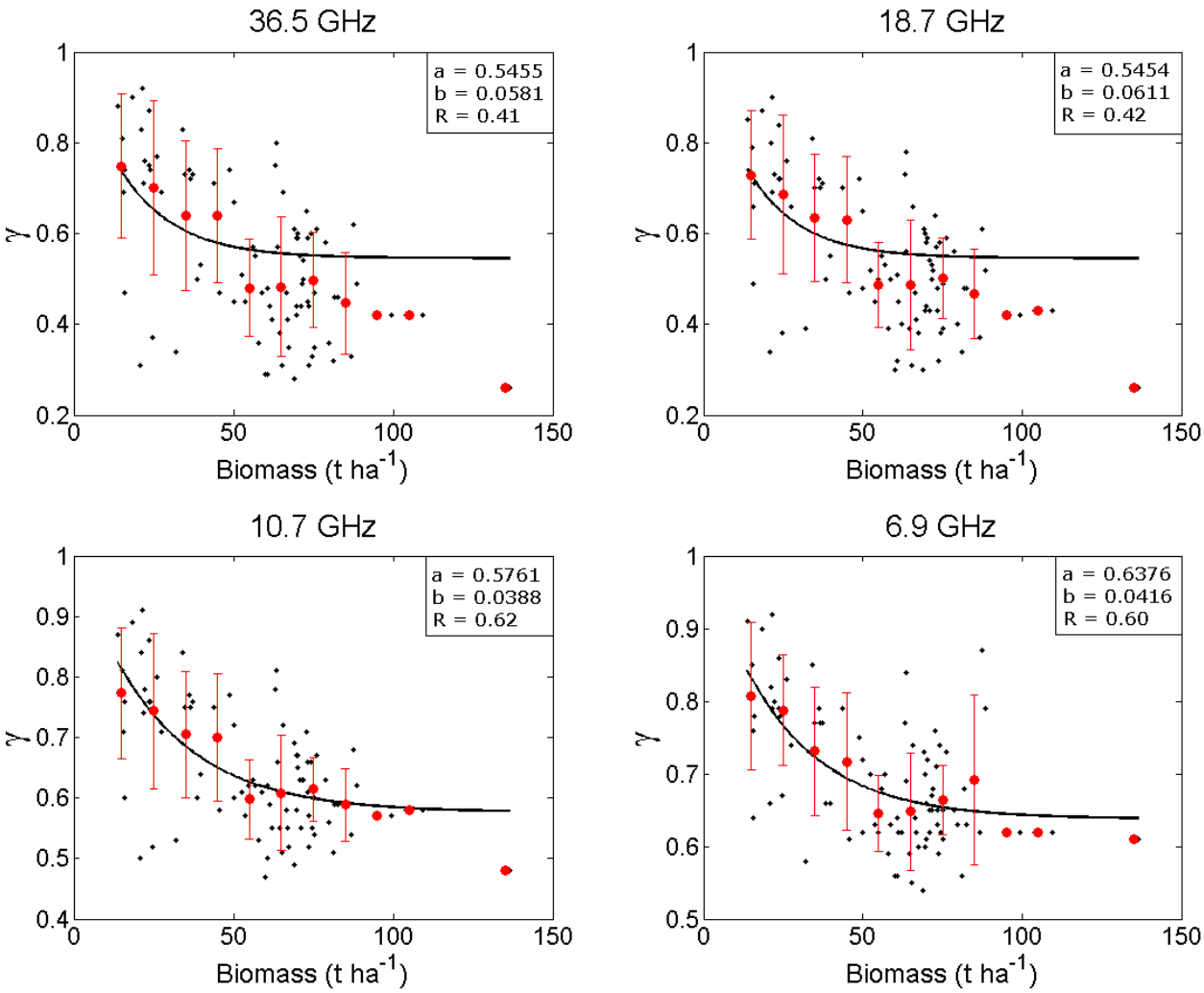

Figure 6.5: Same as figure 6.4, but for biomass. (Red points) Mean values for an interval of 10 t ha^{-1} for biomass.

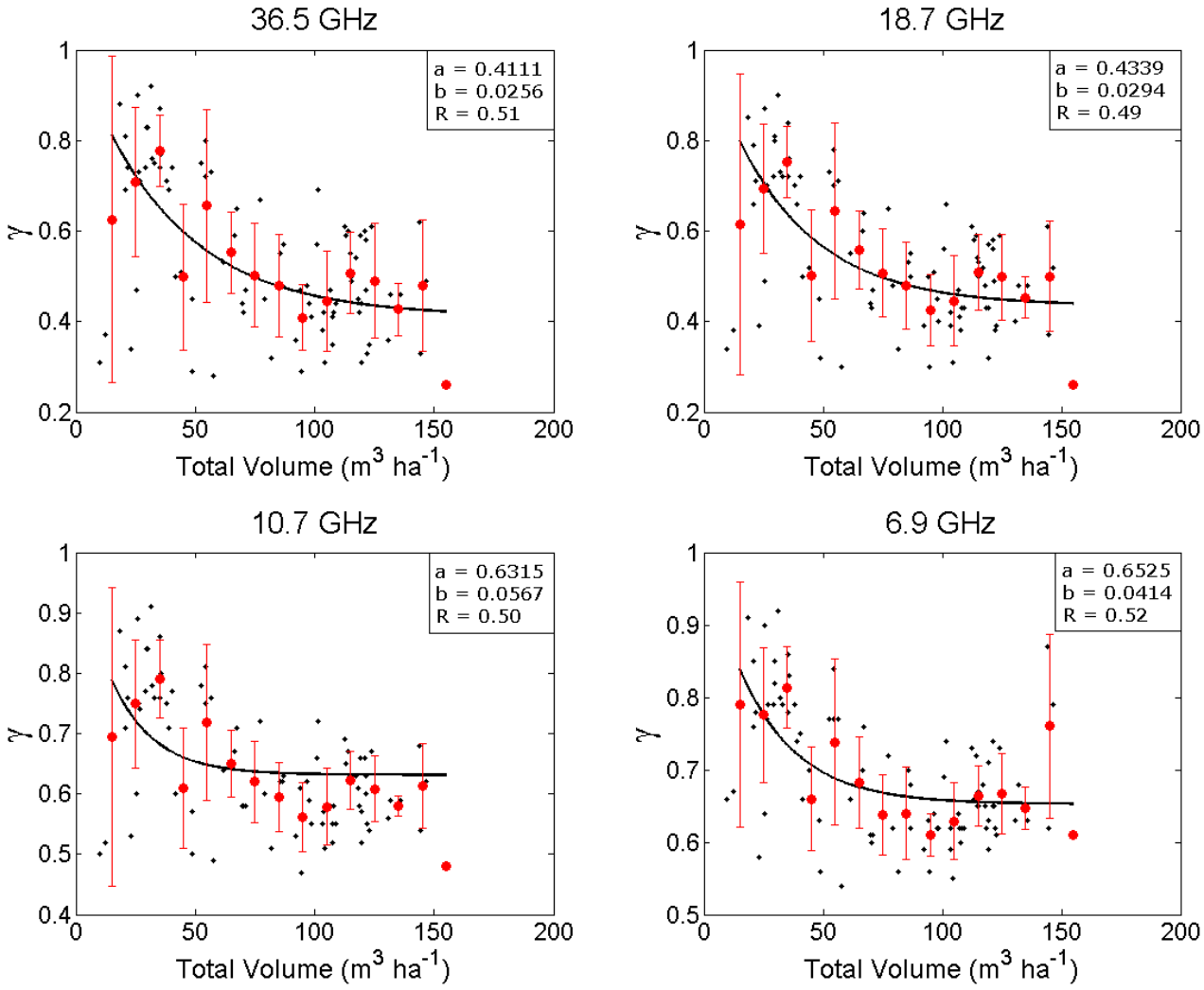

Figure 6.6: Same as figure 6.4, but for total volume. (Red points) Mean values for an interval of 10 m^3 ha^{-1} for total volume.

The Q_R values, which represent the depolarization ratio of the soil, were also calculated for each site and each frequency and values were inversely proportional to frequency (table 6.1). The standard deviations were generally low, but an increase was noted at both 18.7 and 36.5 GHz given the increased sensitivity to soil structural properties at these frequencies.

Table 6.1: Optimized fitted mean Q_R values and standard deviation (std) at the four frequencies.

	36.5	18.7	10.7	6.9
Q_R	0.23	0.25	0.30	0.30
std	0.07	0.06	0.01	0.01

Hence, we found optimized Q_R, H_R and ω values generated the best relationships between γ and forest structural parameters (p-value < 0.01) (figures 6.3 to 6.6) to simulate summer T_B over the

study area. To evaluate the performance of these relationships, two cases were considered for computing the mean RMSE between simulated and measured T_B (four frequencies at both polarizations). For the first case, the RMSE was derived from the retrieved γ and Q_R at each site individually (with the optimized ω and H_R values). This value gave the reference level of the error for the retrieval approach without considering the fitted model. For the second case, the RMSE was derived from the retrieved γ values and mean Q_R values (table 6.1) using the proposed exponential models with the structural parameters (figures 6.3 to 6.6). Table 6.2 shows that the mean RMSE for the individually optimized γ values is very low (2.8 K), and that it is slightly higher (4.5 K to 5.4 K) when using the exponential γ models. Both LAI models generate similar results while the biomass and total volume models give slightly higher RMSE.

Table 6.2: Mean T_B RMSE (K) for the 85 sites considering γ values derived from the relationships between γ and forest structural parameters using eq. 6.2 (excepted for *; $\gamma(FPS) = a \cdot \exp(-b \cdot FPS) + c$).

Frequency (GHz)	36.5	18.7	10.7	6.9	MEAN
Individually optimized γ	2.92	2.66	2.69	2.88	2.79
LAI_{SUMMER} model*	4.05	4.31	4.68	5.16	4.54
LAI_{WINTER} model	4.10	4.39	4.84	5.14	4.62
Biomass model	4.62	5.15	6.07	5.75	5.40
Volume model	5.12	5.30	5.35	5.42	5.30

The obtained ω values were similar to those published by [23] (ω = 0.06) for boreal forest and the one used by [24] (ω = 0.05). The obtained value of γ at 10.7 and 6.9 were however higher than the one found in [25], which reported values that were generally lower than 0.4 in forested regions. These differences might come from the fact that the inversion of γ is strongly dependent of the derived QH values [23]. Indeed, a lower H_R value will lead to a decrease of the derived γ, from a given ω value. As previously mentioned, the convergence of ω and H_R minimizing the RMSE of T_B (figure 6.2) is not narrow and the retrieved values may vary slightly around the minimum solution. The optimized ω value (0.05) found in this study is lower than those found for dense winter boreal forest in [6] (0.063 for airborne dataset and 0.083 for in situ dataset), while the soil reflectivity parameters QH were different. These differences may come from the fact that in [6], the vegetation parameters were inverted in winter conditions and considered as equivalent in summer for QH parameter inversion. In fact, the frozen environment can modify the permittivity of trees in boreal forest [26]. Moreover, note that in the present study, the QH values found should be considered as effective parameters that take into account different aspects of

soils within the boreal forest such as litter contribution (see [23]). The assumption of a single value of H_R and Q_R for the variable boreal forest soil must also be considered as a potential error.

It should also be considered that the γ fits are performed on limited ranges of forest density (FSP). The applicability of the relationships are thus limited to forest densities lower than about 3.0 in LAI_{summer} 0.6 in LAI $_{winter}$ 100 t ha^{-1} in biomass and 150 m^3 ha^{-1} in total volume.

6.6 Conclusion

The objective of this study was to correlate microwave forest transmissivity in a boreal forest environment with different forest structural parameters in order to improve the analysis of surface parameters under the forest canopy using microwave radiometry. Forest transmissivity was calculated for the coniferous boreal forest in northern Québec, Canada, from summer AMSR-E datasets with optimized soil reflectivity parameters (QH model) and forest scattering albedo (γ-ω model). Significant new relationships were generated between the retrieved transmissivity and four different forest structural parameters (LAI_{summer}, LAI_{winter}, biomass, total volume). When using the derived relationships between γ and these structural parameters to simulate T_B, the obtained RMSE between measured (AMSR-E) and simulated T_B are relatively low, at around 5 K. These parameters can thus be used to obtain summer transmissivity at four AMSR-E frequencies (6.9, 10.7, 19.7 and 36.5 GHz) over the boreal forest region evaluated. The comparison between LAI_{summer} and LAI_{winter} using exponential equations (eq. 6.2) [9] shows improved results for LAI_{winter}, which led to the conclusion that the derived transmissivity is mostly attributed to the contribution from trees, while the understory contribution to LAI_{winter} is low as it is hidden by the snow cover.

Finally, the MODIS-derived LAI parameters (summer and winter) generate slightly better results than the biomass or total volume, probably because they incorporated the effects of tree foliage and branches. That product also had the advantage of being available over the entire boreal forest. Results from this study improve our understanding of key surface parameter retrievals from microwave spaceborne brightness temperatures and their relationships with forest structure as defined by LAI, biomass and volume.

Acknowledgments

We thank André Beaudoin and Alexandre Langlois for their helpful comments. Eric Arsenault and Michelle Filiatrault are acknowledged for their work in providing the volume and biomass map data. The Canadian Space Agency is acknowledged for their collaboration and support of the work in generating the column and biomass maps for the forested areas of Canada. We also thank the two reviewers whose comments resulted in improving the quality of the manuscript.

References

[1] J.P. Brandt, "The extent of the North American boreal zone," *Environ. Rev*., vol. 17, pp. 101-161, Dec. 2009.

[2] A. Wramneby, B. Smith, and P. Samuelsson, "Hot spots of vegetation-climate feedbacks under future greenhouse forcing in Europe," *J. Geophys. Res.*, vol. 115, D21119, Nov. 2010.

[3] G.B. Bonan, "Forest and climate change: forcings, feedbacks, and the climate benefits of forests," *Science*, vol. 320, pp. 1444-1449, Jun. 2008.

[4] E.G. Njoku, J.J Jackson, L. Venkataraman, T.K. Chan, S.V. Nghiem, "Soil moisture retrieval from AMSR-E", *IEEE Trans. Geosci. Remote Sens*., vol. 41, no.2, pp.215-229, Feb. 2003.

[5] R.E. Kelly, A.T. Chang,L. Tsang, and J.L. Foster, "A prototype AMSR-E global snow area and snow depth algorithm", *IEEE Trans. Geosci. Remote Sens.*, vol. 41, no.2, pp.230–242, Feb. 2003.

[6] A. Roy, A. Royer, J.-P. Wigneron, A. Langlois, J, Bergeron, P. Cliche, "A simple parameterization for a boreal forest radiative transfer model at microwave frequencies," *Remote Sens. Environ*., vol. 124, pp. 371-383, Sep. 2012.

[7] J.L. Foster, and 11 other authors, "A blended global snow product using visible, passive microwave and scatterometer satellite data," *Int. J. Remote Sens.*, vol. 32, no. 5, pp. 1371-1395, Mar. 2011.

[8] T. Mo, B.J. Choudhury, T.J. Schmugge, J.R. Wang, and T.J Jackson, "A model for microwave emission from vegetation-covered fields," *J. Geophys. Res.*, vol. 87, no.C13, pp. 11229-11237, Dec. 1982.

[9] N. Kruopis, J. Parks, A. Arslan, H. Alasalmi, J. Koskinen, and M. Hallikainen, "Passive microwave measurements of snow-covered forest areas in emac'95," *IEEE Trans. Geosci. Remote Sens*., vol. 37, no. 5, pp. 2699–2705, Sep. 1999.

[10] A. Langlois, A. Royer, F. Dupont, A. Roy, K. Goïta, and G. Picard, "Improved corrections of forest effects on passive microwave satellite remote sensing of snow over boreal and subarctic regions," *IEEE Trans. Geosci. Remote Sens.*, vol. 49, no. 10, pp. 3824-3837, Oct. 2011.

[11] P. Ferrazzoli, L. Guerriero, and J.-P. Wigneron, "Simulating L-band emission of forests in view of future satellite applications," *IEEE Trans. Geosci. Remote Sens.*, vol. 40, no. 12, pp. 2700–2708, Dec. 2002.

[12] R.W. Wang, P.E. O'Neill, T.J. Jackson, and E.T. Engman, "Multifrequency measurements of the effects of soil moisture, soil texture and surface roughness," *IEEE Trans. Geosci. Remote Sens*., vol. GE-21, no. 1, pp. 44–51, Jan. 1983.

[13] R.B. Myneni and 15 other authors, "Global products of vegetation leaf area and fraction absorbed PAR from year one of MODIS data," *Remote Sens. Environ.*, vol. 83, pp. 214-231, Jan. 2002.

[14] M.A. Wulder, J.C. White, M. Cranny, R.J. Hall, J.E. Luther, A. Beaudoin, D.G. Goodenough, and J.A. Dechka, "Monitoring Canada's forests. Part 1: completion of the EOSD land cover project," *Can. J. Remote Sensing*, vol. 34, no. 6, pp. 549-562, Dec. 2008.

[15] R.J. Hall, R.S. Skakun, A. Beaudoin, M.A. Wulder, E.J. Arsenault, P.Y. Bernier, L. Guindon, J.E. Luther, M.D. Gillis, "Approaches for forest biomass estimation and mapping in Canada," *in Proc. IEEE IGARSS*, Honolulu, USA, Jul. 25–30, 2010, pp. 1988-1991.

[16] P. Boudewyn, X. Song, S. Magnussen, and M.D. Gillis, "*Model-based, volume-to-biomass conversion for forested and vegetated land in Canada*," Natural Resources Canada, Canadian Forest Service, Pacific Forestry Centre, Victoria, British Columbia, Information Report BC-X-411, 2007.

[17] M.-C. Lamber, C.H. Ung and F. Raulier, "Canadian national tree above ground biomass equations," *Can. J. For. Res.*, vol. 35, pp. 1996-2018, Sep. 2005.

[18] F. Mesinger, and 15 other authors, "North American regional reanalysis," *Bull. Amer. Meteor. Soc.*, vol. 87, no. 3, pp. 343–360, Mar. 2006.

[19] H. Liebe "MPM - an atmospheric millimeter-wave propagation model," *Int. J. Infrared and Millimeter Waves*, vol. 10, pp. 631-650, 1989.

[20] M. Kurum, P.E. O'Neill, R.H. Lang, A.T. Joseph, M.H. Cosh, and T.J., Jackson, "Effective tree scattering and opacity at L-band," *Remote Sens. Environ.*, vol. 118, pp. 1-9, Mar. 2012.

[21] J.-P. Wigneron and 15 other authors, "L-band microwave emission of the biosphere (L-MEB) model: Description and calibration against experimental data sets over crop fields," *Remote Sens. Environ.*, vol. 107, no. 4, pp. 639–655, Apr. 2007.

[22] E. Santi, S. Paloscia, P. Pampaloni, and S. Pettinato, "Ground-based microwave investigations of forest plots in Italy," *IEEE Trans. Geosci. Remote Sens.*, vol. 47, no. 9, pp. 3016–3025, Sep. 2009.

[23] T. Pellarin, Y. H. Kerr, and J.-P. Wigneron, "Global simulations of brightness temperature at 6.6 and 10.7 GHz over land based on SMMR data set analysis," *IEEE Trans. Geosci. Remote Sens.* vol. 44, no. 7, pp. 2492-2505.

[24] M.O. Jones, L.A. Jones, J.S. Kimball, and K.C. McDonald, "Satellite passive microwave remote sensing for monitoring global land surface phenology." *Remote Sens. Environ.*, vol. 115, pp. 1102-1114, Jan, 2011.

[25] Y. Y. Liu, R. A. M. de Jeu, M.F. McCabe, J.P Evans and A.I.J.M van Dijk, " Global long-term passive microwave satellite-based retrievals of vegetation optical depth, *Geophys. Res. Lett.*, vol. 38, L18402, Sep. 2011

[26] J. Way, and 16 other authors, "The effects of changing environmental conditions on microwave signatures of forest ecosystems: Preliminary results of the March 1998 Alaskan aircraft experiment," *Int. J. Rem. Sens.*, vol. 11, no. 7, pp. 1119-1144.

Chapitre 7 : Discussion - Simulation des températures de brillances d'hiver d'AMSR-E en forêt boréale par le couplage de CLASS et d'un modèle de transfert radiatif pour l'évaluation de la sensibilité au SWE.

7.1 Introduction

Les quatre précédents chapitres présentent les outils et une analyse nécessaires au couplage MTR/CLASS en forêt boréale. Or, nous avons constaté qu'une application directe de ces outils pour le couplage peut amener à des erreurs importantes lorsque les T_B simulées sont comparées aux T_B d'AMSR-E au cours de plusieurs hivers. À la lumière de cette première comparaison, il a été possible d'identifier les trois composantes suivantes à considérer dans les simulations de T_B en forêt boréale d'hiver :

1- Croûtes de glace : comme présenté à la section 2.1.1 (voir figure 2.3) les croûtes de glace (CG) amènent une importante dépolarisation et une diminution significative des T_B surtout en polarisation horizontale (H). Il se trouve que ces événements sont fréquents dans la forêt boréale, et ne doivent pas être négligés.

2- Facteur ϕ : le Chap. 4 montre une légère surestimation des R_{opt} simulés par CLASS-SSA par rapport aux mesures. Ainsi, un ϕ doit être trouvé pour bien représenter le R_{opt} issu de CLASS-SSA en forêt boréale. Pour des sites où la végétation est faible, il a été constaté qu'un ϕ = 3.3 amène une sous-estimation des T_B hivernaux.

3- Différences entre γ-ω d'été et d'hiver : le Chap. 6 présente des relations entre γ-ω et des paramètres structuraux pour des mesures d'AMSR-E d'été. Lorsque ces relations sont utilisées pour des données d'hiver, il apparait un biais positif des simulations par rapport aux mesures qui augmente avec l'augmentation de la végétation à toutes les fréquences. Ces résultats portent à croire qu'il y a une diminution de la contribution de la végétation en hiver (augmentation de γ et/ou diminution de ω).

L'objectif de ce chapitre est d'analyser ces biais en tenant compte des trois éléments soulignés ci-dessus, afin de mieux comprendre la contribution des différentes composantes au signal (neige/grains, forêt, glace). À partir d'une version du modèle MTR/CLASS optimisée, des tests

de sensibilité permettront ensuite de vérifier la sensibilité du signal à différents paramètres, dont le SWE. Ainsi dans un premier temps, pour optimiser les simulations de T_B en forêt boréale, les jours d'hiver précédants une possible fonte sont identifiés en utilisant les températures de l'air ($T_{air} > 0$). Par la suite, en couplant le MTR et CLASS, les périodes précédants une possible fonte sont d'abord utilisées pour inverser le ϕ sur un site où la végétation est très faible l'hiver. Ensuite, les paramètres de végétation d'hiver sont inversés avec les T_B AMSR-E sur des sites avec des couverts de végétation variables (LAI_{winter}). Un algorithme utilisant le ratio de polarisation à 10.7 GHz est utilisé pour identifier l'apparition de CGs, qui sont alors ajoutées dans le modèle DMRT-ML. La comparaison entre l'ensemble des simulations et des T_B AMSR-E est discutée, pour ensuite évaluer la sensibilité du signal MOP au SWE en forêt boréale.

7.2 Méthode

7.2.1 Sites d'étude

L'étude s'effectue sur 22 sites pour 7 hivers consécutifs de 2002-2003 à 2008-2009 (figure 7.1). Ces sites ont été choisis parce qu'ils sont issus de la base historique de mesures nivométriques (SWE et hauteur de neige) d'Hydro-Québec (HQ) et du Ministère du Développement Durable, de l'Environnement et des Parcs du Québec (MDDEP). Cette base de données contient 81 sites au nord du 50^{e} parallèle de 1991-2009 où des mesures nivométriques sont prises mensuellement. En se basant sur le Land Cover Map of Canada 2005 (LCC: Latifovik et al., 2004), rééchantillonné sur une grille EASEgrid 12.5 km X 12.5 km d'AMSR-E, les 22 sites contenant moins de 10 % de plans d'eau ont été sélectionnés. De ces 22 sites, le site avec le plus faible couvert végétal en hiver est utilisé pour inverser la correction à appliquer aux R_{opt} issus de CLASS-SSA (ϕ) (figure 7.1 : point noir). Aussi, trois sites avec des densités de végétation différentes (faible, moyenne et forte) sont choisis pour une analyse des résultats plus spécifique (figure 7.1 : points rouges).

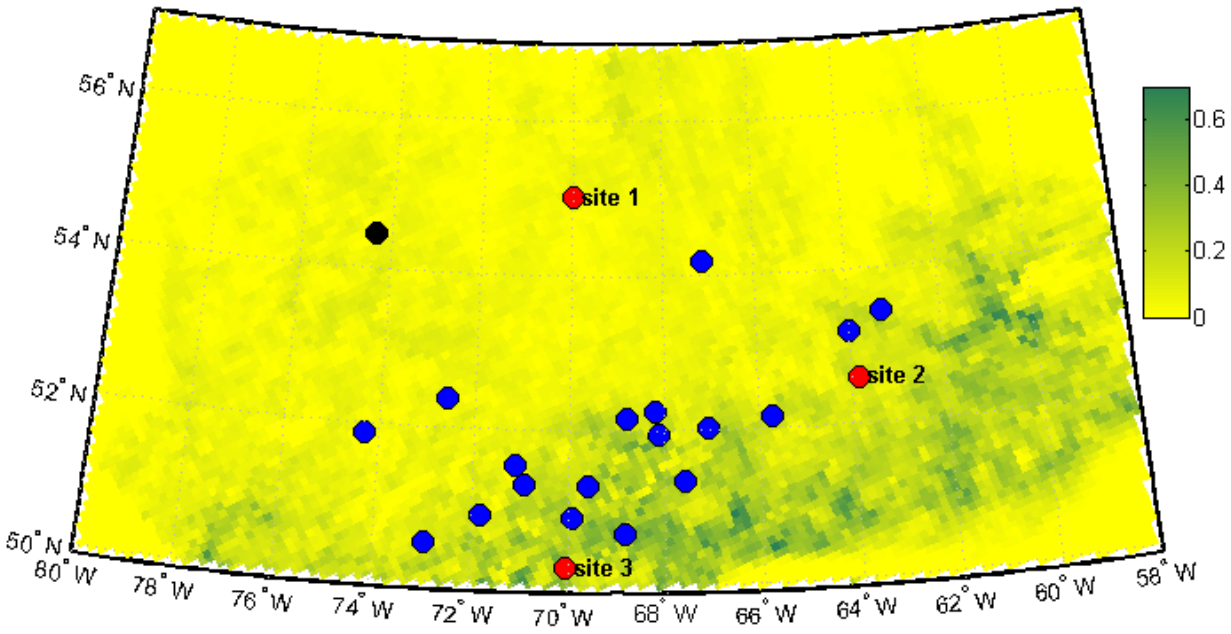

Figure 7.1: Localisation des 22 sites d'étude (la carte de fond est le LAI_{winter}). Noir: site avec très peu de végétation; rouge: trois sites avec des LAI_{winter} différents (aux fins d'analyses spécifiques), bleu: autres.

7.2.2 Données

7.2.2.1 AMSR-E

Les données *AMSR-E/Aqua L2A Global Swath Spatially-Resampled Brightness Temperatures* ont été utilisées dans cette étude. La résolution spatiale de ces données est de 37 km pour les fréquences 10.7, 18.7 et 36.5 GHz. Les données ascendantes (ASC : environ 13h00 heures locales) et descendantes (DSC : environ 3h00 heures locales) sont utilisées, fournissant généralement deux mesures par jours.

7.2.2.2 Données LAI MODIS

Les données de LAI 8-jours dérivées du capteur MODIS TERRA ont été rééchantillonées sur la grille EASE-grid AMSR-E (12.5 km x 12.5 km). Les valeurs moyennes entre le 1er janvier et le 27 février des années 2005 et 2008 ont été calculées afin de retrouver une valeur de LAI_{winter} représentative des conditions hivernales (voir Sect. 6.3.2.2).

7.2.2.3 Relevés nivométriques

La base de données nivométriques d'Hydro-Québec offrent des mesures de SWE et de hauteurs de neige de quatre à sept fois par année, soit à la fin janvier, à la fin février, à la mi-mars, à la fin

mars et au besoin, à la mi-avril, à la fin avril et au début mai. Les valeurs sont la moyenne de dix échantillons pris par un carottier à intervalle de trois mètres dans un milieu considéré comme représentatif (François Vachon, communication personnelle). Le réseau est principalement sous la responsabilité d'Hydro-Québec avec la collaboration du MDDEP.

7.2.2.4 NARR

Les données NARR sont utilisées pour alimenter les modèles. Les données de température de l'air (2 m), d'humidité de l'air, de précipitation, de vitesse de vent (10 m) et du rayonnement incident courte longueur d'onde et infrarouge permettent d'alimenter CLASS et du coup CLASS-SSA. Les valeurs d'humidité de l'air et de température de l'air des 29 couches atmosphériques NARR sont utilisées pour les corrections atmosphériques (voir Sect. 2.3).

7.2.3 Simulations des T_B

Les T_B sont calculées sur les 22 sites à partir de la méthodologie générale présentée à la figure 1.5. Sommairement, CLASS est alimenté par les données NARR. Les sorties de CLASS (CLASS-SSA) sont ensuite utilisées pour alimenter DMRT-ML et le modèle de végétation γ-ω, tandis que les corrections atmosphériques sont apportées à partir des données NARR. Ces trois modèles de transfert radiatif permettent ensuite de simuler des T_B. Les prochaines sections précisent la méthode utilisée et décrivent certaines optimisations effectuées pour raffiner les simulations des T_B.

7.2.3.1 Simulations CLASS

Les simulations CLASS (ainsi que CLASS-SSA) alimentées par les données NARR sont effectuées sur chacun des sites du 1er juillet 2001 au 1er juillet 2009. La première année de simulation (2001 à 2002) sert à initialiser les variables du modèle. Pour chaque site, deux simulations sont effectuées : une en milieu ouvert et une en milieu de forêt de conifères (prise en compte de l'interception et de la sublimation). La moyenne pondérée à la fraction du couvert de végétation (issue du LCC) des variables simulées est ensuite calculée. À noter que les intrants du CRCM pour représenter le type de végétation dans CLASS (Richard Harvey, communication personnelle) sont utilisés.

Afin de minimiser l'erreur reliée au SWE dans les simulations de T_B de MTR/CLASS, les précipitations (intrants) de NARR sont corrigées afin que les simulations de SWE de CLASS équivaillent aux relevés nivométriques. Entre chaque relevé nivométrique, un facteur multiplicatif est ainsi appliqué aux précipitations. Les corrections sont appliquées seulement pour les relevés nivométriques pris avant le début de la fonte (la date où le SWE maximal dans l'hiver est atteint), afin d'éviter de corriger les précipitations alors que c'est principalement le taux de fonte qui influence l'erreur des simulations.

7.2.3.2 Couplage MTR/CLASS

Le couplage de CLASS avec le MTR s'effectue du 1er juillet 2002 au 1er mai 2009. Pour chaque site, le couplage se fait lorsqu'une mesure de T_B d'AMSR-E est disponible (en général deux simulations de T_B par jour : ASC/DSC). Les données de simulations de CLASS ainsi que les SSA de CLASS-SSA (moyennes pondérées à la fraction du couvert de végétation) sont utilisées comme données entrantes dans le modèle de transfert radiatif (DMRT-ML, γ-ω). Lorsqu'il n'y a pas de CG, les simulations de CLASS (une couche) de la température de la neige, de la densité et de la hauteur de la neige (avec précipitations corrigées), ainsi que la moyenne pondérée par la hauteur des R_{opt} simulés par CLASS-SSA, sont insérés comme intrant dans DMRT-ML. Les simulations des températures de la végétation de CLASS (T_{veg}) sont quant à elles utilisées dans le modèle γ-ω. À noter que le couvert de végétation sur un pixel est considéré comme homogène (fraction = 1). Nous considérons qu'à l'échelle des pixels AMSR-E la distribution de la végétation est relativement homogène. Les paramètres atmosphériques sont calculés à partir des données atmosphériques NARR (voir Sect. 2.3).

Le modèle de réflectivité du sol QH est utilisé en considérant les valeurs obtenues au Chap. 6. Considérant les erreurs possibles dans les simulations de l'humidité du sol de CLASS, ainsi que l'ambiguïté des modèles de constante diélectrique pour des sols gelés, le sol n'est jamais considéré comme gelé et l'humidité du sol à 10.7 GHz est optimisée (itération avec des valeurs à l'intérieur de 0.05 à 0.4 d'humidité volumétrique), afin de minimiser la différence entre les T_B simulées et les T_B mesurées à 10.7 GHz pour les deux polarisations ainsi que le passage ASC et DSC (afin de ne pas compenser le cycle diurne à partir de l'humidité du sol). Le 10.7 GHz est utilisé, car il est peu sensible à la neige et sensible à l'humidité du sol. Cette correction des humidités du sol permet ainsi d'avoir des caractéristiques de sol effectives pour le calcul des

réflectivités à 19 et 37 GHz. Il est par contre important de noter qu'une telle approche pourrait compenser certains autres biais qui ne sont pas reliés au sol (végétation, biais sur les températures NARR, etc.). Étant donné que les CG influencent grandement le signal à 10.7 GHz et que la contribution du sol ne devient plus aussi dominante, cette correction est appliquée seulement lorsqu'il n'y a pas de CG dans le couvert nival.

Une première évaluation est aussi effectuée en ce qui a trait à la simulation des T_B en présence de CG. Ainsi, les apparitions de CG sont identifiées à partir des T_B mesurées AMSR-E à 10.7 GHz (voir Sect. 7.2.3.2). Lorsqu'une CG est détectée, une mince couche de 5 mm avec des rayons de sphères de glace nulles (aucune diffusion) est positionnée sur le dessus du couvert nival dans DMRT-ML. Comme l'effet de cohérence n'est pas implémenté dans DMRT-ML pour prendre en compte les effets de l'épaisseur de la CG, la densité de la CG est optimisée (entre 600 et 917 kg m^{-3}) afin de minimiser les RMSE moyens calculés à 19 et 10.7 GHz aux deux polarisations. À noter que la diminution de la densité de la CG dans DMRT-ML diminue l'impact de la CG sur le signal (chute des T_B moins importante en H). Même si la variation de la densité de la CG est physiquement impossible, une telle approche permet de simuler une CG effective, sans que la cohérence ne soit prise en compte. La CG reste à la même position pendant tout l'hiver et la neige continue ainsi de s'accumuler sur celle-ci.

7.2.3.3 Inversion de ϕ et des paramètres de végétation hivernaux

Certaines simulations initiales ont démontré qu'outre les CGs et l'effet du gel/dégel du sol, le ϕ ainsi que la paramétrisation de la végétation doivent être ajustés. Sachant que les événements de gel/dégel ainsi que la formation de CGs ont un effet significatif sur le signal et que leur modélisation est complexe, ces deux paramètres sont ainsi optimisés avec seulement les mesures d'hiver AMSR-E à 37 GHz où il n'y a pas eu d'épisode de fonte précédemment. L'optimisation se fait ainsi en trois phases :

PHASE 1: Identification des épisodes de fonte

Les épisodes de fonte sont identifiés à partir des données de température de l'air NARR. À partir du début de l'apparition de la neige (considéré lorsque les simulations CLASS donnent une épaisseur de neige > 20 cm), lorsque la température de $T_{air} > 0$, le reste de l'hiver est considéré comme influencé par l'effet d'une fonte. Un seuil de 20 cm est choisi pour éviter d'éliminer trop

de mesures, étant donné qu'en début de saison la température oscille autour du point de congélation. Ainsi seulement les périodes précédant un épisode de fonte sont considérées pour l'optimisation.

PHASE 2: Optimisation du ϕ

Le ϕ est optimisé sur un site où le LAI_{winter} est très bas (LAI_{winter} = 0.02; figure 7.1, points noirs). Considérant que la végétation a un faible impact sur ce site, mais tout de même présent, les relations γ_{summer} vs LAI_{winter} (Chap. 6) sont utilisées pour trouver le ϕ optimal qui minimise les T_B simulées (couplage MTR/CLASS pour les jours où il y a de la neige au sol, mais où il n'y a pas eu de fonte) et les T_B d'AMSR-E à 37 GHz en polarisation verticale. Seulement la polarisation verticale est utilisée pour minimiser l'impact de la stratigraphie des couches de neige. Les données à 37 GHz sont utlisées parce qu'elles sont les moins sensibles au sol surtout avec la présence de neige au sol (voir Sect. 3.5.1).

PHASE 3: Inversion des paramètres de végétation hivernaux

Une fois le ϕ trouvé, les paramètres de végétation hivernaux sont inversés sur chacun des sites à partir des mesures AMSR-E à 37 GHz en polarisations verticales et horizontales. Considérant seulement les périodes précédant les épisodes de fonte, une itération sur γ (incrément de 0.01) est effectuée sur les 22 sites afin de trouver le γ_{winter} qui minimise l'erreur entre les T_B issues du couplage (T_B simulées au niveau du satellite) et les T_B AMSR-E et ce, pour différents ω (incrément 0.01). La moyenne des RMSE des 22 sites considérant les γ_{winter} optimaux pour chaque valeur de ω est ensuite calculée pour trouver le ω_{winter} optimal. Une nouvelle relation est ensuite calculée (forme Kruopis et al., 1999; eq. 6.2) entre les γ_{winter} et les LAI_{winter} issus du ω optimal. Une équation polynomiale de 2^e degré est trouvée pour relier γ_{summer} vs γ_{winter}. Cette relation permet ensuite de passer des relations γ_{summer} versus LAI_{winter} à des valeurs corrigées de γ_{winter} à 19 et 10.7 GHz. On pose ici l'hypothèse que l'effet sur γ_{winter} du passage d'une forêt d'été à une forêt d'hiver est la même en fréquence. À noter que les nouvelles valeurs de γ_{winter} et ω_{winter} peuvent influencer le ϕ calculé à la PHASE 2. Les PHASEs 2 et 3 sont donc répétées jusqu'à ce que le ϕ reste constant d'une itération à l'autre. Aux fins de discussion, l'approche sera aussi appliquée, mais considérant des valeurs fixes de ω_{winter} trouvées au Chap. 5 (ω_{winter} = 0.063 issu de données aéroportées, tableau 5.5; ω_{winter} = 0.083 issu de données in situ, tableau 5.6). Ainsi, trois cas sont étudiés:

Cas 1 : Optimisation de γ_{winter} et ω_{winter}

Cas 2 : Optimisation de γ_{winter} avec $\omega = 0.083$ (données in situ, voir tableau 5.6)

Cas 3 : Optimisation de γ_{winter} avec $\omega = 0.063$ (données aéroportées voir tableau 5.5)

7.2.3.4 Identification des croûtes de glace

Une fois les paramètres de végétation hivernaux trouvés, un algorithme développé à partir de données in situ et de simulations basé sur le rapport de polarisation à 10.7 GHz ($PR_{10.7}$) est appliqué pour identifier l'apparition de CGs. Le rapport de polarisation se définit comme :

$$PR_{10.7} = \frac{T_B V_{10.7} - T_B H_{10.7}}{T_B V_{10.7} + T_B H_{10.7}} \tag{7.1}$$

L'algorithme permet d'identifier la présence ou l'absence de CGs dans le couvert nival à partir des données AMSR-E à 10.7 GHz. L'algorithme définit que la présence d'une CG est détectée lorsque le $PR_{10.7}$ est au-dessus de 0.06. Pour s'assurer de ne pas confondre une CG à une croûte de fonte, une CG est considérée comme présente lorsque l'algorithme détecte une CG pour six observations satellitaires consécutives. Il est ensuite considéré qu'il y a une CG pour le reste de l'hiver. Cette approche reste simple mais sera amenée à évoluer dans le cadre de travaux futurs.

7.2.3.5 Résumé de la méthode

La figure 7.2 montre l'ensemble de la méthode qui permet d'obtenir des T_B simulées optimisées qui sont ensuite comparées aux mesures AMSR-E. La partie de droite montre les optimisations (ϕ et γ-ω) effectuées en trois phases menées pour certains sites spécifiques à 37 GHz en considérant seulement les épisodes où il n'y a pas eu de fonte précédemment (Sect 7.2.3.3). À gauche, les données AMSR-E à 10.7 GHz sont utilisées pour optimiser l'humidité et identifier les croûtes de glace. Enfin, l'ensemble des optimisations est ensuite appliquée pour comparer les T_B simulées aux T_B mesurées par AMSR-E aux trois fréquences. Le tableau 7.1 résume les différentes approches pour déterminer les principaux paramètres ainsi que les différentes hypothèses reliées.

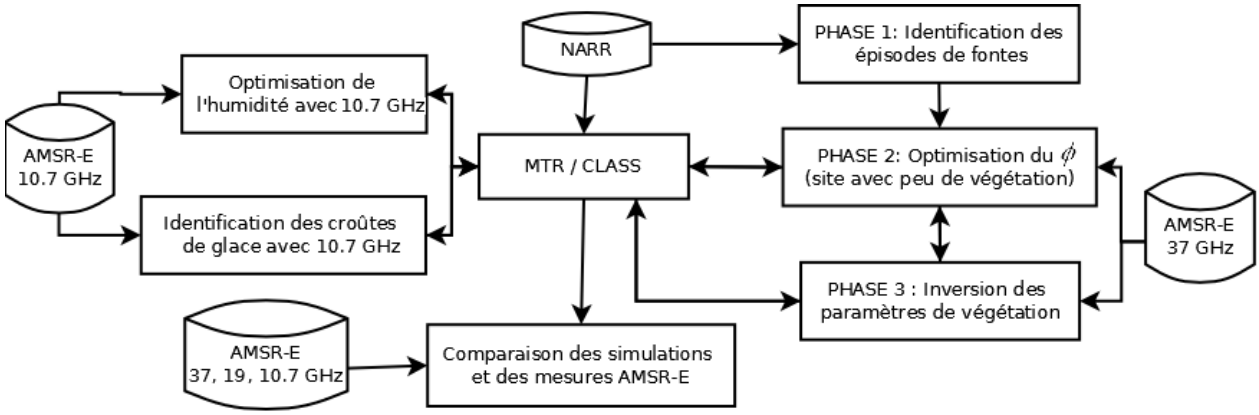

Figure 7.2 : Organigramme méthodologique du présent chapitre.

Tableau 7.1 : Approches et hypothèses pour la détermination des principaux paramètres.

Paramètres	**Détermination**	**Hypothèses**
QH	Par inversion (Chap. 6)	Constant été / hiver
SWE CLASS	Optimisation des précipitations à partir des SWE Hydro-Québec	Erreur CLASS provient principalement des intrants de précipitations
Humidité du sol	Par inversion 10 GHz	Permet d'obtenir des paramètres effectifs de sol
Croûtes de glace	Inversion de la densité avec 10.7 et 19 GHz	Compense pour l'effet de cohérence
ϕ	Par inversion sur le site avec très peu de végétation	Applicable pour l'ensemble des neiges de la forêt boréale
ω_{summer}	Par inversion (Chap. 6)	Constant en fréquence
ω_{winter}	Par inversion avec 37 GHz et MTR/CLASS	Constant en fréquence
γ_{winter}	Par inversion avec 37 GHz et MTR/CLASS	Relation γ_{summer} vs γ_{winter} constant en fréquence

7.3. Résultats

7.3.1. Inversion de ϕ et des paramètres de végétation hivernaux

PHASE 1 : Identification des épisodes de fonte

La figure 7.3 montre que pour les 22 sites, il y a au moins 100 données de mesures AMSR-E précédant un épisode de fonte et en moyenne 465 mesures AMSR-E disponibles. À noter que le site où le ϕ est optimisé (faible végétation) considère 885 mesures. Le nombre de mesures disponibles par site dépend ainsi de la fréquence et du moment dans l'hiver (début ou fin) des épisodes de fontes.

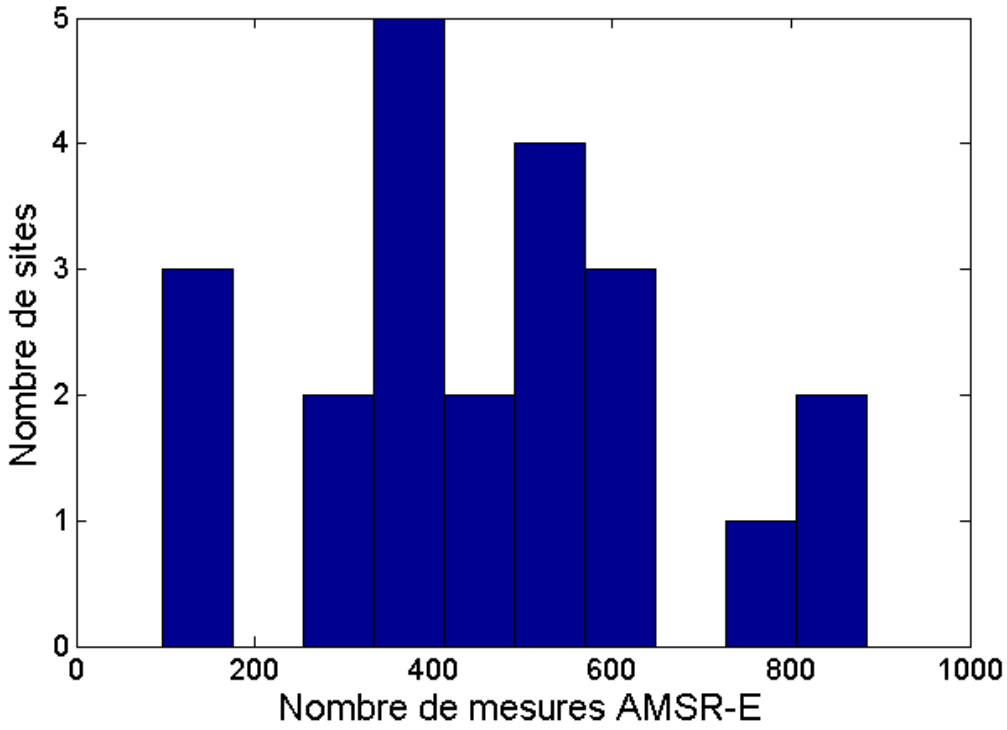

Figure 7.3: Histogramme du nombre de mesures AMSR-E précédants un épisode de fonte pour les 22 sites.

PHASE 2 & 3: Optimisation du ϕ et inversion des paramètres de végétation hivernaux

Dans le Cas 1, où les deux paramètres γ_{winter} et ω_{winter} sont optimisés, les PHASEs 2 et 3 ont été répétées trois fois pour converger vers une valeur fixe de ϕ. Ainsi en considérant les paramètres de végétation γ-ω d'été, un $\phi = 2.9$ a d'abord été trouvé. Ensuite, en utilisant les relations γ_{summer} versus γ_{winter} ainsi que le ω_{winter} calculé avec un $\phi = 2.9$ (PHASE 3), un $\phi = 2.8$ est trouvé. En refaisant à nouveau les PHASEs 3 et 2, on retrouve ainsi $\phi = 2.8$. La figure 7.4 montre ainsi que le ϕ sur le site où la végétation est faible converge après trois itérations. Ce ϕ plus bas que celui de 3.3 trouvé dans Roy et al. (2013a) (Chap. 3) s'explique par la surestimation du R_{opt} dans le modèle CLASS-SSA (Roy et al. 2013b : Chap. 4) par rapport aux mesures. En effet, en comparant les R_{opt} de CLASS-SSA avec les R_{eff} calculées à partir des mesures, un rapport moyen de $\phi = 2.7$ est trouvé.

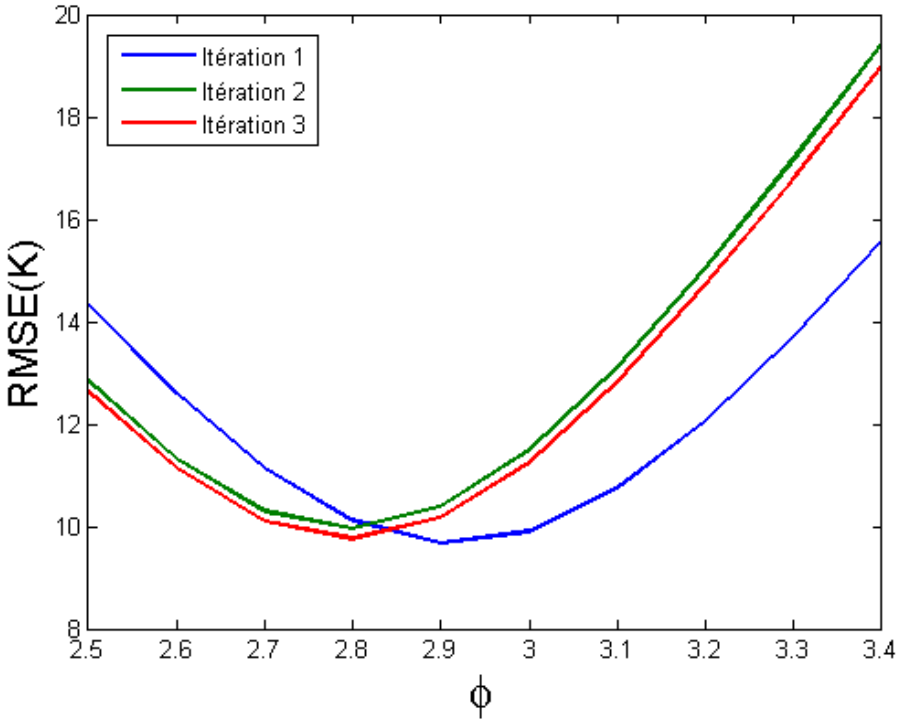

Figure 7.4: RMSE (K) pour l'optimisation de ϕ où la végétation est très faible pour trois itérations des PHASEs 2 et 3.

Les résultats des PHASEs 2 et 3 donnent un ω_{winter} optimal à $\omega_{winter} = 0.13$. Cette valeur est donc plus élevée que le $\omega_{summer} = 0.05$ et indique donc une émissivité de végétation plus basse en hiver. Cette baisse de l'émissivité pourrait être due à la baisse de la constante diélectrique de la végétation lorsque les températures diminuent (Mätzler, 1994; El-Rayes & Ulaby, 1987). La figure 7.5 montre les γ_{winter} optimaux considérant un $\omega_{winter} = 0.13$ pour les 22 sites de l'étude, ainsi que la relation de 2^e degré entre le γ_{summer} versus γ_{winter}. Les γ_{winter} sont légèrement plus élevées que les γ_{summer}, ce qui pourrait encore être du à la baisse de température qui amène un changement dans la constante diélectrique des arbres, mais aussi à la baisse de biomasse en hiver (baisse importante du LAI). Cette optimisation semble néanmoins démontrer que la plus grande partie de la variation de la contribution de la végétation en hiver semble être reliée au changement de ω, et donc à l'émissivité de la canopée.

Pour les Cas 2 et 3 (considération d'un ω_{winter} fixe et optimisation seulement de γ_{winter}), le ϕ converge à ϕ=2.7. La figure 7.6 montre que les transmissivités augmentent davantage en considérant $\omega_{winter} = 0.083$ par rapport à un $\omega_{winter} = 0.13$ optimisé. Le $\omega_{winter} = 0.083$ plus bas implique une émissivité plus forte de la végétation. Ainsi, l'optimisation va augmenter les

transmissivités pour diminuer le biais positif en augmentant la contribution provenant du sol qui est moins émissif à cause de la présence de la neige. La relation γ_{winter} versus LAI_{winter} est aussi davantage linéaire dans la gamme de valeurs de LAI_{winter} et montre qu'au-delà de certaines valeurs de LAI_{winter}, le γ_{winter} serait plus bas que le γ_{summer}. Aussi, à noter que la relation γ_{summer} vs γ_{winter} prend une forme exponentielle. Les résultats considérant un $\omega_{winter} = 0.063$ sont similaires, mais avec des γ_{winter} plus élevées (pas montré). L'utilisation de ω_{winter} fixe semble donc a priori moins cohérente que lorsque le ω_{winter} est optimisé.

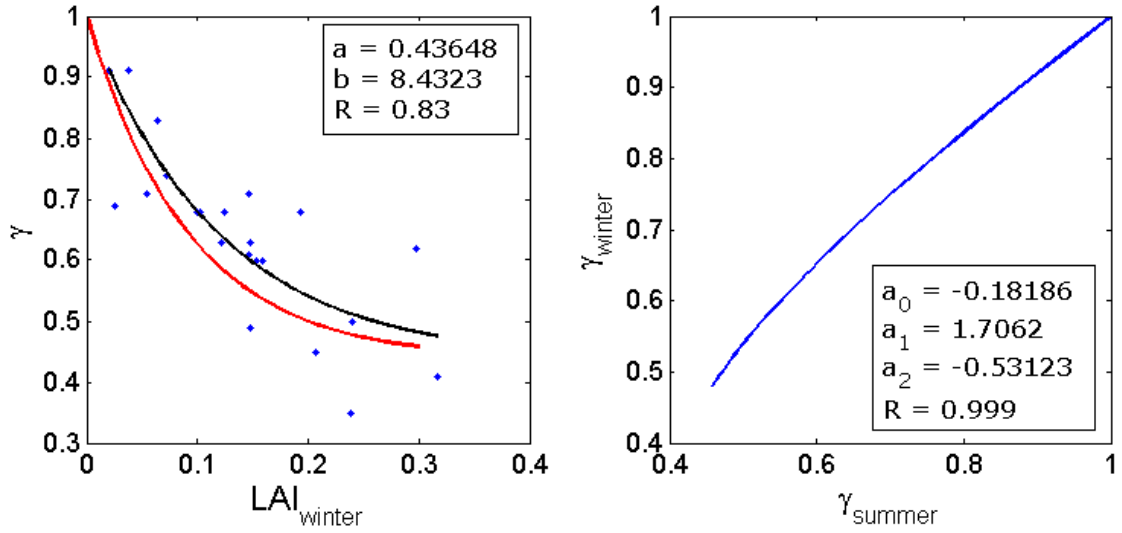

Figure 7.5: Gauche: relation entre les γ_{winter} inversés versus LAI_{winter} (points bleus = γ optimisés; ligne noir = relation exponentielle) ainsi que la relation γ_{summer} versus LAI_{winter} (ligne rouge, tiré du Chap. 6) à 37 GHz; droite : relation (polynome 2^e degré) entre γ_{summer} et γ_{winter}. Résultats pour le Cas 1: optimisation de γ_{winter} et ω_{winter}.

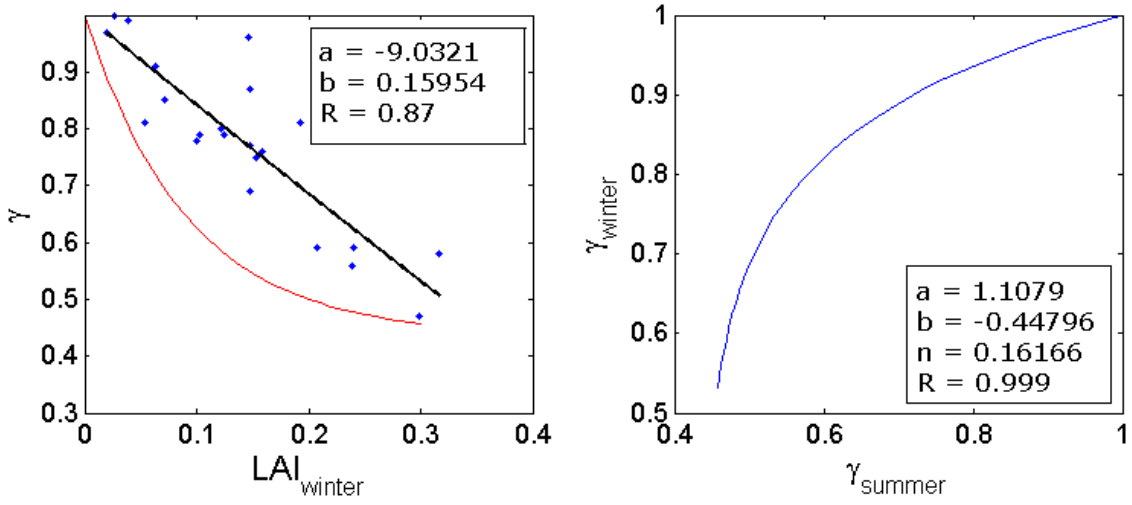

Figure 7.6: Gauche: relation entre les γ_{winter} inversés versus LAI_{winter} (points bleus = γ optimisés; ligne noir = relation exponentielle) ainsi que la relation LAI_{winter} vs γ_{summer} (ligne rouge, tiré du Chap. 6) à 37 GHz; droite : relation $[a(x+b)^n]$ entre γ_{summer} et γ_{winter}. Résultats pour le Cas 2: optimisation de γ_{winter} avec $\omega_{winter} = 0.083$.

7.3.2 Analyse des résultats

Les RMSE et les biais moyens d'hiver pour les 22 sites (comparaison des T_B simulées perçues par un capteur satellitaire par le couplage MTR/CLASS avec les mesures AMSR-E) sont calculés pour les 3 Cas (ω_{winter} optimisé ou fixe). Les données d'hiver consistent aux données comprises entre le début de l'apparition de la neige au sol et l'atteinte du SWE maximal dans l'hiver (basées sur les simulations de SWE de CLASS). Le SWE maximal est considéré comme limite pour éviter les périodes de fontes printanières où le signal MOP est principalement influencé par la teneur en eau liquide dans le couvert nival (voir Sect. 2.1.1). Les statistiques ont aussi été calculées pour des simulations considérant les paramètres de végétation d'été.

Le tableau 7.1 montre les statistiques seulement pour les mesures où il n'y a pas de CG détectées. Les meilleurs résultats sont obtenus dans le Cas 1 où le ω_{winter} = 0.13 est optimisé avec une RMSE autour de 7 K à 37 GHz, 4 K à 19 GHz et 3 K à 10 GHz. Il y a une amélioration des RMSE d'environ 1.5 K par rapport aux Cas 2 (ω_{winter} = 0.083 fixe) à 37 et 19 GHz. On voit aussi qu'avec ω_{winter} = 0.13, les biais positifs diminuent de 4.5 à 0 K en polarisation V. La nette amélioration des biais à 19 GHz semble aussi démontrer que l'hypothèse de la relation γ_{summer} versus γ_{winter} équivalente en fréquence est valide. En effet aucun paramètre n'est optimisé à 19 GHz. Pour leur part, les résultats à 10.7 GHz d'un cas à l'autre sont similaires à cause de l'optimisation de l'humidité du sol à 10.7 GHz. D'autres parts, les résultats, lorsque les paramètres d'été sont utilisés, montrent surtout des biais importants à 37 et 19 GHz (environ 5 K).

En conclusion, les RMSE considérant le ω_{winter}=0.13 optimisé, autour de 7 K à 37 GHz et 4 K à 19 GHz démontrent que le couplage MTR/CLASS permet de bien simuler l'ensemble des composantes du transfert radiatif en forêt boréale d'hiver. Ces RMSE sont moins de la moitié de ce qui a été obtenu à partir de mesures in situ (voir tableau 3.4). Ces résultats sont d'autant plus intéressants considérant que l'ensemble des bruits reliés à la mesure radiométrique et aux effets de rééchantillonnages sont généralement évalués entre 2 et 3 K (Pardé et al., 2007; Kohn et al., 2010).

Tableau 7.2: RMSE/biais (K) moyens de 22 sites pour les mesures en « hiver sans glace ».

	37V	37H	19V	19H	10.7V	10.7H
Cas 1 : $\omega_{winter} = 0.13$	7.1/0.7	7.5/1.5	4.1/-0.0	4.8/1.3	2.5/-0.7	3.5/-0.2
Cas 2 : $\omega_{winter} = 0.083$	8.9/3.6	8.9/2.1	6.1/4.5	5.8/2.6	2.9/1.2	4.7/-2.2
Cas 3 : $\omega_{winter} = 0.063$	9.6/3.7	9.6/2.0	5.6/6.1	3.7/5.7	2.6/1.3	3.2/-1.3
ω_{summer} & γ_{summer}	8.2/5.2	10.0/6.8	4.3/3.1	6.9/5.0	2.1/-0.7	2.6/0.8

Le tableau 7.3 montre les résultats en considérant l'ensemble des données d'hiver, incluant celles avec CGs. Les RMSE sont généralement plus élevés d'environ 2 K lorsque les périodes de CGs sont considérées et modélisées (en considérant le Cas 1 optimum, $\omega_{winter} = 0.13$). Un facteur important de cette augmentation des erreurs est le fait que DMRT-ML ne prend pas en compte l'effet de cohérence dans les CGs (voir figure 2.3). Cependant, l'erreur observée est très nettement inférieure à celle obtenue en ignorant l'existence de ces CG (non montré). Des cas spécifiques de modélisation de CGs seront étudiés un peu plus loin. Il reste que l'implémentation des CGs n'est pas traitée en profondeur dans le cadre de cette étude. Une discussion sur une amélioration de la paramétrisation des CGs est aussi développée à la Sect. 7.4.3.

Tableau 7.3: RMSE/biais (K) moyens de 22 sites pour les mesures en « hiver avec et sans glace » (tous les points d'hiver).

	37V	37H	19V	19H	10.7V	10.7H
Cas 1 : $\omega_{winter} = 0.13$	8.1/1.0	8.4/1.5	5.0/0.8	6.5/2.4	3.2/-0.6	4.8/0.1
Cas 2 : $\omega_{winter} = 0.083$	10.0/3.6	9.8/1.3	7.5/4.6	7.4/3.4	3.8/1.5	6.0/-2.2
Cas 3 : $\omega_{winter} = 0.063$	10.5/3.2	10.8/2.0	7.5/6.1	8.7/5.7	3.0/0.4	3.6/-0.4
ω_{summer} & γ_{summer}	10.1/6.4	11.6/8.0	6.2/4.4	10.0/7.2	3.2/-0.7	5.4/1.6

Le tableau 7.4 montre les RMSE et les biais moyens en été. Avec des RMSE sous les 3 K, ces résultats constituent une validation additionnelle de la paramétrisation des paramètres de végétation d'été effectuée au Chap 6. Les biais se trouvent aussi sous les 1 K. Ces résultats montrent aussi que l'optimisation de l'humidité du sol à 10.7 GHz permet d'obtenir des caractéristiques de sol effectives pour les trois fréquences.

Tableau 7.4: RMSE/biais (K) moyens de 22 sites pour les mesures en été.

	37V	37H	19V	19H	10.7V	10.7H
ω_{summer} & γ_{summer}	2.6/1.0	2.8/-0.7	2.4/0.9	3.0/-0.8	2.5/0.7	2.6/-0.8

Les figures 7.7, 7.9 et 7.10 montrent les simulations aux trois fréquences du couplage MTR/CLASS des T_B perçues par un capteur satellitaire de 2002 à 2009 (7 hivers de 2002-2003 à

2008-2009) sur trois sites de forêt boréale offrant des densités de végétation variables (voir figure 7.1 : points rouges). Les simulations de SWE de CLASS ainsi que les mesures de SWE d'Hydro-Québec sont aussi présentées (graphique du bas). Ces comparaisons de SWE montrent que les corrections des précipitations permettent d'ajuster les SWE simulés afin qu'ils correspondent aux SWE mesurés.

Le premier site (figure 7.7) possède un LAI_{winter} relativement faible à 0.064. Ce site permet d'évaluer davantage les simulations de l'émission micro-onde de la surface (neige et sol). La figure 7.7 montre que les tendances des T_B sont bien représentées par les simulations avec des T_B qui diminuent durant l'hiver surtout à 37 GHz à cause de la présence de la neige et du métamorphisme des grains de neige. Ces tendances à 37 GHz en hiver semblent démontrer que les simulations de CLASS-SSA permettent de représenter relativement bien la taille de grains dans le contexte du transfert radiatif micro-onde dans la neige. L'algorithme basé sur le $PR_{10.7}$ identifie l'apparition de CGs sur cinq hivers, dont deux très tôt dans l'hiver (hiver 2003-2004 et 206-2007). Ces épisodes sont souvent précédés d'une forte augmentation des T_B due à la présence d'eau liquide dans la neige. Pour les simulations des T_B en présence de CGs, il y a généralement une légère sous-estimation des T_B à 10.7 GHz en polarisation H, malgré l'optimisation de la densité de la CGs (pour les cinq CGs, les densités optimisées sont respectivement de 750, 650, 650, 750 et 650 kg m^{-3}). Cette sous-estimation pourrait être expliquée par l'effet de cohérence. En effet, pour des CGs relativement minces (autour de 2 mm), l'effet de cohérence fait en sorte que la chute des T_B à 19 GHz en polarisation H est plus importante qu'à 10.7 GHz (voir figure 2.3). Le modèle DMRT-ML surestime ainsi l'effet de la CG à 10.7 GHz. Mais en général, même si l'optimisation de la densité de la CG est physiquement incorrecte, une telle approche permet de représenter relativement bien l'effet effectif des CGs (Voir Annexe 2). Les basses RMSE à 19 GHz démontrent aussi que l'optimisation de l'humidité du sol à 10.7 GHz permet de trouver un sol effectif à 19 GHz. Les T_B en été montrent une RMSE légèrement plus élevée que la moyenne de l'ensemble des sites (tableau 7.4). Ces erreurs pourraient être reliées aux paramètres de sol QH qui sont considérés constants pour l'ensemble de la forêt boréale. Les RMSE restent tout de même sous les 5 K.

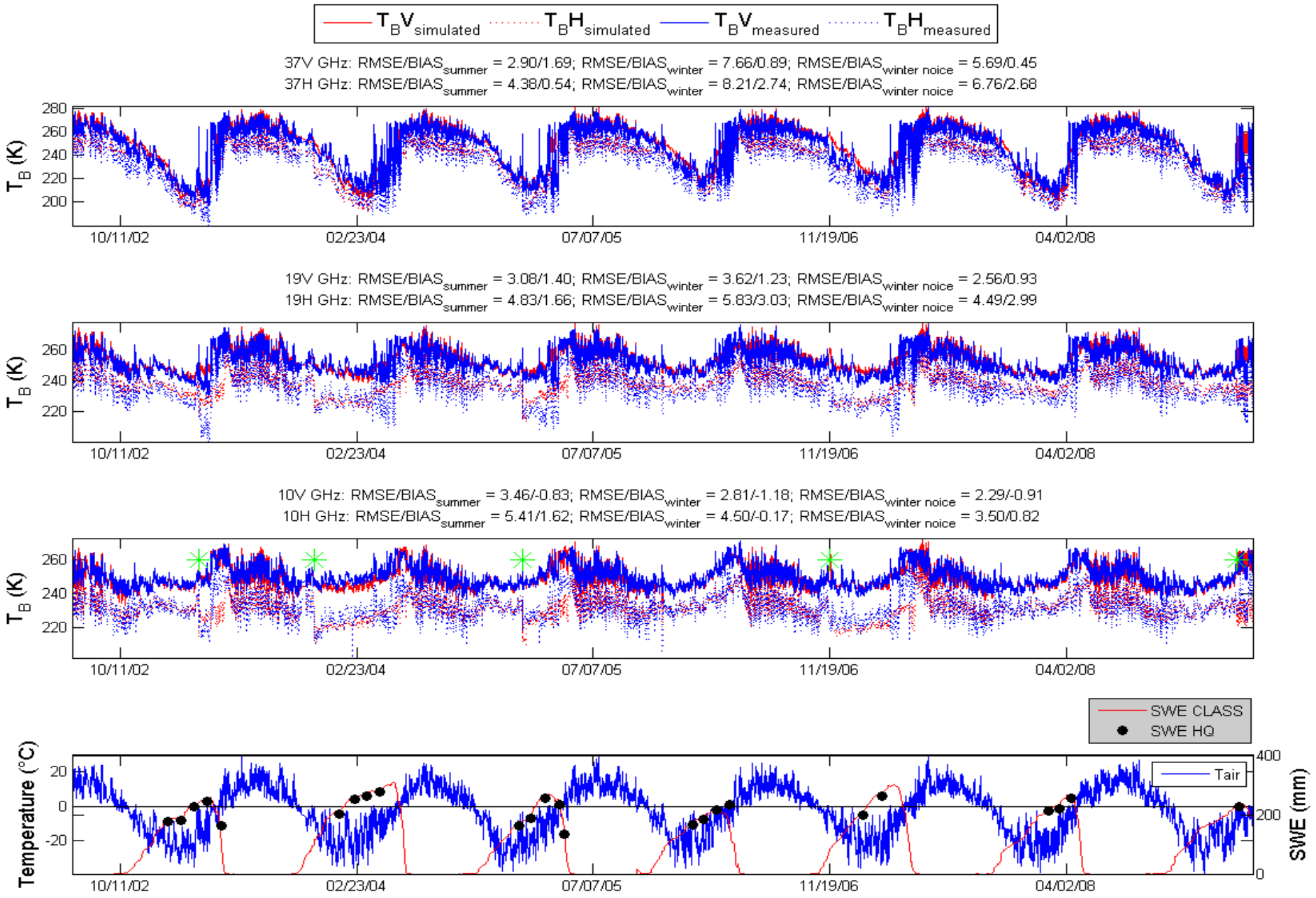

Figure 7.7: Comparaison des simulations issues du couplage MTR/CLASS avec les données AMSR-E sur le site 1 (LAI_{winter} = 0.064). Les étoiles vertes dans le 3^{e} graphique indiquent l'apparition d'une croûte de glace détectée automatiquement à partir du ratio de polarisation à 10.7 GHz (voir texte).

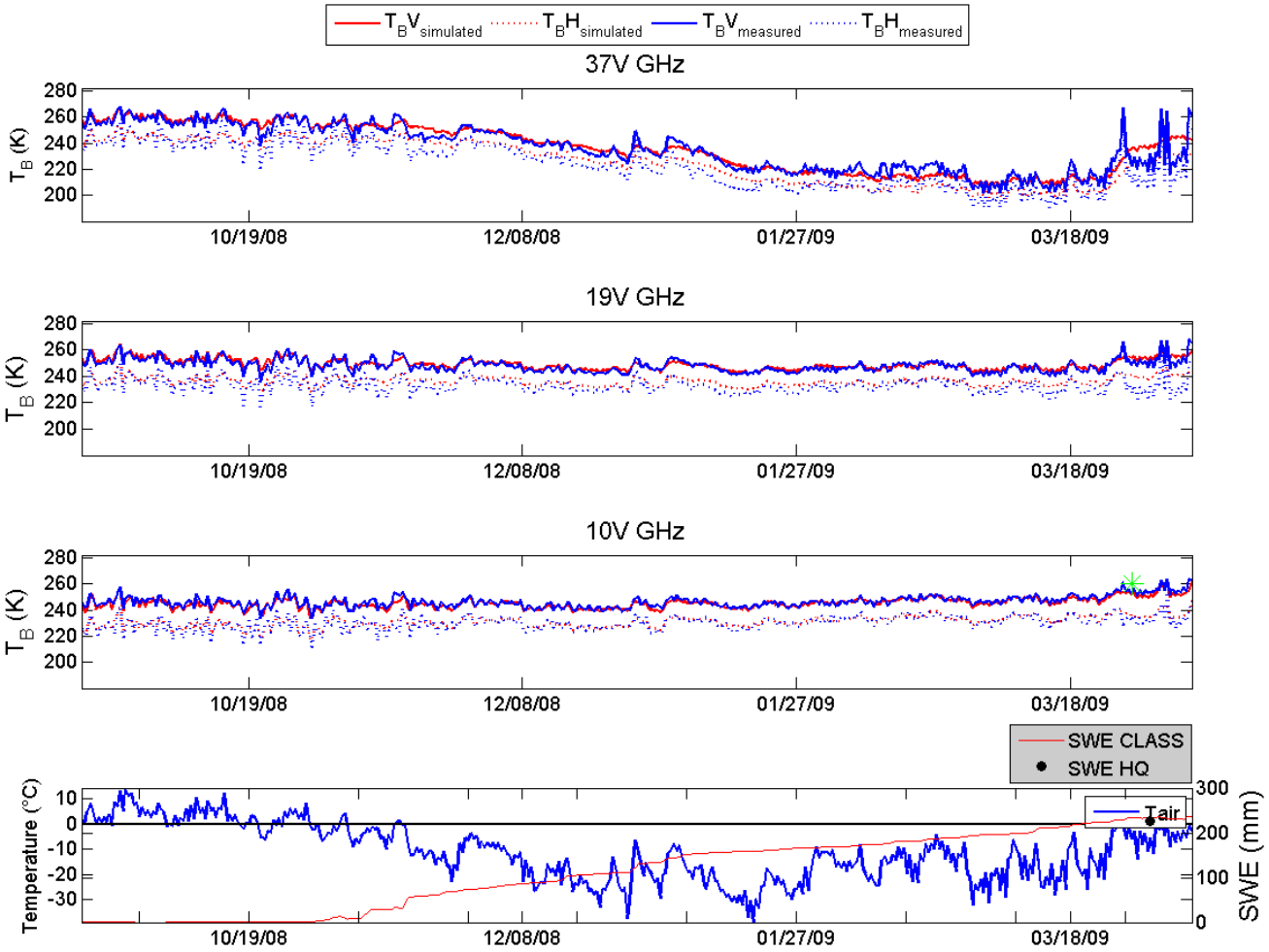

Figure 7.8: Similaire à la figure 7.7 (site 1) mais pour l'année 2008-2009 seulement.

La figure 7.8 montre l'année 2008-2009 en détail. Les tendances sont bien simulées aux trois fréquences. Par contre, il y a certains biais surtout à 37 GHz qui semblent être reliés à la variation des températures de l'air. A priori, étant donné que la végétation devrait suivre davantage les variations de température, ces erreurs pourraient être reliées à une sous-estimation de la transmissivité. Or, une augmentation de la transmissivité induit systématiquement un biais positif parce que la végétation émet plus qu'un sol enneigé avec un $\omega_{winter} = 0.13$ à 37 GHz (« plus chaude en terme de T_B »). Il semble donc que les paramètres de végétation γ-ω pourraient peut-être varier avec la température de l'air à cause de l'influence de la température sur la constante diélectrique des arbres. L'erreur étant principalement à 37 GHz, il serait aussi possible que l'erreur soit reliée à l'inertie de la température de la neige à cause du modèle de neige à une couche.

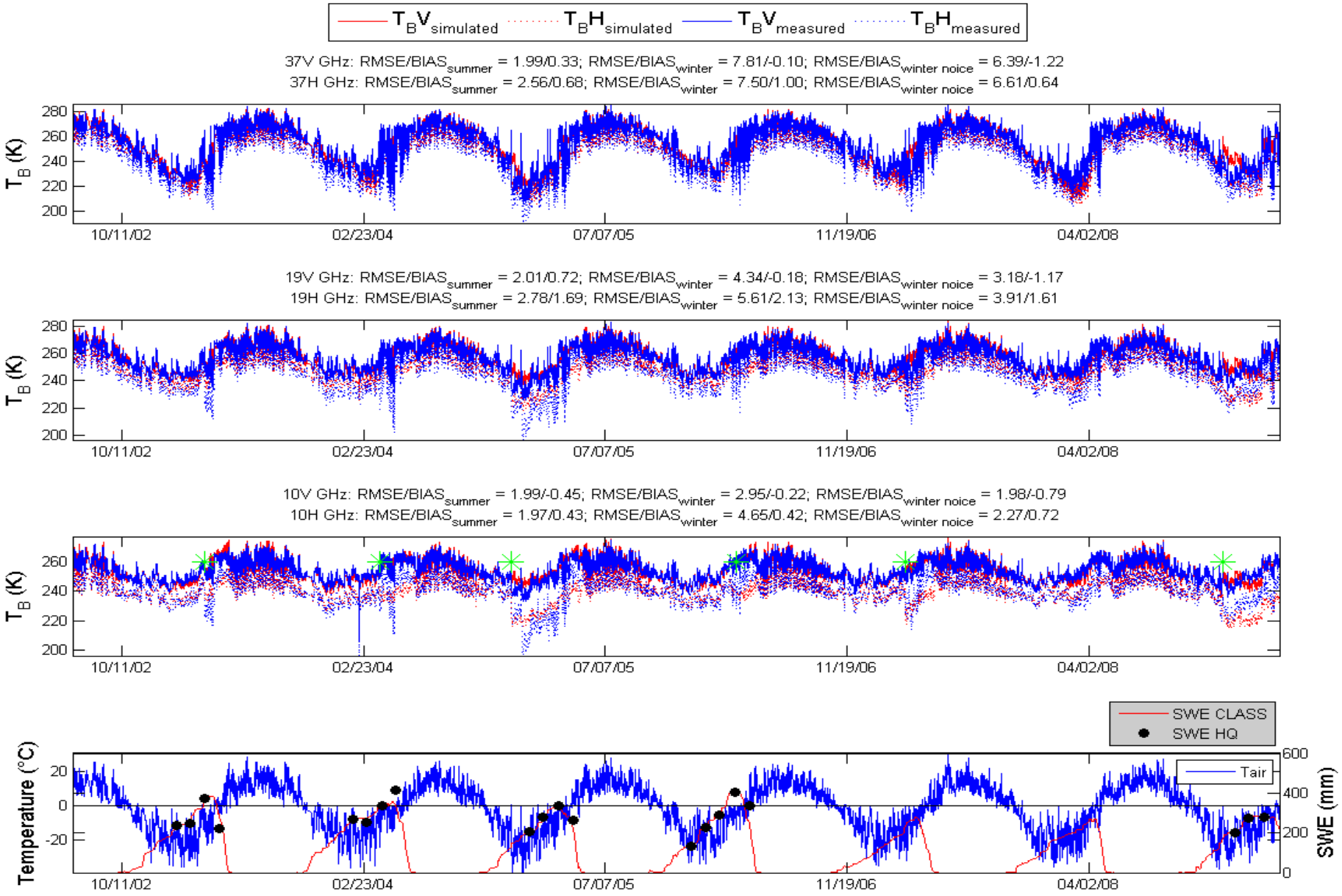

Figure 7.9: Comme à la figure 7.7, mais sur le site 2 (LAI_{winter} = 0.148).

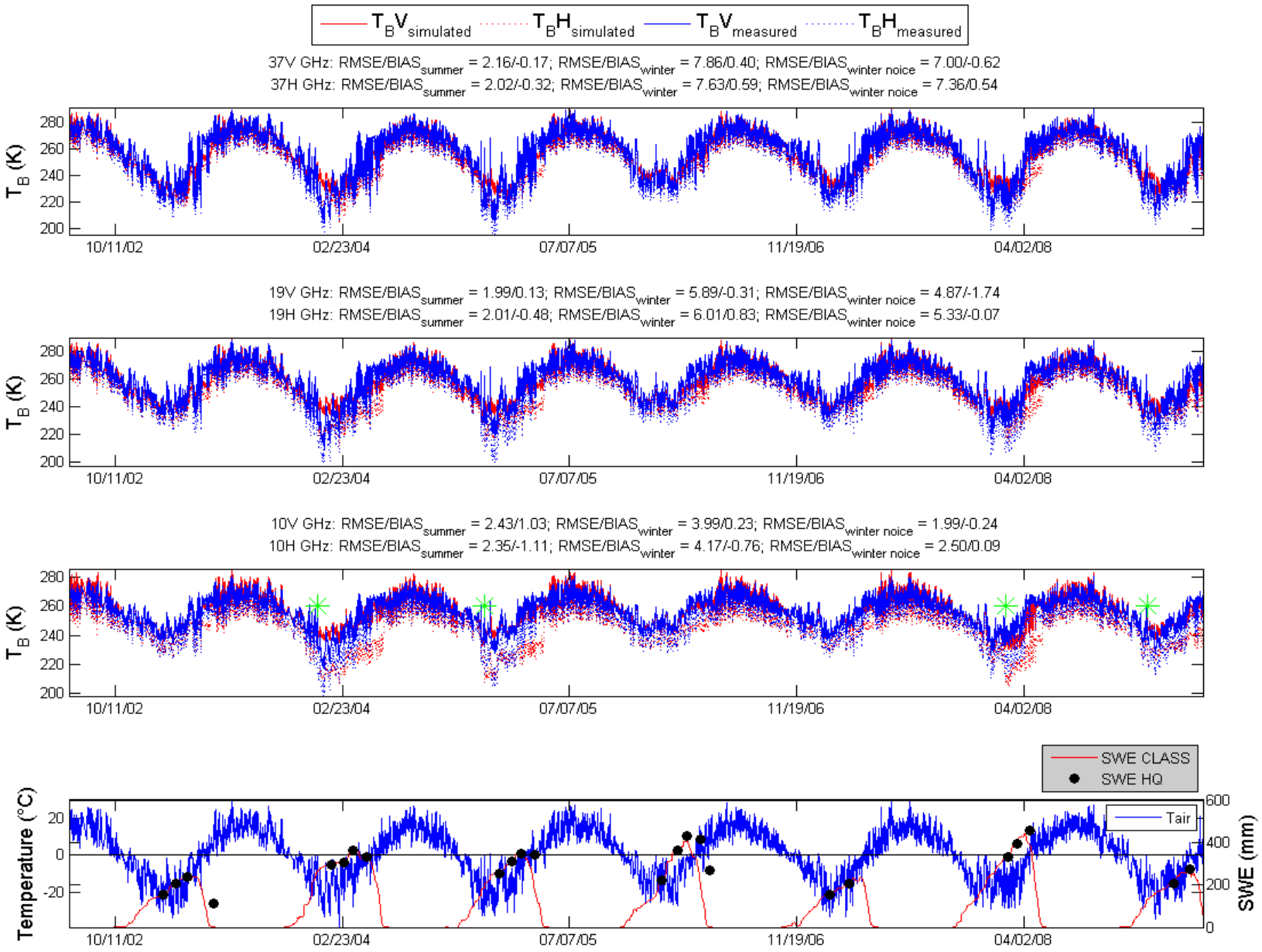

Figure 7.10: Comme à la figure 7.7, mais sur le site 3 (LAI_{winter} = 0.298).

Le LAI_{winter} du deuxième site est de 0.148 (figure 7.9). Les tendances des T_B sont bien captées comme au site 1. On voit aussi que les différences de polarisation sont moins grandes surtout à 10.7 et 19 GHz principalement à cause de la présence plus importante de la végétation. Il y a apparition de CGs en début d'hiver pour les hivers 2004-2005 et 2008-2009. L'année 2004-2005 montre aussi une deuxième chute importante des T_B en H après l'apparition de la CG. Cette deuxième chute est probablement reliée à l'apparition d'une deuxième CG que l'algorithme ne permet pas de détecter (l'algorithme identifie la présence d'une CG, donc il ne permet pas d'identifier l'apparition d'une deuxième CG). Pour les autres hivers, les apparitions des CGs sont davantage à la fin des hivers.

Le troisième site (figure 7.10) possède un LAI_{winter} élevé à 0.298. Pour les années sans CGs, les tendances sont aussi généralement bien simulées. Les hivers 2003-2004 et 2004-2005 où des CGs sont détectées et simulées, il y a une importante surestimation des T_B surtout en polarisation verticale (V). La figure 7.11 montre l'année 2004-2005 en détail. Trois événements de fonte peuvent être distingués où les trois fréquences montrent des pics aux deux polarisations. L'algorithme de CG détecte ainsi une CG au deuxième événement de fonte. L'ajout d'une croûte de glace permet de relativement bien simuler les T_B à 10.7 GHz surtout en polarisation H, tandis que les T_B sont surestimées à 19 et 37 GHz. Ces surestimations concordent généralement avec des températures de l'air très froides. Il semble donc une fois de plus que le MTR/CLASS ne soit pas suffisamment sensible aux températures de l'air. Étant donné que la surestimation est présente au trois fréquences, le phénomène est probablement davantage attribuable à l'effet de la végégation. Il y a néanmoins une diminution des T_B entre chaque événement de fonte, surtout en polarisation H. Il y a donc peut-être aussi formation de croûtes de fonte qui est davantage un mélange de glace et d'air et agit différemment sur le T_B. Certaines mesures effectuées à SIRENE permettent d'affirmer qu'une CG créée par un événement de pluie sur le couvert nival et une croûte de fonte agissent différemment sur les T_B (Langlois et al., en cours). Ces interactions sont par contre complexes et davantage d'analyses de ce type d'événements devront être faites.

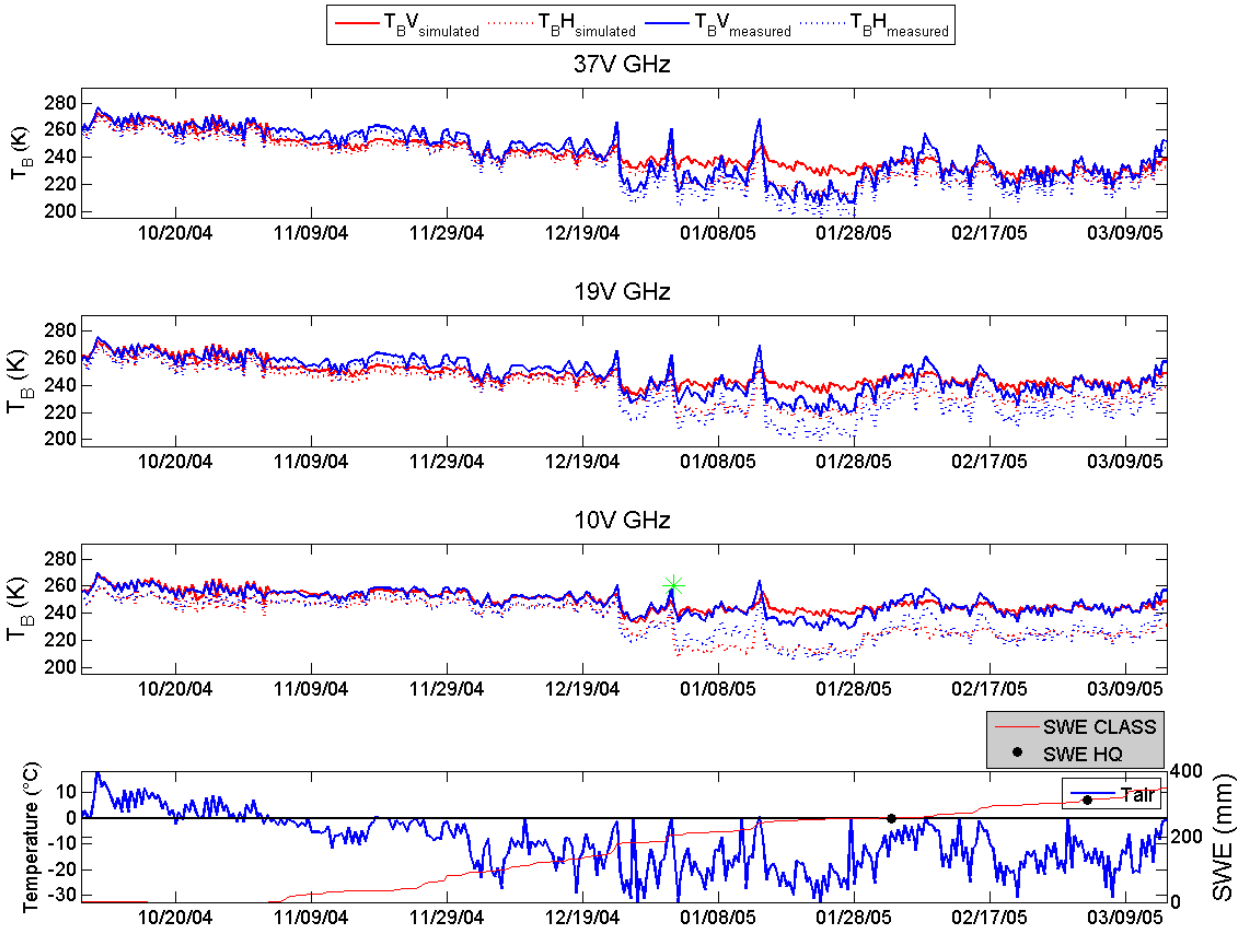

Figure 7.11: Similaire à la figure 7.10 (site 3) mais pour l'année 2004-2005 seulement.

7.4 Discussion

7.4.1 Analyse de sensibilité pour l'estimation du SWE

À partir de MTR/CLASS, des tests de sensibilité sont faits afin d'évaluer la sensibilité des MOP au SWE en forêt boréale. Les données nivométriques mesurées sur les 22 sites sont considérées pour représenter des caractéristiques de neiges typiques.

L'évaluation de la sensibilité des T_B au SWE est réalisée par rapport à la hauteur de neige. Comme mentionné au Chap. 2, la densité et les grains de neige définissent le caractère diffusif du couvert nival, tandis que la hauteur de neige influence directement l'atténuation. La figure 7.12 montre des tests de sensibilité des T_B perçues par un capteur satellitaire pour différentes densités de couvert forestier (LAI_{winter}), pour deux tailles de grains de neige (R_{opt}) différentes (valeurs moyennes des simualtions CLASS-SSA de l'ensemble des sites et les 7 années): R_{opt} = 0.157 mm au 1er janvier et R_{opt} = 0.257 mm lorsque CLASS donne la valeur de SWE maximal dans l'hiver.

La valeur moyenne des densités de neige mesurées par les mesures nivométriques est utilisée (251 kg m^{-3}). À 37 GHz, les simulations montrent que la sensibilité à la hauteur de neige est grandement influencée par la taille des grains de neige. Ainsi, avec de plus gros grains rencontrés à la fin de l'hiver (SWE maximal), le caractère diffusif de la neige est beaucoup plus important et une augmentation de la hauteur de neige influence donc davantage le signal. La sensibilité au SWE augmente ainsi avec le métamorphisme des grains de neige au cours d'un hiver. Il y a par contre une saturation de la sensibilité pour des hauteurs de neige > 1m. La sensibilité aux hauteurs de neige à 19 et 10.7 GHz est faible, même avec une taille de grains plus importante.

L'impact de la densité du couvert forestier sur la sensibilité à la hauteur de neige est aussi important. Les variations du T_B d'un couvert nival de 0.1 m à 1.6 m (valeurs maximales de hauteur de neige mesurées) sont de 49 K en V et 46 K en H lorsque la végétation est nulle et de 13 K en V et en H lorsque le LAI_{winter} est de 0.3 (valeur de LAI_{winter} la plus haute sur les 22 sites). Cette variation est aussi relativement faible pour un LAI_{winter} = 0.15. Cette forte perte de sensibilité au couvert forestier est évidemment reliée à la transmissivité plus faible, mais aussi à l'augmentation du signal descendant réfléchi par le couvert nival ($T_{B\downarrow\text{-}r} = T_{Bveg\text{-}r} + T_{Batm\text{-}r}$). Avec l'augmentation de la hauteur de neige, l'émissivité du couvert nival diminue, donc sa réflectivité augmente. Ainsi avec l'augmentation de la réflectivité, une partie grandissante du signal provenant de la surface sous la canopée provient du signal de l'émission de la végétation (et de l'atmosphère en moindre proportion) qui est réfléchi par la surface couverte de neige ($T_{Bveg\text{-}r} + T_{Batm\text{-}r}$) (figure 7.13). La sensibilité des T_B sous la canopée ($T_{Bsnow} + T_{Bveg\text{-}r}$) à la hauteur de neige devient donc moins importante avec l'augmentation de la végétation à cause de l'augmentation de la réflectivité de la neige.

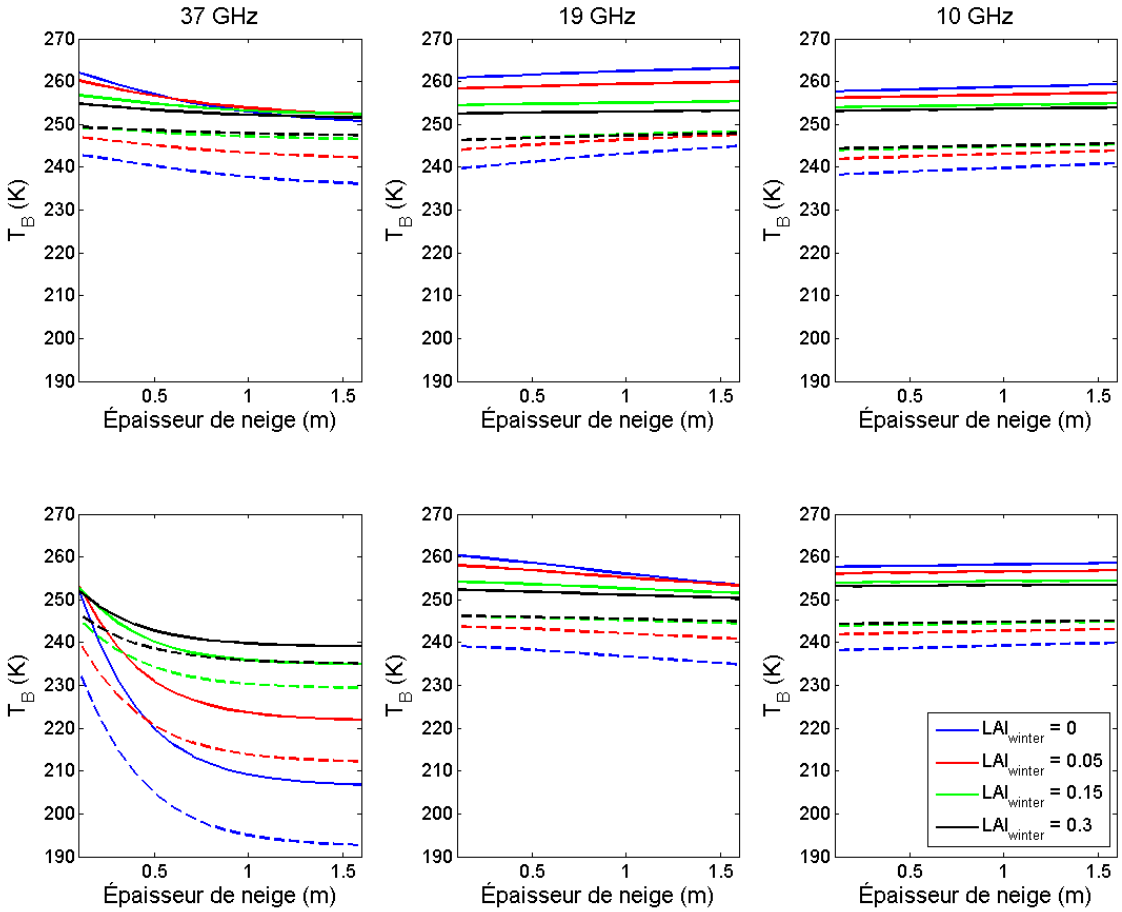

Figure 7.12: Tests de sensibilité des T_B perçues par un capteur satellitaire en fonction de la hauteur de la neige pour différents couverts végétaux à 37 (gauche), 19 (centre) et 10.7 GHz (droite) pour deux tailles de grains (en haut = 0.157 mm; en bas = 0.257 mm). Ligne pleine = V; ligne pointillée = H.

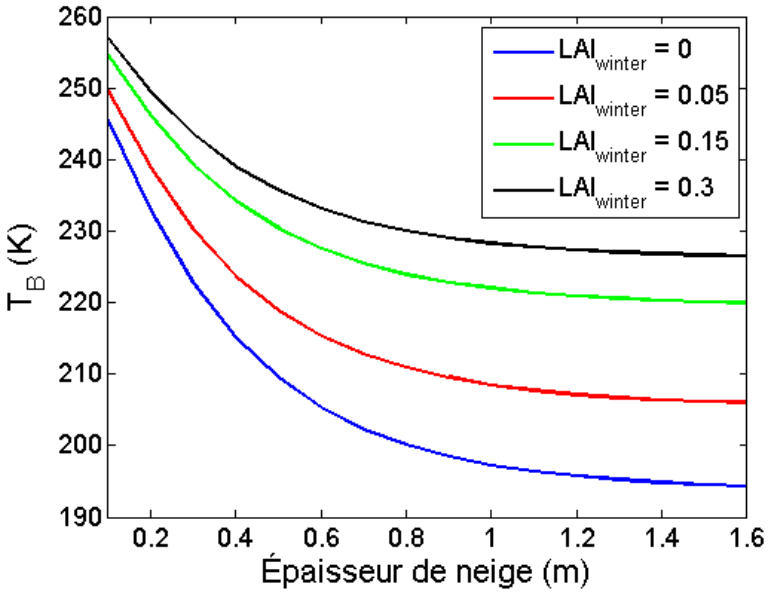

Figure 7.13: Tests de sensibilité des T_B sous la canopée ($T_{Bsnow} + T_{Bveg\text{-}r}$) en fonction de la hauteur de la neige pour différents couverts végétaux à 37 GHz en polarisation V.

Pour vérifier le potentiel des MOP pour corriger les simulations de SWE de CLASS, l'effet de l'erreur type des simulations de hauteurs de neige sur la variation des T_B à 37 GHz est évalué. Ainsi, considérant l'erreur type des simulations de hauteur de neige comparée aux mesures de 0.28 m, l'impact d'une variation de ± 0.14 m de la hauteur de neige sur les T_B perçues par un capteur satellitaire est calculé. À noter que 0.28 m représente un SWE de 70.3 mm pour une neige avec une densité de 251 kg m^{-3}. La figure 7.14 montre que l'erreur type des simulations CLASS donne des variations sous les 7 K avec des LAI_{winter} de 0.15 et plus. Pour des hauteurs de neige moyennes mesurées (0.9 m) ces variations se trouvent généralement sous 5 K. Ces variations sont plus faibles que la précision du modèle MTR/CLASS définie au tableau 7.2.

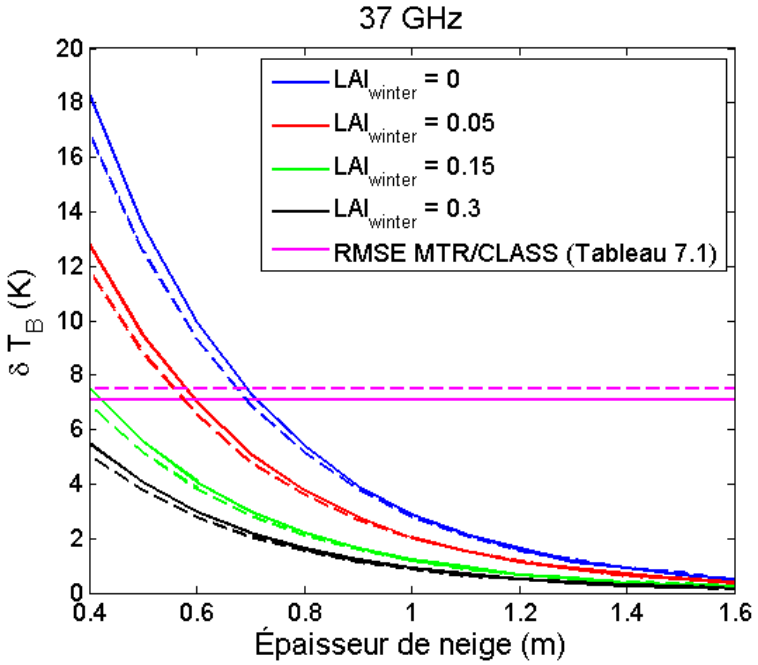

Figure 7.14: Variation des T_B perçues par un capteur satellitaire (δT_B) pour une variation de ± 0.14 m (70.3 mm de SWE) de la hauteur de neige pour différents couverts végétaux à 37 GHz. Ligne pleine = V; ligne pointillée = H.

Même si l'aspect des CGs n'a pas été traité à fond dans ce travail, il est possible d'évaluer l'impact que peuvent avoir les CGs sur la sensibilité des micro-ondes au SWE. La figure 7.15 montre que lorsque la CG est sur le dessus du couvert nival, la sensibilité au SWE reste présente à 37 GHz. Lorsqu'une CG est poisitionnée à une certaine hauteur (20 cm dans ce cas-ci) dans le couvert nival, et que la neige s'accumule ensuite dessus, un saut important des T_B en polarisation H apparait dès qu'une couche de neige se dépose sur la CG. Cette augmentation des T_B est due au

changement de contraste diélectrique à l'interface de la CG. Le plus faible contraste diélectrique entre la CG et la neige par rapport à l'air fait en sorte de diminuer l'atténuation des T_B par la CG (Montpetit et al., 2013). La sensibilité à la hauteur de neige reste néanmoins présente à 37 GHz en polarisation verticale.

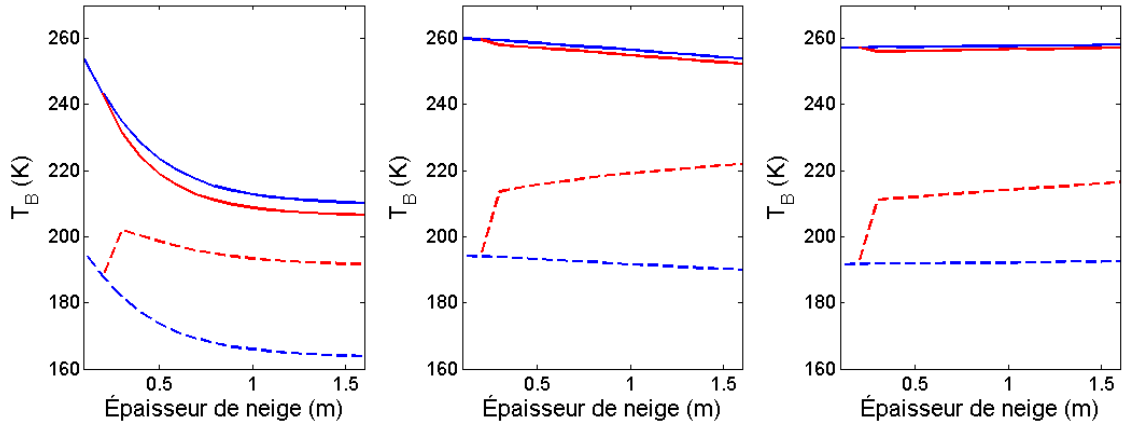

Figure 7.15: Tests de sensibilité des T_B en fonction de la hauteur de la neige avec la présence de CGs (917 kg m^{-3}) à 37 (gauche), 19 (centre) et 10.7 GHz (droite). Bleu: CG en surface; rouge: CG à 20 cm. Ligne pleine = V; ligne pointillée = H.

En conclusion, il semble que la sensibilité des MOP au SWE en présence de végétation dense soit relativement faible. À noter que Vander Jagt et al. (2013) a aussi constaté cette perte de sensibilité pour des couverts de végétation denses. Les sensibilités sont généralement plus basses que les précisions actuelles du MTR/CLASS. Le modèle analysé ne semblerait donc pas permettre d'inverser directement le SWE en présence de végétation dense et pour des couverts nivaux épais. Par contre, pour des pixels où la végétation est plus faible, une certaine sensibilité est présente.

7.4.2 Analyse des paramètres de végétation

L'optimisation du ω_{winter} (0.13) démontre une différence importante avec le ω_{summer} (0.05). Comme mentionnée auparavant, cette différence est probablement expliquée par le fait que la constante diélectrique de la végétation diminue à de faibles températures. Or, cette valeur de ω_{winter} = 0.13 est plus élevée que les ω_{winter} trouvés au Chap. 5 où ω_{winter} = 0.063 a été trouvé à partir de données aéroportées et ω_{winter} = 0.083 pour les données in situ (St-Romain). Ce point soulève encore la difficulté de comparer des données à différentes échelles. Il semble donc que le ω_{winter} = 0.063 soit relativement bas par rapport aux autres. Cette faible valeur provient peut-être des sources d'erreurs possibles dans la méthode d'inversion soulevée dans Langlois et al. (2011).

Le fait d'avoir utilisé des données d'occupation du sol (Land Cover of Canada 2005) de MODIS peut faire en sorte que les pixels considérés comme en milieu ouvert, où les T_{Bsnow} ont été pris, n'en soient pas vraiment considérant que la précision du produit est bonne, mais pas suffisante (précision > 75 %) (Langlois et al., 2011). Ces possibles erreurs donnant une T_{Bsnow} plus élevée que la réalité peuvent expliquer cette basse valeur de $\omega_{winter} = 0.063$. Une autre source d'erreur reliée à cette approche est la considération des paramètres de surface en milieu ouvert équivalent à ceux en milieu fermé. Or, il existe généralement des variations entre les neiges en milieu ouvert et les neiges en milieu forestier (Hedstrom et Pomeroy, 1998). Il reste néanmoins que les hauteurs de neiges mesurées à Sept-Îles lors de la campagne étaient très importantes (+ 1.5 m), ce qui permet de considérer que l'effet de saturation sur la T_B à 37 GHz (Rosenfeld & Grody, 2000) fait en sorte que les T_B en milieu ouvert devraient être semblables à celles retouvées en milieu forestier. La valeur $\omega_{winter} = 0.13$ est aussi plus élevée que celle mesurée sur les sites in situ ($\omega_{winter} = 0.083$). Cette différence pourrait être due aux différences d'échelles des mesures, mais aussi au fait que les paramètres de végétation γ-ω pourraient varier au cours d'un hiver. Finalement, du point de vue satellitaire, les valeurs de LAI (hiver et été) utilisées au Chap. 6 pour spatialiser les transmissivités comportent aussi certaines incertitudes. Yang et al. (2006a) estime que le LAI issu de MODIS surestime le LAI d'environ 12 % par rapport à des données terrains. De plus, la précision des produits LAI MODIS est influencée par le couvert nival (Yang et al., 2006b). Ces imprécisions peuvent apporter des erreurs dans les valeurs de transmissivités utilisées. Par contre, le fait d'utiliser des valeurs moyennes de LAI sur une certaine période de temps permet d'obtenir des paramètres structuraux de la forêt représentatifs pour retrouver des transmissivités en forêt boréale.

Néanmoins, les résultats de cette analyse sur ces 22 sites avec des densités de végétation variables montrent que les simulations des T_B sont optimisées avec $\omega_{winter} = 0.13$. En fait, ce $\omega_{winter} = 0.13$ est peut-être un paramètre optimal pour l'ensemble des hivers, mais il serait aussi possible que le ω ainsi que les γ varient avec la température à cause du changement de la constante diélectrique de la végétation (Mätzler, 1994; Way et al., 1990; El-Rayes & Ulaby, 1987), ce qui expliquerait le manque de sensibilité à la température de l'air du modèle MTR/CLASS (la température de la végétation suit généralement la température de l'air). Il reste par contre difficile de vérifier cette hypothèse à partir de la base de données AMSR-E. Magagi et al. (2002) ont démontré à partir de simulations qu'il existait une diminution du coefficient de

rétrodiffusion radar (bande C) pour des forêts en hiver due au changement de constante diélectrique de la forêt. D'un autre côté, Rahmoune et al. (2013) ont constaté peu de changement de la transmissivité de la végétation en bande L entre des données SMOS de juillet et des données de novembre. Ainsi, à notre connaissance, aucune étude n'a vérifié l'effet du changement de la constante diélectrique sur la transmissivité et l'émission de la végétation dans les micro-ondes-passives. Une série temporelle de mesures in situ, comme présentées à la figure 5.3, couvrant les différentes saisons permettrait ainsi de mieux comprendre les variations de la contribution de la végétation au cours du temps. Des mesures de l'effet de la variation de la température sur la constante diélectrique des conifères en hiver pourraient aussi apporter une information importante. Des mesures intensives pourraient aussi permettre d'alimenter des modèles de transfert radiatif de la végétation plus complexe (Ferrazzoli et al., 2002) pour vérifier la sensibilité de paramètres effectifs (γ-ω) aux différentes configurations de la végétation. Néanmoins, pour l'instant, un $\omega_{winter} = 0.13$ est la valeur optimale trouvée pour la forêt boréale en terme des RMSE moyennes entre les T_B simulées et mesurées, avec des résultats près de 7 K à 37 GHz.

Il faut aussi noter que la valeur de $\omega_{winter} = 0.063$ obtenue à partir de données aéroportées au Chap. 5 est néanmoins très près de la valeur de $\omega_{summer} = 0.05$ trouvé au Chap. 6. Au Chap. 5, les paramètres de végétation sont considérés comme constants en été comme en hiver pour inverser les paramètres de sol à l'échelle du pixel AMSR-E. Cette hypothèse avait été utilisée, mais tout en soulignant les possibles erreurs reliées à une telle hypothèse. Il résulte de cette similitude des valeurs $\omega_{winter} = 0.063$ et $\omega_{summer} = 0.05$, que les paramètres inversés de γ au niveau du pixel AMSR-E en été sont relativement semblables en comparaison aux valeurs obtenues au Chap. 6 pour des forêts boréales denses.

Comme mentionné à la Sect. 5.2, le modèle γ-ω d'ordre 0 est physiquement moins correcte que les modèles de diffusion simple (*single-scattering*) ou un modèle de diffusion multiple (Mätzler et al., 2006). Néanmoins, il faut considérer γ et ω comme des paramètres effectifs qui prennent en compte l'ensemble des processus dans la canopée, incluant la diffusion multiple. Comme mentionné dans Rahmoune et al. (2013), l'éq. 2.7 qui représente la contribution de la végétation, montre que le ω est directement relié à l'émission de la végétation en tant que tel, tandis que le γ partitionne la contribution provenant de la végétation et du sol. Dans ce sens, plusieurs études ont

démontré à partir de modèles physiques complexes que le modèle γ-ω permet de bien simuler les T_B en forêt (Ferrazzoli et al.,2002; Kurum et al., 2012; Zhang et al., 2012). Kurum et al. (2012) ont démontré à partir d'un modèle de 1er ordre, qu'en bande L, un ω effectif ne correspond pas à l'albédo de diffusion simple (*single-scattering albedo*). Ainsi, dans notre cas, il ne faut pas considérer le ω comme un albédo de diffusion simple, mais bien comme un paramètre de diffusion effectif qui permet de représenter l'émissivité de la forêt. Pour leur part, Zhang et al. (2012) ont montré à partir de la technique de « *ray tracing* » et de données radiométriques in situ, que le modèle γ-ω permet de représenter l'atténuation et la diffusion effective de la végétation à 18.7 et 36.5 GHz. Jones et al. (2010) utilise aussi avec succès le modèle γ-ω pour vérifier les cycles saisonniers de l'épaisseur optique de la végétation à 19 GHz.

7.4.3 Analyse des simulations des T_B sol-neige (DMRT-ML)

La figure 7.4 montre que pour un site avec très peu de végétation, les RMSE sont légèrement au-dessus de 10 K. Cette valeur représente une bonne approximation de l'erreur reliée à la modélisation de l'émission d'une surface enneigée sans croûte de glace simulée par DRMT-ML. Cette erreur est légèrement plus faible que celles obtenues sur les sites in situ (13. 8 K) (Chap. 3). Il faut noter que les données in situ sont influencées par la micro-variabilité des conditions de sol et de neige qui peuvent atteindre 4 à 5 K (données non publiées : mesures effectuées à la Baie James à l'hiver 2013). Il reste que les simulations des T_B de neiges saisonnières à 37 GHz descendent rarement sous les 10 K (Kontu et Pulliainen; Montpetit et al., 2013; Derksen et al., 2012; Lemmetyinen et al., 2010; Durand et al., 2008). Comme mentionné au Chap. 3, dans le cas de DMRT-ML, une partie de l'erreur pourrait être reliée à l'agrégation entre les grains de neige et la distribution des grains de neige qui ne sont pas pris en compte dans les simulations. Des nouvelles mesures terrain comme avec le SnowMicroPen (Schneebeli et al., 1999), qui mesure la force de résistance de pénétration dans la neige, permettrait de mieux comprendre les forces d'adhésions des différents types de neige et l'effet sur la « stickiness » dans DMRT-ML. Des mesures de distribution de la taille des grains de neige à partir de la numérisation de photos de grains pourraient aussi permettre de mieux comprendre l'effet de la distribution de la taille des grains sur les simulations dans DMRT-ML.

Par ailleurs, étant donné que CLASS est un modèle à une couche, il semblait naturel d'utiliser DMRT-ML avec une couche. Certains résultats dans le Chap. 3 (tableau 3.5) indiquent qu'un

modèle à une couche permet d'obtenir des RMSE semblables à une approche multicouche. De plus, GlobSnow, un produit opérationnel utilisant le modèle HUT, semble obtenir des résultats satisfaisants avec le MSEM à une couche (Takala et al., 2011). Aussi, d'un point de vue opérationnel, l'utilisation d'un MSEM à une couche simplifie grandement les approches d'inversion et d'assimilation, ainsi que les temps de calcul. Par contre, CLASS-SSA qui est un modèle *offline* multicouche donne la possibilité d'approcher le problème avec DMRT-ML multicouche. Une approche multicouche pourrait permettre de voir une certaine sensibilité du signal à 19 GHz où la taille des grains de neige importante du givre de profondeur qui est diminuée dans un modèle à une couche (à cause de la moyenne), se rapproche de la longueur d'onde à 19 GHz et donc permet d'atténuer une partie du signal (voir la figure 2.1, où les T_B à 19 GHz deviennent sensibles à la taille des grains de neige à partir d'un rayon > 0.6 mm). Aussi, au Chap. 3, les simulations à 19 GHz étaient effectivement plus sensibles à la neige à cause de la présence de givre dans le couvert nival. Il serait donc intéressant de vérifier si malgré les approximations reliées au calcul de la densité multicouche de CLASS-SSA, l'approche permettrait d'améliorer les simulations et augmenter la sensibilité. Durand et Liu (2012) ont montré qu'un modèle multicouche permet de mieux inverser les SWE à partir d'une approche utilisant la méthode des chaines de Markov, comparativement à un modèle à une couche. Par contre, Kontu & Pulliainen (2010) ont démontré qu'en utilisant une correction exponentielle sur la taille des grains, il est possible de compenser jusqu'à un certain point la stratification des couches de neige. De plus, les simulations à 19 GHz montrent des RMSE sous les 5 K ce qui semble démontrer que l'approche une couche est relativement adéquate et que la sensibilité du 19 GHz à la neige est faible. L'approche multicouche pourrait aussi résoudre une partie du manque de sensibilité aux températures de l'air à 37 GHz. Pour des couverts nivaux épais, les températures des couches supérieures, influençant davantage le 37 GHz à cause de sa longueur de pénétration plus faible, suivent davantage les fluctuations des températures de l'air.

L'ajout de la cohérence dans le modèle DMRT-ML permettrait aussi de mieux simuler les croûtes de glace (Montpetit et al., 2013). Même si l'ajustement de la densité de la croûte de glace permet de corriger une partie de l'erreur, l'implémentation de la cohérence permettrait de garder une paramétrisation physique dans le modèle. Il serait ainsi possible d'optimiser l'épaisseur des CGs pour améliorer les simulations des T_B. Il reste par contre que la différenciation de la CG qui

apparait normalement lors d'événements de pluie sur neige par rapport à une croûte de fonte reste à être évaluée plus en profondeur sachant que leurs effets sur le signal sont différents.

Dans le cadre de cette étude, les difficultés reliées à l'estimation de la constante diélectrique du sol et de la réflectivité du sol ont été contournées en optimisant l'humidité du sol à 10.7 GHz afin de retrouver des paramètres de sol effectifs. Les résultats obtenus à 19 GHz semblent démontrer que l'utilisation du 10.7 GHz pour optimiser les paramètres de sol est adéquate. L'humidité du sol reste tout de même un paramètre difficile à estimer à partir des données AMSR-E surtout en présence de végétation (Jugla et al., 2010). Les produit opérationnels d'humidité du sol d'AMSR-E montrent généralement des biais et de faibles amplitudes (Rüdiger et al., 2009). Il reste que MTR/CLASS pourrait être un bon outil pour identifier le gel/dégel du sol et inverser les températures du sol, sachant la faible sensibilité du 10.7 GHz à la neige (Kohn et al., 2010). Dans un tel contexte, une meilleure connaissance des effets du gel du sol sur la constante diélectrique et la réflectivité du sol en forêt boréale est nécessaire. Un modèle de transfert radiatif multicouche de sol serait peut-être même nécessaire (Rautiainen et al., 2012) pour considérer l'évolution de la profondeur du gel dans le sol.

7.4.4 MTR/CLASS pour l'estimation du SWE

L'analyse de sensibilité des MOP au SWE a démontré que l'erreur du MTR/CLASS à 37 GHz est généralement supérieure à la variation des T_B issues des erreurs moyennes de CLASS (70.3 mm de SWE). Ce résultat montre une certaine limite du MTR/CLASS pour des inversions de SWE ponctuelles dans l'espace et le temps comme effectuées par Langlois et al. (2012). Par contre, le couplage développé dans ce travail peut permettre l'utilisation de méthodes d'assimilation plus complexes comme le filtre de Kalman d'Ensemble (Touré et al., 2010; Durand et al., 2009) et les 4-D var (Jia et al., 2013) qui permettraient d'ajuster les variables clés du modèle de neige (SWE, taille de grains) dans l'espace et dans le temps en considérant les erreurs sur les simulations, mais aussi sur les observations. Dans cet ordre d'idée, la connaissance des erreurs sur la SSA issues des simulations CLASS-SSA est intéressante et nécessaire. De telles approches d'assimilation doivent permettre d'exploiter l'information temporelle que les données satellitaires MOP permettent d'obtenir. L'assimilation des T_B dans le temps permettrait de contraindre les variables clés simulées (SWE et taille de grains) tout au cours de l'hiver. La présente étude démontre aussi que les incertitudes reliées à la modélisation des T_B par le MTR varient en fonction des

caractéristiques du milieu. Un schéma d'assimilation pourrait permettre de prendre en compte l'augmentation de l'incertitude reliée à la présence de CG dans le couvert nival. L'erreur considérée en polarisation H serait donc plus grande et son poids dans l'optimisation en serait diminué. En milieu forestier dense, un filtre de Kalman d'Ensemble (voir Sect. 2.4) permettrait de constater la faible sensibilité du SWE au T_B et considérerait peu ou pas les T_B pour corriger le SWE du modèle. Les prochaines études devront aussi vérifier différentes combinaisons spectrales ou de polarisations pour trouver davantage de sensibilité au SWE en milieu ouvert. Outre les combinaisons spectrales classiques 19-37 GHz (Derksen et al., 2010; Langlois et al., 2012; Dupont et al., 2013) d'autres combinaisons comme 10-19 GHz permettraient d'obtenir une certaine sensibilité pour des neiges plus épaisses (Derksen et al., 2008). Pour des applications en hydrologie, des approches davantage axées sur des T_B mesurées à l'échelle d'un bassin versant pourraient aussi augmenter la sensibilité à la neige (Vander Jagt et al., 2013; Li et al., 2012).

7.5 Conclusion

L'objectif de cette section était d'abord de corriger certains biais dans les simulations du MTR/CLASS reliés à trois principaux facteurs: les croûtes de glace, les paramètres de végétation d'hiver qui diffèrent de ceux d'été et la correction sur la taille de grains (ϕ) issue des simulations CLASS-SSA. L'étude montre l'impact majeur des croûtes de glace sur le signal MOP à l'échelle du pixel AMSR-E en forêt boréale. Ces croûtes de glace ont été modélisées dans DMRT-ML, mais l'implémentation de l'effet de cohérence dans le modèle permettrait une meilleure paramétrisation physique dans le modèle. L'étude semble aussi démontrer qu'il existe une différence entre les paramètres de végétation d'été et ceux d'hiver. L'émissivité de la végétation, reliée directement au ω_{winter}, semble plus faible en hiver, tandis que les transmissivités sont légèrement plus élevées. Il reste tout de même que les simulations ne semblent pas suffisamment sensibles aux variations de températures de l'air. Ce phénomène pourrait être dû au changement de la constante diélectrique de la végétation avec les températures, mais aussi à l'inertie de la température de la neige simulée par un modèle de neige à une couche. Une étude plus approfondie devra être menée pour mieux comprendre ces interactions. Le MTR/CLASS permet néanmoins de bien représenter les tendances des T_B en hiver aux trois fréquences.

Des tests de sensibilité sur la hauteur de neige ont ensuite été évalués. Les simulations montrent que pour des couverts de végétation denses, la sensibilité au SWE à 37 GHz est grandement

diminuée à cause de la transmissivité qui diminue, mais aussi à cause du signal de la végétation qui se réfléchit sur le couvert nival. En polarisation 19 et 10.7 GHz, la sensibilité est faible. Lorsqu'une CG est dans le couvert nival, la sensibilité en polarisation V reste présente à 37 GHz, mais diminue grandement en H.

L'étude permet ainsi d'amener une meilleure compréhension des différentes contributions au signal en forêt boréale. Certaines incertitudes persistent néanmoins et davantage d'études ciblées sur les problématiques spécifiques permettraient d'améliorer les simulations MTR/CLASS.

Références

Derksen, C., Toose, P., Rees, A.,Wang, L., English, M.,Walker, A. et Sturm, M. (2010) Development of a tundra-specific snow water equivalent retrieval algorithm for satellite passive microwave data, *Remote Sensing of Environment*, vol. 114, p. 1699-1709.

Derksen, C. (2008) The contribution of AMSR-E 18.7 and 10.7 GHz measurements to improved boreal forest snow water equivalent retrievals, *Remote Sensing of Environment*, vol. 112, p. 2701-2710.

Dupont, F. (2013) Télédétection micro-onde de surfaces enneigées en milieu arctique : étude des processus de surface de la calotte glaciaire Barnes, Nunavut, Canada, Thèse de doctorat, Grenoble, France.

Durand, M. et Liu, D. (2012) The need for prior information in characterizing snow water equivalent from brightness temperatures, *Remote Sensing of Environment*, vol. 126, p. 248-257.

Durand, M., Kim, E. J. et Margulis, S. A. (2009) Radiance assimilation shows promise for snowpack characterization, *Geophysical Research Letters*, vol. 36, L02503, doi :10.1029/2008GL035214.

Durand, M., Kim E. J., et Margulis, S. A. (2008) Quantifying uncertainty in modeling snow microwave radiance for a mountain snowpack at the Point-Scale, including stratigraphic effects, *IEEE Transactions on Geoscience and Remote Sensing*, vol. 46, no. 6, p. 1753–1767, 2008.

El-Rayes, M. A. et Ulaby, F. T. (1987) Microwave Dielectric Spectrum of Vegetation- Part I: Exprimental Observations, *IEEE Transactions on Geoscience and Remote Sensing*, vol. GE-25, p. 541-549.

Ferrazzoli, P., Guerriero, L. et Wigneron, J. -P. (2002) Simulating L-band emission of forests in view of future satellite applications, *IEEE Transactions on Geoscience and Remote Sensing*, vol. 40, p. 2700–2708.

Hedstrom, N. et Pomeroy, J. (1998) Measurements and modelling of snow interception in the boreal forest, *Hydrological Processes*, vol. 12, p. 1611–1625.

Jia, B., Tian, X., Xie, Z., Liu, J. et Shi, C. (2013) Assimilation of microwave brightness temperature in a land data assimilation system with multi-observation operators, *Journal of Geophysical Research*, vol. 118, doi:10.1002/jgrd.50377.

Juglea, S., Kerr, Y., Mialon, A., Lopez-Baeza, E., Braithwaite, D. et Hsu K. (2010) Soil moisture modelling of a SMOS pixel: interest of using the PERSIANN database over the Valencia Anchor Station, *Hydrological Earth System Science*, vol. 14, p. 1509-1525.

Kohn, J. et Royer, A. (2010) AMSR-E data inversion for soil teperature estimation under snow cover, *Remote Sensing of Environment*, vol. 114, p. 2951-2961.

Kontu, A. et Pulliainen, J. T. (2010) Simulation of spaceborne microwave radiometer measurements of snow cover using in situ data and brightness temperature modeling, *IEEE Transactions on Geoscience and Remote Sensing*, vol. 48, p. 1031-1044.

Kruopis, N., Praks, J., Arslan, A.N., Alasalmi, H. M., Koskinen, J. T. et Hallikainen, M. T. (1999) Passive Microwave measurements of snow-covered forest area in EMAC'95, *IEEE Transactions on Geoscience and Remote Sensing*, vol. 37, p. 2699-2705.

Kurum, M., O'Neill, P. E., Lang, R. H., Joseph, A. T., Cosh, M. H. et Jackson, T. J. (2012) Effective tree scattering and opacity at L-band, *Remote Sensing Environment*, vol.118, p. 1-9.

Langlois, A., Royer, A., Dupont, F., Roy, A., Goïta, K. et Picard, G. (2011) Improved corrections of forests effects on passive microwave satellite remote sensing of snow over boreal and subartic regions, *IEEE Transactions on Geoscience and Remote Sensing*, vol. 49, p. 3824-3837.

Langlois, A., Royer, A., Derksen, C., Montpetit, B., Dupont, F., Goïta, K. (2012) Coupling the snow thermodynamic model SNOWPACK with the microwave emission model of layered snowpacks for subarctic and arctic snow water equivalent retrievals, *Water Resources Research*, vol. 48, W12524.

Langlois, A., Bergeron, J., Brown, R., Royer, A., Harvey, R., Roy, A., Wang, L. et Thériault, N. (2013) Evaluation of CLASS 2.7 and 3.5 simulations of snow cover from the Canadian Regional Climate Model (CRCM4) over Québec, Canada, *Journal of Hydrometeorology*, AMSJHM-S-13-00073, soumis.

Latifovic, R., Zhu, Z.-L., Cihlar, J., Giri, C. et Olthof, I. (2004) Land cover mapping of North and Central America – Global Land Cover 2000. *Remote Sensing Environment*, Vol. 89, p. 116-127.

Lemmetyinen, J., Pulliainen, J., Rees, A., Kontu, A., Qiu, Y. et Derksen, C. (2012) Multiple-layer adaptation of HUT snow emission model: Comparison with experimental data, *IEEE Transactions on Geoscience and Remote Sensing*, vol. 48, p. 2781-2794.

Li, D., Durand, M. et Margulis, S. A. (2012) Potential for hydrologic characterization of deep mountain snowpack via passive microwave remote sensing in the Kern River bassin, Sierra Nevada, USA, *Remote Sensing of Environment*, vol. 125, p. 34-48.

Liu, Y. Y., de Jeu, R. A. M., McCabe, M. F., Evans, J. P. et Dijk, A. I. J. M. (2011) Global long-term passive microwave satellite-based retrievals of vegetation optical depth, *Geophysical Research Letters*, vol. 38, L18402.

Magagi, M., Bernier, M., Bouchard, M. -C. (2002) Use of ground observations to simulate the seasonal changes in the backscattering coefficient of the subarctic forest, *IEEE Transactions on Geoscience and Remote Sensing*, vol. 40, p. 281–297.

Mätzler, C. (1994) Microwave transmissivity of forest canopy: experiments made with a beech, *Remote Sensing of Environment*, vol. 48, p. 172-180.

Mätzler, C. (2006) Comparison of emission models for covered surfaces. *In* Mätzler, C., Rosenkranz, P.W., Battaglia, A. & Wigneron, J.-P. (eds.) *Thermal Microwave Radiation - Applications for Remote Sensing*. IET Electromagnetic Waves Series 52. London. UK, p. 227-240.

Montpetit, B., Royer, A., Roy, A., Langlois, A. et Derksen, C. (2013) Snow microwave emission modeling of ice lenses within a snowpack using the microwave emission model for layered snowpacks, *IEEE Transactions on Geoscience and Remote Sensing*, vol. 51, p. 4705-4717.

Pulliainen, J., Hallikainen, M. et Grandell, J. (1999) Hut snow emission model and its applicability to snow water equivalent retrieval, *IEEE Transactions on Geoscience and Remote Sensing*, vol. 37, p. 1378–1390.

Rahmoune, R., Ferrazzoli, P., Kerr, Y. H. et Richaume, P. (2013) SMOS level 2 retrieval algorithm over forests: description and generation of global maps, *IEEE Journal of Selected Topics in Applied Earth Observations and Remote Sensing*, vol. 6, p. 1430-1439.

Rautiainen, K., Lemmetyinen, J., Pulliainen, J., Vehviläinen, M. D., Kontu, A., Kainulainen, J. et Seppänen, J. (2012) L-band radiometer observations of soil processes in boreal and subarctic environments, *IEEE Transactions on Geoscience and Remote Sensing,* vol. 50, p. 1483-1497.

Rosenfeld, S. et Grody, N. (2000) Anomalous microwave spectra of snow cover observed from Special Sensor Microwave/ Imager measurements, *Journal of Geophysical Research*, vol. 105, p. 14913-14926.

Rüdiger, C., Calvet, J. -C., Gruhier, C., Holmes, T. R. H., de Jeu, R. A. M., et Wagner, W. (2009) An Intercomparison of ERS- SCAT and AMSR-E Soil Moisture Observations with Model Simulations over France, *Journal of Hydrometeorology*, vol. 10, p. 431-447.

Schneebeli, M., Pielmeier, C. et Johnson, J. (1999) Measuring snow microstructure and hardness using a high resolution penetrometer, *Cold Regions Science and Technology*, vol. 30, p. 101-114.

Takala, M., Luojus, K., Pulliainen, J., Derksen, C., Lemmetyinen, J., Kärnä, J. -P., Koskinen, J. et Bojkov, B. (2011) Estimating northern hemisphere snow water equivalent for climate research through assimilation of space-borne radiometer and ground-based measurements. *Remote Sensing of Environment*, vol. 115, p. 3517–3529.

Toure, A., Goïta, K., Royer, A., Kim, E., Durand, M., Margulis, S. et Lu, H. (2011) A Case study of using a multilayered thermodynamical snow model for radiance assimilation, *IEEE Transactions on Geoscience and Remote Sensing*, vol. 9, p. 2828-2837.

Vander Jagt, B. J., Durand, M., Margulis, S. A., Kim, E. J. et Molotch, N. P. (2013) The effect of spatial variability on the sensitivity of passive microwave measurements to snow water equivalent, *Remote Sensing of Environment*, vol. 136, p.163-179.

Way, J., Paris, J., Kasischke, E., Slaughter, C., Viereck, L., Christensen, N., Dobson, M. C., Ulaby, F. T., Richards, J., Milne, A., Sieber, A., Ahem, F. J. Simonett, D., Hoffer, R., Imhoff, M., et Weber J. (1990) The effects of changing environmental conditions on microwave signatures of forest ecosystems: Preliminary results of the March 1998 Alaskan aircraft experiment, *International Journal of Remote Sensing*, vol. 11, no. 7, p. 1119-1144.

Yang, W., Huang, D., Tan, B., Stroeve, J. C., Shabanov, N. V., Knyazikhin, Y., Nemani, R. R. et Myneni, R. B. (2006) Analysis of leaf area index and fraction of PAR absorbed by vegetation products from the Terra MODIS Sensor: 2000–2005, *IEEE Transactions on Geoscience and Remote Sensing*, vol. 44, no. 7, p. 1829–1842.

Yang, W., Tan, B., Huang, D., Rautiainen, M., Shabanov, N. V., Wang, Y., L. P. Jeffrey, Huemmrich, K., F., Fensholt, R., Sandholt, I., Weiss, M., Ahl, D. E., Gower, S. T., Nemani, R. R., Knyazikhin, Y. et Myneni, R. B. (2006) MODIS leaf area index products: from validation to algorithm improvement, vol. 44, p. 1885-1898.

Zhang, Z. J., Zhang, L. X., Sun, G. Q., Zhao et S. J. (2012) Estimation of effects of a freezing enviroment on vegetation using model simulation and a truck-mounted microwave radiometer, *International Journal of Remote Sensing*, vol. 33, p. 6994-7009.

8. Conclusion

La recherche présentée dans cette thèse représente une avancée dans la compréhension et la modélisation de l'émission micro-onde hivernale en forêt boréale. L'étude développe et paramétrise des outils permettant de simuler les principaux éléments contribuant au signal MOP en forêt boréale à partir d'un couplage avec le Canadian Land Surface Scheme (CLASS). Se basant sur les principales difficultés soulevées dans les travaux antérieurs (voir références aux Chap. 3 et Chap. 5), nous avons exploré principalement l'effet de la taille des grains dans l'émission micro-onde de la neige ainsi que les effets du sol et de la végétation sur le signal. L'aspect de la taille des grains a été traité à partir d'une nouvelle métrique pour représenter la taille des grains de neige, la surface spécifique de la neige (SSA), qui a pour principal avantage de permettre des mesures précises et reproductibles sur le terrain à partir de la mesure de la réflectance dans l'infrarouge à onde courte (SWIR). Au niveau de la végétation, la paramétrisation du modèle γ-ω a été évaluée à partir de différentes bases de données.

L'implémentation d'un module de réflectivité du sol dans le modèle d'émission micro-onde DMRT-ML a permis d'utiliser le modèle pour des neiges saisonnières. L'analyse à partir de mesures radiométriques et de neige in situ, dont la SSA, a permis de démonter la pertinence de l'utilisation de cette métrique pour représenter la taille de grains dans le transfert radiatif de la neige. Par contre, à cause de la simplification de la représentation des grains dans la théorie DMRT, considérés comme un ensemble de sphères de glace équivalentes, un facteur de correction doit être appliqué. Des simulations ont néanmoins permis de démontrer que l'adhésion entre les particules (*stickiness*) forme des agrégats qui interagissent avec les micro-ondes comme des objets plus gros que la taille des grains. Cette augmentation de la taille de grains effective augmente ainsi la diffusion et explique en partie le facteur à appliquer à la SSA. La distribution de la taille de grains considérée comme mono-disperse dans DMRT-ML peut aussi expliquer en partie ce facteur. À cause de la non-linéarité de l'impact de la taille de grains sur la diffusion, une collection de sphères avec des rayons variables, comme rencontrée dans des neiges naturelles, diffusera davantage qu'une collection de sphères identiques. La quantification de ces deux composantes reste difficile et davantage de travaux devront être menés pour déterminer la variation de ces deux paramètres selon le type de neige. L'étude a tout de même permis de mieux

comprendre les interactions complexes dans le transfert radiatif micro-onde de la neige. De plus, l'utilisation d'un simple facteur ϕ appliqué au rayon optique dérivé de la SSA permet de bien représenter les caractéristiques diffusives de la neige et a ainsi été utilisé dans le cadre du couplage MTR/CLASS.

Un modèle de métamorphisme de la neige a été implémenté dans CLASS. Ce modèle simple, qui calcule l'évolution de la SSA pour différentes couches de neige en fonction du gradient de température, permet ainsi d'alimenter DMRT-ML pour représenter l'effet de la taille de grains sur la diffusion de la neige. Le modèle offre une méthode simple pour calculer la SSA à partir d'un modèle de neige à une couche sans avoir à modifier ce dernier. Cette approche serait facilement applicable pour d'autres modèles à une couche qui sont utilisés de façon opérationnelle au Canada (Turcotte et al., 2007; Bélair et al., 2003), ainsi qu'à la nouvelle implémentation du schéma de surface dans le GEM.

Au niveau de l'effet de la végétation sur le signal MOP aux hautes fréquences, une première étude menée sur des forêts de conifères denses à différentes échelles a montré l'importance de la considération de la diffusion (ω) pour estimer l'émission de la végétation. Étant donné que γ-ω sont des paramètres effectifs semi-empiriques, les différentes configurations de prises de mesures peuvent influencer l'inversion de ces paramètres. Des relations entre les transmissivités et les paramètres structuraux, dont les LAI, ont ensuite été établies pour des forêts boréales en été. À notre connaissance, aucune autre étude n'a relié la transmissivité de la végétation avec le LAI pour les hautes fréquences (19 et 37 GHz), à l'échelle satellitaire en considérant la diffusion (ω). Nous verrons par contre que cette paramétrisation semble changer pour une forêt en hiver. Ces études soulèvent ainsi la difficulté de comparer des paramètres γ-ω entre différentes bases de données. Davantage d'études devront ainsi être menées pour mieux comprendre les variations γ-ω en fonction des conditions de la forêt boréale.

La paramétrisation de la réflectivité du sol a aussi été étudiée. Les données radiométriques in situ au Chap. 3 ont démontré la difficulté de définir l'effet de rugosité sur la réflectivité du sol. Des paramètres effectifs (QH) doivent ainsi être inversés pour représenter la réflectivité du sol. L'étude propose de nouvelles valeurs de QH pour les fréquences d'AMSR-E (37 19 10.7 et 6.9 GHz) en forêt boréale. D'autres parts, le manque d'information sur la constante diélectrique des

sols gelés a été contourné en optimisant l'humidité du sol à 10.7 GHz. Cette optimisation permet de retrouver des paramètres effectifs pour les autres fréquences. Avec une connaissance plus approfondie de l'effet du gel/dégel du sol sur la constante diélectrique, la fréquence 10.7 GHz pourrait être utilisée pour estimer les paramètres du sol à partir d'inversions ou de schéma d'assimilation.

La comparaison des simulations issues du MTR/CLASS et des mesures AMSR-E montre que le modèle donne une bonne représentation des tendances des T_B. Des RMSE de l'ordre de 7 à 3 K pour des simulations à l'échelle d'AMSR-E en forêt boréale semblent bonnes comparativement aux autres études où les erreurs surtout à 37 GHz se trouvent généralement au-dessus de 10 K (Kontu & Pulliainen, 2010). Il reste par contre que le modèle montre un manque de sensibilité à la température de l'air. La considération de paramètres de végétation fixes l'hiver ainsi que l'inertie de la température de la neige pour un modèle de neige à une couche pourraient expliquer cette erreur. À noter que, l'été, la considération de paramètres fixes de végétation a néanmoins permis d'obtenir des RMSE entre 2 et 3 K (Chap. 6). De plus, les tests de sensibilité issus de MTR/CLASS montrent les limites de l'utilisation du MTR/CLASS pour l'inversion des SWE à partir des MOP en forêt boréale. En effet, l'erreur reliée à MTR/CLASS est généralement plus élevée que la sensibilité des MOP à l'erreur typique de CLASS. Ces limites sont d'autant plus importantes en présence de végétation dense et pour des couverts nivaux épais. Certaines améliorations au MTR/CLASS pourraient être amenées afin d'augmenter cette sensibilité. Une approche multicouche dans le transfert radiatif de la neige pourrait permettre d'augmenter la sensibilité au SWE surtout à 19 GHz. Cette fréquence serait utile pour des couverts nivaux épais où le signal à 37 GHz sature. La considération de paramètres variables de γ-ω en hiver permettrait aussi de réduire l'erreur et l'incertitude de MTR/CLASS. De plus, même si la sensibilité pour des couverts de végétation denses semble très faible, certaines approches d'assimilation pourraient permettre d'améliorer les estimations de SWE pour des sites où le couvert végétal est plus faible.

L'effet important de croûtes de glace dans le couvert nival sur le signal MOP a été constaté. Ces croûtes de glace diminuent ainsi la sensibilité au SWE surtout en polarisation horizontale. L'effet de ces croûtes a été simulé avec DMRT-ML en ajoutant des couches sans grains de neige. Il reste que DMRT-ML ne permet pas de considérer l'effet de cohérence (interférence lorsque l'épaisseur

de la couche est de l'ordre de la longueur d'onde du signal mesuré) qui apparait important pour la plupart des croûtes observées. L'optimisation de la densité de la croûte de glace permet néanmoins d'obtenir des résultats intéressants, malgré l'incohérence physique d'une telle approche.

L'étude a donc permis de mettre au point des outils permettant de représenter les principaux éléments contribuant au signal MOP en forêt boréale. Ces outils relativement simples ont été développés dans une optique d'application opérationnelle future dans un contexte d'implémentation des systèmes établis comme le *Canadian Land data Assimiliation System* (CaLDAS). Le MTR/CLASS développé permettra l'assimilation des températures de brillance satellite en forêt boréale, milieu où il n'y a pratiquement pas de données au sol, et permettra en principe de générer des analyses de neige plus précise qu'avec un modèle seul (i.e. sans assimilation d'observations).

9. Références (hors articles)

Amlien, J. (2008) Remote sensing of snow with passive microwave radiometers. A review of current algorithms. Norsk Regnesentral, Rapport N°. 1019. Oslo, Norvège.

Andreadis, K. M. et Lettenmaier, D. P. (2006) Assimilating remotely sensed snow observations into a macroscale hydrology model, *Advances in Water Resources*, vol. 29, p. 872-886.

Arnaud, L., Picard, G., Champollion, N., Domine, F., Gallet, J., Lefebvre, E. Fily, M. et Barnola, J. (2011) Measurement of vertical profiles of snow specific surface area with a 1 cm resolution using infrared reflectance: instrument description and validation, *Journal of Glaciology*, vol. 57, p. 17-29.

Aschbacher, J. (1989) Land surface studies and atmospheric effects by satellite microwave radiometry, Thèse de doctorat, Université d'Innsbruck, Innsbruck, Autriche.

Bartelt, P. et Lehning, M. (2002) A physical SNOWPACK model for the Swiss avalanche warning Part I: numerical model, *Cold Regions Science and Technology*, vol. 35, p. 123-145.

Bélair, S., Brown, R., Mailhot, J., Bilodeau, B. et Crevier, L. (2003) Operational implementation of the ISBA land surface scheme in the Canadian regional weather forecast model. Part II: Cold season results, *Journal of Hydrometeorology*, vol. 4, p. 371-386.

Bergeron, J. (2012) Estimation de la superficie du couvert nival à partir d'une combinaison des données de télédétection MODIS et AMSR-E dans un contexte de prévision des crues printanières au Québec, Mémoire de maîtrise, Université de Sherbrooke, Sherbrooke, Canada, p. 134.

Bergeron, J., Royer, A., Turcotte, R. et Roy, A. (2013) Snow cover estimation using blended MODIS and AMSR-E data for improved watershed-scale spring streamflow forecasts in Québec, Canada, *Hydrological Processes*, accepté (HYP-12-0524).

Bernier, P. Y. (1987) Microwave remote sensing of snowpack properties - Potential and limitations, *Nordic Hydrology,* vol. 18, p. 1-20.

Bourque, A. et Simonet, G. (2008) « Québec », *in* Vivre avec les changements climatiques au Canada : édition 2007, Lemmen, D.S., Warren, F.J., Lacroix, J., Bush, E. (éditeurs), Gouvernement du Canada, Ottawa (Ontario), 2008, p. 171-226.

Brandt, J. P. (2009) The extent of the North American boreal zone, *Environmental Reviews*, vol. 17, pp. 101-161.

Brown, R., Bartlett, P., MacKay, M. et Verseghy, D. (2006) Evaluation of snow cover in CLASS for SnowMIP, *Atmosphere-Ocean*, vol. 44, p. 223-238.

Brucker, L., Picard, G., Arnaud, L., Barnola, J.-M., Schneebeli, M., Brunjail, H., Lefebvre, E. et Fily, M. (2011) Modelling time series of microwave brightness temperature at Dome C,

Antarctica, using vertically resolved snow temperature and microstructure measurements, *Journal of Glaciology*, vol. 57, p. 171-182.

Carmagnola , C. M., Morin, S., Lafaysse, M., Domine, F., Lesaffre, B., Lejeune, Y., Picard, et Arnaud, L. (2013) Implementation and evaluation of prognostic reprenstations of the optical diameter of snow in the detailed snowpack model SURFEX/ISBA-Crocus, The Cryosphere Discussion, vol. 7, p. 4443-4500.

Caya, D. et Laprise, R. (1999) A semi-implicit semi-Lagrangian regional climate model: The Canadian RCM, *Monthly Weather Review*, vol. 127, p. 341-362.

Chang, A. T. C, Foster, J. L. et Hall, D. K. (1987) Nimbus-7 SMMR derived global snow cover parameters, *Annals of Glaciology*, vol. 9, p. 39-44.

Comtois-Boutet, F. (2007) Évaluation de modèles de regression linéaire pour la cartographie de l'équivalent en eau de la neige dans la prvince du Québec avec le capteur micro-ondes passives AMSR-E, Mémoire de maîtrise, Université de Sherbrooke, Sherbrooke, 91 p.

Derksen, C., Walker, A. et Goodison, B. (2005) Evaluation of passive microwave snow water equivalent retrievals across the boreal forest-tundra transition of western Canada, *Remote Sensing of Environment*, vol. 96, p. 315-327.

Derksen, C. (2008) The contribution of AMSR-E 18.7 and 10.7 GHz measurements to improved boreal forest snow water equivalent retrievals, *Remote Sensing of Environment*, vol. 112, p. 2701-2710.

Déry, S. J., Hernandez-Henriquez, M. A, Burford, J. E. et Wood, E. F. (2009) Observational evidence of an intensifying hydrological cycle in the northern Canada, *Geophysical Research Letters*, vol. 36, L13402.

Dobson, M. C., Ulaby, F. T., Hallikainen, M. T. et El-Rayes, M. A. (1985) Microwave dielectric behaviour of wet soil part II: Dielectric mixing models, *IEEE Transactions on Geoscience and Remote Sensing*, vol. GE-23(1), p. 35–46.

Domine, F., Albert, M., Huthwelker, T., Jacobi, H.-W., Kokhanovsky, A. A., Lehning, M., Picard, G. et Simpson, W. R. (2008) Snow physics as relevant to snow photochemistry, *Atmospheric Chemistry and Physics*, vol. 8, p. 171–208.

Doraz, F. et Brown, R. (2008) Évaluation des simulations du couvert nival sur le Québec par les modèles MRCC 4.2.3 et GEMCLIM 3.3.0, Rapport de recherche, Ouranos, 41pp.

Dupont, F., Picard, G., Royer, A., Fily, M. et Roy, A., Champollion, N. (2013) Modeling the microwave emission of bubbly ice; Applications to blue ice and superimposed ice in the Antarctic and Arctic, *IEEE Transactions on Geoscience and Remote Sensing*, soumis (TGRS_2012-01104).

Durand, M., Kim, E. J. et Margulis, S. A. (2009) Radiance assimilation shows promise for snowpack characterization, *Geophysical Research Letters*, vol. 36, L02503, doi :10.1029/2008GL035214.

Dutra, E., Kotlarski, S., Viterbo, P., Balsamo, G., Miranda, P. M. A., Schär, C., Bissolli, P. et Jonas, T. (2011) Snow cover sensitivity to horizontal resolution, parameterizations, and atmospheric forcing in a land surface model, *Journal of Geophysical Research*, vol. 116, D21109.

Ellis, C. R., Pomeroy, J. W., Brown, T. et MacDonald, J. (2010) Simulation of snow accumulation and melt in needleleaf forest environments, *Hydrology and Earth System Sciences*, vol. 14, p. 925-940.

ESA (2012) Report for mission selection: CoReH_2O, ESA, SP-1324/2 (3 volume series), European Space Agency, Noordwijk, Netherlands.

Foster, J. L., Hall, D. K., Eylander, J. B., Riggs, G. A., Nghiem, S. V., Tedesco, M., Kim, E. J., Montesano, P., Kelly, R. E. J., Casey, K. A. et Choudhury, B. (2011) A blended global snow product using visible, passive microwave and scatterometer data, *International Journal of Remote Sensing*, vol. 32, p. 1371-1395.

Gallet, J., Domine, F., Zender, C. et Picard, G. (2009) Rapid and accurate measurement of the specific surface area of snow using infrared reflectance at 1310 and 1550 nm, *The Cryosphere,* vol. 3, p. 167-182.

Goïta, K, Walker, A. E. et Goodison, B. E. (2003) Algorithm development for the estimation of snow water equivalent in the boreal forest using passive microwave data, *International Journal of Remote Sensing*, vol. 24, p. 1097-1102.

Gouttevin, I., Menegoz, M., Domine, F., Krinner, G., Koven, C., Ciais, P., Tarnocai, C. et Boike, J. (2012) How the insulating properties of snow affect soil carbon distribution in the continental pan-arctic area, *Journal of Geophysical Research*, vol. 117, G02020, doi:10.1029/2011JG001916.

Grenfell, T. C. et Putkonen, J. (2008) A method for the detection of the severe rain-on-snow event on Banks Island, October 2003, using passive microwave remote sensing, *Water Resources Research*, vol. 44, W03425, doi:10.1029/2007WR005929.

Hall, D. K., Riggs, G. A. et Salomonson, V. V. (1995) Development of methods for mapping global snow cover using moderate resolution imaging spectroradiometer data, *Remote Sensing of Environment*, vol. 54, p. 127-140.

Hallikainen, M. T., Ullaby, F. T., Dobson, M. C., El-Rayes, M. A. et Wu, L. -K. (1985) Microwave dielectric behavior of wet soil – Part I: empirical models and experimental observations, *IEEE Transactions on Geoscience and Remote Sensing*, vol. GE-23, p. 25-34.

Jia, B., Tian, X., Xie, Z., Liu, J. et Shi, C. (2013) Assimilation of microwave brightness temperature in a land data assimilation system with multi-observation operators, *Journal of Geophysical Research*, vol. 118, doi:10.1002/jgrd.50377.

Jin, Y. Q. (1994) *Electromagnetic scattering modelling for quantitative remote sensing*, World Scientific, 1994.

Kelly, R. et Chang, A. (2003) Development of a passive microwave global snow depth retrieval algorithm for Special Sensor Microwave Imager (SSM/I) and Advance Microwave Scanning Radiometer-EOS (AMSR-E) data, *Radio Science*, vol. 38, doi:10.1029/2002RS002648.

Kerr, Y. H. et Njoku E. G. (1990) A semiempirical model for interpreting microwave emission from semiarid land surfaces as seen from space, *IEEE Transactions on Geoscience and Remote Sensing*, vol. 28, p. 384-393.

Klein, A. G. et Strove, J. (2002) Development and validation of a snow albedo algorithm for the MODIS instrument, *Annals of Glaciology*, vol. 34, p. 45-52.

Klingaman, N. P., Hanson, B. et Leathers, D. J. (2008) A teleconnection between forced great plains snow cover and European winter climate, *Journal of Climate*, vol. 21, p. 2466-2483.

Kohn, J. et Royer, A. (2010) AMSR-E data inversion for soil temperature estimation under snow cover, *Remote Sensing of Environment*, vol. 114, p. 2951-2961.

Kruopis, N., Praks, J., Arslan, A. N., Alasalmi, H. M., Koskinen, J. T., Hallikainen, M. T. (1999) Passive Microwave measurements of snow-covered forest area in EMAC'95, *IEEE Transactions on Geoscience and Remote Sensing*, vol. 37, p. 2699-2705.

Langlois, A., Brucker, L., Kohn, J., Royer, A., Derksen, C., Cliche, P., Picard, G., Willemet, J. M., and Fily, M. (2009) Simulation of snow water equivalent (SWE) using thermodynamic snow models in Québec, Canada, *Journal of Hydrometeorology*, vol. 10, p. 1447-1463.

Langlois, A., Royer, A., Dupont, F., Roy, A., Goïta, K. et Picard, G. (2011) Improved corrections of forest effects on passive microwave satellite remote sensing of snow over boreal and subarctic regions, *IEEE Transactions on Geoscience and Remote Sensing*, vol.49. p. 3824-3837.

Langlois, A., Royer, A., Derksen, C., Montpetit, B., Dupont, F., Goïta, K. (2012) Coupling the snow thermodynamic model SNOWPACK with the microwave emission model of layered snowpacks for subarctic and arctic snow water equivalent retrievals, *Water Resources Research*, vol. 48, W12524.

Langlois, A., Bergeron, J., Brown, R., Royer, A., Harvey, R., Roy, A., Wang, L. et Thériault, N. (2013) Evaluation of CLASS 2.7 and 3.5 simulations of snow cover from the Canadian Regional Climate Model (CRCM4) over Québec, Canada, *Journal of Hydrometeorology*. soumis (AMSJHM-S-13-00073).

Le Dimet, F.-X. et Talagrand, O. (1986) Variational algorithms for analysis and assimilation of meteorological observations: theoretical aspects, *Tellus*, vol. 38A, p. 97-110.

Liebe, H. (1989) MPM - an atmospheric millimeter-wave propagation model, *International Journal or Infrared and Millimeter Waves*, vol. 10, p. 631-650.

Lemmetyinen, J., Pulliainen, J., Rees, A., Kontu, A., Qiu, Y. et Derksen, C. (2012) Multiple-layer adaptation of HUT snow emission model: Comparison with experimental data, *IEEE Transactions on Geoscience and Remote Sensing*, vol. 48, p. 2781-2794.

Mironov, V. L., De Roo, R. D. et Savin, I. G. (2010) Temperature-dependable microwave dielectric model for an Arctic soil, *IEEE Transactions on Geoscience and Remote Sensing*, vol. 48, p. 2544-2556.

Montpetit, B. Royer, A., Langlois, A., Cliche, P., Roy, A., Champollion, N., Picard, G., Domine, F. et Obbard, R. (2012) New shortwave infrared albedo measurements for snow specific surface area retrieval, *Journal of Glaciology*, vol. 58. p. 941-952.

Montpetit, B., Royer, A., Roy, A., Langlois, A. et Derksen, C. (2013) Snow microwave emission modeling of ice lenses within the snowpack using the Microwave emission Model for Layered Snowpacks (MEMLS), *IEEE Transactions on Geoscience and Remote Sensing*, vol. 51, p. 4705-4717.

Music, B. et Caya, D. (2007) Evaluation of the hydrological cycle over the Mississippi River basin as simulated by the Canadian Regional Climate Model (CRCM), *Journal of Hydrometeorology*, vol. 8, p. 969-988.

Musselman, K. N., Molotch, N. P. et Brooks, P. D. (2008) Effects of vegetation on snow accumulation and ablation in a mid-latitude sub-alpine forest, *Hydrological Processes*, vol. 22, p. 2767-2776.

Nagler, T. et Rott, H. (2000) Retrieval of wet snow by means of multitemporal SAR data, *IEEE Transactions on Geoscience and Remote Sensing*, vol. 39, p. 774-765.

Pampaloni, P. (2004) Microwave radiometry of forests, *Waves Random Media*, vol. 14, p. 275-298.

Pardé, M., Goïta, K. et Royer, A. (2007) Inversion of a passive microwave snow emission model for water equivalent estimation using airborne and satellite data, *Remote Sensing of Environment*, vol. 111, p. 346-356.

Picard, G. et Fily, M. (2006) Surface melting observations in Antarctica by microwave radiometers: correcting 26-year time series from changes in acquisition hours, *Remote Sensing Environment*, vol. 104, p. 325-336.

Picard, G., Brucker, L., Roy, A., Dupont, F., Fily, M. et Royer, A. (2013a) Simulation of the microwave emission of multi-layered snowpacks using the dense media radiative transfer theory: the DMRT-ML model, *Geoscientific Model Development*, vol. 6, p. 1061-1078.

Picard, G., Royer, A., Arnaud, L. et Fily, M. (2013b) Influence of meter-scale wind-formed features on the variability of the microwave brightness temperature around Dome C in Antarctica, *The Cryosphere Discussion*, vol. 7, p. 3627-3674.

Pulliainen, J. (2006) Mapping of snow water équivalent ans snow depth in boréal and subarctic zones by assimilating space borne microwave radiometer data, *Remote Sensing of Environment*, vol. 101, p. 257-269.

Pulliainen, J. et Hallikainen, M. (2001) Retrieval of regional snow water equivalent from space-borne passive microwave observations, *Remote Sensing of Environment*, vol. 75, p. 76-85.

Pulliainen, J., Hallikainen, M. et Grandell, J. (1999) Hut snow emission model and its applicability to snow water equivalent retrieval, *IEEE Transactions on Geoscience and Remote Sensing*, vol. 37, p. 1378-1390.

Rautiainen, K., Lemmetyinen, J., Pulliainen, J., Vehviläinen, M. D., Kontu, A., Kainulainen, J. et Seppänen, J. (2012) L-band radiometer observations of soil processes in boreal and subarctic environments, *IEEE Transactions on Geoscience and Remote Sensing,* vol. 50, p. 1483-1497.

Rees, A., Lemmetyinen, J., Derksen, C., Pulliainen, J. et English, M. (2010) Observed and modelled effects of ice lens formation on passive microwave brightness temperatures over snow covered tundra, *Remote Sensing of Environment*, vol. 114, p. 116–126.

Reichle, R. H. (2008) Data assimilation methods in the earth sciences, *Advances in Water Resources*, vol. 31, p. 1411-1418.

Rosenfeld, S. et Grody, N. (2000) Anomalous microwave spectra of snow cover observed from Special Sensor Microwave/ Imager measurements, *Journal of Geophysical Research*, vol. 105, p. 14913-14926.

Rosenkranz, P. W. (1998) Water vapor microwave continuum absorption: A comparison of measurements and models, *Radio Science*, vol. 33, p. 919- 928.

Rott, H., Yueh, S. H., Cline, D. W., Duguay, C., Essery, R., Haas, C., Hélière, F., Kern, M., Macelloni, G., Malnes, E., Nagler, T., Pulliainen, J., Rebhan, H. et Thompson, A. (2010) Cold regions hydrology high-resolution observatory for snow and cold lands processes, *Proceedings of the IEEE*, vol. 98, p. 752–765.

Roy, A., Royer, A. et Hall**,** R. (2013) Relationship between forest microwave transmissivity and structural parameters for Canadian boreal forest, *Geoscience and Remote Sensing Letters*. soumis (GRSL-00262-2013).

Roy, A., Picard, G., Royer, A., Montpetit, B., Dupont, F., Langlois, A., Derksen, C. et Champollion, N. (2013a) Brightness temperature simulations of the Canadian seasonal snowpack driven by measurements of snow specific surface area, *IEEE Transactions on Geoscience and Remote Sensing*, vol. 51, p. 4692-4704.

Roy, A., Royer, A., Montpetit, B., Bartlett, P. A. et Langlois, A. (2013b) Snow specific surface area simulation using the one-layer snow model in the Canadian Land Surface scheme (CLASS). *The Cryopshere*, vol.7, p. 961-975.

Roy, A., Royer, A., Wigneron, J.-P., Langlois, A., Bergeron, J. et Cliche, P. (2012) A simple parameterization for a boreal forest radiative transfer model at microwave frequencies. *Remote Sensing of Environment*, vol. 124. p. 371-383.

Roy, A., Royer, A. et Turcotte, R. (2010a) Analyse de l'identification de la fonte de neige printanière avec QuickSCAT dans le Sud du Québec, Canada, *Canadian Journal of Remote Sensing*, vol. 36, p. 89-98.

Roy, A., Royer, A. et Turcotte, R. (2010b) Improvement of springtime streamflow simulations in a boreal environment by incorporating snow-covered area derived from remote sensing data, *Journal of Hydrology*, vol. 390, p. 35-44.

Rutter, N. et 50 autres auteurs (2009) Evaluation of forest snow processes models (SnowMIP2), *Journal of Geophysical Research*, vol. 114, D06111.

Saunders, R., Matricardi, M. et Brunel, P. (1999) An improved fast radiative transfer model for assimilation of satellite radiance observations, *Quarterly Journal of Royal Meteorological Society*, vol. 125, p. 1407-1425.

Schmugge, J. (1985) *Remote Sensing of Soil Moisture, in Hydrological Forecasting*, M. G. Anderson and T. P. Burt, Eds. New York: Wiley.

Scinocca, J. F., McFarlane, N. A., Lazare, M., Li, J. et Plummer, D. (2008) Technical Note: The CCCma third generation AGCM and its extension into the middle atmosphere, *Atmospheric Chemistry and Physics*, vol. 8, p. 7055-7074.

Shih, S., Ding, K., Kong, J. A., Yang, Y. E., Davis, R. E., Hardy, J. P. et Jordan, R. (1997) Modeling of millimeter wave backscatter of time-varying snowcover, *Progress in Electromagnetic Research*, vol. 16, p. 305-330.

Snyder, P. K., Delire, C. et Foley, J. A. (2004) Evaluating the influence of different vegetation biomes on the global climate, *Climate Dynamics*, vol. 23, p. 279-302.

Takala, M., Pulliainen, J., Metsämäki, S. J. et Koskinen, J. T. (2009) Detection of snowmelt using spaceborn microwave radiometer data in Eurasia from 1979 to 2007, *IEEE Transactions on Geoscience and Remote Sensing*, vol. 47, p. 2996-3007.

Takala, M., Luojus, K., Pulliainen, J., Derksen, C., Lemmetyinen, J., Kärnä, J. -P., Koskinen, J. et Bojkov, B. (2011) Estimating northern hemisphere snow water equivalent for climate research through assimilation of space-borne radiometer and ground-based measurements. *Remote Sensing of Environment*, vol. 115, p. 3517–3529.

Toure, A., Goïta, K., Royer, A., Kim, E., Durand, M., Margulis, S. et Lu, H. (2011) A Case study of using a multilayered thermodynamical snow model for radiance assimilation, *IEEE Transactions on Geoscience and Remote Sensing*, vol. 9, p. 2828-2837.

Tsang, L. et Kong, J. A. (2001) *Scattering of Electromagnetic Waves*, *3, Advanced Topics*, New York, NY, USA: Wiley, 2001.

Tsang, L., Kong, J. A., Ding, K. -H. et Ao, C. O. (2001) *Scattering of Electromagnetic Waves: Numerical Simulations*. New York, NY, USA: Wiley, 2001.

Trujillo, E., Ramirez, J. A. et Elder, K. J. (2009) Scaling properties and spatial organization on snow depth fields in sub-alpine forest and alpine tundra, *Hydrological Processes*, vol. 23, p. 1575-1590.

Turcotte, R., Lacombe, P., Dimnik, C. et Villeneuve, J. P. (2004) Prévisions hydrologiques distribuées pour la gestion des barrages publics du Québec, *Canadian Journal of Civil Engineering*, vol. 34, p. 308-320.

Turcotte, R, Fortin, L. G., Fortin, V., Fortin, J. P. et Villeneuve, J. P. (2007) Operational analysis of spatial distribution and the temporal evolution of the snowpack water equivalent in southern Québec, Canada, *Nordic Hydrology*, vol. 38, p. 211-234.

Ullah, S., Frasier, R., Pelletier, L. et Moore, T. R. (2009) Greenhouse gas fluxes from boreal forest soil during the snow-free period in Quebec, Canada, *Canadian Journal of Forest Research*, vol. 39, p. 666-680.

Ulaby, R., Moore, K. et Fung, A. K. (1982) *Microwave Remote Sensing Active and Passive*. Norwood, MA: Artech House, 1982, vol. I.

Vachon, F., Goïta, K., De Sève, D., Royer, A. (2010) Geophysical inversion of a physical-based model combined with *in situ* data assimilation for snow water equivalent monitoring, *IEEE Transactions on Geoscience and Remote Sensing*, vol. 48, p. 59-71.

Vavrus, S. (2007) The role of terrestrial snow cover in the climate system, *Climate Dynamic*, vol. 29, p. 73-88.

Verseghy, D. (1991) CLASS - A Canadian land surface scheme for GCMs, I. Soil model, *International Journal of Climatology*, vol. 11, p. 111-133.

Wang, L., MacKay, M., Brown, R., Harvey, R. et Langlois, A. (2013) Evaluating radiation, albedo, and the snow cover season in the canadian regional climate model over Québec, Canada, *Journal of Hydrometeorology*, soumis, JHM-0331708.

Wang, Z., Zeng, X. et Decker, M. (2010) Improving snow processes in the Noah land model, *Journal of Geophysical Reasearch*, vol. 115, D20108.

Wang, R. W., O'Neill, P. E., Jackson, T. J. et Engman, E. T. (1983) Multifrequency measurements of the effects of soil moisture, soil texture and surface roughness, *IEEE Transactions on Geoscience and Remote Sensing*, vol. GE-21(1), p. 44-51.

Wegmüller, U. et Mätzler, C. (1999) Rough bare soil reflectivity model, *IEEE Transactions on Geoscience and Remote Sensing*, vol. 37, p. 1391-1395.

Wiesmann, A. et Mätzler, C. (1999) Microwave emission model of layered snowpacks, *Remote Sensing of Environment*, vol. 70, p. 307-316.

Wramneby, A., Smith, B. et Samuelsson, P. (2010) Hot spots of vegetation-climate feedbacks under future greenhouse forcing in Europe, *Journal of Geophysical Research*, vol. 115, D21119.

Zhang, T., Aarmstrong, R. L. et Smith, J. (2003) Investigation of the near-surface soil freezethaw cycle in the contiguous United States: algorithm development and validation, *Journal of Geophysical Research*, vol. 108, doi:10.1029/2003JD003530.

ANNEXE 1 : Complément à la figure 4.8

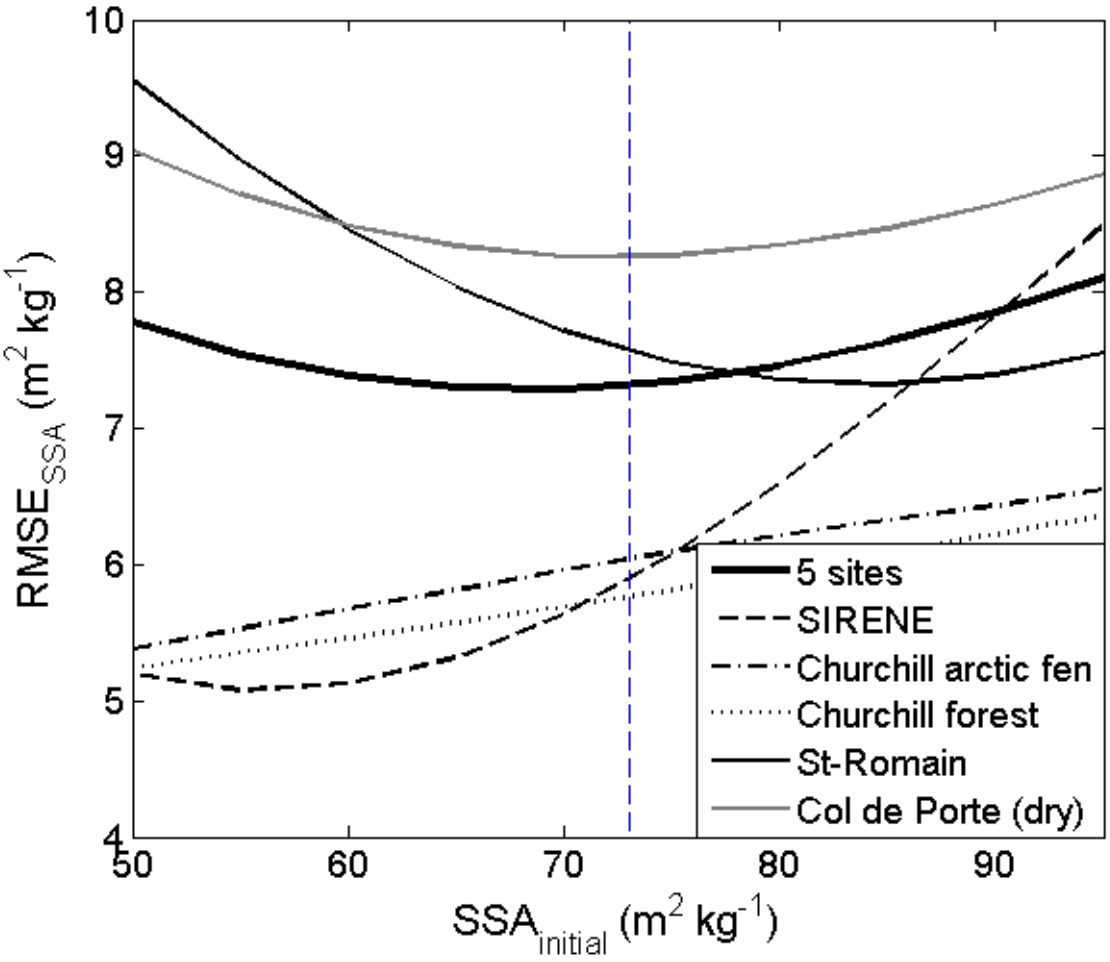

RMSE between the measured SSA and the simulated SSA using CLASS-SSA as a function $SSA_{initial}$ (the vertical dotted blue line represents the $SSA_{initial}$ set in CLASS-SSA at 73.0 m_2 kg_{-1}). Voir figure 4.8.

La figure montre que pour l'ensemble des sites, le minimum se retrouve près de la valeur de $SSA_{initial}$ choisie dans l'étude (73.0 m^2 kg^{-2}). Les minimums de chaque site indépendamment varient de 50 m^2 kg^{-2} (Churchill) à 85 m^2 kg^{-2} (St-Romain).

ANNEXE 2 : Croûtes de glace dans DMRT-ML

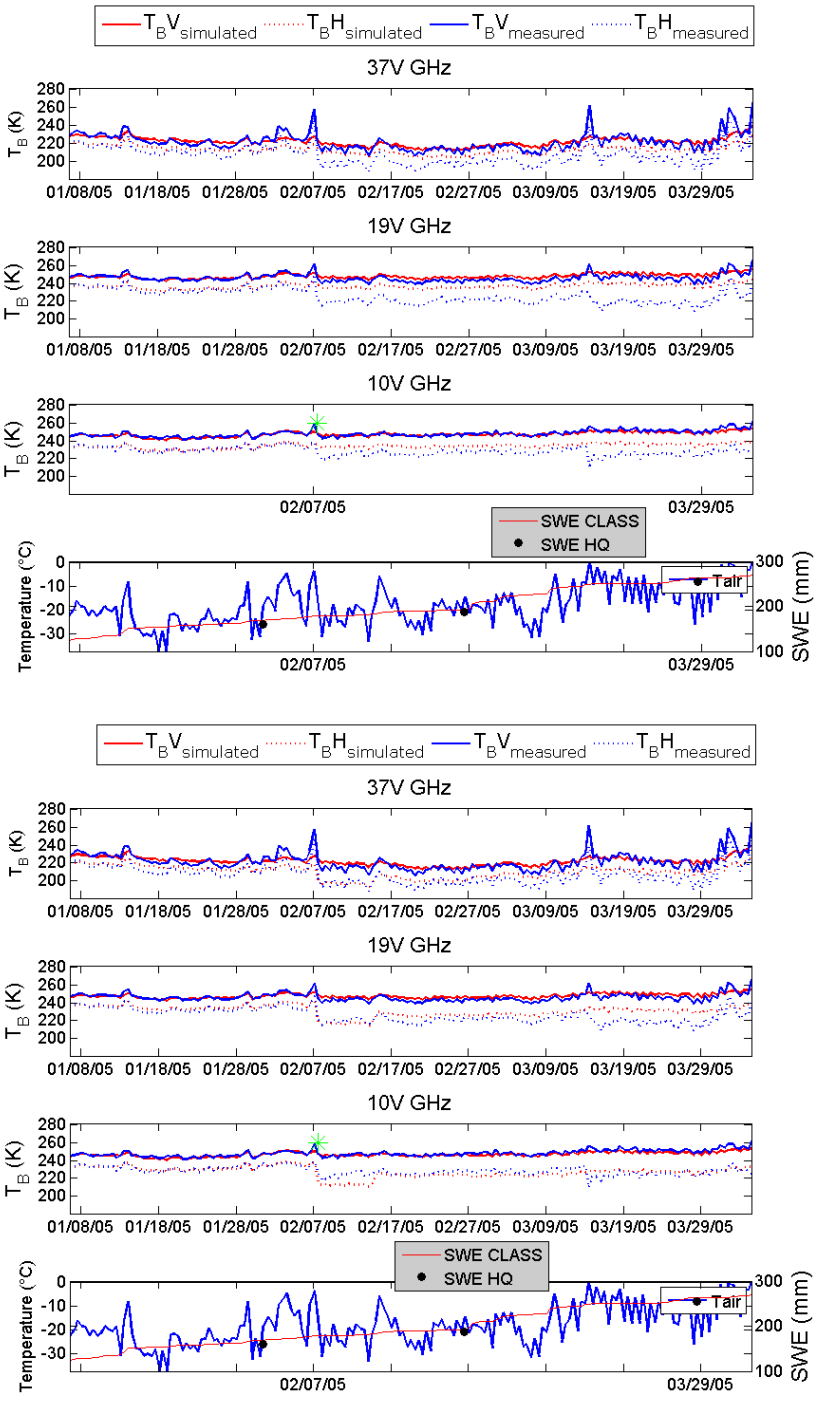

Comparaison de simulations de T_B sans (haut) et avec (bas) l'implémentation d'une croûte de glace dans DMRT-ML sur le site 1 (voir figure 7.7).). Les étoiles vertes dans le 3^e graphique indiquent l'apparition d'une croûte de glace détectée automatiquement à partir du ratio de polarisation à 10.7 GHz.

ANNEXE 3: Publications à titre de premier auteur et co-auteur

Dans cette annexe sont détaillées les publications à titre de premier auteur et de co-auteur. Les « ● » après chaque référence indiquent les contributions amenées dans la cadre de la thèse.

Bergeron, J., Royer, A., Turcotte, R. et **Roy, A.** (2013) Snow cover estimation using blended MODIS and AMSR-E data for improved watershed-scale spring streamflow forecasts in Québec, Canada, *Hydrological Processes*, accepté (HYP-12-0524).

- Implémentation pour l'insertion des données de couvert nival dans le modèle hydrologique

Dupont, F., Picard, G., Royer, A., Fily, M. et **Roy, A.**, Champollion, N. (2013) Modeling the microwave emission of bubbly ice; Applications to blue ice and superimposed ice in the Antarctic and Arctic, *IEEE Transactions on Geoscience and Remote Sensing*, soumis (TGRS_2012-01104).

- Développement de la modélisation du substrat dans DMRT-ML

Langlois, A., Royer, A., Dupont, F., **Roy, A.**, Goïta, K. et Picard, G. (2011) Improved corrections of forest effects on passive microwave satellite remote sensing of snow over boreal and subarctic regions, *IEEE Transactions on Geoscience and Remote Sensing*, vol. 49. p. 3824-3837.

- Aide au développement de méthodes d'inversion des transmissivités
- Validation de la carte d'occupation du sol LCC

Langlois, A., Bergeron, J., Brown, R., Royer, A., Harvey, R., **Roy, A.**, Wang, L. et Thériault, N. (2013) Evaluation of CLASS 2.7 and 3.5 simulations of snow cover from the Canadian Regional Climate Model (CRCM4) over Québec, Canada, *Journal of Hydrometeorology*. soumis (AMSJHM-S-13-00073).

- Modélisation CLASS "offline" pour l'interprétation des résultats

Montpetit, B. Royer, A., Langlois, A., Cliche, P., **Roy, A.,** Champollion, N., Picard, G., Domine, F. et Obbard, R. (2012) New shortwave infrared albedo measurements for snow specific surface area retrieval, *Journal of Glaciology*, vol. 58. p. 941-952.

- Participation aux campagnes terrains (mesures IRIS et caméra SWIR)

Montpetit, B., Royer, A., **Roy, A.**, Langlois, A. et Derksen, C. (2013) Snow microwave emission modeling of ice lenses within the snowpack using the Microwave emission Model for Layered Snowpacks (MEMLS), *IEEE Transactions on Geoscience and Remote Sensing*, vol. 51, p. 4705-4717.

- Participation aux campagnes terrains
- Élaboration de la base de données

Picard, G., Brucker, L., **Roy, A.**, Dupont, F., Fily, M. et Royer, A. (2013a) Simulation of the microwave emission of multi-layered snowpacks using the dense media radiative transfer theory: the DMRT-ML model, *Geoscientific Model Development*, vol. 6, p. 1061-1078.

- Développement de la modélisation du substrat dans DMRT-ML

- Validation du modèle

Roy, A., Royer, A. et Hall**,** R. (2013) Relationship between forest microwave transmissivity and structural parameters for Canadian boreal forest, *Geoscience and Remote Sensing Letters*. soumis (GRSL-00262-2013).

- Élaboration de la base de données
- Analyse des résultats

Roy, A., Picard, G., Royer, A., Montpetit, B., Dupont, F., Langlois, A., Derksen, C. et Champollion, N. (2013a) Brightness temperature simulations of the Canadian seasonal snowpack driven by measurements of snow specific surface area, *IEEE Transactions on Geoscience and Remote Sensing*, vol. 51, p. 4692-4704.

- Participation aux campagnes terrains (Churchill, SIRENE, St-Romain)
- Élaboration de la base de données
- Implémentation de modèle de réflectivité du sol dans DMRT-ML
- Analyse des résultats

Roy, A., Royer, A., Montpetit, B., Bartlett, P. A. et Langlois, A. (2013b) Snow specific surface area simulation using the one-layer snow model in the Canadian Land Surface scheme (CLASS). *The Cryopshere*, vol.7, p. 961-975.

- Participation aux campagnes terrains (Churchill, SIRENE, St-Romain)
- Élaboration de la base de données
- Implémentation de CLASS-SSA
- Analyse des résultats

Roy, A., Royer, A., Wigneron, J.-P., Langlois, A., Bergeron, J. et Cliche, P. (2012) A simple parameterization for a boreal forest radiative transfer model at microwave frequencies. *Remote Sensing of Environment*, vol. 124. p. 371-383.

- Participation aux campagnes terrains (IPY, St-Romain)
- Élaboration de la base de données
- Implémentation du modèle γ-ω et analyse des résutlats

ANNEXE 4

Article Montpetit et al. (2012)

« New shortwave infrared albedo measurements for snow specific surface area retrieval »

Journal of Glaciology, Vol. 58, No. 211, 2012 doi: 10.3189/2012JoG11J248 941

Instruments and Methods

New shortwave infrared albedo measurements for snow specific surface area retrieval

B. MONTPETIT,[1] A. ROYER,[1] A. LANGLOIS,[1] P. CLICHE,[1] A. ROY,[1]
N. CHAMPOLLION,[2] G. PICARD,[2] F. DOMINE,[2] R. OBBARD[3]

[1]*Centre d'Applications et de Recherche en Télédétection (CARTEL), Université de Sherbrooke, Sherbrooke, Québec, Canada*
E-mail: benoit.montpetit2@usherbrooke.ca
[2]*Laboratoire de Glaciologie et Géophysique de l'Environnement, CNRS/Université Joseph Fourier – Grenoble I, Grenoble, France*
[3]*Thayer School of Engineering, Dartmouth College, Hanover, NH, USA*

ABSTRACT. Snow grain-size characterization, its vertical and temporal evolution is a key parameter for the improvement and validation of snow and radiative transfer models (optical and microwave) as well as for remote-sensing retrieval methods. We describe two optical methods, one active and one passive shortwave infrared, for field determination of the specific surface area (SSA) of snow grains. We present a new shortwave infrared (SWIR) camera approach. This new method is compared with a SWIR laser-based system measuring snow albedo with an integrating sphere (InfraRed Integrating Sphere (IRIS)). Good accuracy (10%) and reproducibility in SSA measurements are obtained using the IRIS system on snow samples having densities greater than 200 kg m^{-3}, validated against X-ray microtomography measurements. The SWIRcam approach shows improved sensitivity to snow SSA when compared to a near-infrared camera, giving a better contrast of the snow stratigraphy in a snow pit.

INTRODUCTION

Snowpack state variables such as depth, density, wetness, temperature and snow grain morphology are important for many climate and hydrological applications such as surface energy balance, avalanche predictions and water resources management (e.g. Hall, 2004; Armstrong and Brun, 2008; Brown, 2010; Foster and others, 2011). Characterizing the seasonal and vertical snow grain size is key for snow grain-size retrieval from visible and near-infrared (NIR) satellite data (Jin and others, 2008; Fernandes and others, 2009; Lyapustin and others, 2009), for snow water equivalent (SWE) retrieval from passive microwave satellite data (e.g. Chang and others, 1982; Mätzler, 2006; Pulliainen, 2006; Durand and others, 2008; Derksen and others, 2010; Langlois and others, 2010a; Takala and others, 2011) and for studies of atmospheric/snow chemical interactions (Grannas and others, 2007; Domine and others, 2008). Grain size has also been shown to be the most sensitive parameter of all the snow physical properties in microwave radiative transfer models such as the Microwave Emission Model of Layered Snowpacks (MEMLS; Durand and others, 2008; Langlois and others, 2010a; Brucker and others, 2011), the Helsinki University of Technology model (HUT; Butt and Kelly, 2008; Kontu and Pulliainen, 2010) and the dense-media radiative transfer model (DMRT; Tedesco and Kim, 2006; Grody, 2008; Brucker and others, 2010). Previous studies used different methods to measure snow grain size to validate the MEMLS model, as discussed below (Mätzler and Wiesmann, 1999; Wiesmann and Mätzler, 1999; Toure and others, 2008). Nonetheless, these analytical models still need to be further validated with more reliable and accurate ground-based snow grain measurements to improve their modeling accuracy.

The greatest diameter, D_{max}, of a snow grain has long been used as a classical parameter for characterizing grain size (Fierz and others, 2009). Given the variety of grain shapes and its relevance to radiative transfer models, the definition of grain size remains ambiguous (Aoki and others 2000; Mätzler, 2002; Taillandier and others, 2007). Moreover, demarcation of individual snow grains is ambiguous as the boundaries between grains are not always clearly identifiable (Domine and others, 2008). This reduces the repeatability of such snow grain measurements, due to the subjectivity of the observer. There are several methods for characterizing the physical properties of snow grain size, including stereology (e.g. Matzl and Schneebeli, 2010), methane adsorption measurements (Domine and others, 2001), X-ray computed microtomography (μ-CT; Flin and others, 2005; Chen and Baker, 2010) and optical methods (Matzl and Schneebeli, 2006; Painter and others, 2007; Gallet and others, 2009; Langlois and others, 2010b; Arnaud and others, 2011). Here we focus on optical approaches allowing in-field or in situ measurements. As the spectral reflectance (or its hemispherical component: spectral albedo, hereafter referred to as albedo) of snow is very sensitive to grain size (e.g. Wiscombe and Warren, 1980; Nolin and Dozier, 2000; Kokhanovsky and Zege, 2004; Domine and others, 2006; Xie and others, 2006) and shape (e.g. Jin and others, 2008; Picard and others, 2009), albedo can be used to derive snow grain size and, more precisely, the specific surface area (SSA), a fundamental geometrical characteristic of porous materials. Here SSA quantifies the ice surface-to-volume ratio of a snow grain. Several studies have illustrated the usefulness of SSA measurements, and different methods have been developed for measuring it (Domine and others, 2001; Matzl and Schneebeli, 2006;

Painter and others, 2007; Gallet and others, 2009; Langlois and others, 2010b; Arnaud and others, 2011).

Matzl and Schneebeli (2006) suggested a method based on the use of a commercial camera modified to measure the NIR albedo near 900 nm. The advantage of this method is that it yields vertical SSA profiles rapidly from photos of the snow-pit wall. However, despite its robustness, the method is limited to the NIR spectrum due to the charge-coupled device's (CCD) sensitivity spectrum that abruptly drops above 1000 nm, which reduces the sensitivity to SSA measurement when compared to SWIR albedo measurements (Gallet and others, 2009). This limited sensitivity renders this method difficult to accurately calibrate, and results are hard to reproduce, particularly under variable illumination conditions in deep snow pits, even with a modified protocol as discussed by Langlois and others (2010b). Painter and others (2007) suggested a system based on directional spectral reflectance measurements of snow using a spectroradiometer in the range 950–1050 nm under controlled illumination. However, the resolution of this measurement (2 cm) is rather coarse and is inadequate to properly characterize thinner snow layers (<1 cm) within the snowpack. Also, these wavelengths are more sensitive to absorbing impurities which affect the snow reflectance (Warren and Wiscombe, 1980; Flanner and others, 2007). In addition, Grenfell and Warren (1999) suggest that to reach higher effective grain-size accuracy, hemispherical reflectance is better than biconical reflectance measured by Painter and others (2007). Nonetheless, this method is less destructive and avoids possible snow grain alteration from sampling. Gallet and others (2009) developed a shortwave infrared (SWIR) albedo measurement system using an integrating sphere and laser diodes at 1310 and 1550 nm as illumination sources. This system, DUal-Frequency Integrating Sphere for Snow SSA (DUFISSS), requires extraction of a snow sample, which can be difficult in weakly cohesive snow hoar layers and in the presence of ice lenses. The vertical resolution is also less detailed than with photographs since these measurements are punctual. However, using such a device in a fixed position (in more controllable measurement conditions) improves the accuracy and reproducibility of such measurements. Arnaud and others (2011) modified the method using a profiler, Profiler Of Snow Specific Surface area Using SWIR reflectance Measurement (POSSSUM), to measure a normalized SWIR reflectance within a drilled hole up to 20 m deep. POSSSUM retrieves SSA profiles with an effective vertical resolution of 10–20 mm, but the drilling approach is not applicable in non-cohesive seasonal snow. To limit the issues due to the destructiveness of drilling a hole in seasonal snow, the Laboratoire de Glaciologie et Géophysique de l'Environnement (LGGE) developed the Alpine Snow Specific Surface Area Profiler (ASSSAP) which measures the reflectance profile within a cylindrical dug hole using the same principles as POSSSUM. This instrument is still in development by the LGGE.

Here we present a new approach based on a SWIRcam (hereafter referred to as SWIRcam), at wavelengths comparable to the SWIR integrating sphere system used in this study (InfraRed Integrating Sphere (IRIS)) developed at Université de Sherbrooke, southeastern Québec, Canada, and based on the DUFISSS design (Gallet and others, 2009). Compared to IRIS and DUFISSS, this new camera gives high-resolution SSA profiles. Hence, the main objective of this paper is to analyze and compare the two optically based field retrieval methods of snow grain size (SWIRcam and IRIS) and to discuss their accuracy and reproducibility with various measurements taken in arctic, subarctic and southern regions of Canada.

The next section briefly recalls the theory behind the snow spectral albedo. The different systems used are then described: the new SWIRcam and IRIS. Finally, the advantages and drawbacks of each approach are discussed.

BACKGROUND

In radiative transfer studies, the 'optical' diameter of particles, D_o, is commonly used to characterize particle sizes using the volume (V) to surface area (A) ratio where $D_o = 6(V/A)$ (e.g. Grenfell and Warren, 1999). The optical diameter of a particle is defined as the diameter of a sphere having optical properties identical to those of the measured particle regardless of its shape. For a single size distribution of spheres, D_o corresponds to their diameter. The optical diameter can also be related to the SSA of particles. For snow, SSA can be defined either by its surface-area-of-ice (A) to volume-of-ice (V) ratio ($\mathrm{SSA}_V = A/V$) (m^{-1}) or its surface area of ice per unit of mass of ice (M) ($\mathrm{SSA} = \frac{A}{M} = \frac{A}{\rho_{\mathrm{ice}} V}$) ($\mathrm{m}^2\,\mathrm{kg}^{-1}$), where ρ_{ice} is the density of pure ice ($917\,\mathrm{kg\,m}^{-3}$ at 0°C). The latter definition of SSA can be related to gas adsorption measurements as described by Domine and others (2001). The relationship between the optical diameter and the SSA is then

$$D_o = \frac{6}{\mathrm{SSA}_V} = \frac{6}{\rho_{\mathrm{ice}} \mathrm{SSA}} \tag{1}$$

The SSA of snow can be related to its albedo using a simple optical equation model suggested by Kokhanovsky and Zege (2004), hereafter referred to as KZ04:

$$\begin{aligned} R_{\mathrm{a},\lambda}(\xi) &= \exp\left(-K_0(\xi) b \sqrt{\gamma_\lambda \left(\frac{6}{\rho_{\mathrm{ice}} \mathrm{SSA}}\right)}\right) \\ &= \exp\left(-K_0(\xi) b \sqrt{\gamma_\lambda D_o}\right) \end{aligned} \tag{2}$$

where $R_{\mathrm{a},\lambda}(\xi)$ is the spectral albedo at the wavelength λ and illumination angle ξ, γ_λ is the absorption coefficient of ice which depends on the imaginary part of the refraction index of ice (W.J. Wiscombe, ftp://climate1.gsfc.nasa.gov/wiscombe/), the constant b represents the shape factor of snow grains (b ranges from 4.53 for spheres to 3.62 for tetrahedral grains; Picard and others, 2009), D_o is the optical diameter of the snow grain and K_0 is the escape function which determines the angular distribution of light escaping the medium and depends mainly on the incident lighting conditions (9/7 for normal incidence albedo and 1 for spherical albedo). Figure 1 shows the spectral spherical albedo ($K_0 = 1$) of snow simulated with the KZ04 model for different grain sizes, D_o, and a shape factor, b, of 4.3. Figure 1 shows the higher sensitivity of snow albedo to D_o in the SWIR region (>1.2 μm) compared to the NIR region (<1.0 μm). For a fixed value of $b = 4.3$, a variation of $\Delta D_o = 0.8$ mm (SSA of $8.2\,\mathrm{m}^2\,\mathrm{kg}^{-1}$), for instance, gives a variation of $\Delta R_a = 0.275$ at 1.3 μm, while this variation is only $\Delta R_a = 0.172$ at 0.9 μm. In other words, a given error in measured albedo translates into a larger error on D_o at 0.9 μm than at 1.3 μm.

Simulations with the KZ04 model using different values of b were compared to computed spectral spherical albedo

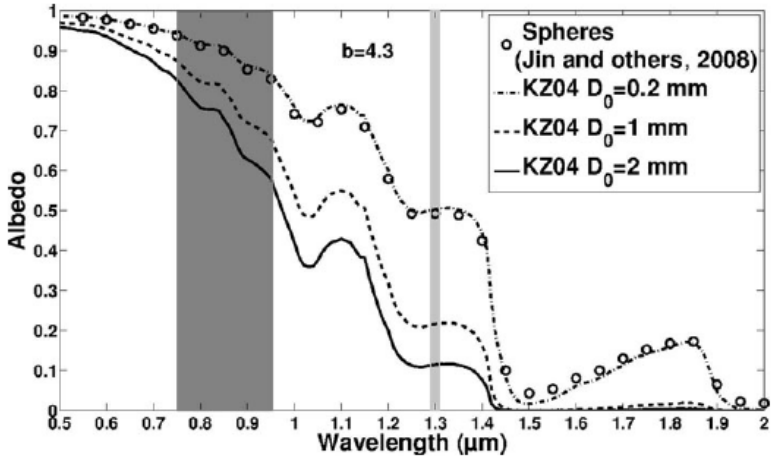

Fig. 1. Spectral albedo of snow for different grain sizes, D_o, simulated with the KZ04 model (Eqn (2)) for spherical albedo ($K_0 = 1$). A shape factor, b, of 4.3 fitted best for spheres in the data presented by Jin and others (2008). The spectral responses of the NIR (dark gray rectangle) and SWIR (light gray rectangle) cameras are displayed. The wavelength of the IRIS and that of the DUFISSS laser system are included in the SWIRcam spectral response.

using the improved geometric–optics method (IGOM) developed by Yang and Liou (1996) (derived from the data of Jin and others, 2008; Z. Jin and others, personal communication, 2011). Using an iterative approach to optimize the correlation between the KZ04 and Jin and others (2008) models, we sought the value of b that provides the best fit. Results show that $b = 4.3$ for spheres gives the best correlation (rmse = 0.01; Fig. 1). The spectral albedo variations (Fig. 1) computed for monodispersed sizes of idealized particle shapes suggest (not shown) that the shape of snow grains could be important in the retrieval procedure, as also outlined by Jin and others (2008) and Picard and others (2009). In practice, however, snow samples include different sizes and shapes giving a polydispersed particle distribution and theoretically affect the shape factor b (Picard and others, 2009). The shape and size variability within a snow sample can clearly be seen in microtomography measurements (e.g. Chen and Baker, 2010; Matzl and Schneebeli, 2010). However, Gallet and others (2009) and Arnaud and others (2011), based on simultaneous measurements of SSA using CH_4 adsorption and IR reflectance of natural snow samples, could not detect any effect of grain shape and fitted their data using the b value adequate for spheres. This indicates that shape effects may cancel out in natural snow, which then behaves as a collection of disconnected spheres.

DATA AND METHODS

Study sites

Intercomparison field campaigns include snow-pit measurements from: (1) the Centre d'Applications et de Recherche en Télédétection (CARTEL) experimental site SIRENE at Université de Sherbrooke throughout several winters since 2008, and (2) Barnes Ice Cap, Baffin Island, Nunavut, Canada, in March 2011 (Dupont and others, 2012).

The first site is an open mid-latitude area where different types of snow grains from fresh snow, rounded grains to depth hoar are found. The second site is an arctic ice cap where the observed snow grains were mostly dense rounded grains, wind crusts and depth hoar. No firn was observed between the ice layers and the seasonal snow. Further details are provided by Dupont and others (2012).

Two other datasets were collected for calibration purposes (12 samples overall) in cold rooms at Dartmouth College, Hanover, New Hampshire, USA, and Québec City, Canada. The grains measured were mainly rounded grains and depth hoar. One fresh snow sample was observed at the time of the measurements in Québec City (Table 1).

LASER ALBEDO MEASUREMENTS

Instrument description

The first system used to measure snow albedo was the Shortwave InfraRed Integrating Sphere (IRIS) system, similar to that developed by Gallet and others (2009), using an integrating sphere (Labsphere®; 10 cm diameter) with three ports. The main difference between the IRIS and the DUFISSS systems is the sphere geometries. DUFISSS has a larger inner diameter (15 cm) and wider ports. The first port of the IRIS system is for illumination by a 1.33 μm laser (1.31 μm for the DUFISSS system) with a 1 cm beam expander. The second port, in front of the laser, is placed in front of the target (snow sample), and the third one, in the perpendicular plane, is for an indium gallium arsenide (InGaAs) photodiode detector. A diaphragm is placed in front of the laser beam in order to measure the dark current and possible stray light entering the sphere. A first measurement with, and a second without, the diaphragm is done. Subtracting the first measurement (dark current and stray light) from the second (signal of the sample) determines the exact signal of the laser reflected on the snow sample. This lightweight and simple system is used in a fixed mode where a snow sample is extracted (Fig. 2) and placed under the integrating sphere, rather than a mobile mode where the integrating sphere is placed against the snow wall. It should be noted that the surface of the snow sample is slightly lower than the sphere's inner surface, giving an effective solid

Fig. 2. The IRIS sampler before extraction of the snow sample within the snow cover (left) and after the sample extraction with the cut surface (right).

angle of the reflected radiation lower than 2π steradians. The sample cup is an aluminum cylinder (10 cm in diameter and 6 cm high) with a metallic plate that slides at the bottom portion of the cylinder (Fig. 2). The sampler was built sufficiently large and deep to limit errors due to possible internal reflections within the sampler (Gallet and others, 2009, p. 171–172).

Calibration and measurements

To provide accurate albedo measurements, the IRIS system is calibrated to albedo for each snow pit using reference Lambertian Spectralon reflectance targets (0.01, 0.07, 0.12, 0.27, 0.47, 0.64, 0.86 and 0.99 at 1330 nm) taking into account any possible shift in the laser intensity between every measurement session. Two calibrations, before and after snow measurements, are done to check the stability of the laser measurements. Figure 3 shows an example of a calibration curve. The nonlinear response is due to a reillumination effect of the reference panels by reflected light (the higher the albedo, the stronger is the reillumination; Gallet and others 2009). A fit is computed using a third-degree polynomial (rmse of 0.008 albedo and $R^2 = 0.999$). The mean measured variability before and after snow-pit measurements (15–30 min) is of the order of 1.3% which is comparable to the variability of the DUFISSS system (1%) (Gallet and others, 2009). This variability is mainly due to the temperature dependency of the laser (Park and others, 1999). Note that the calibration curve does not pass through zero; such an offset is due to photons diffracted by the beam expender and directly reflected by the inner sphere surface toward the InGaAs detector, thus giving a signal even if the albedo sample is zero. This offset is taken into account by the calibration curve (Fig. 3).

To extract an undisturbed snow sample, the sampler is slid inside the snow pit from the surface at desired depth with a 3 cm vertical resolution (the top portion of the sampler corresponds to the measurement height). The sample is then placed under the integrating sphere, three measurements are made to ensure measurement stability and the mean value is taken. To ensure no external light penetrates the integrating sphere, the system is placed inside an enclosed box and the sample is placed directly under the sphere, leaving no space between the sphere port and the sample.

SWIR PHOTOGRAPHS ALBEDO MEASUREMENTS

Instrument description

The other instrument used in this study is a camera sensitive to the NIR and SWIR (0.9–1.7 μm) based on a cooled InGaAs array (320 × 256 pixels) (© Xenics Xeva-320). A filter centered at 1.295 ± 0.012 μm (Edmund NT62-863) is placed in front of the lens to narrow the range. This wavelength was

Table 1. Study sites for the intercomparison field campaigns (SIRENE and Barnes) and the instrument calibration (Québec City and Dartmouth College)

Site	Lat.	Long.	Altitude m	Date	SSA instruments
SIRENE, Sherbrooke, Qué., Canada	45°22′ N	71°56′ W	300	Winters 2008–11	IRIS, NIR and SWIRcams
Barnes Ice Cap, Baffin Island, Nunavut, Canada	70° N	73° W	1124	Mar 2011	IRIS, NIR and SWIRcams
IRIS calibration sites					
Dartmouth College, Hanover, NH, USA	43°42′ N	72°17′ W	161	Feb 2011	IRIS and μ-CT
Québec City, Qué., Canada	46°48′ N	71°12′ W	15	Apr 2012	IRIS and DUFISSS

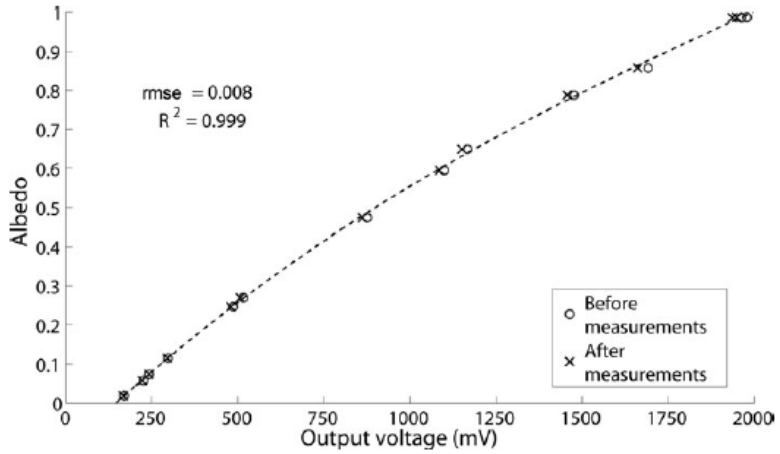

Fig. 3. Example of an IRIS calibration curve. The relationship is $R=(3.23\times10^{-11})V^3-(2.11\times10^{-7})V^2+(8.53\times10^{-4})V-0.12$. The nonlinear response is due to a reillumination effect of the reference panels by reflected light inside the integrating sphere.

chosen for the best compromise between sensitivity of the spectrum albedo to SSA and signal intensity (Fig. 1). The advantage of such an instrument compared to a commercial camera (Matzl and Schneebeli, 2006; Langlois and others, 2010b) is the possibility of directly deriving (after calibration) SSA from the KZ04 model with greater precision as shown in the previous section (Eqn (2)).

Measurement and calibration

The SWIRcam measurement protocol was based on that suggested by Langlois and others (2010b) for snow NIR photographs. Some modifications were made to the protocol concerning control of the ambient lighting conditions and transmission of light through the top layers of the snow pit, in order to improve the accuracy and reproducibility of the measurements. After the snow pit is dug and a clean snow profile has been prepared with a sharp spatula, the camera is placed perpendicularly in front of the snow wall. All measurements were made under diffuse lighting conditions using a white translucent cover, avoiding direct solar illumination. Also, to avoid measurement artifacts due to direct light transmission penetrating the snow cover from the surface to the top portion of the snow profile, a large Styrofoam panel is placed on top of the snow profile (at the snow-cover surface). For calibration from grayscale values to albedo, five reference targets (Lambertian Spectralon targets: 0.06, 0.25, 0.59, 0.79 and 0.99 at 1300 nm) and a rigid ruler are placed along the snow profile (Fig. 4). A first picture is taken with a Styrofoam panel placed in front of the snow wall and the reference targets. This picture is used for image normalization to correct illumination variations over the image. Prior to the snow measurements, the mean albedo ($R_{a,\lambda}=0.97$) and standard deviation (0.00) of this reference panel (80 cm × 80 cm) was measured under controlled illumination (using a 600 W halogen lamp, Q60-SGL). A picture of the snow profile without the Styrofoam panel is then taken. Both photos (snow and reference panel) are taken with a minimum time lag (seconds). The diffuse solar conditions are assumed constant between the two photographs (Fig. 4).

Before calibrating the photographs from grayscale to albedo, the photograph is normalized by dividing, pixel by pixel, the grayscale values of the snow wall picture with the grayscale values of the Styrofoam panel picture (Fig. 4). This corrects illumination variations along the snow profile as seen in Figure 4 where the bottom part of the profile is less dark on the normalized picture (right picture, Fig. 4) than the original snow picture (left picture, Fig. 4). After normalization, a calibration is done between the measured normalized grayscale pixels of the reference target and their albedo values given by the manufacturer (Fig. 5). Figure 5 shows the expected linearity of the calibration (rmse = 0.01; $R^2=0.99$). Such linear relationships are computed for each snow pit taking into account relative lighting and geometric conditions specific to each snow pit. No geometric deformation within the pictures was detected. The pixel to cm conversion is thus vertically constant. To produce an albedo profile, a section of the snow wall (~5–10 cm wide) is extracted in the SWIR picture and the mean horizontal albedo value is then associated with its height. In this study, the mean SWIR photograph resolution was 2 mm pixel^{-1} since no thin layer (<2 mm) was observed. Nonetheless, if there were thin snow or ice layers within the snowpack, multiple pictures of the snow wall (taken at different depth) could be taken, with a minimal time lag, closer to the snow wall to increase the image resolution.

RESULTS AND DISCUSSION

In this section, various albedo and SSA measurements from both SWIR instruments (IRIS and SWIRcam) acquired during several field campaigns in mountainous, northern temperate, subarctic and arctic regions are compared. To limit any possible artifacts due to the sample holder of the IRIS system (Gallet and others, 2009), measurements from snow layers having a density lower than 200 kg m^{-3} have been rejected. These layers were all fresh snow layers and comprised 6% of the overall data given in the following subsections.

IRIS albedo measurement validation for SSA

Figure 6 shows the relationship between albedo measurements taken with the IRIS system and SSA values obtained from two different methods: (1) SWIR albedo measurements with DUFISSS (Gallet and others, 2009) and (2) X-ray computed microtomography (μ-CT) (Chen and Baker, 2010).

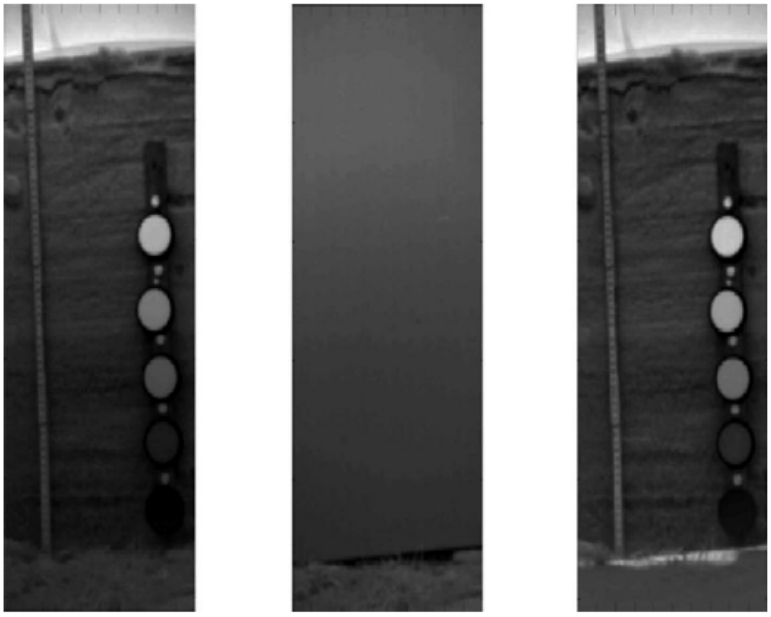

Fig. 4. Example of a snow profile picture (left), a reference Styrofoam panel picture (middle) and a normalized picture (right) taken at the SIRENE study site on 16 February 2011. The normalized picture is the product of the snow profile picture divided by the reference panel picture.

The DUFISSS dataset was fitted to the KZ04 model (Eqn (2)) to validate both the IRIS measurement and the KZ04 simulations.

Albedo measurements from both instruments (IRIS and DUFISSS) were taken from the same snow samples. In fact, the samples were taken with the same sampler and placed under both systems with a minimal time lag (a few minutes) in order to limit any changes in the physical properties. The SSA was then derived from the DUFISSS measurements with the Gallet and others (2009) relationship and compared to the IRIS albedo measurements. Since there are differences in the geometries of both spheres (sphere inner diameter and port geometry and inner diameters) and in the wavelengths used in both systems (1310 nm for DUFISSS and 1330 nm for IRIS), directly comparing the albedo measurements is not adequate. As discussed by Gallet and others (2009) and Arnaud and others (2011), these IR albedo integrating sphere systems do not directly measure directional-hemispherical albedo but rather a combination of directional-hemispherical and diffuse-hemispherical albedos that are highly dependent on the sphere's geometry (Gallet and others, 2009, equation 6).

Nine samples ranging from 6.0 to 57.4 $m^2\,kg^{-1}$ were measured in a cold room in Québec City. Results show good

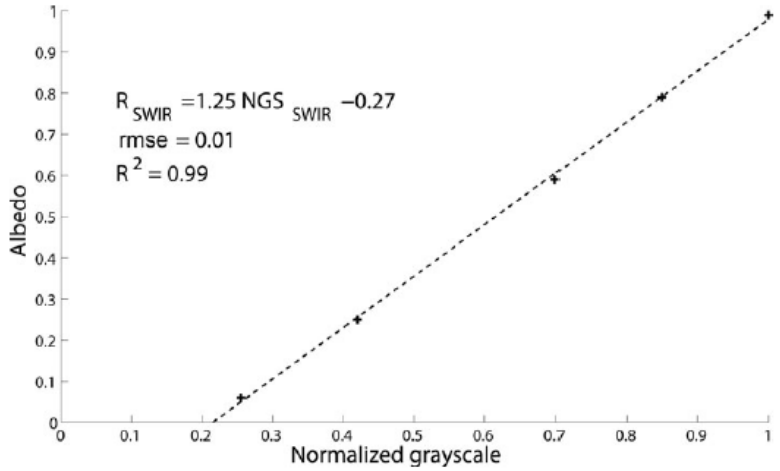

Fig. 5. Example of a calibration curve between the normalized grayscale values and the manufactured albedo values for the SWIRcam.

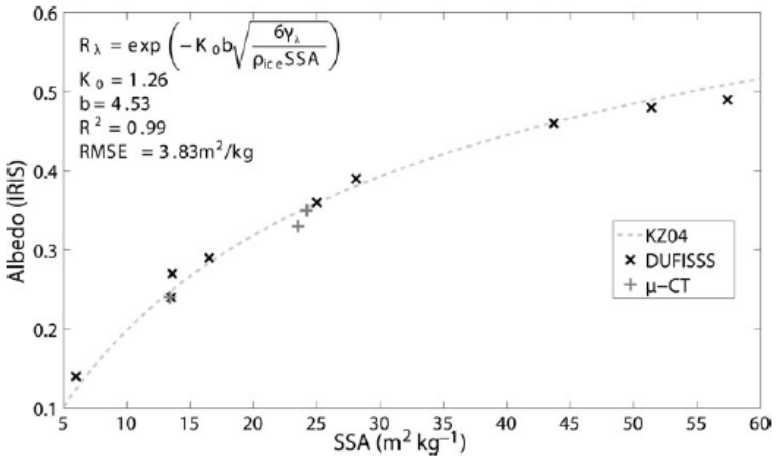

Fig. 6. Relationship between the IRIS-derived albedo and SSA measurements from the DUFISSS system (×) and μ-CT measurements (+). Dashed line corresponds to the KZ04 albedo model (Eqn (2)).

agreement with the KZ04 model using a shape factor b of 4.53 (snow grain shape corresponding to spheres according to Picard and others, 2009) and an escape function K_0 of 1.26 ($R^2 = 0.99$; rmse $= 2.33\,m^2\,kg^{-1}$), meaning that the snow grain shape does not scatter the points in these conditions. This calibration is, however, valid over a limited range of SSA (SSA $< 57.4\,m^2\,kg^{-1}$) and may differ for SSA values higher than $57.4\,m^2\,kg^{-1}$. Arnaud and others (2011) showed that directional-hemispherical albedo SSA measurements tend to give a shape factor corresponding to spheres ($b = 4.53$; Picard and others, 2009) with $K_0 = 9/7$ as used for the SSA retrieval using the SWIRcam. The difference with the escape function given in Figure 6 ($K_0 = 1.26$) is explained by the combination of directional/diffuse-hemispherical albedo measured with IRIS compared to the SWIRcam measurements.

Another independent dataset was used to validate this relationship. The albedo measurements were acquired on the same samples with the IRIS system and the SSA measurements obtained from the μ-CT at Thayer School of Engineering, Hanover. The rmse from the model is $1.33\,m^2\,kg^{-1}$. The overall accuracy of the IRIS system using the KZ04 model for retrieving the SSA in comparison to these two SSA datasets is $1.89\,m^2\,kg^{-1}$, i.e. of the order of 7%.

SWIRcam comparison

Figure 7 shows an example of a normalized image acquired with the NIR (left) and SWIR (right) cameras with their respective albedo profiles. The NIR image was taken with the same measurement protocol as the SWIRcam; details of the apparatus are provided by Langlois and others (2010b). One should note that the differences in the albedo profiles (0.8–0.9 for the NIR picture and 0.25–0.3 for the SWIR picture) are simply due to a difference in wavelengths (~850 nm for the NIR image and 1300 nm for the SWIR image). The NIR image shows a better vertical resolution ($1.3\,mm\,pixel^{-1}$), but the SWIR image ($2.0\,mm\,pixel^{-1}$) shows a much more detailed snow-pit stratigraphy (i.e. more sensitive to changes in SSA). This is shown by the albedo profiles beside the pictures. There is much more variability, especially in the top portion of the profile where the albedo

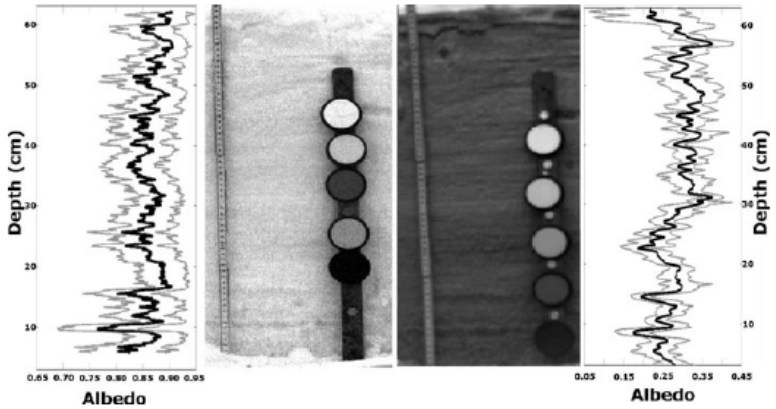

Fig. 7. Albedo profile taken with NIR (left) and SWIR (right) pictures with their mean horizontal (black), minimum and maximum (gray) profiles.

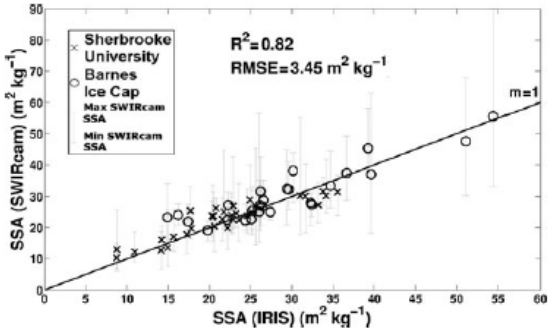

Fig. 8. Compared SSA measurements of the IRIS system and the SWIRcam taken at the experimental site SIRENE (×) and Barnes Ice Cap (○) during the 2011 winter. The error bars give the minimum and maximum horizontal SWIRcam albedo variation at their respective heights.

range is ~0.1 for the NIR picture and ~0.2 for the SWIR picture. This variability is mainly due to the presence of an ice lens near the surface which is not clearly visible in the NIR picture because of its high sensitivity to lighting conditions. This shows the advantage of using instruments in the SWIR spectrum rather than the NIR spectrum since the SWIRcam is less sensitive to lighting conditions.

To validate the albedo measurements taken with the SWIRcam, five profiles were taken during the 2011 winter and compared with point measurements taken with the IRIS system along those profiles. Figure 8 shows the comparison between the SSA data derived from the SWIRcam and IRIS measurements taken at SIRENE (three profiles) and on Barnes Ice Cap (two profiles). The error bars correspond to the minimum and maximum SWIRcam SSA horizontal values of the snow wall section. The SSA measurements derived from the SWIRcam were calculated using equation 6 of Arnaud and others (2011) since the SWIRcam albedo measurements are hemispherical-directional ($K_0 = 9/7$). The SSAs measured with both SWIRcam and IRIS systems are in good agreement, with little variability ($R^2 = 0.82$; rmse = 3.45 m^2 kg^{-1}). There is some variability in the SWIRcam measurements because the values extracted from the profiles are averaged over 5–10 cm horizontally. The averaged horizontal length depends on the length available within the picture and can vary from one site to another. This averaging does not eliminate the possibility of extracting two-dimensional SSA information within a SWIR picture. It is done mainly to extract the overall vertical variability due to the layering of snowpack stratigraphy. The mean standard deviation over the averaged values is of the order of 2.0 m^2 kg^{-1}, which is comparable to the rmse. This explains most of the variability in the comparison between the two instruments.

The SWIRcam also provides more information than the IRIS system, by allowing characterization of the stratigraphy within the snow pit. Figures 9–11 show examples of SWIR photographs (right side) taken with the camera and the derived SSA profile (left side) taken at the SIRENE experimental site (Figs 9 and 11) and on Barnes Ice Cap (Fig. 10). SSA measurements taken with the IRIS system along the same profiles are also shown.

As mentioned by Langlois and others (2010b), the use of a passive-based camera to measure snow albedo is complex because numerous variables (lighting conditions, camera angle, lighting normalization) affect the measure-

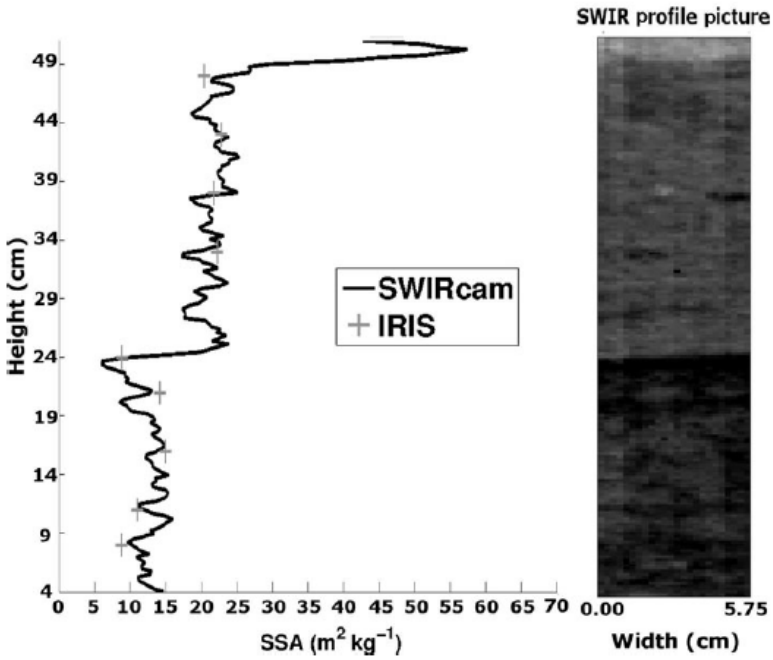

Fig. 9. SSA profile derived from the IRIS system and the SWIRcam taken at SIRENE during the 2011 winter. The picture on the right shows the portion of the snow pit (5.75 cm width) from which the mean SWIR albedo was computed.

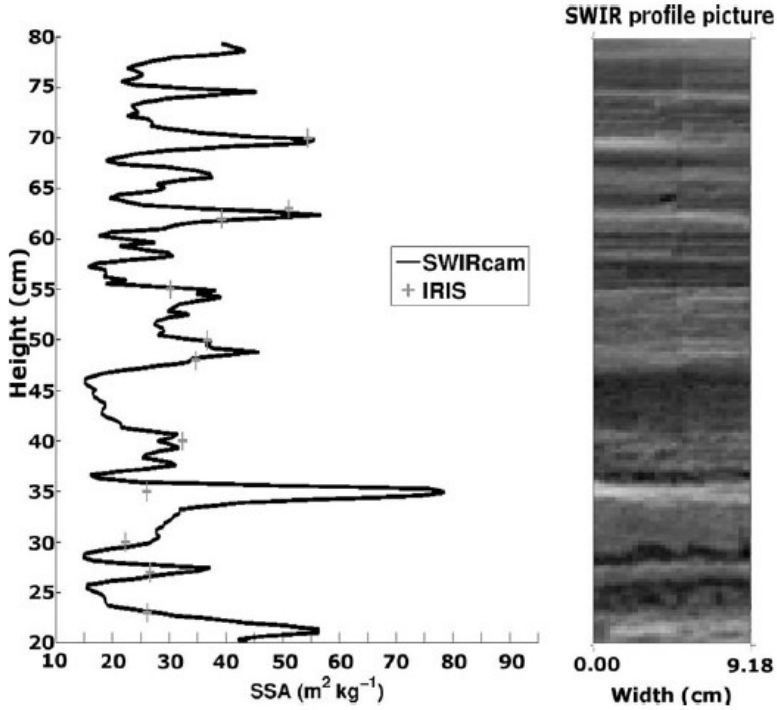

Fig. 10. SSA profile derived from the IRIS system and the SWIRcam taken on Barnes Ice Cap in March 2011. The picture on the right shows the portion of the snow pit (9.18 cm width) from which the mean SWIR albedo was computed.

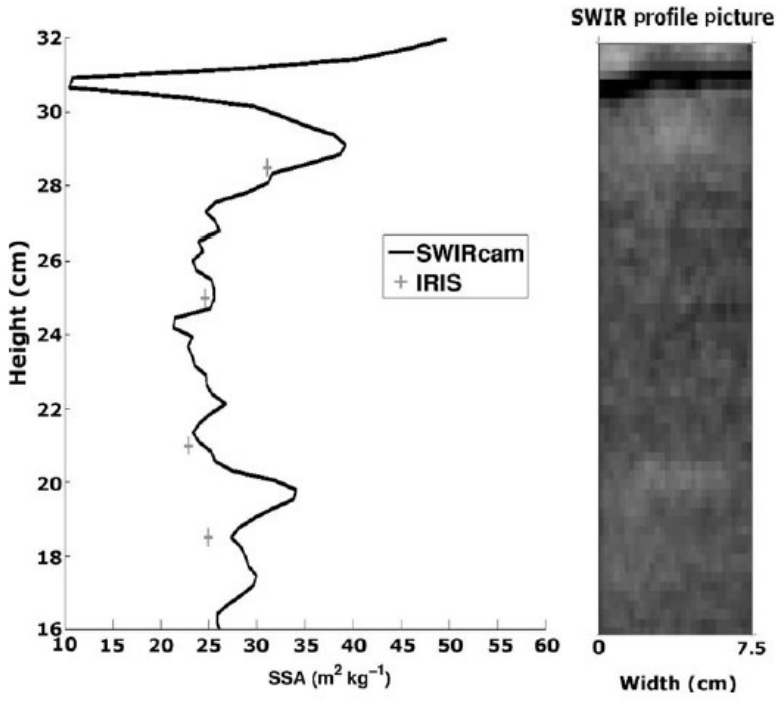

Fig. 11. SSA profile derived from the IRIS system and the SWIRcam taken at SIRENE during the 2011 winter. The picture on the right shows the portion of the snow pit (7.5 cm width) from which the mean SWIR albedo was computed. The ice lens (height ~31 cm) can clearly be distinguished by its dark region at the top of the snow pit.

ments. This reduces the accuracy and reproducibility of the measurements compared to those made with IRIS. The Figure 9 profile was measured twice with a 5 min interval, the set-up was dismantled between measurements, and the mean albedo variation between the two measurements along the entire profile was 5%, with an rmse of 0.02. Another interesting feature of these measurements (Figs 9–11) is the albedo variability provided at 2 mm vertical resolution. At this resolution, one can distinguish from the SSA profile a fresh snow layer (49–50 cm; $39\,m^2\,kg^{-1} < SSA < 55\,m^2\,kg^{-1}$, mean SSA = $47.4\,m^2\,kg^{-1}$), a dense rounded snow grain slab (25–49 cm; $17.0\,m^2\,kg^{-1} < SSA < 27.0\,m^2\,kg^{-1}$, mean SSA = $21.6\,m^2\,kg^{-1}$) a hard snow crust (21–24 cm; $5.0\,m^2\,kg^{-1} < SSA < 13.0\,m^2\,kg^{-1}$, mean SSA = $9.0\,m^2\,kg^{-1}$) and a coarse depth-hoar layer (4–21 cm; $8.0\,m^2\,kg^{-1} < SSA < 16.0\,m^2\,kg^{-1}$, mean SSA = $12.8\,m^2\,kg^{-1}$).

The SWIR image (Fig. 10, right) from which the SSA profile was extracted also reveals the fine vertical variability of SSA well. Figure 10 is a good example of the vertical information that the SWIRcam provides. Compared to Figure 9, Figure 10 shows much more vertical SSA variability on Barnes Ice Cap, which could be omitted by IRIS measurements. In fact, thin (~2 cm) high-SSA ($>50\,m^2\,kg^{-1}$) layers could be missed with IRIS since the sampler is 6 cm high. This shows the importance of high-resolution SSA profiles. This high resolution can even distinguish a 4 mm thick ice lens within the snow pit as shown in Figure 11. The dark region with a minimal SSA of $4.6\,m^2\,kg^{-1}$ at 31 cm was visually associated with a clear ice lens. The value shown of $10.5\,m^2\,kg^{-1}$ at 31 cm on the SSA profile (Fig. 11) is caused by the slight inclination of the ice lens. Thus, the horizontal mix of snow with ice raises the averaged SSA value at that height.

Since ice lenses affect the snow microwave signature considerably (Grody, 2008; Rees and others, 2010), it is essential that they be detected and characterized. With the SWIRcam it is possible to characterize fairly precisely the position of the lens and its thickness along a certain horizontal width. This is another excellent application of this new SWIRcam.

CONCLUSION

The main objective of this paper was to test the robustness of the determination of snow SSA from SWIR albedo measurements using two methods that differ in their sampling technique, lighting conditions and detector type. The two instruments presented in this paper, which are based on passive optical solar measurements (SWIRcam) or active laser-based devices (IRIS), have been compared. The IRIS measurements were validated with an independent method (μ-CT) and have proven to be accurate for SSA measurements within 10%. For both instruments, we used the Kokhanovsky and Zege (2004) model to derive the snow grain SSA, showing the usefulness of this equation with a fixed shape factor (b) value for the different shapes measured (fresh snow, rounded grains, depth hoar) and an escape function, K_0, adapted to the type of albedo measured (directional and/or hemispherical).

Among the optical methods tested here, the most accurate and precise instrument for determining snow SSA is the IRIS system (relative variations of 3–5% on SSA measurements). Similar to the DUFISSS instrument (Gallet and others, 2009), the mean accuracy of the IRIS device is on the order of 10% compared to the methane adsorption method (considered as reference measurement). The downside of such a system is the need to extract snow samples for measurements, which can be difficult depending on snow conditions and stratigraphy (ice lenses, non-cohesive layers) and which lengthens the acquisition time to complete a full snow profile (15–30 min). Also, the vertical resolution of this system is lower than NIR and SWIRcams or with POSSSUM.

The lower sensitivity to illumination conditions (Fig. 7) and the lower sensitivity to absorbing snow impurities make the SWIRcam a more accurate instrument for snow grain-size retrieval than the 850 nm NIR camera used by Langlois and others (2010b). Also, the vertical resolution for albedo measurements using the SWIRcam (~2 mm) gives more detailed stratigraphic information than the IRIS system (Fig. 10) and can detect thin ice lenses within the snowpack (Fig. 11). Another version of the SWIRcam used in this study was developed by © Xenics with a better spatial resolution, meaning the SWIR image could have a better resolution without having to take multiple pictures closer to the snow wall to increase the resolution.

In addition to other types of profile measurements for density, thermal conductivity (Morin and others, 2010) or liquid water content using capacitance plates (e.g. Denoth, 1989) or snow forks (e.g. Sihvola and Tiuri, 1986), the precise determination of vertical profiles of snow grain SSA and stratigraphy (layering) using a lightweight optical system is essential for improving snow and radiative transfer models. A thorough comparison between existing methods for SSA determination – optical, stereology, methane adsorption and X-ray microtomography – is needed to further define the accuracy and limitations of each approach.

ACKNOWLEDGEMENTS

We thank Ian Baker who allowed us to acquire the μ-CT grain-size measurements. The research at Dartmouth College was supported by US National Science Foundation (NSF) grant OPP-0821056. The views and conclusions contained herein are those of the authors and should not be interpreted as necessarily representing official policies, either expressed or implied, of the NSF or the US Government. We thank Jean-Charles Gallet who processed and provided the methane adsorption measurements, and Z. Jin who provided albedo calculations for different grain shapes (Fig. 1). All of our colleagues who helped us during the field campaigns in France and Canada are also gratefully acknowledged. This work was supported by the Natural Sciences and Engineering Research Council of Canada, the Canadian Polar Continental Shelf Program (Barnes Ice Cap field campaign), Environment Canada (principal investigator Anne Walker), Centre National de la Recherche Scientifique (CNRS), France, Institut Paul-Émile Victor (IPEV; French Polar Institute), the Programme International de Collaboration Scientifique (PICS) of CNRS, and the Ministère des Relations Internationales du Québec and Ministère des Affaires Étrangères et Européennes de la République Française (Consulat Général de France à Québec) in the framework of the 63e Session de la Commission Permanente de Coopération Franco-Québécoise.

REFERENCES

Aoki T, Aoki T, Fukabori M, Hachikubo A, Tachibana Y and Nishio F (2000) Effects of snow physical parameters on spectral albedo

and bi-directional reflectance of snow surface. *J. Geophys. Res.*, **105**(D8), 10 219–10 236 (doi: 10.1029/1999JD901122)

Armstrong RL and Brun E eds. (2008) *Snow and climate: physical processes, surface energy exchange and modelling*. Cambridge University Press, Cambridge

Arnaud L and 7 others (2011) Measurement of vertical profiles of snow specific surface area with a 1 cm resolution using infrared reflectance: instrument description and validation. *J. Glaciol.*, **57**(201), 17–29 (doi: 10.3189/002214311795306664)

Brown RD (2010) Analysis of snow cover variability and change in Québec, 1948–2005. *Hydrol. Process.*, **24**(14), 1929–1954 (doi: 10.1002/hyp.7565)

Brucker L, Picard G and Fily M (2010) Snow grain-size profiles deduced from microwave snow emissivities in Antarctica. *J. Glaciol.*, **56**(197), 514–526

Brucker L and 7 others (2011) Modeling time series of microwave brightness temperature at Dome C, Antarctica, using vertically resolved snow temperature and microstructure measurements. *J. Glaciol.*, **57**(201), 171–182 (doi: 10.3189/002214311795306736)

Butt MJ and Kelly REJ (2008) Estimation of snow depth in the UK using the HUT snow emission model. *Int. J. Remote Sens.*, **29**(14), 4249–4267 (doi: 10.1080/01431160801891754)

Chang ATC, Foster JL, Hall DK, Rango A and Hartline BK (1982) Snow water equivalent estimation by microwave radiometry. *Cold Reg. Sci. Technol.*, **5**(3), 259–267 (doi: 10.1016/0165-232X(82)90019-2)

Chen S and Baker I (2010) Evolution of individual snowflakes during metamorphism. *J. Geophys. Res.*, **115**(D21), D21114 (doi: 10.1029/2010JD014132)

Denoth A (1989) Snow dielectric measurements. *Adv. Space Res.*, **9**(1), 233–243

Derksen C and 6 others (2010) Development of a tundra-specific snow water equivalent retrieval algorithm for satellite passive microwave data. *Remote Sens. Environ.*, **114**(8), 1699–1709 (doi: 10.1016/j.rse.2010.02.019)

Domine F, Cabanes A, Taillandier AS and Legagneux L (2001) Specific surface area of snow samples determined by CH_4 adsorption at 77 K and estimated by optical microscopy and scanning electron microscopy. *Environ. Sci. Technol.*, **35**(4), 771–780 (doi: 10.1021/es001168n)

Domine F, Salvatori R, Legagneux L, Salzano R, Fily M and Casacchia R (2006) Correlation between the specific surface area and the short wave infrared (SWIR) reflectance of snow. *Cold Reg. Sci. Technol.*, **46**(1), 60–68 (doi: 10.1016/j.coldregions.2006.06.002)

Domine F and 7 others (2008) Snow physics as relevant to snow photochemistry. *Atmos. Chem. Phys.*, **8**(2), 171–208 (doi: 10.5194/acp-8-171-2008)

Dupont F and 7 others (2012) Monitoring the melt season length of the Barnes Ice Cap over the 1979–2010 period using active and passive microwave remote sensing data. *Hydrol. Process.* (doi: 10.1002/hyp.9382)

Durand M, Kim EJ and Margulis SA (2008) Quantifying uncertainty in modeling snow microwave radiance for a mountain snowpack at the point-scale, including stratigraphic effects. *IEEE Trans. Geosci. Remote Sens.*, **46**(6), 1753–1767 (doi: 10.1109/TGRS.2008.916221)

Fernandes R, Zhao H, Wang X, Key J, Qu X and Hall A (2009) Controls on Northern Hemisphere snow albedo feedback quantified using satellite Earth observations. *Geophys. Res. Lett.*, **36**(21), L21702 (doi: 10.1029/2009GL040057)

Fierz C and 8 others. (2009) *The international classification for seasonal snow on the ground*. UNESCO–International Hydrological Programme, Paris (IHP Technical Documents in Hydrology 83)

Flanner MG, Zender CS, Randerson JT and Rasch PJ (2007) Present-day climate forcing and response from black carbon in snow. *J. Geophys. Res.*, **112**(D11), D11202 (doi: 10.1029/2006JD008003)

Flin F and 9 others (2005) Adaptive estimation of normals and surface area for discrete 3-D objects: application to snow binary data from x-ray tomography. *IEEE Trans. Image Process.*, **14**(5), 585–596 (doi: 10.1109/TIP.2005.846021)

Foster JL and 10 others (2011) A blended global snow product using visible, passive microwave and scatterometer satellite data. *Int. J. Remote Sens.*, **32**(5), 1371–1395 (doi: 10.1080/01431160903548013)

Gallet J-C, Domine F, Zender CS and Picard G (2009) Measurement of the specific surface area of snow using infrared reflectance in an integrating sphere at 1310 and 1550 nm. *Cryosphere*, **3**(2), 167–182 (doi: 10.5194/tc-3-167-2009)

Grannas AM and 34 others (2007) An overview of snow photochemistry: evidence, mechanisms and impacts. *Atmos. Chem. Phys.*, 7(16), 4329–4373 (doi: 10.5194/acp-7-4329-2007)

Grenfell TC and Warren SG (1999) Representation of a non-spherical ice particle by a collection of independent spheres for scattering and absorption of radiation. *J. Geophys. Res.*, **104**(D24), 31 697–31 709 (doi: 10.1029/2005JD005811)

Grody N (2008) Relationship between snow parameters and microwave satellite measurements: theory compared with Advanced Microwave Sounding Unit observations from 23 to 150 GHz. *J. Geophys. Res.*, **113**(D22), D22108 (doi: 10.1029/2007JD009685)

Hall A (2004) The role of surface albedo feedback in climate. *J. Climate*, **17**(7), 1550–1568 (doi: 10.1175/1520-0442(2004)017<1550:TROSAF>2.0.CO;2)

Jin Z, Charlock TP, Yang P, Xie Y and Miller W (2008) Snow optical properties for different particle shapes with application to snow grain size retrieval and MODIS/CERES radiance comparison over Antarctica. *Remote Sens. Environ.*, **112**(9), 3563–3581 (doi: 10.1016/j.rse.2008.04.011)

Kokhanovsky AA and Zege EP (2004) Scattering optics of snow. *Appl. Opt.*, **43**(7), 1589–1602 (doi: 10.1364/AO.43.001589)

Kontu A and Pulliainen J (2010) Simulation of spaceborne microwave radiometer measurements of snow cover using in situ data and brightness temperature modeling. *IEEE Trans. Geosci. Remote Sens.*, **48**(3), 1031–1044 (doi: 10.1109/TGRS.2009.2030499)

Langlois A, Royer A and Goïta K (2010a) Analysis of simulated and spaceborne passive microwave brightness temperatures using in situ measurements of snow and vegetation properties. *Can. J. Remote Sens.*, **36**(S1), S135–S148 (doi: 10.5589/m10-016)

Langlois A and 8 others (2010b) On the relationship between snow grain morphology and *in-situ* near infrared calibrated reflectance photographs. *Cold Reg. Sci. Technol.*, **61**(1), 34–42 (doi: 10.1016/j.coldregions.2010.01.004)

Lyapustin A, Tedesco M, Wang Y, Aoki T, Hori M and Kokhanovsky A (2009) Retrieval of snow grain size over Greenland from MODIS. *Remote Sens. Environ.*, **113**(9), 1976–1987 (doi: 10.1016/j.rse.2009.05.008)

Matzl M and Schneebeli M (2006) Measuring specific surface area of snow by near-infrared photography. *J. Glaciol.*, **52**(179), 558–564 (doi: 10.3189/172756506781828412)

Matzl M and Schneebeli M (2010) Stereological measurement of the specific surface area of seasonal snow types: comparison to other methods, and implications for mm-scale vertical profiling. *Cold Reg. Sci. Technol.*, **64**(1), 1–8 (doi: 10.1016/j.coldregions.2010.06.006)

Mätzler C (2002) Relation between grain-size and correlation length of snow. *J. Glaciol.*, **48**(162), 461–466 (doi: 10.3189/172756502781831287)

Mätzler C (2006) *Thermal microwave radiation: applications for remote sensing*. Institution of Engineering and Technology, London (IET Electronic Waves Series 52)

Mätzler C and Wiesmann A (1999) Extension of the microwave emission model of layered snowpacks to coarse-grained snow. *Remote Sens. Environ.*, **70**(3), 317–325 (doi: 10.1016/S0034-4257(99)00047-4)

Morin S, Domine F, Arnaud L and Picard G (2010) In-situ monitoring of the time evolution of the effective thermal

conductivity of snow. *Cold Reg. Sci. Technol.*, **64**(2), 73–80 (doi: 10.1016/j.coldregions.2010.02.008)

Nolin AW and Dozier J (2000) A hyperspectral method for remotely sensing the grain size of snow. *Remote Sens. Environ.*, **74**(2), 207–216 (doi: 10.1016/S0034-4257(00)00111-5)

Painter TH, Molotch NP, Cassidy M, Flanner M and Steffen K (2007) Contact spectroscopy for determination of stratigraphy of snow optical grain size. *J. Glaciol.*, **53**(180), 121–127 (doi: 10.3189/172756507781833947)

Park G, Huffaker DL, Zou Z, Shchekin OB and Deppe DG (1999) Temperature dependence of lasing characteristics for long-wavelength (1.3-μm) GaAs-based quantum-dot lasers. *Photon. Technol. Let.*, **11**(3), 301–303

Picard G, Arnaud L, Domine F and Fily M (2009) Determining snow specific surface area from near-infrared reflectance measurements: numerical study of the influence of grain shape. *Cold Reg. Sci. Technol.*, **56**(1), 10–17 (doi: 10.1016/j.coldregions.2008.10.001)

Pulliainen J (2006) Mapping of snow water equivalent and snow depth in boreal and sub-arctic zones by assimilating space-borne microwave radiometer data and ground-based observations. *Remote Sens. Environ.*, **101**(2), 257–269 (doi: 10.1016/j.rse.2006.01.002)

Rees A, Lemmetyinen J, Derksen C, Pulliainen J and English M (2010) Observed and modelled effects of ice lens formation on passive microwave brightness temperatures over snow covered tundra. *Remote Sens. Environ.*, **114**(1), 116–126 (doi: 10.1016/j.rse.2009.08.013)

Sihvola A and Tiuri M (1986) Snow fork for field determination of the density and wetness profiles of a snow pack. *IEEE Trans. Geosci. Remote Sens.*, **24**(5), 717–721 (doi: 10.1109/TGRS.1986.289619)

Taillandier A-S, Domine F, Simpson WR, Sturm M and Douglas TA (2007) Rate of decrease of the specific surface area of dry snow: isothermal and temperature gradient conditions. *J. Geophys. Res.*, **112**(F3), F03003 (doi: 10.1029/2006JF000514)

Takala M and 7 others (2011) Estimating northern hemisphere snow water equivalent for climate research through assimilation of space-borne radiometer data and ground-based measurements. *Remote Sens. Environ.*, **115**(12), 3517–3529 (doi: 10.1016/j.rse.2011.08.014)

Tedesco M and Kim EJ (2006) Retrieval of dry-snow parameters from microwave radiometric data using a dense-medium model and genetic algorithms. *IEEE Trans. Geosci. Remote Sens.*, **44**(8), 2143–2151 (doi: 10.1109/TGRS.2006.872087)

Toure AM, Goïta K, Royer A, Mätzler C and Schneebeli M (2008) Near-infrared digital photography to estimate snow correlation length for microwave emission modeling. *Appl. Opt.*, **47**(36), 6723–6733 (doi: 10.1364/AO.47.006723)

Warren SG and Wiscombe WJ (1980) A model for the spectral albedo of snow. II. Snow containing atmospheric aerosols. *J. Atmos. Sci.*, **37**(12), 2734–2745 (doi: 10.1175/1520-0469(1980)037<2734:AMFTSA>2.0.CO;2)

Wiesmann A and Mätzler C (1999) Microwave emission model of layered snowpacks. *Remote Sens. Environ.*, **70**(3), 307–316 (doi: 10.1016/S0034-4257(99)00046-2)

Wiscombe WJ and Warren SG (1980) A model for the spectral albedo of snow. I. Pure snow. *J. Atmos. Sci.*, **37**(12), 2712–2733 (doi: 10.1175/1520–0469(1980)037<2712:AMFTSA>2.0.CO;2)

Xie Y, Yang P, Gao B, Kattawar G and Mishchenko M (2006) Effect of ice crystal shape and effective size on snow bidirectional reflectance. *J. Quant. Spectrosc. Radiat. Transfer*, **100**(1–3), 457–469 (doi: 10.1016/j.jqsrt.2005.11.056)

Yang P and Liou KN (1996) Geometric-optics–integral-equation method for light scattering by nonspherical ice crystals. *Appl. Opt.*, **35**(33), 6568–6584 (doi: 10.1364/AO.35.006568)

MS received 30 November 2011 and accepted in revised form 25 May 2012